DYNAMIC, STRUCTURAL, AND MECHANISTIC STUDY OF GLUTATHIONE TRANSFERASES

By

Lawrence C. Thompson

Dissertation

Submitted to the Faculty of the

Graduate School of Vanderbilt University

in partial fulfillment of the requirements

for the degree of

DOCTOR OF PHILOSOSPHY

in

Biochemistry

August, 2006

Nashville, Tennessee

Approved:

Professor Richard N. Armstrong

Professor Lawrence J. Marnett

Professor Micheal R. Waterman

Professor Charles R. Sanders

Professor Albert H. Beth

To my wife, Stacy, who has held my hand throughout this entire journey

and

To my two amazing daughters, Abigail and Blake, who were given to me along the way

ACKNOWLEDGEMENTS

This work could not have been possible without the generous financial support of the National Institute of Health or the Center for Molecular Toxicology at the Vanderbilt University Medical Center.

I would like to thank all the members of the Mass Spectrometry Research Center including Dr. David Hachey, Lisa Manier, and Dawn Overstreet for all of their help in organizing and executing all the mass spectrometry experiments.

I would like to thank Simona Codreanu from whom I inherited the HDX project. For pioneering this technique in our lab thereby giving me a jumpstart in my graduate career.

I would like to thank the Center for Structural Biology for use of the X-ray facility and Dr. Joel Harp who assisted me in all aspects of crystallography and data collection.

I would like to thank Dr. Jane Ladner who collaborated with us and solved all of the crystal structures shown in this thesis.

I would like to thank Dr. Heini Dirr and his associates who collaborated on the dimer interface mutants. Their folding data made our HDX-MS work meaningful.

I would like to thank Dr. Kerry Filgrove who taught me how to be an enzymologist. His example of dedication and forethought was vital to my success. He was also a good friend to me along the way.

Finally, I would like to thank my boss, Dr. Richard Armstrong, for allowing me to work in his lab and providing me with a project that had significant challenges and resulted in great rewards.

TABLE OF CONTENTS

LIST OF TABLES

LIST OF FIGURES

LIST OF ABBREVIATIONS

GSH	reduced glutathione
GSSG	oxidized glutathione
GSO_3^-	glutathione sulfonate
ROS	reactive oxygen species
MAPEG	membrane associated proteins in ecosanoid and glutathione metabolism
VOC	vicinal oxygen chelate
Grx1	glutaredoxin 1
Grx2	glutaredoxin 2
DsbA	Disulfide Bond Isomerase A
rGSTM1-1	rat glutathione transferase class Mu isozyme 1-1
cHBPA	cis-*o*-Hydroxybenzylidene pyruvic acid
HCCA	2-Hydroxychromene-2-carboxylic acid
tHBPA	trans-*o*-Hydroxybenzylidene pyruvic acid
ATP	adenosine 5'-triphosphate
NADPH	nicotine adenine dinucleotide phosphate
tMBPA	trans-*o*-Methoxybenzylidene pyruvic acid
MCCA	2-Methoxychromene-2-Carboxylic acid
DTNB	dithiobis-2-nitrobenzoic acid
CDNB	1-chloro-2,4-dinitrobenzene
EDTA	ethylene-diaminedtetraacetic acid
DTT	dithiothreitol

LB	Luria broth
IPTG	isopropyl-β-D-thiogalactopyranoside
DEAE	Diethylaminoethyl
SP	Methyl sulfonate
HEPES	4-(2-Hydroxyethyl)-1-Piperazineethansulfonic acid
Tris	Tris(hydroxymethyl)aminomethane
MOPS	3-[N-Morpholino]propanesulfonic acid
TFA	trifluoroacetic acid
D_2O	deuterium oxide
DMSO	dimethyl sulfoxide
HA	hydroxyappetite
PCR	polymerase chain reaction
OD	optical density
SDS-PAGE	sodium dodecyl sulfate polyacrylamide gel electrophoresis
MW	molecular weight
UV-Vis	ultraviolet-visible
CD	circular dichroism
MALDI	matrix assisted laser desorption ionization
RP-HPLC	reverse phase high pressure liquid chromatography
FPLC	fast protein liquid chromatography
HDX-MS	hydrogen-deuterium exchange mass spectrometry
ESI-MS	electrospray ionization mass spectrometry
NMR	nuclear magnetic resonance

CHAPTER I

INTRODUCTION

Toxicology and Xenobiotic Metabolism

Toxicology is the study of the affects of endo/xenobiotics on organisms, the environment, etc. It traces its roots back to the study and use of poisons as weapons of war, assassination, and survival (*1*). Modern toxicology began during the industrial revolution. One of the by-products of this new productivity was the exposure of many workers to new toxins and the release of these toxins into the environment. Beginning in the 1800's, advances in analytical chemistry allowed detection and identification of these new compounds and in turn, how they affected those who were exposed (*1*). In more recent years, the tools of the toxicologist have become refined so that effects of endo/xenobiotics on the cellular and molecular level can be measured. These tools have been of great importance in the pharmaceutical industry. Drugs (xenobiotics by definition) and their metabolites are screened prior to use to eliminate most unwanted side effects. Millions of dollars are saved because many molecular scaffolds are avoided at the outset because their metabolism is known to lead to toxic intermediates. In many ways, the desire to find new drugs has driven the study of xenobiotic metabolism (*1*).

A large majority of xenobiotics are not absorbed into the host cells and upon exposure are simply excreted; however, for those that do make it in, there are large numbers of enzymes that recognize, bind, react/conjugate, and excrete these invaders (*1*). Most organs or cell types express some version of these enzymes but they are in highest

abundance in the liver. Those that perform chemistry on xenobiotics are grouped (based on chemistry) into either Phase I or Phase II enzymes (Figure 1).

Reaction	Enzyme	Localization
Phase I		
Hydrolysis	Esterase	Microsomes, cytosol, lysosomes, blood
	Petidase	Blood, lysosomes
	Epoxide hydrolase	Microsomes, cytosol
Reduction	Azo- and nitro-reduction	Microflora, microsomes, cytosol
	Carbonyl reduction	Cytosol, blood, microsomes
	Disulfide reduction	Cytosol
	Sulfoxide reduction	Cytosol
	Quinone reduction	Cytosol, microsomes
	Reductive dehalogenation	Microsomes
Oxidation	Alcohol dehydrogenase	Cytosol
	Aldehyde dehydrogenase	Mitochondria, cytosol
	Aldehyde oxidase	Cytosol
	Xanthine oxidase	Cytosol
	Monoamine oxidase	Mitochondria
	Diamine oxidase	Cytosol
	Prostaglandin H synthase	Microsomes
	Flavin-monooxygenases	Microsomes
	Cytochrome P450	Microsomes
Phase II		
	Glucuronide conjugation	Microsomes
	Sulfate conjugation	Cytosol
	Glutathione conjugation	Cytosol, microsomes
	Amino acid conjugation	Mitochondria
	Acylation	Mitochondria, cytosol
	Methylation	Cytosol, microsomes, blood

Figure 1. Enzymatic paths for the biotransformation of endo and xenobiotic compounds. Reproduced from (*1*) page 136 with the permission of the McGraw-Hill Companies.

Phase I enzymes perform reactions whose primary consequence is alteration of the oxidation state of the compound; while, Phase II enzymes conjugate the compound with another construct (Figure 1). The resulting conjugate is either immediately exported and excreted or is broken down further and then excreted (*1*).

Of the Phase II pathways, GSH and its transferase enzymes (GSH transferases) are one of the most studied. This is most likely due to GSH's constitutive presence in almost all cell types. In the liver, GSH concentrations can be as high as 10mM (*1, 2*).

GSH Synthesis, Regulation, and Chemistry

GSH (γ-Glu-Cys-Gly) is a tripeptide that carries out many important cellular reactions. Its chemistry is derived from its structure (Figure 2). The γ-glutamate linkage gives the molecule a unique signature in the cytosol allowing for its regulation by specific peptidases and affording resistance to non-specific peptidases allowing its concentration to reach chemoprotective levels. The cysteine gives the molecule its redox/nucleophilic characteristics with the sulfur side chain performing almost all of its chemistry (*1-6*).

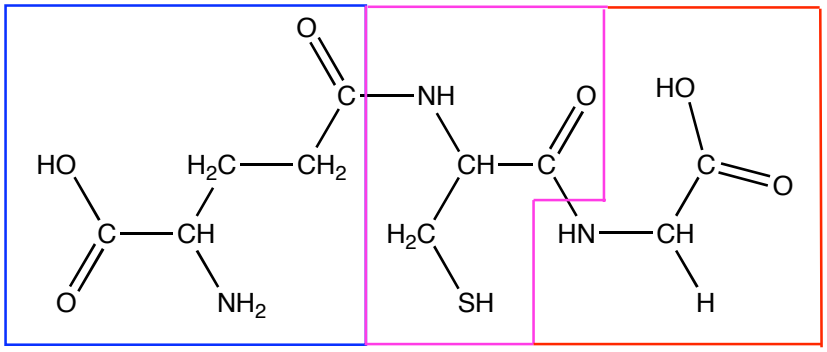

Figure 2. Chemical structure of GSH (from left to right): **γ-glumate**, **cysteine**, and **glycine**

The GSH concentration in the cell is maintained through a cycle of GSH synthesis and catabolism via the γ-glutamyl cycle (Figure 3). It is synthesized in two ATP dependent reactions. The first step is the formation of a peptide bond between the glutamate side

chain and cysteine by γ-glutamylcysteine synthethase. In the second step, glycine is attached to the C-terminus of the cysteine moiety via GSH synthetase. Following its synthesis, GSH can either perform chemistry or be catabolized. It is catabolized in two steps. First, the γ-glutamate is transferred to another amino acid (AA) by γ-glutamyl transpeptidase. In the second step, cysteine and glycine are separated by a general peptidase. γ-glutamate-AA is then transformed back into glutamate by two other enzymes (Figure 3). This cycle is controlled by feed-back inhibition so that the cellular GSH levels remain constant (*2, 3, 5-7*).

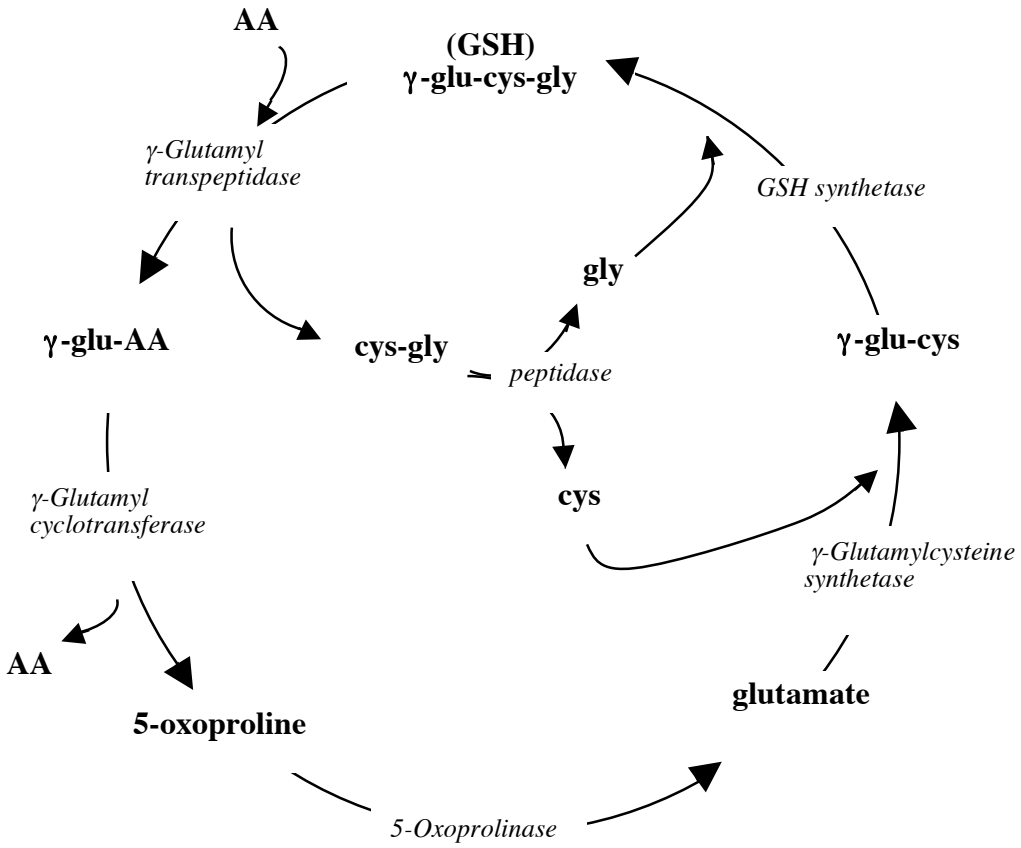

Figure 3. The γ-glutamyl cycle [adapted from (*2, 6, 7*)]. 5-Oxoprolinase, γ-glutamylcysteine synthetase, and GSH synthetase are all ATP dependent enzymes.

GSH performs many chemical reactions in the cell. Most of these fall into two categories: redox and nucleophilic substitution. Both chemistries are accessible because of the chemical/physical properties of the sulfur atom. As a group VI element, sulfur completes its octet of electrons with two lone pairs and two covalent bonds (similar to oxygen, also group IV). As a period 3 element, it has a complete s/p shell (that oxygen lacks) so it is not as electronegative; therefore sulfur is stable in its reduced (RSH), anionic (RS^-), and oxidized (RSSR) states. This also makes it a better nucleophile than oxygen because the valence electrons are more distant from the nucleus, therefore more polarizable. These characteristics are similar to the pattern seen in the halogens.

GSH's redox chemistry involves recycling GSH from its reduced to oxidized (GSSG) states and back (Figure 4). GSH is oxidized non-enzymatically by ROS and enzymatically via peroxidases and thioltransferases. Peroxidase enzymes use GSH to reduce peroxides to water/alcohols. Thioltransferases use GSH to mediate the oxidation state of proteins and small molecule thiols. GSH reductase reduces GSSG back to free thiol while oxidizing NADPH (Figure 4) (*2, 3, 5, 8*).

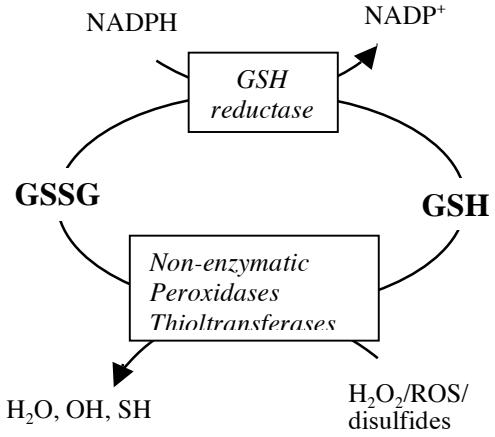

Figure 4. GSH redox cycle [adapted from (*2, 3*)].

The second major chemistry of GSH is nucleophilic substitution. This chemistry can be summarized in the generic nucleophilic substitution reaction (Scheme 1), where R is the electrophile and X is the leaving group. Attack of the sulfur displaces the leaving group and yields the GSR conjugate. The reduced form will react uncatalyzed with most electrophiles to some appreciable rate. In its anionic (GS^- or thiolate) form, GSH is orders of magnitude more reactive (*4, 9, 10*).

$$GSH + RX \longrightarrow GSR + HX$$ **Scheme 1**

Fate of GSH Conjugates: Metabolism versus Catabolism

In most biological systems, GSH conjugates are metabolized and excreted. However, some bacteria form GSH conjugates on pathways of xenobiotic catabolism (*11, 12*). Some biosynthetic pathways form GSH conjugates or are GSH dependent (*4, 13-18*); however, those functions and pathways are beyond the scope of this thesis.

When a GSH conjugate falls into a metabolic pathway, it is recognized, broken down, and excreted. The initial steps of its catabolism follow the normal GSH catabolic pathway (Figure 3). γ-Glutamyl transpeptidase and another peptidase remove the glutamate and glycine moieities in turn. The resulting cysteine conjugate falls out of the γ-glutamyl cycle and into excretory pathways. It can be passed intact through the bile or travel to the kidney where it is acylated (by Acetyl-CoA) to a mercapturic acid and excreted. It can be broken down further by β lyase to the free thiol (HSX). This free thiol can now fall into other Phase II pathways like methylation or glucuronidation for further processing and excretion (*1, 2, 6, 19, 20*).

Though bacterial genomes contain many of the same GSH transferases responsible for xenobiotic metabolism, additional GSH transferases have been discovered that form conjugates as intermediates during xenobiotic catabolism (Figure 5) (*11, 12*). The chemistries here are the same as seen previously: nucleophilic substitution (Figure 5a,b, and d) and reductions (Figure 5c). However, the fate of the conjugate is different: it is only a transient partner during the catabolism (Figure 5). The GSH is added and then removed. The altered molecule is then passed to the next enzyme in the pathway.

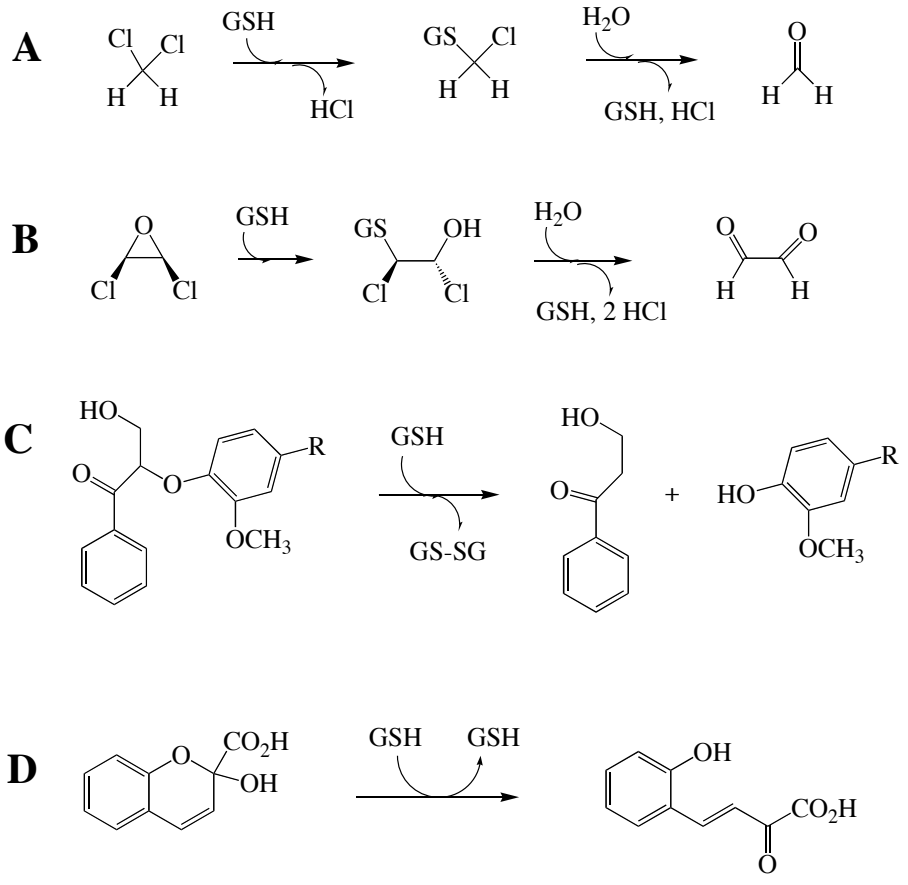

Figure 5. GSH and xenobiotic catabolism: (A) dehalogenation of dicholoromethane (B) opening of the expoxide ring arising from the oxidation of cis-1,2-dichloroethene and isoprene (C) ether bond cleavage of phenolic ethers of lignin (D) isomerization of 2-hydroxychromene-2-carboxylate [selected reactions from Figure 2 (*12*)].

GSH Transferases: Evolution, Catalysis, and Secondary Structure

The GSH transferases are a superfamily of enzymes that are present in almost all aerobic organisms. Within the GSH superfamily lie four family groups: the cytoplasmic (canonical), mitochondrial (kappa), microsomal (MAPEG), and fosfomycin/glyoxalase (VOC) families (*16, 17, 21-23*). Enzymes are placed into a particular family based on sequence and/or structural homology. Within each family, enzymes are classified based on higher homology constraints, catalytic function, etc (*4, 15, 23*). For example, within the canonical GSH transferases higher order constraints have given rise to various classes (alpha, mu, pi, sigma, theta, zeta, omega, etc.). Within each class, isozymes are numbered 1, 2, etc depending on their sequence homologies. I will focus on the evolutionary, structural, and functional aspects of the canonical and kappa families.

The primary difference between these two families is their structural topology: a result of their divergent evolution. Both families contain two structural elements: a thioredoxin/glutaredoxin fold and an all alpha helical domain (*22-27*). The thioredoxin/glutaredoxin fold consists of two structural motifs (an αβα motif and a ββα motif) tied together by a connecting helix (Figure 6a). These two motifs are arranged into a β-sheet to make one fold and form the active site structure. In the canonical family, the alpha helical domain is attached to the end of the thioredoxin/glutaredoxin fold. In the kappa family, the alpha helical domain is inserted into the fold in place of the connecting helix (Figure 6a). Location of the helical domain seems to have little effect on the overall structure of the thioredoxin fold (Figure 6b) and GSH transferase catalysis, but major implications about how these two families evolved (Figure 6c) (*22, 23*).

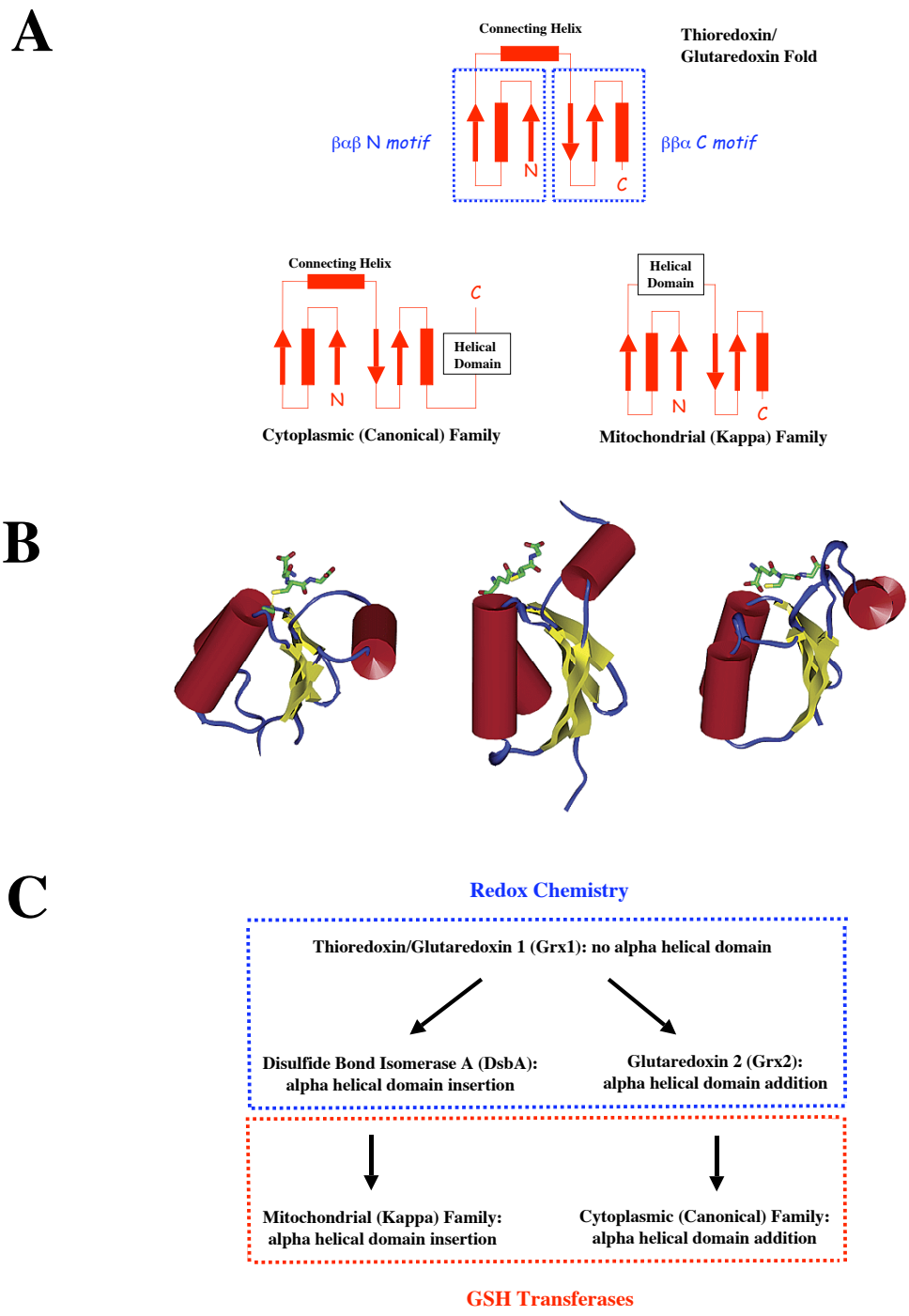

Figure 6. Evolution of the cytoplasmic (canonical) and mitochondrial (Kappa) GSH transferase families. Panel A shows that one evolved following a helical domain addition and the other an insertion. Panel B shows the similarity of the thioredoxin fold structure of glutaredoxin (C14S) (left), the Kappa enzyme rGSTK1 (center), and the canonical enzyme rGSTM1-1 (right) [Reprinted with permission from (*22*). Copyright 2004 American Chemical Society]. Panel C shows the redox enzymes that formed prior to the appearance of GSH transferase activity (*22, 23, 28*).

Interestingly, this divergence occurred prior to the evolution of GSH transferase activity (Figure 6b). It seems early GSH transferase related enzymes performed redox chemistry. The canonical family shows sequence and structural homology with Grx2 while the kappa family shows similar homology with DsbA (*22, 23*). The appearance of Grx2 and DsbA was not only a branching point for structural topology but was also a branching point in catalysis. Grx2 is a GSH-dependent reductase (*22, 23, 29*), while DsbA is responsible for the formation of disulfide bonds within periplasmic proteins (*30-32*). Grx2 maintained reducing capabilities (like its precursors) while DsbA shifted its chemistry to oxidizing protein thiols (there is no evidence to this point that this structural alteration led to the shift in chemistry) (*33-35*). Because both families arose following an evolutionary branch point, GSH transferase chemistry in the canonical and kappa families must have converged independently (unless some unknown event, like a circular permutation, linked the families down the line) (*22*).

Even though they seem to have arisen independently, their tools for GSH catalysis are similar. Beyond binding of GSH (in the G-site) and the xenobiotic (in the H-site), both families enhance the reactivity of GSH by assisting its ionization to GS^- (*4, 9, 10, 22, 27*). In general, a side chain hydroxyl group is used to lower the pKa of the thiol proton from ~9 to ~6.5. This allows the majority of the bound GSH to exist as GS^- (at physiological pH) and, as mentioned previously, enhances the nucleophilicity of the sulfur. This enhancement is accomplished in either a base (Figure 7a) or hydrogen bonding (Figure 7b) assisted manner. The canonical family most often uses a tyrosine residue for this purpose. A few classes (theta and zeta) use a serine residue (*4, 15*). The kappa family use only a serine residue (*22, 36*).

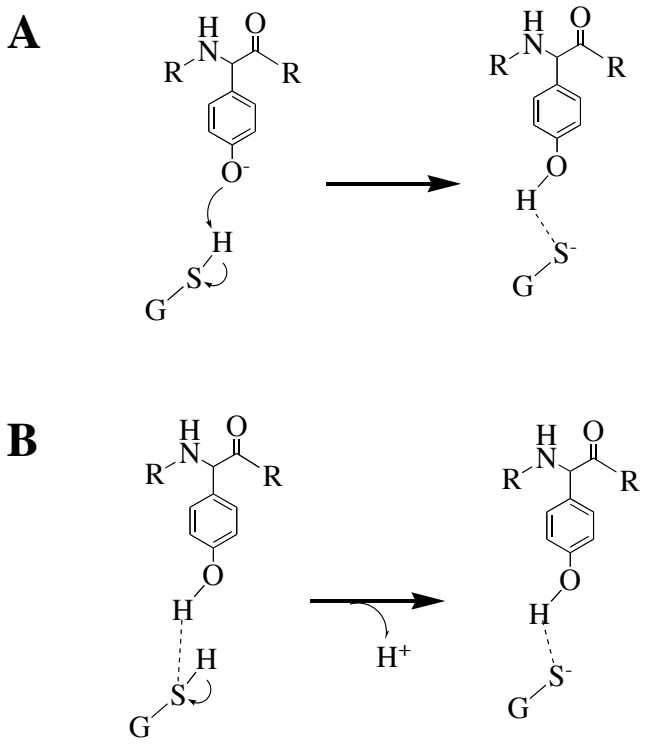

Figure 7. GSH transferase assisted ionization of GSH via the hydroxyl group of a tyrosine residue. Panel A shows a based assisted mechanism while panel B shows a hydrogen bonding assisted mechanism. Dashed line indicates a hydrogen bond.

Tertiary/Quaternary Structure of the Mu Class GSH Transferase

The canonical GSH transferases are dimeric enzymes with a monomer molecular weight of ~25 kD. As mentioned previously, each monomer contains both a thioredoxin/glutaredoxin domain (domain 1) and a helical domain (domain 2). These domains are connected via a loop and packed tightly together to form a single subunit (Figure 8). Despite the fact that GSH transferase subunits from different classes are structurally similar (Figure 8), molecular recognition at the dimer interface is highly specific. *In vivo*, only subunits from within the same class (e.g., mu) associate to form homodimers (e.g., M1-1, M2-2) and heterodimers (e.g., M1-2) (*4, 27, 37*).

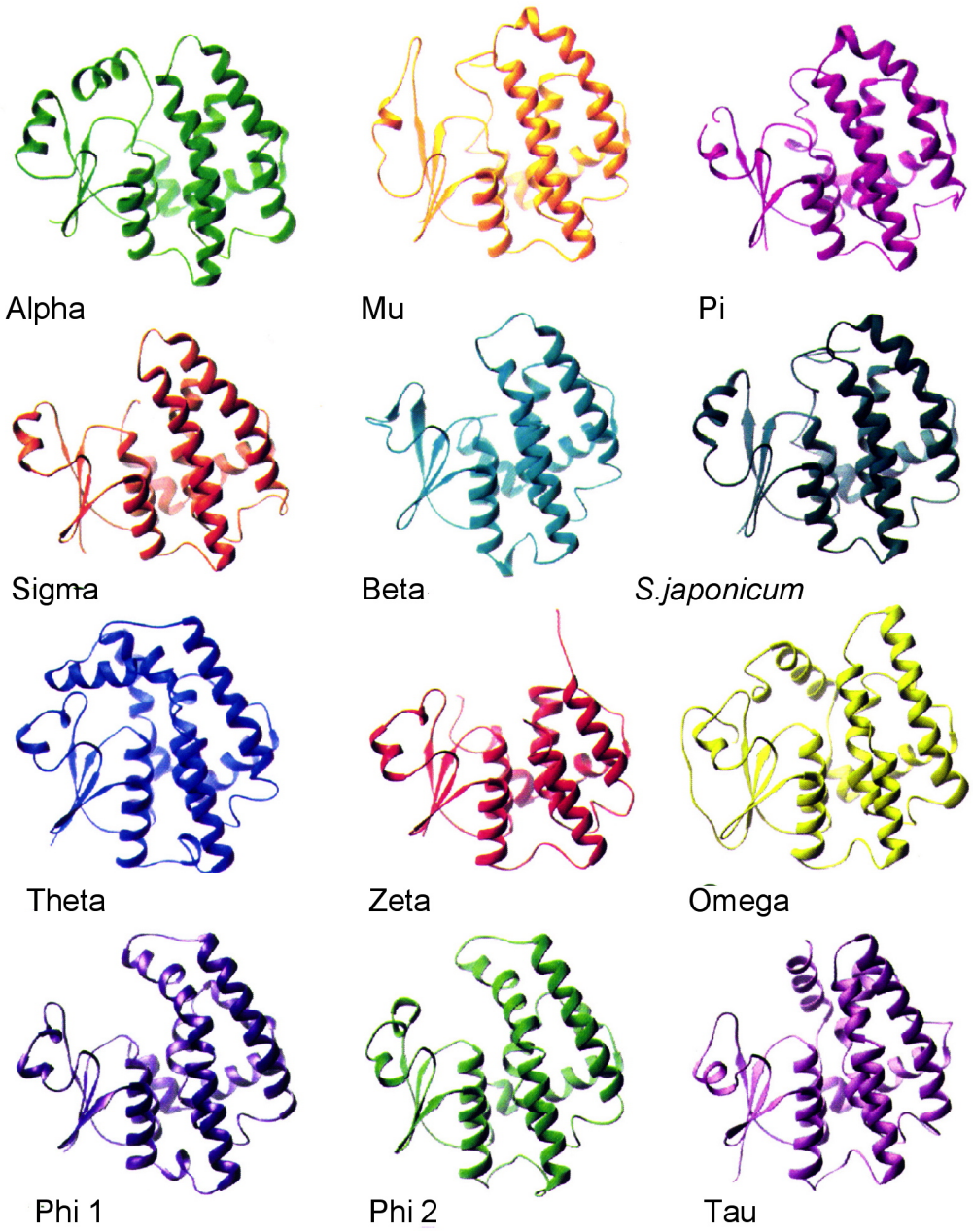

Figure 8. Ribbon diagrams of the individual subunits from various classes of the canonical GSH transferase family. They are oriented so that the thioredoxin/glutaredoxin fold is on the left (contains the β sheet), on the right is the helical domain, and between these is the connecting loop (on the bottom): Alpha (1gse), Mu (4gst), Pi (1gss), Sigma (2gsq), Beta (1a0f), S. japonicum (1gta), Theta (1ljr), Zeta (1e6b), Omega (1eem), Phi 1 (1gnw), Phi 2 (1axd), and Tau (gstu2). Reprinted with permission from (*38*). Copyright 2002 American Chemical Society.

The specificity for interclass dimerization is a result of key electrostatic and hydrophobic interactions created across the subunit/subunit interface (*15, 27, 37, 39-41*). The Mu class GSH transferase is a good example. In this case, the dimer is stabilized via a series of intrasubunit interactions between domains 1 and 2 of opposing monomers (Figure 9c) (*37*). The key structural elements that form the interface are illustrated in Figure 9 for the Mu class rGSTM1-1. The first is a hydrophobic ball-and-socket motif between F56 located on a loop (56-loop) in domain 1 and a group of hydrophobic side chains on the α4 and α5 helices of domain 2 (Figure 9). The second is a cluster of electrostatic interactions between β4/α3 of domain 1 and α4 of domain 2. These interactions include a salt link between R81 of domain 1 and E90/D97 of domain 2 (Figure 9).

Both of these interaction motifs appear to be important for dimer stability in Mu class as well as other GSH transferase classes with similar interface structures. Interruption of the ball-and-socket motif (F56S) in rGSTM1-1 increased the K_d of the dimer 42-fold to 0.5 μM relative to the native enzyme (*42*). Individual disruption of both motifs (F52A and R69E) in the rGSTA1-1 isoenzyme, as well as both mutations combined, results in a shift in the equilibrium from dimer toward monomer in sedimentation assays (*43*).

Binding of ligand to the F56S mutant of rM1-1GST has been shown to return the mutant to a native-like structure including stabilization of the dimer (*42*); however, the mechanism of this rescue is unknown. It is also not known what effect mutations in both the "ball-and-socket" motif and the electrostatic core would have on the quaternary structure of rGSTM1-1. In Chapter IV, we used HDX-MS to explore the dynamic behavior of the native and F56S mutant in both "apo" and ligand (GSH and/or GSO^-)

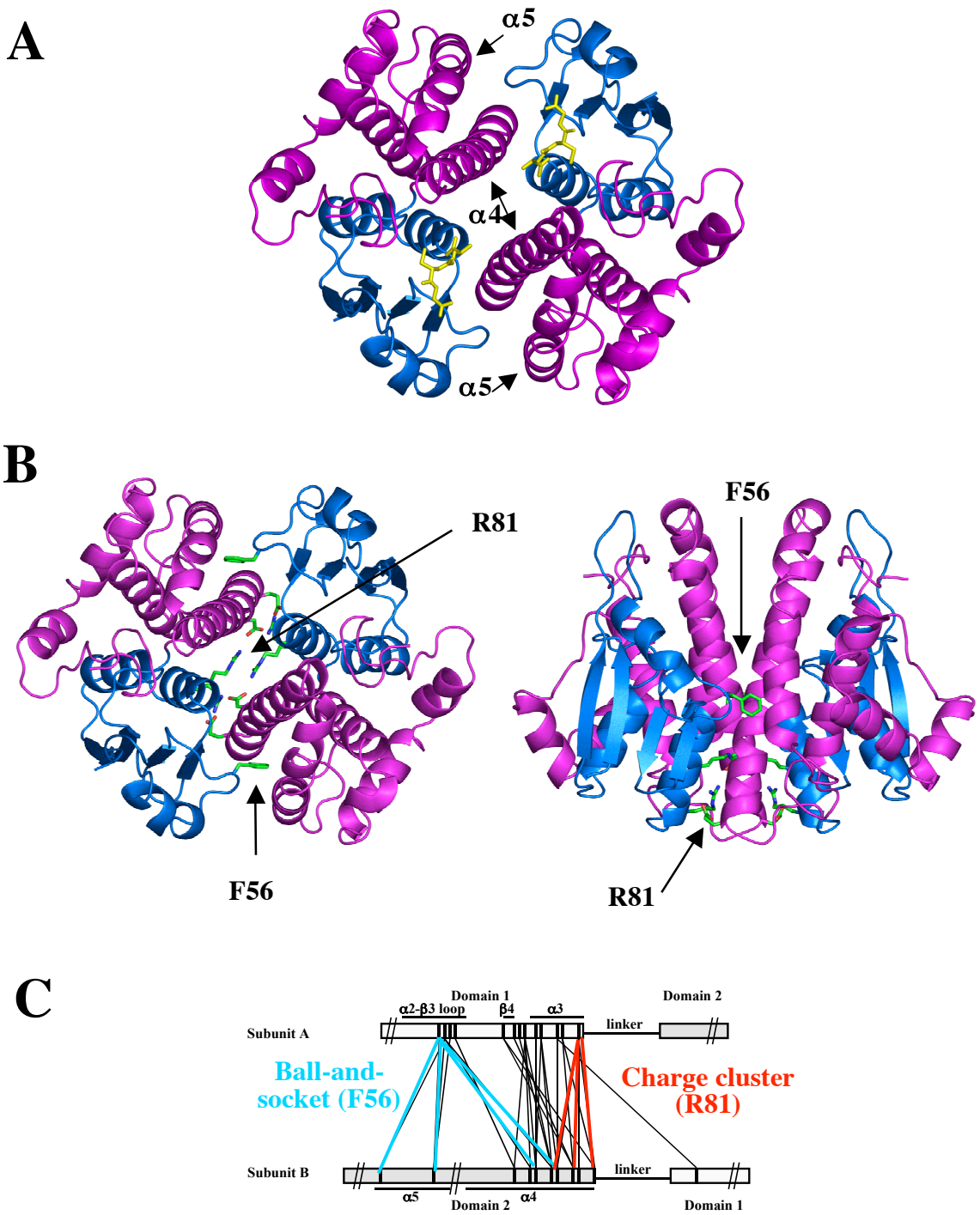

Figure 9. Primary interactions across the dimer interface of rGSTM1-1. Panels A and B are ribbon diagrams of the protein backbone: domain 1 (blue) and domain 2 (magenta). Panel A shows GSH (yellow) bound in domain 1 and α helices 4 and 5 of domain 2. Panel B shows the side chains representative of the hydrophobic "ball and socket" motif (F56 "the ball") as well as the charge cluster (R81). Panel C shows all of the intersubunit interactions with those in cyan for the "ball and socket" motif and those in red for the charge cluster. This figure was made using the program Pymol (*44*).

bound forms to determine how ligand was affecting both the native and F56S mutant structures. We were able to show that the mutation primarily affected domain 1 and that binding of ligand to the F56S mutant restored this region to HDX kinetics similar to that of the native enzyme. The results indicate that the "ball-and-socket" motif not only stabilizes the dimer but also stabilizes the active site in the absence of ligand. In Chapter V, a mutant was made containing both a "ball-and-socket" (F56S) as well as a charged-cluster (R81A) mutation and were able to create a soluble monomer. HDX-MS was used in this case to show that the monomer maintained a native-like structure and allowed us to hypothesize a mechanism for intersubunit (domain 1 and 2) cooperativity.

The Kappa Class GSH Transferases from Sequence to Structure

In 1991, mitochondrial matrix fractions of rat livers were shown to have GSH/CDNB conjugating activity (*45*). N-terminal sequencing of the purified enzyme showed that it had sequence similarity to the Theta class. This new enzyme stayed in that class until its DNA was cloned (*46*). This study showed that this enzyme had no sequence similarity to any other GSH transferase and was given its own class name: Kappa. After this new classification, many studies investigated its kinetics, cellular location, and expression levels (*46-49*) but its disconnect from the other canonical GSH transferases remained a mystery. Upon the determination of the structure of the rGSTK1-1 (*22*), the answer was revealed. As mentioned previously, the sequence similarity was lost due to the helical domain insertion. This firmly placed Kappa into a family of its own. Since then other studies have confirmed its status (*23, 28, 36*).

Tertiary/Quaternary Structure of the Kappa Class GSH Transferase

Like the canonical GSH transferases, Kappa is a dimer with a monomer molecular weight of ~26 kD (*45*); however, because of the helical domain insertion, the quaternary structure is quite different (Figure 9 & 10) (*22*). The canonical enzymes are fairly spherical in structure while Kappa is elongated (*22*). The dimer interface interactions of the canonical family are located at one end of the molecule (Figure 9b). This forms a V-shaped crevice along the dimer interface (Figure 9b) and a channel to the active site. There is no crevice in Kappa because the dimer interface interactions are spread among all domains (the dimer buries 2798 $Å^2$ of surface area along its interface) (*22*). This difference pushes the GSH sulfur toward the surface (Figure 10a) allowing better access to the active site and may be one of the reasons this enzyme is highly active (*22*).

Because of the orientation of the thioredoxin folds, the active sites are much closer together as well. The N1 atoms of the bound GSH molecules are only 5.4 Å apart (*22*). It is not surprising then that a couple of the GSH interactions come from the opposing monomer (figure 10b). The GSH binding site is made of similar interactions (Figure 10b), as seen in the canonical family, although they differ in the number of interactions (*4, 22, 27*). Canonical GSH transferases have between 12 to 15 interactions with GSH (*4, 27*) while Kappa only has eight (Figure 10b; L183 has two interactions: main chain amide and carbonyl). This reduction of interactions does not seem to affect the binding energy. For example, the K_d for GSH is ~30 μM (*22*): a typical value for the canonical GSH transferases (*4, 27, 50*). This may indicate that the Kappa fold contains an intrinsic feature that adds binding energy and supplements for the reduction in GSH interactions.

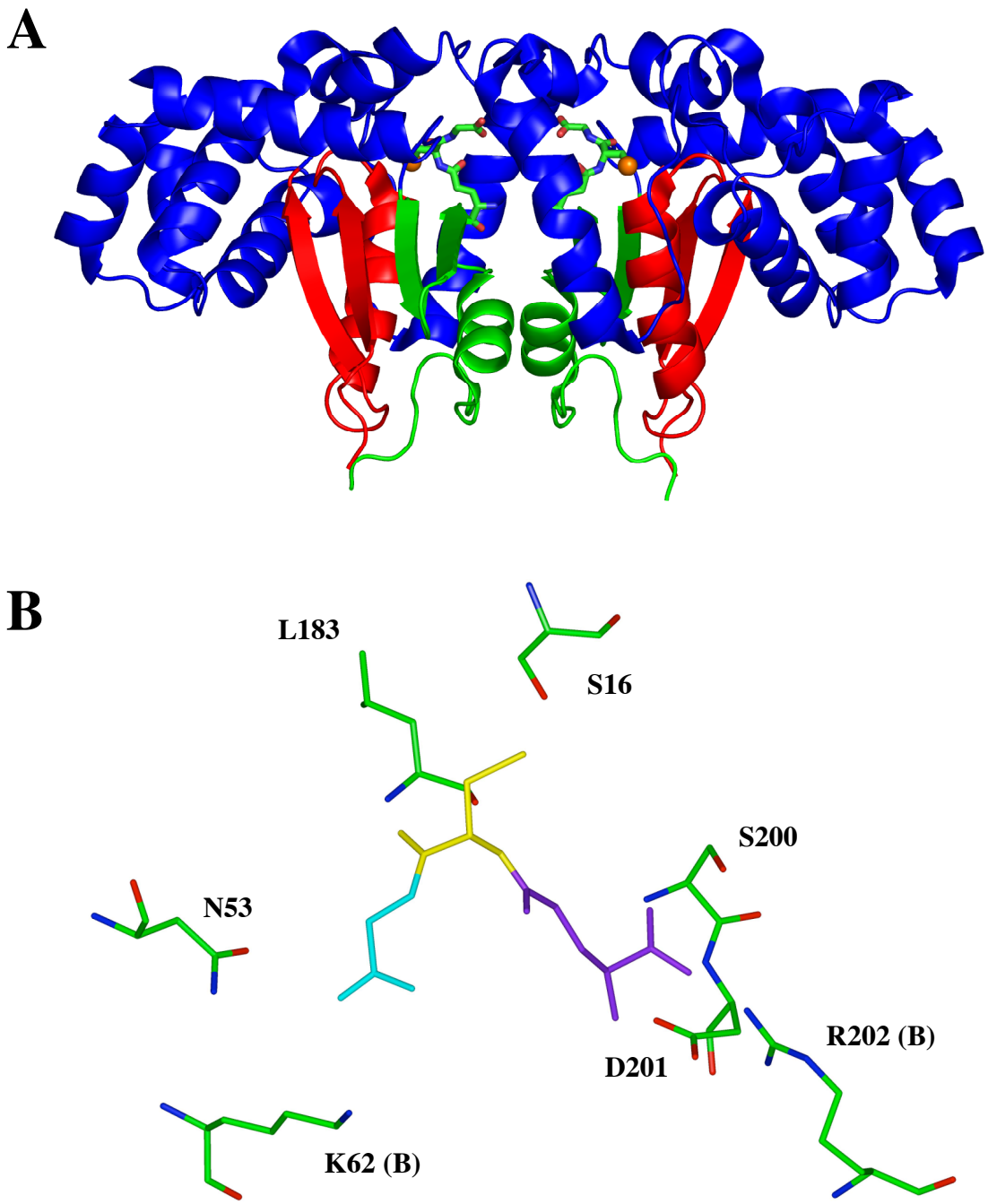

Figure 10. Ribbon diagram and active site of the Kappa GSH transferase rKGST1-1. Panel A shows one dimer with the thioredoxin folds [N-terminal αβα motif (red) and the C-terminal ββα motif (green)] and the intervening helical domains (blue). GSH (colored by atom with the cysteine sulfur highlighted) is shown as a stick in the active site. This figure was created with Pymol (*44*). Panel B is a blow up of the active site with all of the GSH [glycine (cyan), cysteine (yellow) and γ-glutamate (purple)] binding residues labeled. Residue labels are located near the side chain. Note: K62 and R202 are interactions from the opposing monomer (B). This figure was created with InsightII (*51*).

HCCA Isomerase and the Kappa GSH Transferase Connection

There are two proteins to which Kappa shows sequence homology (~20% sequence identity each). They are the bacterial enzymes DsbA and HCCA Isomerase. DsbA has the same topology as Kappa (Figure 6) (*31*); however, its active site is fundamentally different. DsbA has a cysteine (that performs redox chemistry) residue in place of the GSH ionizing serine (S16) residue (Figure 11) (*22, 32*). Even though the sequence identity between Kappa, DsbA and HCCA Isomerase is similar, alignment of Kappa and HCCA Isomerase (Figure 11) demonstrates that both are more closely related to each other than either is to DsbA. HCCA Isomerase retains all of the residues important for GSH binding (with two conservative alterations) including conservation of the catalytic serine. Coupled with the suggestion that HCCA Isomerase is GSH dependent (*52-54*) it seems that this enzyme could be a Kappa GSH transferase. The case for a Kappa connection is even more compelling because recent modeling results suggest HCCA Isomerase has a Kappa fold (*28*).

```
                  *
Kappa  7  VLELFYDVLSPYSWLGFEVLCRYQHLWNIKLKLRPALLAGIMKDSGNQPPAM--VPHKGQ  64
Iso    2  IVDFYFDFLSPFSYLANQRLSKLAQDYGLTIRYNAIDLARVKIAIGNVGPSNRDLKVKLD  61

Kappa 65 YILKEIPLLKQLFQVPMSVPKDFFGEHVKKGTVNAMRFLTAVSMEQPEMLEKVSRELWMR 124
Iso   62 YLKVDLQRWAQLYGIPLVFPANYNSRRMNIGF-----YYSGAEAQAAAYVNVVFNAVW-- 114

Kappa 125IWSRDEDITESQNILSA--AEKAGMATAQAQHLLNKISTELVKSKLRETTGAACKYGAFG 182
Iso   115----GEGIAPDLESLPALVSEKLGWDRSAFEHFL---SSNAATERYDEQTHAAIERKVFG 167

Kappa 183LPTTVAHVDGKTYMLFGSDRMELLAYLLG 211
Iso   168VPTMFLGDE----MWWGNDRLFMLESAMG 192
```

Figure 11. Sequence alignment of rKGST1-1 and the *P. putida* HCCA Isomerase from the nah7 plasmid. Identities are shown in bold. Kappa GSH binding residues including S16 (*) and the corresponding residues in HCCA Isomerase are shown in blue.

Naphthalene Catabolism in *Pseudomonads*

In the late 1950's, Fernley and Evans compiled their work and that of others and first hypothesized a pathway for the oxidative catabolism of naphthalene by soil *Pseudomonads* (*55*). Over the next few decades, the chemistry of many of the enzymes (*56-59*) and the location and inducers of the pathway were elucidated (*60-62*). This work culminated in two papers by Eaton et. al. who sequenced much of the operon (*63*) and quelled the debate about the last of the controversial steps (*52*). Figure 12 shows the finalized details of the upper catabolic pathway on the nah7 plasmid. The first three steps are dioxygenation, oxidation, and dioxygenation (A, B, and C, respectively) transforming naphthalene into HCCA. This is the acetal version of cHBPA and stabilizes the cis configuration such that the equilibrium is about 55% cis to 45% trans (*52*). The uncatalyzed approach to equilibrium is slow (6 hours to reach it at room temperature in H_2O at pH 7.0) (*52*). HCCA Isomerase increases the rate dramatically so that the naphthalene can be utilized on a relevant time scale. Following isomerization, the pyruvate is cleaved in a retro-aldol reaction (step E, Figure 12). The resulting salicylaldehyde is oxidized and passed on to the lower pathway (step F, Figure 12) (*52*).

Eaton et. al. cleared up the debate about the exact structures of the substrates and products of the HCCA Isomerase step (D, Figure 12); however, the enzymatic mechanism remained unclear. He and others have shown that GSH activates the enzyme but might or might not be involved in chemistry (*52-54*). It has been suggested that GSH activates the enzyme by reducing a catalytic cysteine residue (*53, 54*); however, that has been ruled out because alkylating agents were shown not to affect catalysis (*53*). In

A

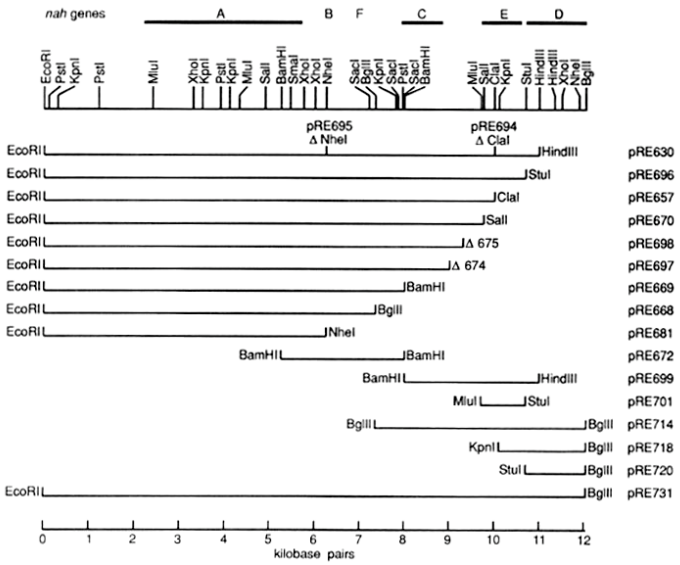

B

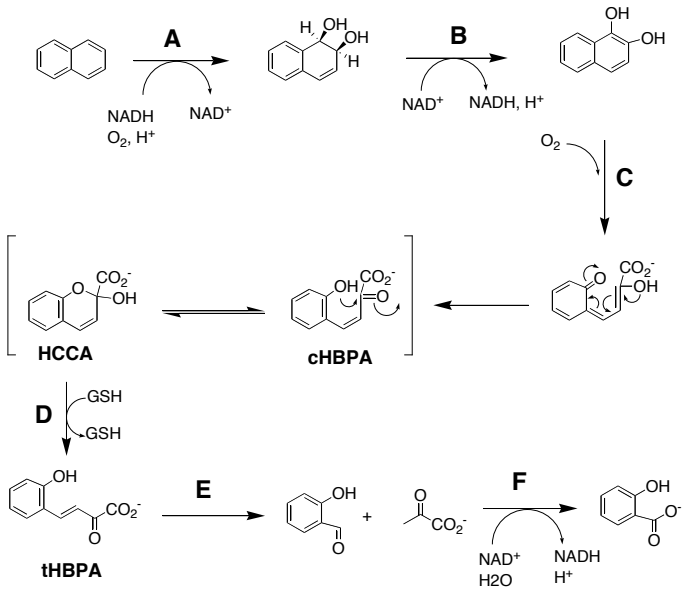

Figure 12. The upper naphthalene catabolic pathway on the nah7 plasmid from *P. putida* (*52, 63*). Panel A shows the organization of upper pathway on the nah7 plasmid (top) and the series of fragments created (*52*) to analyze the enzymes and substrates/products of each step [Reprinted with permission from (*52*). Copyright 1992 American Society for Microbiology]. Panel B shows the substrates/products of the individual steps and the associated enzymes: A, naphthalene-1,2-dioxygenase; B, 1,2-dihydroxy-1,2-dihydronaphthalene dehydrogenase; C, 1,2-dihydroxynaphthalene dioxygenase; D, 2-hydroxychromene-2-carboxylate isomerase; E, trans-*o*-hydroxybenzylidene pyruvate adolase; F, salicylaldehyde dehydrogenase (*52, 63*). Molecules most relevant to this study: cHBPA, cis-*o*-hydroxybenzylidene pyruvate; HCCA, 2-hydroxychromene-2-carboxylate; and tHBPA, trans-*o*-hydroxybenzylidene pyruvate.

Chapter VI, the role of GSH in the enzymatic mechanism was investigated and a crystal structure was solved confirming HCCA Isomerase has a Kappa fold. In Chapter VII, transient state kinetics measurements of the enzymatic reaction with HCCA/tHBPA and the analogs MCCA/tMBPA were used to probe the reaction mechanism. Single turnover multiwavelength stopped-flow experiments showed that cHBPA builds up in the active site during catalysis and that the enzyme can perform Michael chemistry. A crystal structure with the product analog (tMBPA) in the active site and demonstrated that a covalent intermediate could be formed during the reaction coordinate. This data allowed us to hypothesize an enzymatic mechanism. In addition, global modelling showed that our mechanism is plausible.

CHAPTER II

HDX-MS: THEORY AND PRACTICE

Because of their labile nature, protons exchange readily with solvent on experimentally relevant time scales. This fact combined with advances in detection has made hydrogen-deuterium exchange (HDX) an excellent probe for study of a proton's local environment. For efficient use of this technique to study proteins, we must be able to differentiate among different kinds of protons in the polypeptide.

Intrinsic HDX Rates in Polypeptides

Peptides and polypeptides (proteins) contain many different kinds of protons (Figure 13a). They fall into three main classes (based on HDX rates): main chain amide (on all amino acids except proline), side chain (carboxyl/amine/thiol), and hydrocarbon (Figure 13a). Because of the nature of the carbon-hydrogen bond, the hydrocarbon group does not exchange on experimentally relevant time scales; however, the other two classes do (*64-67*). Their intrinsic exchange rates versus pH are given in figure 13b. Note that around pH 2.5 the rate of exchange at the backbone amide is two orders of magnitude slower than that of any other proton (*64, 67, 68*). This allows capture of only amide protons. First, all protons are exchanged at high pH (Figure 13). Then the sidechain deuterium is selectively removed by backexchanging all side chains off at low pH (where backbone amides are slow): the key to the HDX-MS experiment (*64-66, 69, 70*).

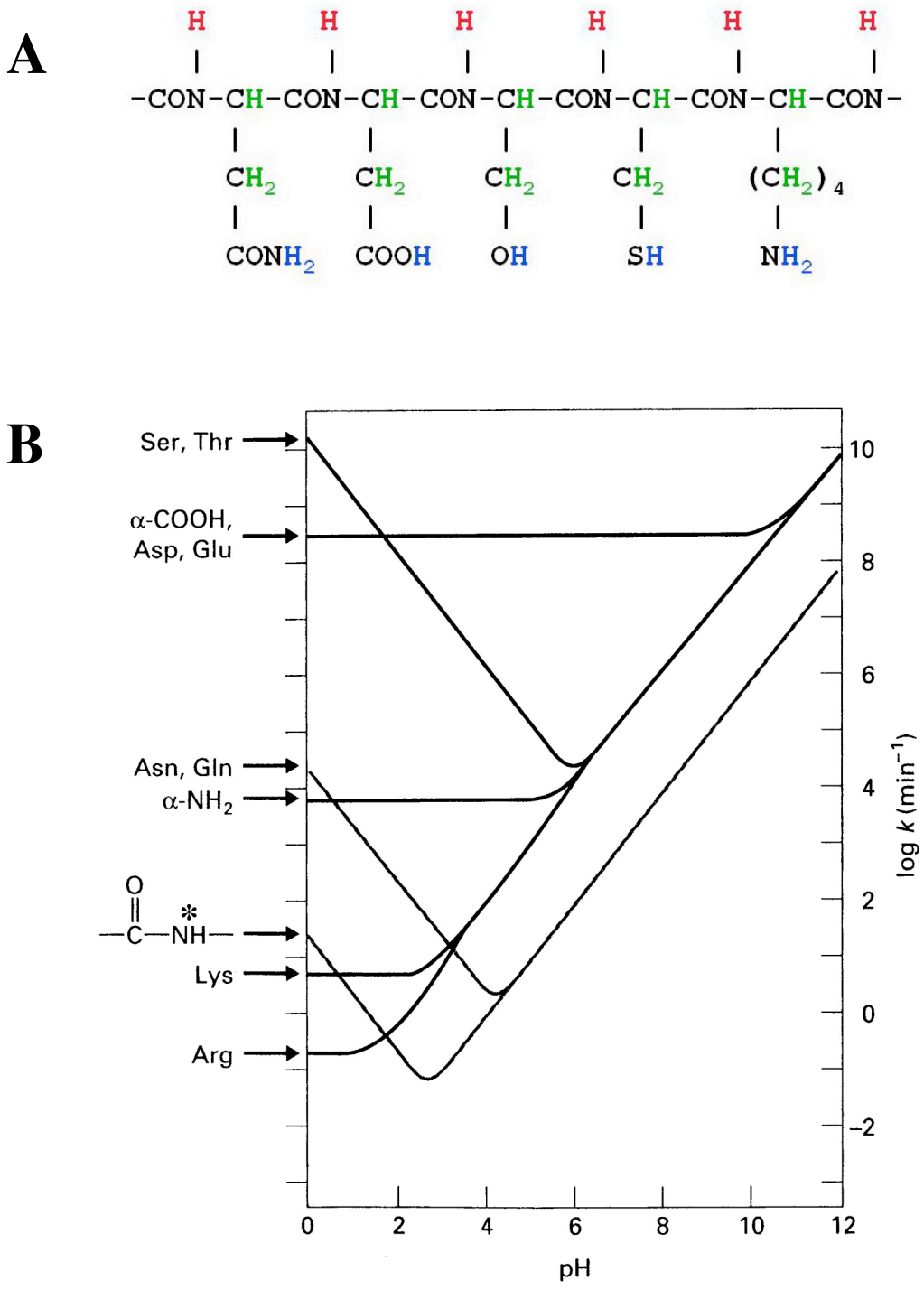

Figure 13. Exchangeable peptide protons (A) and the intrinsic exchange rates of those protons versus pH (B). Panel A is the theoretical polypeptide NDSCK with the hydrocarbon (green), side chain (blue), and amide (red) protons labeled. Panel B is the exchange rate profile of various side chain protons as well as that of the main chain amide* (*64, 67, 68*). Because of their extremely slow exchange, hydrocarbon protons are not shown.

Protein Dynamics and HDX at the Backbone Amide

Amide protons that are fully exposed to solvent exchange on millisecond timescales (at neutral pH) (*67, 68*). However, some amide protons (in proteins) are known to take seconds to minutes to hours to days to years to exchange (*64-66, 70*). This reduction in HDX rates is due to the loss of solvent accessibility to the backbone amide proton. Exclusion of solvent is a result of the protein's secondary/tertiary/quaternary structure.

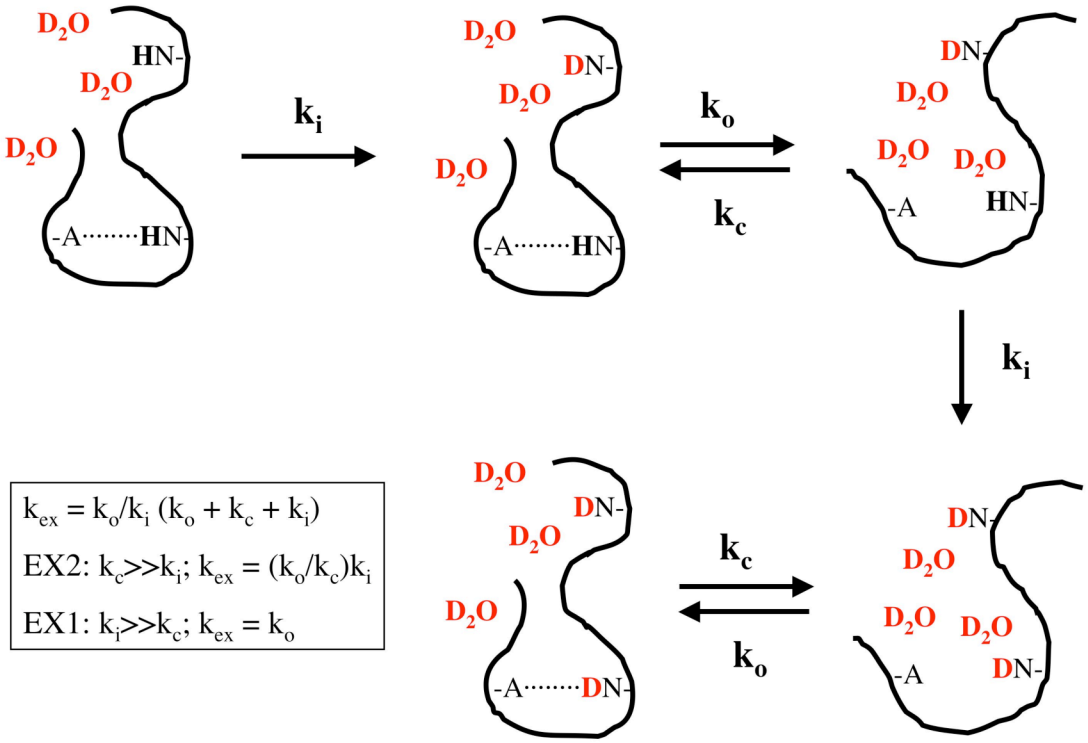

Figure 14. Linderstrøm-Lang model of HDX (*64, 71*). Backbone amides that are accessible to solvent will exchange (step 1) at the intrinsic rate constant (k_i). Those that are inaccessible must first be exposed to solvent (step 2) via unfolding or opening (k_o) and can then exchange (step 3). Once they exchange they can be trapped in the folded structure (step 4) via to refolding or closing (k_c). The equation that defines the overall rate constant of exchange (k_{ex}) can be simplified to either of two cases: $k_c >> k_i$ (EX2) or $k_i >> k_c$ (EX1). This figure is based on Figure 1 from (*65*).

The kinetic basis for this reduction in HDX rate was first described by Linderstrøm-Lang in 1955 (*64, 71*) (Figure 14). Their model suggests that the exchange rate (k_{ex}) of a particular amide proton is dependent on both the intrinsic rate (k_i) of exchange and the rate of opening (k_o) and closing (k_c) of the protein structure (Figure 14). It also suggests that because in most proteins k_c is much slower than k_i (EX1 exchange, Figure 14) such that k_{ex} can be simplified to k_c (*64*). In essence, the rate of HDX is a direct measure of the closing rate or the stability of a certain region of protein structure. Combining this model with the ability to capture only backbone amides in their deuterated state, we can explore the dynamic characteristics of a protein by examining the amount of deuteration along the protein backbone over time.

The HDX-MS Experiment

The HDX-MS experiment gives us the ability to measure the amount and locality of amide deuteration. Our method is a modified version of that used by others (*72-74*). The first step is to sequence the protein. This involves optimization of peptidase (pepsin in this case) digestion to yield the most and highest abundance of peptides. Each digest is then optimized for separation on RP-HPLC and ionization by the ESI-MS. Then the peptides are sequenced to identify their location (we used a pepsin map generated previously (*73*)). Once this is complete, the HDX-MS experiment can commence.

A schematic of our experiment is given in Figure 15. Protein at high concentration is diluted 10 fold with D_2O and then labeled for various time points. After the appropriate amount of time, the deuteration is "stopped" by lowering the pH and temperature. It is then digested and run on the HPLC (in an ice bath) and into the ESI-MS. During HPLC

(which is done at low pH) side chains are backexchanged so that the amide deuterons are all that is left (note: ~10-15% backexchange and exchange-in is corrected for by controls). The amount of deuteration is measured by the change in mass of the isotopic envelope of a particular peptide versus a completed deuterated peptide. This change is plotted versus time and fit to single/multiexponential terms to determine the rate constants and amplitudes for groups of amide sites.

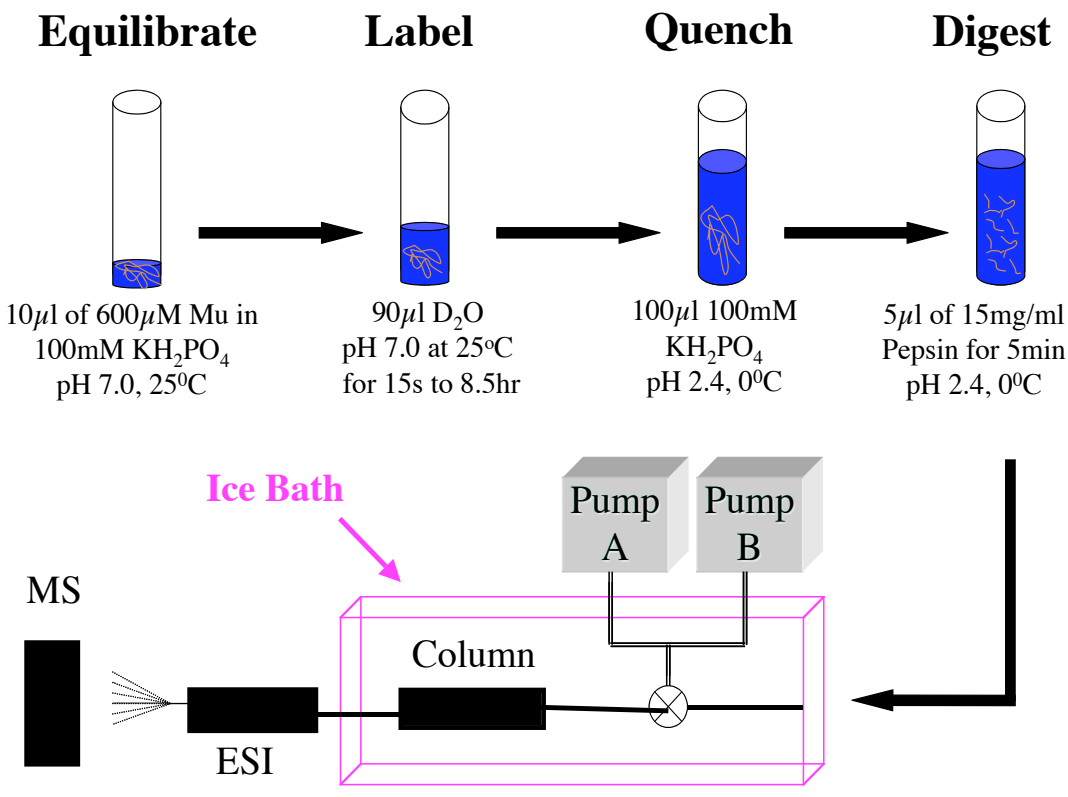

Figure 15. Schematic of the HDX-MS experiment.

CHAPTER III

MATERIALS AND METHODS

Materials

CDNB, DTNB, D_2O (99.9 atom % D), TFA, GSH, GSO_3^-, protease inhibitor cocktail (P2714), streptomycin sulfate, pepsin, chloramphenicol, lysozyme, *o*-methoxybenzyaldehyde, 2'-hydroxyacetophenone, pyruvic acid, glyoxylic acid (50% in water), pyrrolidine, $NaBH_4$, *p*-toluenesulfonic acid, dioxane (anhydrous), and toluene (anhydrous) were purchased from Sigma-Aldrich Corporation (St. Louis, MO). SDS-PAGE ready gels and HA were purchased from Bio-Rad Laboratories (Hercules, CA). DEAE and SP-sepharose (both fast flow) resins, pre-packed Superdex S-200 (25 ml analytical) and Sephacryl S-100/200 (120 ml preparatory) columns as well as the standards for gel filtration calibration were purchased from GE-Healthcare (formerly Amersham Biosciences) (Piscataway, NJ). $DMSO_{d6}$ (99.9 atom % D) was purchased from Cambridge Isotope Laboratories (Andover, MA). Methanol, 2-propanol, acetonitrile (all HPLC grade), ethanol (100%, laboratory grade), formic acid (90% in water), ethyl ether, Tris, NaCl, KCl, KH_2PO_4, MOPS, and HEPES were purchased from Fisher Scientific (Pittsburgh, PA). LB, DTT, IPTG, and ampicillin were purchased from Research Products International (Mt. Prospect, Il). The pET20b(+) expression vector, the *E. coli* strains [BL21(DE3), B834 (DE3), DH5α, and Tuner], the restriction enzymes (*XbaI* and *EcoRI*), benzonase, T4 ligase, and the DNA Wizard kit were purchased from Novagen (Madison, WI). The *E. coli* strain XL-1 Blue cells and the Quick Change® kit

were purchased from Stratagene (Cedar Creek, TX). Cloning primers were purchased from Invitrogen (Carlsbad, CA). Crystallography screen Wizard I #27 was purchased from Emerald Biostructures (Bainbridge Island, WA). Plasmids pRE657 and pRE718 were gifts from the Environmental Protection Agency. GSH concentrations were confirmed by titration with DTNB (*75*).

Preparation of Proteins

Preparation of Native and F56S mutant rGSTM1-1. The expression vectors for native and the F56S mutant had been generated previously (*42*). These vectors were transformed into the *E. coli* strain BL21(DE3) for overexpression. Cells were grown in LB medium containing ampicillin (100 μg/mL). The cell culture was grown at 37° C with vigorous shaking until the OD_{600} = 0.8. Cells were induced with IPTG for 3h (0.5 mM final concentration). Cells were then harvested by centrifugation (6,500 x g, 15 min, 4° C) and pellets resuspended in 20 mM MOPS buffer containing 1 mM EDTA and DTT at pH 6.8. Cells were lysed by sonication, were treated with 1 mL of 10X protease inhibitor cocktail solution, and cell debris was removed by centrifugation (35,000 x g, 35 min, 4° C). The supernatant was then treated with benzonase for 2 h at room temperature to digest nucleic acids, and then dialyzed against 20 mM MOPS buffer containing 1 mM EDTA and DTT at pH 6.8. The proteins were applied to a cationic exchange SP-sepharose column (2 x 15 cm), previously equilibrated with the same buffer and eluted with linear salt gradient (0-500 mM NaCl) in the same buffer. Fractions containing protein were pooled together and dialyzed against 20 mM KH_2PO_4 buffer containing 1 mM DTT (pH 6.8). The protein solutions were further applied to a HA column (2 x 10

cm), previously equilibrated with the phosphate buffer, and eluted with gradient buffer (20–400 mM KH_2PO_4) containing 1 mM DTT (pH 6.8). The appropriate fractions where pooled together and then dialyzed against 100 mM KH_2PO_4 (pH 7.0). The purity of the proteins was assessed by SDS-PAGE and their identity was confirmed by MALDI-MS. The proteins were concentrated, flash-frozen, and stored at –80°C. The protein was stored as 125 μl aliquots at a concentration of 600 μM protein for apo and 900 μM for ligand bound studies. Each aliquot was sufficient for 20 HDX-MS analyses and was used within one day of thawing. Protein concentrations for the monomeric species of native and the F56S mutant enzymes was determined spectrophotometrically using a molar extinction coefficient of 40,060 $M^{-1}cm^{-1}$ at 280 nm (*76*).

Preparation of the F56S/R81A Mutant rGSTM1-1. The expression vectors for the F56S/R81A mutant of rGSTM1-1 were generated by site-specific mutagenesis using Quick Change® protocol (Stratagene). The plasmid DNA containing the F56S mutation (*42*) was used as the template for the R81A change. The codon CGC (R) in the pET20b vector of the F56S mutant was switched to GCC (A) via PCR amplification with the primers: 5' CGC TAC CTT GCC **GCC** AAG CAC CAC CTG TGT 3' and 5' ACA CAG GTG GTG CTT **GGC** GGC AAG GTA GCG 3' (mutation in bold). The R81A mutation was confirmed by submission to the Vanderbilt Sequencing Core. The mutant enzyme was overexpressed in *E. coli* strain BL21(DE3) Tuner®. The cell culture was grown at 30° C in LB media, with ampicillin (100 mg/mL) and vigorous shaking until the OD_{600} = 1.0. Cells were cooled to 15° C and then induced with IPTG for 16 h (0.1 mM final concentration). Cells were then harvested by centrifugation (7,000 x g, 30 min, 4°

C) and pellets resuspended in 20 mM MOPS buffer (pH 6.8). Cells were treated with lysozyme for 30 min, lysed by sonication, treated with 1 mL of 10X protease inhibitor cocktail solution, and then cell debris was removed by centrifugation (15,000 x g, 60 min, 4° C). The supernatant was then treated with benzonase for 1 h at room temperature to digest nucleic acids, and then dialyzed against 20 mM MOPS buffer containing 1 mM EDTA and DTT (pH 6.8). The proteins were applied to a cationic exchange SP-Sepharose column (2 x 15 cm), previously equilibrated with the same buffer and eluted with linear salt gradient (0-300 mM NaCl) in the same buffer. Fractions containing protein were pooled together and dialyzed against 20 mM KH_2PO_4 buffer containing 1 mM DTT (pH 6.8). The protein solutions were further applied to a HA column (2 x 10 cm), previously equilibrated with the phosphate buffer, and eluted with a buffer gradient (20–400 mM KH_2PO_4) containing 1 mM DTT (pH 6.8). Fractions containing protein were pooled together and dialyzed against 100 mM KH_2PO_4 buffer (pH 7.0). The protein was then loaded onto a 120 ml Sephacryl S-100 gel filtration column that was pre-equilibrated with the same buffer. Peaks containing protein were pooled together. The purity of the protein was confirmed by visual inspection of a commassie stained SDS-PAGE and the mass was confirmed by ESI-MS. Protein was concentrated to 600 μM and then separated into 125 μL aliquots. Individual aliquots were flash frozen on dry ice and stored at -80^0 C. Samples were thawed on ice and used the same day. Protein concentration was measured spectrophotometrically using a molar extinction coefficient of 40,060 $M^{-1}cm^{-1}$ at 280 nm (*76*).

Preparation of native HCCA Isomerase (from the nah7 plasmid). The HCCA Isomerase gene was subcloned from plasmid pRE618 (figure 13) via PCR using the following primers: 5'AAAAAATCTAGACATATGATTGTCGATTTTTATTTCGAT3' and 5'AAAAAAGGATCCGAATTCTCAACTACTTAAATCGGCATTTTG3'. The PCR product was purified with an agarose gel. Both the PCR product and the plasmid pET20b(+) were digested sequentially with *XbaI* for 2 h and then *EcoRI* overnight . They were ligated with T4 ligase at 15^0C for 16 h. The ligated product was transformed into XL-1 Blue cells, plated onto LB plates containing 100 μg/ml ampicilin, and then placed in an incubator at 37^0C overnight. Using a Wizard kit, DNA was harvested from an overnight culture of one colony from the LB/ampicilin plate. The sequence was confirmed by submission to the Vanderbilt Sequencing Core.

The harvested DNA was transformed into *E. coli* BL-21 (DE3) Tuner cells for protein expression. A glycerol stock of transformed cells was used to inoculate a starter LB culture containing 100 μg/ml ampicilin. The cells were grown for 20 h at 28^0C ($OD_{600} \approx$ 0.4) and then used to inoculate 5 x 1L LB expression cultures (containing 100 μg/ml ampicilin). The cells were grown in Fernbach® flasks at 30^0C for 8h (OD ≈ 0.8) and then cooled to 15^0C. Each culture was induced with 50 μM IPTG for 18 h. Cells were harvested at 7,000 x g for 1 h. The cells were stored at -80^0C (after removing the media).

All 5 L of cells were resuspended into 225 ml of 20mM Tris, 1mM EDTA and DTT pH 7.4 (at 25^0C) containing 40 mg of lysozyme. The cells were stirred for 2 h at room temperature and then cooled in an ice bath. They were lysed with a Bronson sonicator (8power/70%duty) in 5 x 3 min cycles with 5 min for cooling. Sigma P2714 protease inhibitors were added to the lysate and then the cell debris was removed at 15,000 x g.

The supernate was removed and treated with 2 g of streptomycin sulfate (in 10 ml H_20) for 15 min at 4^0C. The precipitate was removed at 15,000 x g for 1 h. The supernate was removed and placed into dialysis (see below).

HCCA Isomerase was purified based on a previously published protocol (*53*) with the following alterations. The protein was dialyzed, purified, and concentrated at 4^0C unless otherwise noted. The supernate was dialyzed in 6 L of 100 mM NaCl, 20 mM Tris, 1mM EDTA and DTT pH 7.4 (at 25^0C) for 24 h., and then 6 L of 20 mM Tris, 1 mM EDTA and DTT pH 7.4 (at 25^0C) for 24 h. The protein was then loaded onto a 450 ml DEAE Separose Fast Flow column pre-equilibrated with the same buffer. The column was washed with 4 L of the same buffer at ~4 ml/min until the protein eluted (the first major peak after the flow through). All the fractions in that peak were pooled and concentrated to 50 ml in a nitrogen concentrator. The protein was placed into dialysis against 2 L of 50 mM HEPES, 150 mM NaCl, 1 mM EDTA and DTT pH 7.0. The protein was concentrated to 30 mg/ml and then loaded in 4 x 2 ml injections onto a 125 ml Sephacryl S-200 column pre-equilibrated with the same buffer (column was run at 25^0C). The column was washed with the same buffer at 1 ml/min. Peaks containing protein were captured, moved immediately to 0^0C, pooled, and concentrated to >20 mg/ml for storage. The protein was quantified based on the number of tyrosine and tryptophan residues per monomer using an extinction coefficient of 41,950 $M^{-1}cm^{-1}$ (*76*). Protein purity was determined by visual inspection of a commassie stained SDS PAGE and its identity was confirmed by MALDI mass spectroscopy. Protein was flash frozen on dry ice and then stored at -80^0C. The final yield was ~25 mg–per-liter of culture.

Preparation of HCCA Isomerase containing selenomethionine. Protein was prepared as described above with the following alterations. The pET 20b(+) vector containing the HCCA Isomerase gene was transformed into *E. coli* B834 (DE3) methionine auxtrophic cells for expression. Protein expression was performed in minimal media (1L final volume) containing: M9 salts, 2 ml of 1M $MgSO_4$, 0.1 ml of 1M $CaCl_2$, 20 mg of thiamin, biotin, and uracil, 50 mg of each amino acid, and 20 ml of 20% glucose. Overnight starter cultures were inoculated with transformed auxtrophic cells. The next day these starters were used to inoculate 3 x 1L cultures. Once cells reached an OD_{600} of 0.8 they were harvested via centrifugation, and then resuspended into 3 x 1L expression cultures containing 50 mg selenomethionine. Once the cells were back in the shaker, 50 μl of 1M IPTG was added to each culture and expression continued as normal. Harvest, lysis, and purification was performed just as native enzyme except 5 mM DTT (and not 1 mM) was used throughout the purification.

HDX-MS of Native and Mutant rGSTM1-1

HDX Protocol. HDX experiments were designed similarly to those reported previously (figure 15) (*73, 74*). Deuterium exchange was initiated by diluting 10 μL of the equilibrated protein solution (600 μM) 10-fold with 90 μL D_2O. The protein/D_2O solution was incubated at 25° C for various times (from 15 s to 8 h). At each time point, the reaction was quenched by cooling (tubes transferred to an ice bath), and acidified by adding 100 μL of quench buffer, [0.1 M KH_2PO_4, (pH 2.4) in H_2O at 0° C]. After 30 s, 5 μL of pepsin (15 mg/mL in H_2O at 0° C) was added to the quenched sample and

incubated on ice for 5 min. All of the samples for one protein (12 time points and 3 controls) were prepared individually and run on the same day.

The following changes were used to study the HDX of the native enzyme or the F56S mutant with ligand bound. At the start of the day, concentrated protein stocks were mixed with GSH or GSO_3^- (ligand solutions prepared in 0.1 M potassium phosphate buffer, pH 7.0) to a final concentration of 600 μM protein and 2 mM GSH (native), 1.5 mM GSO_3^- (native), or 200 mM GSO_3^- (F56S). The addition of D_2O results in a final concentration of 60 μM protein and 200 μM GSH, 150 μM GSO_3^-, or 20 mM GSO_3^- respectively. Final ligand concentrations are equal to 5 x K_m for native + GSH and 5 x K_i for native or F56S + GSO_3^-. The protein/ligand/D_2O solution was incubated at 25° C for various times (from 15 s to 8.5 h) to generate a total of twelve time points.

Electrospray Ionization Mass Spectrometry. The extent of deuterium incorporation into the peptide fragments was determined by LC/MS using the same protocol described previously (*64, 69, 73, 74*). Mass determinations for the free proteins were performed using a Finnigan MAT TSQ-7000 triple quadrupole mass spectrometer (Finnigan Corp., San Jose, CA), and for the ligand bound proteins using a Finnigan TSQ® Quantum triple quadrupole mass spectrometer (Finnigan Corp., San Jose, CA), both equipped with a standard electrospray ionization source outfitted with a 100 micron I.D. deactivated fused silica capillary. The mass spectrometer was operated in full scan mode using Quad 1. The analyzer was calibrated and tuned to unit resolution with a peak width at half-height of 0.7. The data were collected from 300 to 900 m/z with a 1-s scan time.

Data acquisition and spectral analysis were conducted using Finnigan Xcalibur software (version 1.3) on a Dell Optiplex GX270 computer running Microsoft® Windows 2000 operating system. The centroid data were analyzed using MagTran 1.0 beta9 software written by Zhang and Marshall (*77*).

Kinetic Analysis of Deuterium Incorporation. The amount of deuterium incorporated in each peptide was adjusted for back-exchange and exchange-in as described previously (*64, 69, 73, 74*), and plotted versus time. Two data sets were averaged for each experiment. Progress curves for individual peptides were fitted to the sum of first order rate terms according to equation **1**, using the program Prism 4.0 (Graphpad Software), where D is the deuterium content of a peptide, N is the number of peptide amide protons, k_i is the exchange rate constant for each amide hydrogen, and t is the time allowed for isotope exchange.

$$D = N - \sum_{i=1}^{N} \exp(-k_i t) \qquad \textbf{(1)}$$

The total number of exponential terms chosen was based on the goodness of each fit. The minimum number of terms were used to get the best fit and smallest error. The data are listed as $A_1(D)$, $A_2(D)$, etc. and $k_1(D)$, $k_2(D)$, etc. These refer to the number of deuterons exchanged for exponentials 1, 2, etc. and the rate-constant for the exchange of the deuterons for exponential 1, 2, etc.

Hydrodynamic Behaviour of Proteins

Size Exclusion Chromatography. The hydrodynamic behavior of the native and F56S/R81A mutant rGSTM1-1 as well as HCCA Isomerase was first characterized by size exclusion chromatography using a Varian HPLC system equipped with a Tosohass TSK-GEL G3000SW_{XL} column (7.8 mm x 300 mm). The system was preequillibrated with 100 mM KH_2PO_4 buffer and 1 mM EDTA (pH 7.0). 20 μl (20 mg/ml)samples of protein stock were injected onto the system and then eluted with the same buffer at 0.5 ml/min. Elution of proteins was monitored by absorption at 280 nm. The system was calibrated using known standards, and then the molecular weight of the native and mutant proteins was determined by correlating their elution volume to the standard curve.

Molecular Mass from Multi-Angle Laser Light Scattering. The solution molecular masses of the native GSH transferase (rGSTM1-1) and its double mutant (F56S/R81A) were determined by multi-angle laser light scattering and interferometric refractometry. Samples were subjected to gel filtration chromatography (Shodex KW-802.5; 8 mm X 300 mm; 0.5 mL/min) in 50 mM HEPES, 100 mM NaCl, 0.1 mM EDTA buffer (pH 7.5) prior to in line analysis with a DAWN EOS multi-angle light scattering detector, a Optilab DSP refractive index detector, and an Agilent 1000 UV detector. All samples were filtered with a 0.2 micron filter just prior to analysis. Injection volume was 20 μL. Stock protein solutions were 600 μM (mutant) or 770 μM (native). Molecular masses were calculated with the ASTRA software package (*78*).

Enzymatic Activity Toward CDNB

Enzymatic conjugation of GSH and CDNB was measured spectrophotometrically at 340 nm as described previously (*79*) with the following alterations for the rGSTM1-1 mutant F56S/R81A and HCCA Isomerase.

Enzymatic Activity of F56S/R81A. All kinetic experiments were carried out in 100 mM KH_2PO_4 buffer (pH 6.5) and 25^0 C with 500 nM enzyme. The final concentration of CDNB was 1.0 mM while that of GSH was 10-40 mM. All rates are corrected for the background reaction.

Enzymatic Activity of HCCA Isomerase. All kinetic measurements were carried out in 100 mM KH_2PO_4 buffer (pH 7.0) at 25^0 C. CDNB dependent kinetic parameters were determined with 1 μM enzyme, 250 μM GSH and CDNB varied from 50 μM-1000 μM (subsaturating but solubility limit). A linear fit of velocity vs [CDNB] was used to determine k_{cat}/K_m^{CDNB}.

GSH Binding to HCCA Isomerase

Removal of exogenous GSH. The exogenous GSH was removed from the protein by further dialysis steps following gel filtration. The protein was sequentially dialyzed against 1 M KCl, 50 mM HEPES, 1 mM EDTA and DTT. 64 L total was needed to remove almost all of the GSH from the protein assayed in Figure 3. 174 L was needed to remove 93% of the GSH from the protein used for the binding assays in Figure 4. The

removal of GSH was confirmed by titration of free thiols [Ellman assay (*75*) in 8 M urea] and the CDNB/HPLC assay described below.

RP-HPLC of GSH-CDNB adduct. GSH-CDNB adducts were loaded (25 μl injections) onto a Beckman-Coulter (Fullerton, CA) 4.6 mm x 250 mm C-18 column and then washed for 5 min with 50 mM sodium acetate pH 5.0. Peaks were then eluted with a linear gradient of 0%-90% acetonitrile over 10 min and monitored at 340 nm. GSH-CDNB standard was formed in a reaction of 1 mM GSH and 5 mM CDNB in 200 mM Tris pH 8.0 at 25^0C for 3h. The adduct concentration was determined at 340 nm (ε = 9,600 $M^{-1}cm^{-1}$) (*79*) and then a standard curve of adduct concentration versus area-under-the-curve was generated via 25 μl injections of serial dilution of the GSH-CDNB stock. The amount of GSH remaining in any protein preparation was measured by adding 1 μl of 100mM CDNB (in ethanol) to 100 μl of protein (200-600 μM range) and allowing it to react for 1 hr at room temperature. The reaction was quenched via the addition of 100 μl of chloroform. The sample was vortexed, centrifuged, and then a 25 μl aliquot was analyzed on the HPLC.

Kinetics of GSH binding. Approach to equilibrium kinetic data for GSH binding were carried out on an Applied Photophysics Ltd. Model SX17MV stopped–flow spectrometer with a 0.2 cm pathlength cell. All experiments were done in 100 mM KH_2PO_4 pH 7.0 at 10^0C. The rate of appearance (k_{obs}) of thiolate anion (GS^-) was measured in absorbance mode at 239 nm by mixing HCCA Isomerase (10μM final) with varying [GSH] from 20 μM to 2000 μM final. An average of 4-6 shots was fit to a double exponential. The off-

rate of thiolate anion (GS^-) was determined by measuring the loss of absorbance at 239 nm using a Perkin-Elmer (Boston, MA) *lambda* 45 double-beam spectrometer equipped with a 0.2 cm pathlength cell. A solution of HCCA Isomerase (10 μM final) and GSH (100 μM final) was mixed with GSO_3^- (5mM to 200mM) and the drop in absorbance at 239 nm was fit to a double exponential. Each [GSO_3^-] was repeated in triplicate and averaged together. The change in intrinsic protein fluorescence (k_{obs}) was monitored (excitation at 275 nm and emission above 320 nm) upon mixing HCCA Isomerase (500nM final) with varying [GSH] from 10 μM to 250 μM final. An average of 4-6 shots was fit to a triple exponential. The final phase (slow phase) of the exponential decay was monitored independent of the first two phases for [GSH] from up to 100 mM final. An average of 4-6 shots was fit to a single exponential (when the first 2s of the reaction were discarded).

Synthesis and Purification of HCCA, tHBPA, tMBPA, and MCCA

Synthesis and purification of HCCA and tHBPA. HCCA and tHBPA were synthesized as stated previously with the following alterations. The plasmid pRE657 (figure 15) was transformed into *E. coli* strain DH5α and selected with 100 μg/ml chloramphenicol. 5 x 1 L of cultures of LB were grown in Fernbach flasks at 37^0C to OD_{600} = 0.8 and then induced with 1 mM IPTG. Cells were harvested after 2 h of expression at 7.000 x g for 30 min (just prior to turning blue). The supernate was removed and the cells were stored at -80^0C. The next day the cells were resuspended into a Fernbach flask containing 1L M9 salts, 2 mM $MgSO_4$, 0.1 M $CaCl_2$, 25 mM glycerol, and 2 mM $FeSO_4$. The cells were placed at 37^0C for 2h. Then 10 ml of 50 mg/ml naphthalene (in ethanol) was added and

the cells were left at 37^0C for 24 h. Formation of HCCA and tHBPA was checked as described previously. The cells were removed at 7.000 x g for 2 h. The supernate was stored at 4^0C.

The supernate was extracted with ether and the organic layer was discarded. The aqueous layer was acidified with 6 M HCl and then extracted again with ether. The ether was removed via rotovapor and the remaining residue was dissolved in a small amount of acetonitrile. The isomers were separated on a Ranin Instrument Company, Inc. (Woburn, MA) Microsorb reverse phase C18/C5 (C18 guard) column with an isocratic gradient of 75% H_2O, 25% actetonitrile, and 0.05% TFA. The elution of the isomers was followed at 256 nm, and the peaks were trapped on dry ice (HCCA elutes first). Each peak was extracted with ether. The organic layer was then washed with 100 mM KP pH 7.0. The aqueous layer was separated, frozen on dry ice, and then lyophilized to powder. For elemental analysis, tHBPA was not returned to the aqueous phase with buffer. The ether was removed via roto-vapor and the sample was dried under vacuum.

Characterization of HCCA and tHBPA. UV-Vis spectra were collected on a Perkin-Elmer (Boston, MA) *lambda*45 double-beam spectrometer. NMR spectra were collected on a Bruker (Germany) 300Mhz NMR. Elemental analysis was preformed by Atlantic Microlab, Inc. (Norcross, GA). UV-Vis spectra of HCCA and tHBPA showed identity to those given in (*52*). Ratios of ε_{256}, ε_{296}, and ε_{340} were consistent with pure isomers. ^{1}H NMR (300 Mhz, 100 mM KP pH 7.0 in 50% D_2O) HCCA: δ 5.88, d (J = 9.8); δ 6.78, d (J = 9.8); δ 6.97, m; δ 7.23, m. tHBPA: δ 6.70, m; δ 6.79, d (J= 16.4); δ 7.20, t; δ 7.50, d; δ

7.96, d (J = 16.4). Elemental analysis of tHBPA: cal. C = 62.5, H = 4.2, O = 33.3 and found C = 61.8, H = 4.4, O = 32.0.

Synthesis, purification, and characterization of MCCA and tMBPA. UV-Vis spectra were collected on a Perkin-Elmer (Boston, MA) *lambda*45 double-beam spectrometer. NMR spectra were collected on a Bruker (Germany) 300Mhz NMR. APCI-MS data were collected on a Finnigan MAT TSQ-7000 triple quadrupole mass spectrometer (Finnigan Corp., San Jose, CA). Elemental analysis was preformed by Atlantic Microlab, Inc. (Norcross, GA).

tMBPA was synthesized and purified as described in (*80*). ^{1}H NMR (300Mhz, $DMSO_{d6}$) δ 3.90, (3H,s); δ 7.03, (1H, t); δ 7.14, (1H, d); δ 7.28, (1H, d) (J= 16.5); δ 7.50, (1H, t); δ 7.90, (1H, d); δ 7.98, (1H, d) (J = 16.5). APCI-MS of tMBPA; cal M+H = 206.20 and found M+H = 206.22. UV showed maxima at A_{297} (ε = 9,700 $M^{-1}cm^{-1}$) and A_{343} (ε = 7,300 $M^{-1}cm^{-1}$).

MCCA synthesis began the formation of the chromanone using the Kabbe condensation (*81, 82*). 200 mmol *o*-hydroxy benzyaldehyde and 200 mmol pyruvic acid were added to 250 ml of 70% isopropanol. The reaction was moved to an ice bath and 90 ml of 2 M potassium hydroxide (180mmol) was added dropwise. Once the reaction was cool, 150mmol of pyrrolidine was added dropwise, the ice bath was removed, and the reaction was stirred for 3 d at room temperature. The reaction was then heated to 70^{0} C for 3 d. Products were separated from the reactants by lowering the pH and extracting the reaction with ether. The ether was removed via rotovapor, and the residue was used without further purification. The resulting product (2-methylchromanone-2-carboxylic

acid, 22.5g) was dissolved in 40 ml of 100% ethanol. It was mixed with 200 ml of dry dioxane. The reaction was cooled in an ice bath and then 10 g of $NaBH_4$ was added slowly to avoid heating. After the addition, the bath was removed and the reaction was allowed to stir overnight under argon. The solvent was removed via rotovapor and then the products were dissolved into H_2O. The aqueous layer was removed, acidified, and then extracted with ether. The ether was evaporated and the resulting residue was used without further purification. The product (2-methylchromanol-2-carboxylic acid, 20 g) was dissolved in 250 ml of toluene. Then 4 g of *p*-Toluenesulfonic acid was added to the reaction and it was refluxed for 2 hrs using a Dean-Stark trap to capture evolved H_2O. The reaction was cooled and extracted with basic H_2O. The aqueous layer was removed, acidified, extracted with ether and then discarded. The organics were evaporated to dryness and then recrystallized in toluene. The overall yield was 18% for 2-methylchromene-2-carboxylic acid. ^{1}H NMR (300Mhz, $DMSO_{d6}$) δ 1.60, (3H, s); δ 5.82, (1H, d) (J= 9.6); δ 6.32, (1H, d) (J = 9.6); δ 6.84, (2H, m); δ 7.12, (2H, m). ^{13}C NMR (300Mhz, $DMSO_{d6}$) 25.47, 78.12, 115.98, 120.50, 121.54, 124.11, 126.18, 127.05, 129.89, 153.00, 173.18. Elemental analysis: cal. C = 69.5, H = 5.3, O = 25.3 and found C = 69.3, H = 5.5, O = 25.2. UV showed maxima at A_{263} (ε = 3,700 $M^{-1}cm^{-1}$) and A_{305} (ε = 2,200 $M^{-1}cm^{-1}$).

Steady State Assay of HCCA Isomerase with Native Ligands and Analogs

HCCA Isomerase activity assay. The standard activity assay included 20 nM HCCA Isomerase, 100 μM GSH, and 920 μM HCCA (ε_{256} = 7,790 $M^{-1}cm^{-1}$) (*52*) in 100 mM KH_2PO_4 (pH 7.0) at 25^{0}C. Activity without the addition of GSH was measured at protein

concentrations from 200 nM to 2 μM. Product production was followed at 340 nm (ε_{340} = 8,530 $M^{-1}cm^{-1}$) (*52*) in a Perkin-Elmer (Boston, MA) *lambda* 45 double-beam spectrometer. Velocities were calculated from a linear fit of the first 60 s of the reaction and then corrected for background isomerization.

Steady-state kinetics. Steady-state kinetics of the HCCA to tHBPA and tHBPA to HCCA isomerization were measured as described above (activity assay) with the following alterations. HCCA Isomerase (100 nM final) and GSH (100 μM final) were rapidly mixed with varying concentrations of HCCA (5-750 μM final) or tHBPA (10-2000 μM final) in an Applied Photophysics Ltd. Model SX17MV stopped–flow spectrometer with a 0.2 cm pathlength cell. The concentration dependence of GSH on the isomerization was done similarly using HCCA Isomerase (100 nM final) and HCCA (920 μM final) while varying the [GSH] (0.5 to 200 μM final). Changes in A_{340} were fit to a single exponential followed by a linear steady state. The constants k_{cat}, K_m, k_{cat}/K_m, and K_i were derived from direct fit of the initial velocities extracted from the linear phase to the Michealis-Menten equation (HCCA and GSH) or to the Michealis-Menten with incomplete substrate inhibition (tHBPA) (*83*). The dissociation constant, K_d, was determined for HCCA and GSH via a hyperbolic fit to the concentration dependence of the amplitude of the exponential phase of the reaction. All fits were done using the program Prism (Graphpad Software, Inc.). All reactions were corrected for any background.

HCCA Isomerase activity toward tMBPA and MCCA. All activity measurements were carried out in 100 mM KH_2PO_4 (pH 7.0) at 25^0C. The presence or absence of enzymatic conjugation of GSH to tMBPA or MCCA was measured spectrophotometrically on a Perkin-Elmer (Boston, MA) *lambda*45 double-beam spectrometer via loss of absorbance by collecting periodic scans from 400 to 220 nm (5 min between scans for tMBPA and 50 min for MCCA). Activity toward tMBPA was measured with 2 μM enzyme + 80 μM tMBPA + 800 μM GSH and MCCA with 2 μM enzyme + 250 μM tMBPA + 500 μM GSH. All background reactions were assayed as well.

Steady state kinetic measurements were carried out in 100 mM KH_2PO_4 (pH 7.0) at 25^0C. Enzymatic conjugation of GSH to tMBPA was measured spectrophotometrically via loss of absorbance at 343 nm. tMBPA dependent kinetic parameters were determined with 2 μM enzyme, 1 mM GSH and tMBPA varied from 2.5 μM-100 μM. The kinetic constants k_{cat}, K_m, K_i and k_{cat}/K_m were derived from direct fit of the initial velocities to the Michealis-Menten equation with complete substrate inhibition (*83*) using the program Prism (Graphpad Software, Inc.). All reactions were corrected for any background.

Characterization of GS-tMBPA adduct. HCCA Isomerase dependent GSH/tMBPA reactions were loaded onto a Beckman-Coulter (Fullerton, CA) 4.6 mm x 250 mm C-18 column and then washed for 2 min at 1 ml/min with 20 mM ammonium formate pH 3.5 (5% acetonitrile) using a Varian HPLC system. Peaks were then eluted with a linear gradient of 5%-95% acetonitrile over 18min at 1 ml/min and monitored at 280 nm. The product eluted as two peaks (corresponding to the two diastereomers) at 9.0 and 9.3 min,

respectively. Peaks were captured for UV-Vis spectra collection on a Perkin-Elmer (Boston, MA) *lambda*45 double-beam spectrometer. LC-MS data were collected on a Finnigan MAT TSQ-7000 triple quadrupole mass spectrometer (Finnigan Corp., San Jose, CA) using the same column, solvent system, and gradient. The peaks showed a M+H mass of 514.05 and 514.15, respectively. Theoretical M+H for GS-tMBPA is 514.14.

Transient State Kinetics of HCCA Isomerase with HCCA, tHBPA, and tMBPA

Single-turnover reactions of HCCA Isomerase with HCCA, tHBPA, and tMBPA. Transient state kinetic measurements were carried out in 100 mM KH_2PO_4 (pH 7.0) at $25^{O}C$. They were acquired on an Applied Photophysics Ltd. Model SX17MV stopped–flow spectrometer with a 1 cm pathlength cell for HCCA/tHBPA and a 0.2 cm for tMBPA. Each wavelength of data is an average of 4 to 6 shots. Multiwavelength experiments were done by collecting data (averages) at every other wavelength from 360 to 250 nm. Fitting of the multiwavelength data was done using ®Pro K software created by Applied Photophysics Ltd.

HCCA/tHBPA single turnover reactions were carried out with 25 μM HCCA Isomerase, 250 μM GSH and 20 μM isomer. The instrument was zeroed on a background of enzyme, GSH, and isomers at equilibrium. Data for single wavelength shots were fit to a double exponential to extract the amplitudes and observed rate constants (k_{obs}). Data from multiwavelength experiments were fit to a two-step model to extract UV spectra and observed rate constants (k_{obs}).

tMBPA single turnover reactions were carried out with 25 μM HCCA Isomerase, 25 μM GSH and 20 μM tMBPA. The instrument was zeroed on a background of enzyme, GSH, and tMPBA at equilibrium. Data for single wavelength shots were fit to a single exponential (starting at 2 ms) to extract the amplitudes and observed rate constants (k_{obs}). Data from multiwavelength experiments were fit to a one-step model (starting at 2 ms) to extract UV spectra and observed rate constants (k_{obs}).

pH dependence of the nonenzymatic isomerization

pH dependence of the approach to equilibrium of between HCCA and tHBPA. HCCA was obtained as described previously (Thompson, 2006). Periodic UV-Vis scans from 500 to 200 nm of 110 μM HCCA in 50 mM citrate, 50 mM KH_2PO_4, 50 mM borate (pH 2.0 to 14.0 at 25^{O}C) were taken on a Perkin-Elmer (Boston, MA) *lambda*45 double-beam spectrometer. Buffer alone was used in the second beam as a background. The time dependence of the absorbance change at 296 nm (average of two runs) was fit to a single exponential using the program Prism (Graphpad Software, Inc.).

pH titration and UV-Vis spectra of HCCA and tHBPA. HCCA and tHBPA were obtained as described previously (Thompson, 2006). UV-Vis scans from 500 to 240 nm of 50 μM HCCA or tHBPA in 50 mM citrate, 50 mM KH_2PO_4, 50 mM borate (pH 7.0 to 14.0 at 25^{O}C) were taken on a Perkin-Elmer (Boston, MA) *lambda*45 double-beam spectrometer immediately after introduction to buffer. The pH dependence of absorbance at 420 nm (average of three scans) was fit to a double pKa model using the program Prism (Graphpad Software, Inc.).

Crystallography of HCCA Isomerase GSH and HCCA/tHBPA

Crystallization. Stocks of native protein (and selenomethionine protein) with GSH, and HCCA/tHBPA were made as follows: the protein was thawed on ice and then mixed with GSH and HCCA to a final concentration of 10 mg/ml protein, 1 mM GSH and 1mM HCCA (in the storage buffer). Protein/ligand stock was mixed 1:1 (3µl each) with Emerald Biostructures (Bainbrigde Island, WA) Wizard I #27: 1.2 M NaH_2PO_4, 0.8 M K_2HPO_4, 0.2 M $LiSO_4$, and 0.1 M CAPS pH 6.1. All crystals were grown under 7 ml of Al's oil in a 72 well microbatch plate from Hampton Research (Laguna Niguel, CA). The crystal trays were stored at 21^0C. Crystals normally grew in 1-2 weeks. Crystals were removed from the drop and dipped into a cryoprotectant solution (80% Wizard #27 and 20% ethylene glycol) just prior to mounting on the X-ray goniometer and flash cooling in the cold flow.

X-ray data collection and processing. Data for the native crystals were collected using a Rigaku R-Axis IV image plate area detector on a Rigaku RU-200 rotating-anode X-ray generator operated at 5.0 kW. Crystals were maintained at 100 K using an X-Stream cryostat. Data for the selenomethionine crystal were collected using a Rigaku Micro Max 007 rotating anode generator and a Rigaku RAXIS IV^{++} detector (Rigaku/MSC, The Woodlands, TX). The crystal was cooled to 106 K with a Rigaku Xtream 2000 cryocooler. The diffraction data for the native and selenomethionine crystals were processed with CrystalClear/d*Trek. The statistics are shown in table 12.

Structure determination. The structure was solved using the technique of single isomorphous replacement combined with single wavelength anomalous dispersion. The protein has six methionines and a total length of 203 residues. The Matthews coefficient assuming one molecule in the asymmetric unit is 2.22. The data sets for a native and a selenomethionine crystal were both collected at 1.541 Å. Using SOLVE, six Se sites were identified and the initial figure-of-merit was 0.45 to 2.0 Å. RESOLVE was used in an iterative script with REFMAC5 to build the model. The best model was built in cycle 9; it included 175 residues with sidechains identified for 170 of the residues. The overall R factor for this model was 0.339 and the R_{free} was 0.365. The model was completed in cycles of viewing and modeling with XtalView and refining with REFMAC5. The final model includes all of the residues (1-203), one molecule of glutathione, three molecules of CAPS and 199 water molecules. Nineteen of the residues, the sulfide group of the glutathione, and the CAPS molecule found next to the glutathione are modeled with double conformations. Another of the CAPS molecules is found on the two-fold axis. Using sigma-a weighted f_o-f_c difference maps as a guide, the occupancy for the selenium was set at 0.8 for all of the selenomethionine residues. The electron density for residues 200-203 and 98-99 is weak in both structures. The final refinement statistics are shown in table 13.

Crystallography of HCCA Isomerase with GSH and tMBPA

Crystallization. Stocks of native protein with GSH and tMPBA were made as follows: protein was thawed on ice and mixed with GSH and tMPBA to a final concentration of 10mg/ml protein, 1mM and 1mM respectively. Protein/ligand stock was mixed 1:1 (3µl

each) with Emerald Biostructures (Bainbrigde Island, WA) Wizard I #27: 1.2M NaH_2PO_4, 0.8M $K_2HP\ O_4$, 0.2M $LiSO_4$, and 0.1M CAPS pH 6.1. All crystals were grown under 7ml of Al's oil in a 72 well microbatch plate from Hampton Research (Laguna Niguel, CA). The crystal trays were stored at 21^0C. Crystals grew in 1-2 days. Crystals were removed from the drop and dipped into a cryoprotectant solution (80% Wizard #27 and 20% ethylene glycol containing 10mM tMPBA) just prior to mounting on the X-ray goniometer and flash cooling in the cold flow.

X-ray data collection and processing. Data for the native crystal with the analog tMBPA in the active site were collected using a Bruker-AXS Proteum PT135 CCD area detector and a four-circle kappa goniometer mounted on a Bruker-AXS Microstar microfocus rotating anode X-ray generator operated at 2.7 kW. Crystals were maintained at 100 K using a Bruker-AXS KryoFlex cryostat (Bruker AXS, Germany). Data were integrated and scaled using HKL2000 (*84*). The statistics are shown in table 17.

Structure determination. The analog containing model was solved by molecular replacement using a refined structure of the native protein. The initial R factor when dropping in the protein with only the glutathione molecule was 0.230. The model was completed by alternately viewing and adjusting the model in XtalView and refining it with REFMAC5. In this structure, three residues are modeled with two sidechain conformations. The Ramachandran plot has 95.6% of the residues in the most favored region and 4.4% in the additional allowed region. A substrate analog has been modeled in the active site, and there are three molecules of CAPS, two phosphate ions, and 193

water molecules. The electron density for residues 200-203 and 98-99 is weak. The final refinement statistics are shown in table 18.

CHAPTER IV

LIGAND INDUCED STABILITY OF DIMER INTERFACE MUTANT OF THE RAT GLUTATHIONE-S-TRANSFERASE ISOZYME M1-1 EXAMINED BY AMIDE HYDROGEN-DEUTERIUM EXCHANGE MASS SPECTROMETRY

It has been shown previously that mutation of F56 (the "ball") in rMGST1-1 (Figure 9) impairs its catalytic function and destabilizes its quaternary structure (*42*). The same work demonstrated that introduction of ligand (GSH) could restore native-like dimer stability and CD spectrum in the F56S mutant; however, the mechanism and extent of rescue are still unanswered questions.

Results

Backbone Amide HDX Kinetics of the Native Enzyme (Apo). Rapidly backbone amides ($k_x > 4$ min^{-1}) are the best predictors of solvent accessibility and protein secondary structure (*67, 70, 85*). Figure 16a illustrates the extent of exchange in the rapid kinetic phase for the native enzyme. The N-terminal thioredoxin-like domain shows a modest amount (15 to 30%) of fast exchange in the absence of substrate. Solvent exclusion is much more apparent in the α-helical domain beginning with the α4-helix and extending through the core of the molecule through the α8-helix. The first two helices (α4 and α5) of this domain show no rapidly exchanging amides while the loop that connects them (peptide 114-126) is 30%-exchanged after 15 s. Solvent exclusion

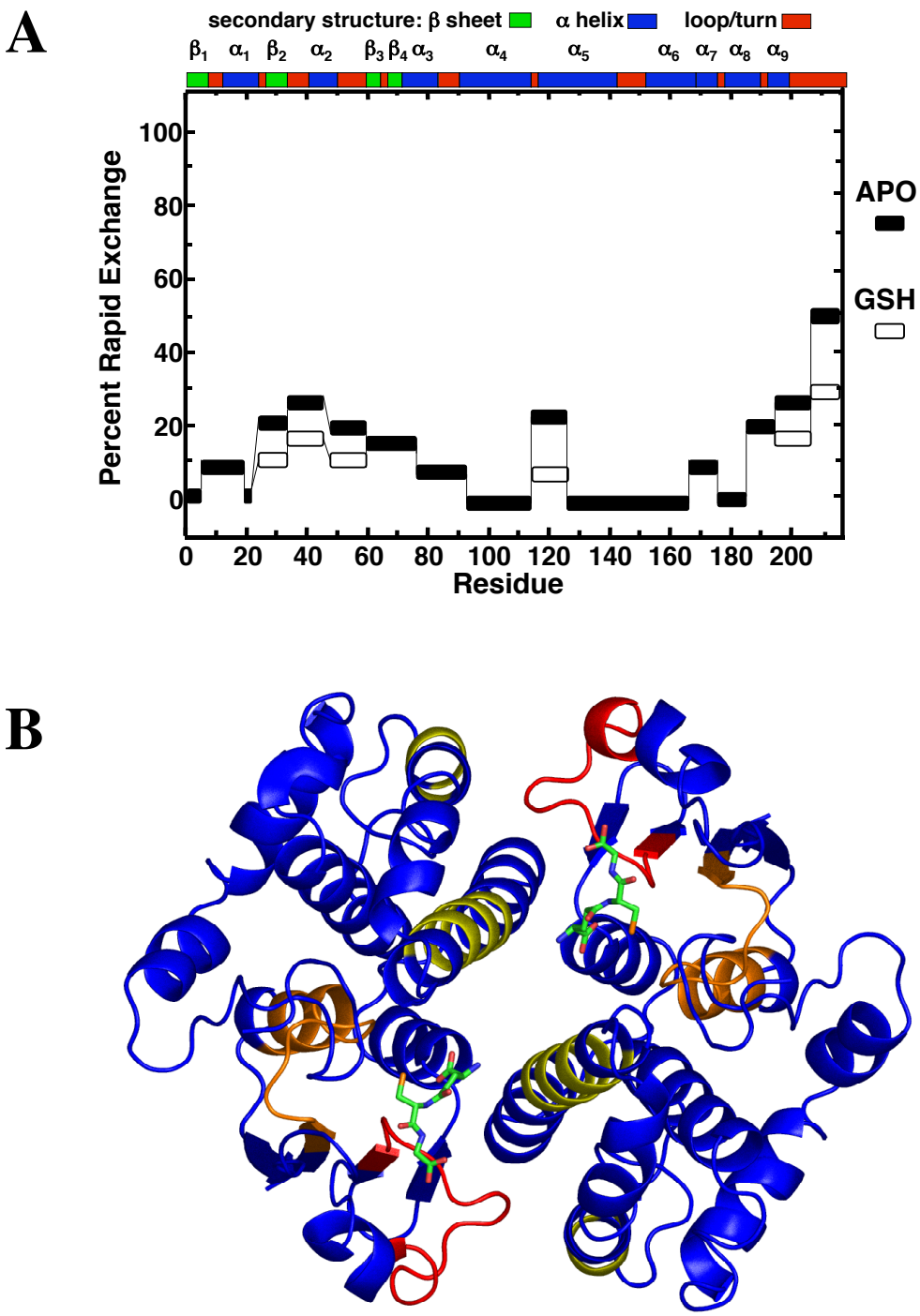

Figure 16. Amide HDX profile of the native enzyme. Panel A shows the amide HDX profile of rapidly exchanging amides (those that are exchanged within 15 sec) first across the native M1-1 sequence in both apo (solid bars) and ligand bound forms (open bars). Ligand bound enzyme showed similar exchange profiles except where noted. Panel B is a ribbon diagram of the rM1-1 backbone (blue) showing peptides that probe vital regions of the structure: the active site = 5-20 (orange), the F56 loop = 49-62 (red), the hydrophobic pocket = 101-110 of α4 and 137-140 of α5 (yellow).

from these helices is consistent with the tight dimer interface packing seen in the crystal structure (*37*). The last 30 residues of the enzyme show a gradual increase in solvent accessibility. The C-terminal tail, peptide 209-217 is the most solvent exposed with 50% of its amides exchanging in the first 15 s. The last helix (α9) and the C-terminal tail are on the surface of the protein and would be expected to exchange rapidly.

There are three peptides in the native enzyme that show no exchange over the 8.5 hr length of the experiment (Figure 16a). These are peptides 19-21, 92-100, and 158-163. Peptide 92-100 is contained in α4 and, as mentioned above, is tightly packed against the opposing monomer. It is also in close contact with α5. Peptide 158-163 is located in the core of a helical-bundle involving α4, α5, and α6. This bundle is believed to be responsible for the overall stability of the C-terminal domain. The lack of exchange in this region is consistent with that hypothesis. Peptide 19-21 is located in the center of α1, which is sandwiched between the β-sheet of the N-terminal domain and α5 of the C-terminal domain (*37*).

The digestion gave four peptides that are good probes of the local dynamics at the active site, the site of mutation, and the hydrophobic pocket (Figure 16b). Peptide 5-20 (including 5-18, 7-18, 7-20 and 8-20) is a good probe of the active site because it contains some of the GSH binding residues including Y7 (binds to sulfur of GSH). Peptide 49-62 covers the entire loop region including F56. Peptides 101-100 and 137-140 cover the majority of the hydrophobic binding pocket.

Backbone Amide HDX Kinetics of the Native Enzyme with Ligand Bound. Backbone amide HDX experiments where performed in the presence of 200 μM GSH or 150 μM

GSO_3^-. The enzyme-GSH complex exhibits decreases in HDX in several regions of the protein. These are best illustrated by the rapidly exchangeable amides (Figure 16a). The decreases in the exchange kinetics are observed in but not confined to the GSH binding site. Interestingly, there is a marked reduction in the extent of rapid exchange at the turn between the α4 and α5 helices (peptide 114-126) and the C-terminal tail including the α9 helix. These structural elements define the channel for the approach to the active site (*37*).

The kinetic profiles for the amide HDX of native enzyme in the presence of either GSH or the substrate analogue GSO_3^- are identical except for four peptides (5-18, 7-18, 7-20 and 8-20) at the active site (Figure 17). The enzyme-GSO_3^- complex exhibits small but reproducible changes in the amplitudes and rate constants for exchange of amides in the intermediate and slow time regime ($k_x < 4$ min^{-1}). Although the overall changes are small, all four peptides across this region show similar behavior. The spatial resolution can be increased by subtraction of the kinetic data from two overlapping peptides as illustrated in figure 17b for the backbone N-H of N7. The side chains of the two residues, W7 and Y6 contribute hydrogen-bonding interactions with the cysteinyl carbonyl oxygen and the sulfur of GSH, respectively (*37*). The amide HDX kinetics are sufficiently sensitive to detect the difference between a thiolate anion and sulfonate group in the active site.

Backbone Amide HDX Kinetics of the F56S Mutant. Not surprisingly, the impact of the F56S on the amide HDX kinetics is greatest at the site of mutation (peptide 49-62), and in the hydrophobic binding pocket (peptides101-110 and 137-140). Significant changes also extend into the GSH binding site (peptide 5-18).

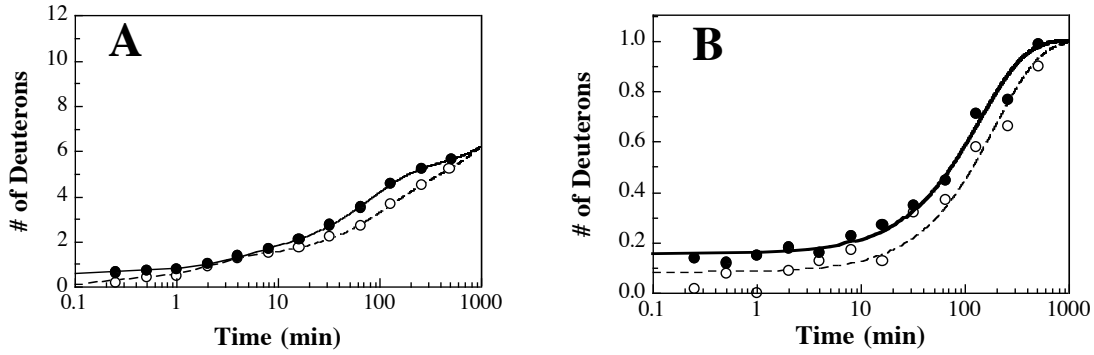

Figure 17. Alteration in the backbone amide HDX between GSH and GSO_3^- in the active site. Panel A is the backbone amide HDX profile of peptide 7-20 in the presence of 200 μM GSH (●) or 150 μM GSO_3^- (O). Panel B is the difference in the backbone amide HDX profile (peptide 7-20 minus peptide 8-20) in the presence of 200 μM GSH (●) or 150 μM GSO_3^- (O). The lines are fits of the data to exponentials with the amplitudes and rate constants given in Table 1.

Table 1: Rate constants and amplitudes for backbone amide HDX into peptides 7-20 and 8-20 in the presence of GSH or GSO_3^-. [a] Difference kinetics isolating the main-chain amide of N7 in the presence GSH and GSO_3^-.

Peptide/ ligand	A_1(D)	k_1 (min^{-1})	A_2 (D)	k_2 (min^{-1})	A_3 (D)	k_3 (min^{-1})
7-20/GSH	0.86 ± 0.05	0.27 ± 0.04	3.6 ± 0.1	0.013 ± 0.002	7.0 ± 0.1	(1.8 ± 0.3) x 10^{-4}
8-20/GSH	0.85 ± 0.07	0.25 ± 0.04	3.1 ± 0.1	0.013 ± 0.001	6.6 ± 0.2	(8 ± 5) x 10^{-5}
(7-20)-(8-20)[a]	0.84 ± 0.02	(7.0 ± 0.6) x 10^{-3}				
7-20/GSO_3^-	1.26 ± 0.09	0.5 ± 0.1	2.8 ± 0.5	0.01 ± 0.002	7.9 ± 0.5	(3 ± 1) x 10^{-4}
8-20/GSO_3^-	1.19 ± 0.06	0.50 ± 0.06	2.8 ± 0.5	0.008 ± 0.001	6.9 ± 0.5	(1 ± 1) x 10^{-4}
(7-20)-(8-20)[a]	0.92 ± 0.02	(5.1 ± 0.6) x 10^{-3}				

The F56S mutant shows increases in the fraction of rapidly exchanging amides in the loop harboring the mutation, a fact that is indicative of a higher degree of solvent access or increased loop dynamics (Figure 18). The F56S mutant retains the ability to bind the substrate analogue inhibitor GSO_3^- (K_i = 4 mM) (*5*), and the addition of ligand (GSO_3^-) to the F56S mutant tends to restore native-like HDX kinetic profile as shown in Figure 18.

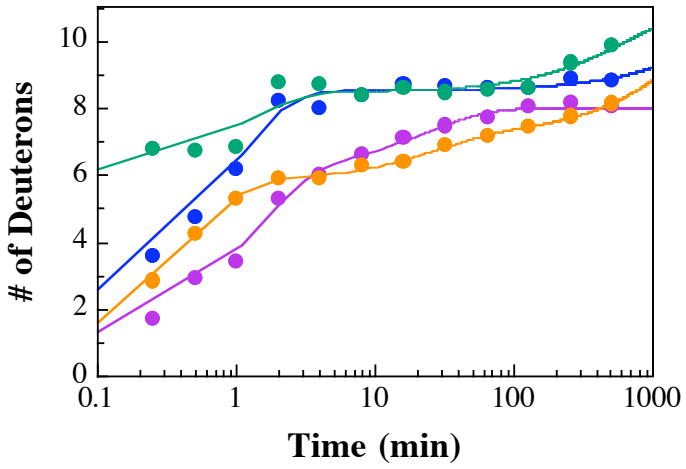

Figure 18. Kinetic profiles for backbone amide HDX at the site of mutation, peptide 49-62. The native (blue) and F56S mutant (green) without ligand and native with 200 μM GSH (magenta) and F56S mutant with 20 mM GSO_3^- (orange) are shown. The solid lines are fits of the data to single/multiple exponentials with the rate constants and amplitudes given in Table 2.

Table 2: Rate constants and amplitudes for backbone amide HDX into the F56 loop at the dimer interface (peptide 49-62).

sample	A_1 (D)	k_1 (min^{-1})	A_2 (D)	k_2 (min^{-1})	A_3 (D)	k_3 (min^{-1})
Native	3.6 ± 0.2	0.7 ± 0.1	2.5 ± 0.1	(2 ± 2) x 10-4		
F56S	1.7 ± 0.1	0.24 ± 0.05				
Native/GSO_3^-	4.7 ± 0.5	0.7 ± 0.2	1.4 ± 0.4	0.024 ± 0.016	3.8 ± 0.1	(6 ± 1) x 10^{-4}
F56S/GSO_3^-	5.4 ± 0.3	2.4 ± 0.2	1.4 ± 0.1	0.04 ± 0.01		

Like the loop that harbors F56, the helices that define the hydrophobic pocket in both the F56S mutants exhibit increases in the amide HDX rates relative to the native enzyme (Figure 19). However, the increases observed are in the intermediate and slow phase regimes of the exchange kinetics. This suggests that the α4/α5 helices have not been perturbed structurally but that the dynamics of this region have been increased. Addition of ligand to the F56S mutant also produces a reduction in exchange kinetics when

compared to the apoenzyme. However, the rescue of native-like behavior is not complete particularly with respect to the α5-helix, peptide 137-140 (Figure 19b). The F56S mutant still shows enhanced exchange kinetics in the slow phase regime. Thus, binding of GSO_3^- does not completely restore the native structure or dynamics of this region.

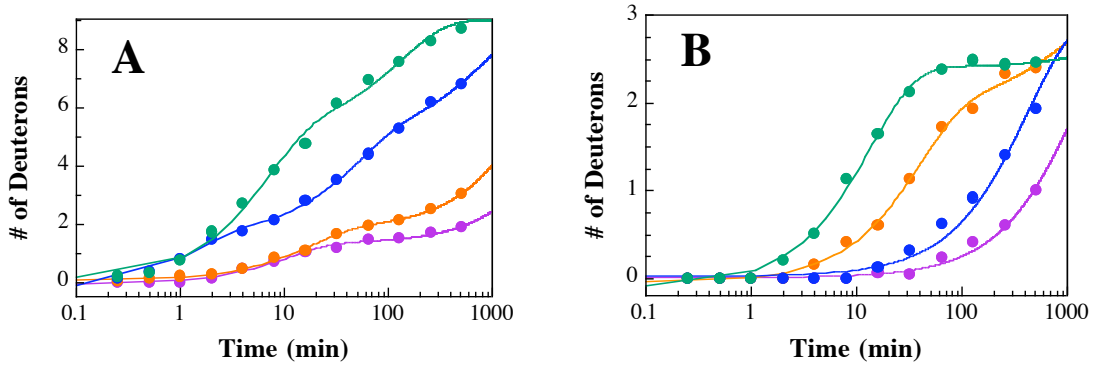

Figure 19. Kinetic profiles for backbone amide HDX of peptides surrounding the hydrophobic pocket. Panel A shows the α4 peptide101-110 and panel B shows the α5 peptide137-140. The native (blue) and F56S mutant (green) without ligand and native with 200 μM GSH (magenta) and F56S with 20 mM GSO_3^- (orange) are shown. The solid lines are fits of the data to single/double exponentials with the rate constants and amplitudes given in Table 3.

Table 3: Rate constants and amplitudes for backbone amide HDX near the hydrophobic pocket between the α4- and α5-helices at the dimer interface (peptides 101-110 and 137-140).

peptide/sample	A_1 (D)	k_1 (min^{-1})	A_2 (D)	k_2 (min^{-1})
101-110 Native	3.3 ± 0.4	0.04 ± 0.01	5.3 ± 0.4	(1.9 ± 0.3) x 10^{-4}
101-110 F56S	3.6 ± 0.3	0.07 ± 0.01	5.1 ± 0.3	(3.9 ± 0.4) x 10^{-3}
101-110 Native/GSO_3^-	1.4 ± 0.1	0.09 ± 0.01	7.7 ± 0.1	(1.5 ± 0.2) x 10^{-3}
101-110 F56S/GSO_3^-	1.1 ± 0.1	0.13 ± 0.02	7.85 ± 0.05	(1.5 ± 0.3) x 10^{-4}
137-140 Native	0.6 ± 0.1	0.08 ± 0.02	2.5 ± 0.1	(1.8 ± 0.1) x 10^{-3}
137-140 F56S	2.2 ± 0.2	0.030± 0.004	0.6 ± 0.2	(2.6 ± 1.3) x 10^{-3}
137-140 Native/ GSO_3^-	2.96 ± 0.02	(9.0 ± 0.6) x 10^{-4}		
137-140 F56S/GSO_3^-	2.0 ± 0.1	0.026 ± 0.003	1.0 ± 0.1	(1.2 ± 0.4) x 10^{-3}

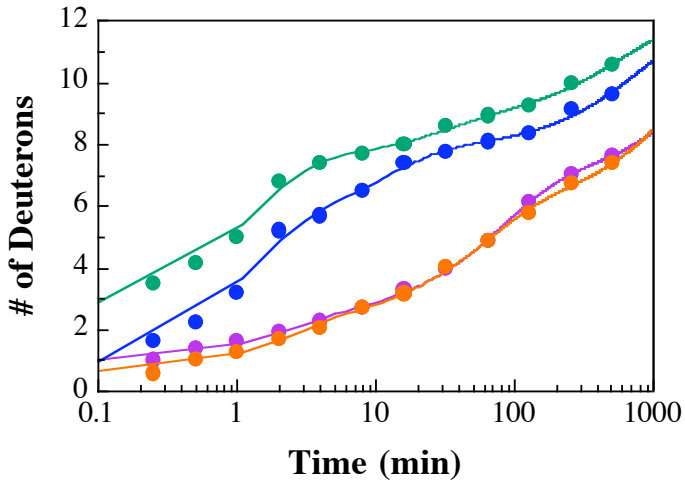

Figure 20. Kinetic profiles for backbone amide HDX exchange at the GSH binding site, peptide 5-18. The native (blue) and F56S mutant (green) without ligand and native with 200 μM GSH (magenta) and F56S with 20 mM GSO_3^- (orange) are shown. The solid lines are fits of the experimental data to multiple exponentials with rate constants and amplitudes given in Table 4.

Table 4. Rate constants and amplitudes for backbone amide HDX near the GSH binding site (peptide 5-18).

sample	A_1 (D)	k_1 (min^{-1})	A_2 (D)	k_2 (min^{-1})	A_3 (D)	k_3 (min^{-1})
Native	4.7 ± 0.2	0.21 ± 0.03	3.9 ± 0.1	(1.9 ± 0.2) x 10^{-3}		
F56S	5.1 ± 0.2	0.47 ± 0.06	4.5 ± 0.1	(1.8 ± 0.2) x 10^{-3}		
Native/GSO_3^-	1.7 ± 0.2	0.5 ± 0.1	3.7 ± 1.5	0.007 ± 0.003	5.9 ± 1.6	(4 ± 4) x 10^{-4}
F56S/GSO_3^-	1.7 ± 0.2	0.4 ± 0.1	3.6 ± 0.3	0.017 ± 0.004	6.1 ± 0.4	(6 ± 2) x 10^{-4}

The mutations at the dimer interface also influence the backbone amide HDX behavior in the GSH binding site as illustrated in Figure 20 for peptide 5-18. All of the mutants (F56S, E, and R) studied previously (*42*) have large increases in the K_M for GSH and K_i for GSO_3^- (*42*) which indicates that the mutations introduce a functional disruption of the active site. Though the F56S mutant is also functionally impaired, the backbone HDX

kinetics are much more native-like. In fact, with the addition of GSO_3^- (Figure 20), the native and F56S mutants are almost indistinguishable in their exchange profiles.

Discussion

Substrate Binding and the Dimer Interface. Previous functional studies have suggested that there is close link between the structure of the dimer interface and the GSH binding site (*5*). This link is apparent in the influence of GSH binding on the backbone amide HDX kinetics. In addition to the reduction in exchange rates at the GSH binding sight, there are notable decreases at the dimer interface including the loop harboring F56, the junction between the α4 and α5-helices and more remotely at the C-terminal tail as illustrated in Figure 21. These results are consistent with previous observations of decreased backbone amide HDX by NMR spectroscopy in the human class mu enzyme upon ligand binding at the active site (*20*). The reduced rates of exchange at the subunit interface and the C-terminal tail that do not directly interact with GSH are likely due to a damping of low-frequency ($>10^{-6}$ s) conformational excursions that lead to increased solvent exposure of the backbone. In this regard it is important to point out that the side-chain of P60 and the base of the 56-loop is in van der Waals contact with Y6, a residue that directly interacts with the sulfur of GSH.

The substrate analogue inhibitor, GSO_3^-, has essentially the same effect on the HDX kinetics of the native enzyme with the exception of subtle changes that occur in peptides located close to the thiolate or sulfonate groups. The 30% reduction in the rate constant for backbone amide HDX at N7 in the E•GSO_3^- complex compared to the E•GS^- complex (Figure 17, Table 1) suggests that GSO_3^- forms a tighter complex that more effectively

limits conformational fluctuations at the active site. This observation is also consistent with the fact that GSO_3^- has a lower off rate than GS^- (*14*).

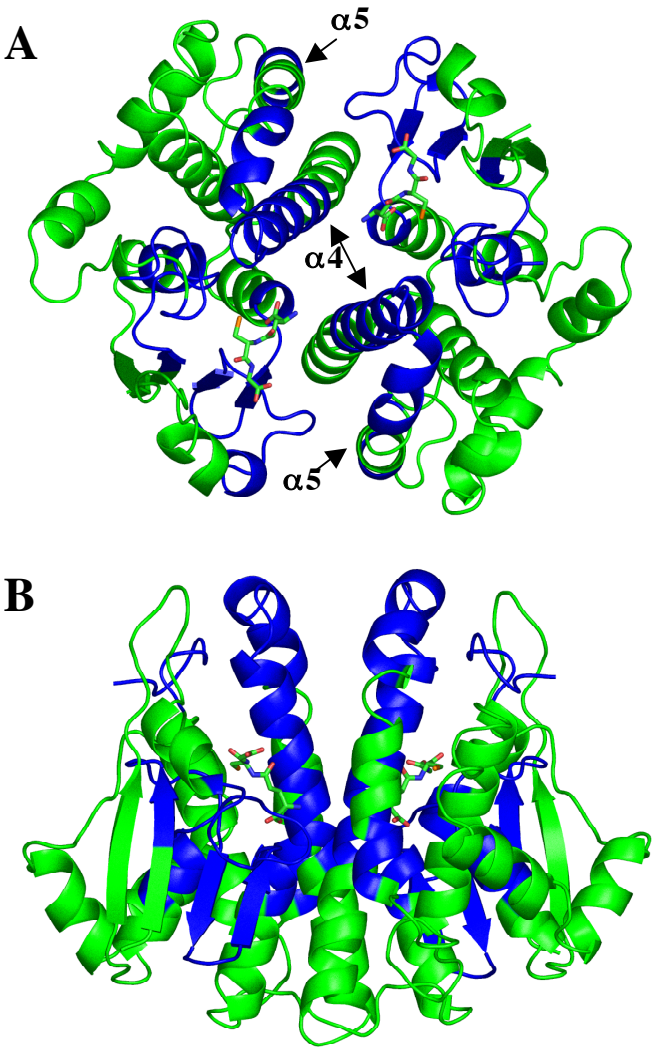

Figure 21. Decreases (blue) in backbone amide HDX kinetics in the native + GSH versus the apoenzyme. These changes are viewed down the two-fold axis of the dimer (A) and perpendicular to the two-fold axis (B). The GSH molecule and Y6 are shown in stick representation. The figure was rendered with the program PyMol (*10*).

Structure and Dynamics of the F56S Dimer Interface Mutant. "Ball and socket" hydrophobic interactions are common stabilizing motifs in oligomeric protein structures

(*39*). The mutational disruption of this type of interaction in the class Mu GSH transferase has been previously demonstrated to alter dimer stability and impair the catalytic function of the mutants (*5*). The loss of catalytic function is associated with a

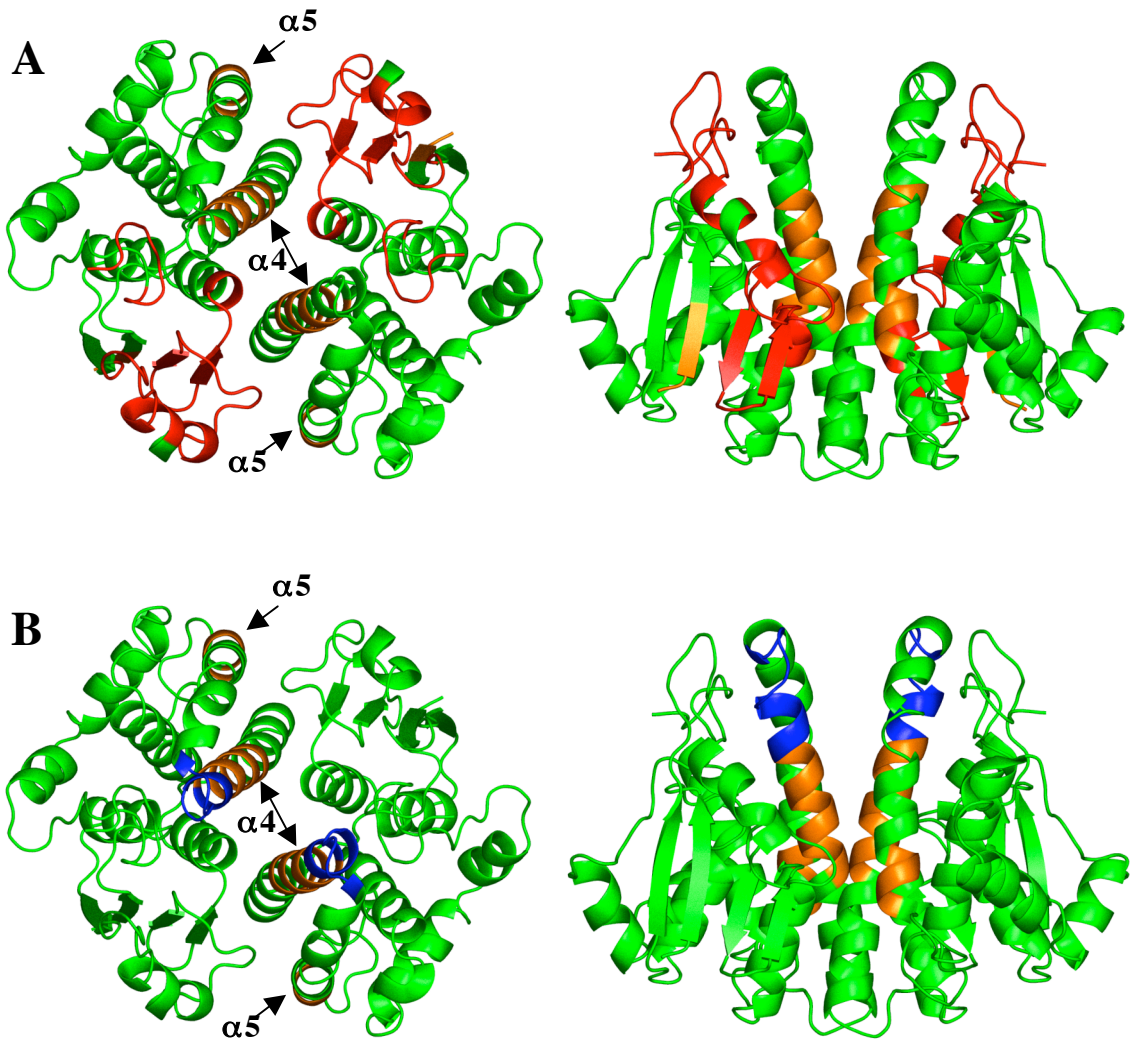

Figure 22. Overview of the changes in backbone amide HDX behavior of the F56S mutant. Changes in the F56S mutant versus native are shown as increases in the rapid phase (red) and slower phases (orange) or decreases (blue). Panel A shows the difference in apo enzymes and panel B shows those containing ligand (GSH for native and GSO_3^- for the F56S mutant). The figure was rendered with the program PyMol (*44*).

disruption of the structure of the GSH binding site. Because the predominant species is dimer [all enzymes at 60 μM (*42*) during deuteration (see methods)] in these experiments, the changes in backbone amide HDX kinetics exhibited by the mutant enzyme provides new insight into the structural bases for the altered behavior. The F56S mutant shows enhanced exchange at the dimer interface as well as in the active site indicating that the mutation results in larger coupled conformational excursions in these regions (Figure 22).

The changes in the backbone amide HDX kinetics are most apparent in the α4 (peptide 101-110) and the α5 (peptide 137-140) helices (Figure 22a) and are not reversed when the GSH binding site is occupied with the inhibitor GSO_3^- (Figure 22b). Thus it is not clear that the conformation of the GSH binding site is completely coupled to the conformational integrity of the dimer interface. Residues Y137 and F140 form part of the hydrophobic socket located between the α4- and α5-helices. It could be the case that the dynamics of the dimer interface in the F56S mutant are similar to the native enzyme. The small hydrophilic side-chain of S56 may simply facilitate entry of solvent into the socket and therefore enhance exchange in peptide 137-140.

Conclusions. Main-chain amide HDX kinetics provides a direct readout of the effect of mutations on the structure and dynamics on the dimer interface of rGSTM1-1 and the remote influence on enzyme function. Disruption of the hydrophobic "ball and socket" motif leads to an impairment of catalytic function irrespective of whether dimer stability or protein dynamics at the subunit interface are increased or decreased.

CHAPTER V

A DOUBLE MUTATION AT THE SUBUNIT INTERFACE OF THE RAT GLUTATHIONE-S-TRANSFERASE ISOZYME M1-1 RESULTS IN A STABLE FOLDED MONOMER

Our collaborator on the F56 project, Dr. Heini Dirr, was investigating the role of the charge cluster motif (Figure 9) on the stability of the rGSTM1-1 dimer structure and discovered that a R81A mutation in an F56S background gave a stable monomer structure. His student, John Walters, performed the initial gel filtration study, CD/fluorescence spectroscopy, GSO_3^- binding, unfolding work, and ANS binding. Jim Parsons performed the dynamic light scattering experiment. I did a basic kinetic work-up and then used HDX-MS to investigate this mutant and showed that its monomer structure was native-like.

Results

Global Structura1 Properties. Gel filtration experiments with the F56S/R81A mutant indicate that the protein elutes as a single species at concentrations ranging from 0.2 to 600 μM (data not shown). The elution volume on a calibrated Tosohaas TSKGEL $G2000SW_{XL}$ column (7.8 mm x 300 mm) corresponds to the expected size of 26 kDa for a folded monomer. This initial observation was confirmed by combining gel filtration chromatography with multi-angle laser light scattering (see methods) of both the native and mutant proteins. These analyses show that the F56S/R81A mutant is a single species with a molecular mass moment of 25,400 ± 200 g/mol, consistent with the protein being a

monomer. As expected, the native enzyme behaves as a single species with a mass of 51,500 ± 200 g/mol. When a mixture of the two proteins is analyzed, the native enzyme and the F56S/R81A mutant are well resolved (Figure 23), and return molecular masses consistent with those from analysis of the individual samples (Figure 23, legend).

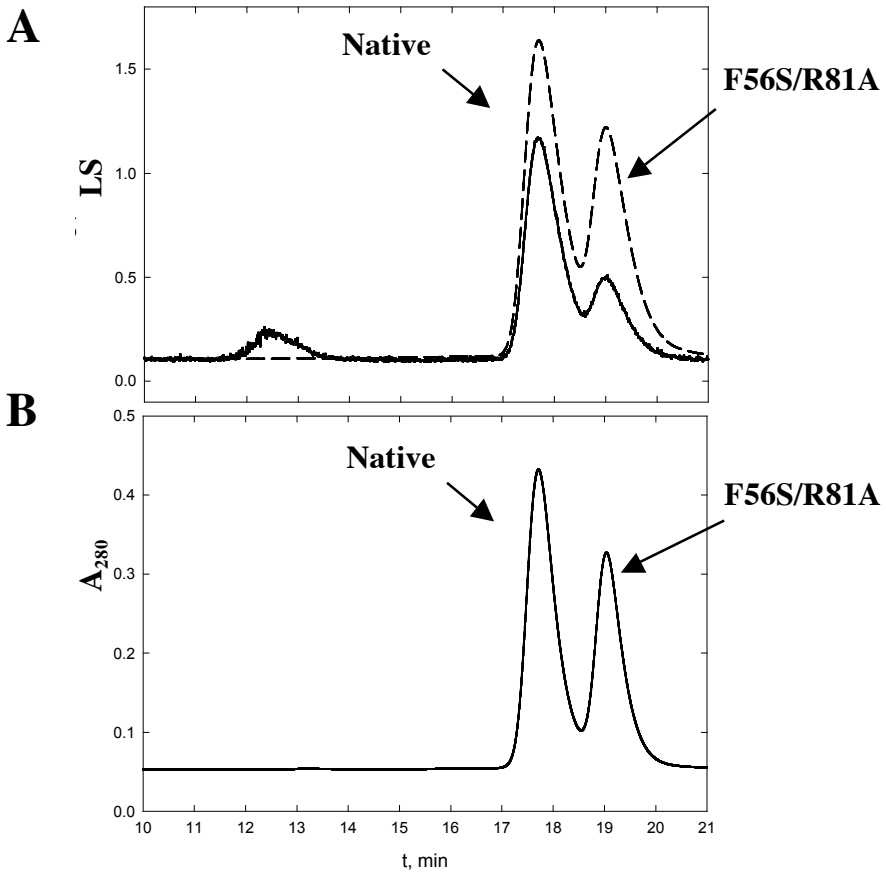

Figure 23. Quaternary structure of the F56S/R81A rGSTM1-1 mutant. Panel A shows the chromatogram the output signal from the DAWN light scattering detector (solid line) and the concentration trace from the refractometer (dashed line) while panel B shows the output from the UV detector (280 nm). The signal at 12.5 min from the 90° light-scattering channel (panel A) represents a small amount of protein aggregate found in both samples. The molecular mass moments from the multi-angle laser light scattering analysis were 26,100 ± 300 g/mol for the F56S/R81A mutant and 50,800 ± 200 g/mol for the native enzyme.

Far and near-UV CD and tryptophan fluorescence spectroscopy indicate that the double mutant has a secondary structure that is native-like. Small perturbations in the environments of the tryptophan residues in the mutant are evident from the far UV portion of the CD spectra and the fluorescence emission spectra (data not shown). The spectra of the F56R/R81A mutant resembles those of the F56S mutant of rGSTM1-1 (*42*) and the related isoenzyme, rGSTM2-2 (*86*).

Functional Properties of F56S/R81A rGSTM1. The binding affinity of GSO_3^- for F56S/R81A was determined by fluorescence titration (K_d = 24 mM). The affinity is substantially less than that for the native dimer (K_d = 2.8 μM) and indicates a loss of about 9.2 kcal/mol in binding energy for the monomeric protein. Unlike the F56S mutant, which shows saturation kinetics and can achieve or exceed wild-type-like activity at saturating GSH (*42*), the reaction velocity of the F56S/R81A mutant exhibited a linear concentration dependence up 40 mM GSH. Linear regression of the data resulted in a k_{cat}/K_M^{GSH} for the double mutant that was reduced by a factor of 10^5 compared to the native enzyme (*87*) (Table 5). The K_M for GSH is >> 40 mM.

Table 5: Efficiency of CDNB conjugation in the native and dimer interface mutants.

Enzyme	k_{cat} (s^{-1})	K_m^{GSH} (mM)	k_{cat}/K_m^{GSH} ($M^{-1}s^{-1}$)
Native[a]	18 ± 2	0.036 ± 0.004	(5.0 ± 0.8) x 10^5
F56S[b]	90 ± 10	20 ± 2	(4.5 ± 0.7) x 10^3
F56S/R81A	>> 0.2	>> 40	5.2 ± 0.4

[a] Data from reference (*87*). [b] Data from reference (*42*).

ANS Binding. The location of the binding site for ANS in the mutant proteins F56S and F56S/R81A is unknown, but the dye has been shown to bind to many GSH transferases at the active site (*88*) and/or along the dimer interface (*89, 90*) making the fluorescent dye a useful probe for monitoring intersubunit and intrasubunit structural alterations (*42, 86, 88*). The spectral properties of ANS bound to F56S/R81A differ from those of the native enzyme (data not shown) but are similar to those for the dye bound to the F56S mutant (*42*). This result suggests that the dye-binding site in the double mutant is affected primarily by the loss of the ball-and-socket motif and not by disruption of the dimeric structure and provides further evidence that the loss of the dimer interface does not substantially destabilize the individual subunits.

Equilibrium Unfolding of F56S/R81A rGSTM1. Like native rGSTM1-1 and its F56S variant, the monomeric F56S/R81A mutant unfolds reversibly. Urea-induced unfolding of F56S/R81A, monitored by far-UV CD and tryptophan fluorescence is shown in Figure 24. Both probes yield overlapping transitions indicating a two-state unfolding process with the simultaneous loss of secondary and tertiary structures. The monomeric mutant does not appear to sample high-energy, partially unfolded states under native (0-3 M urea) and denaturing (>3 M urea) conditions. In contrast, the native enzyme and F56S mutant, unfold via a three-state process (N ↔ 2I ↔ 2U) with the dimer-monomer equilibrium shifted towards the monomeric intermediate, I, for the F56S mutant (*86*) (see Table 6). The lower C_m and ΔG (H_2O) values for F56S/R81A, when compared to those for the I ↔ U transitions of native enzyme and the F56S mutant (Table 6), indicate a reduced stability of the monomeric mutant. Furthermore, the lower experimental *m*-value

than that predicted for the double mutant (Table 6) indicates that its unfolding is less cooperative and that less surface area becomes exposed to solvent upon unfolding.

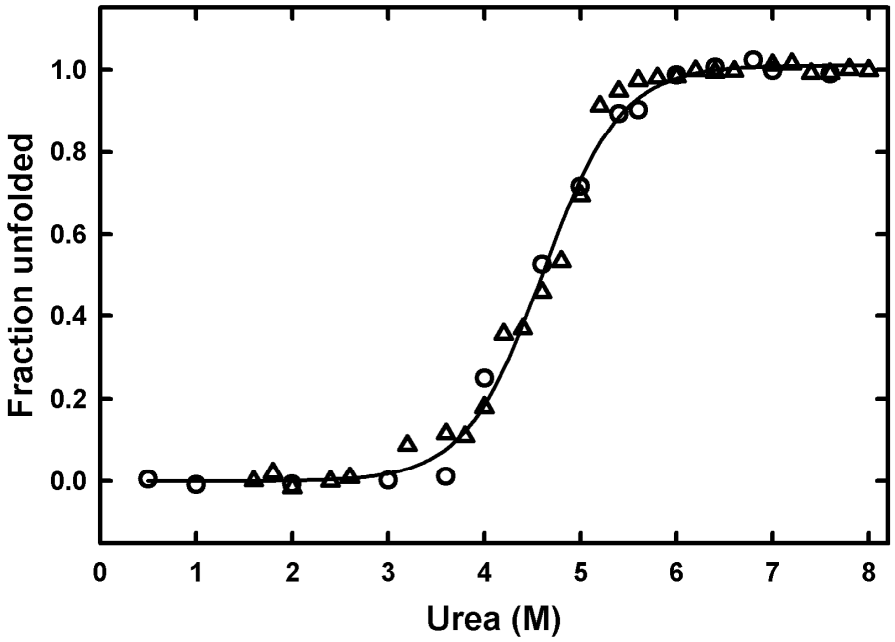

Figure 24. Unfolding curves of the F56S/R81A rGSTM1-1 mutant. Fluorescence (circles) and CD ellipticity at 222 nm (triangles). The solid line represents a nonlinear least-squares regression fit to the data according to a two-state model with folded and unfolded monomers (*16*).

Table 6: Data from equilibrium unfolding of the native M1-1, F56S, and F56S/R81A rGSTM1-1 mutants[a].

rGST M1-1	model	C_m (M urea)	$\Delta G(H_2O)$ (kcal/mol)	*m*-value (kcal/mol M^{-1} urea)
native	$N_2 \leftrightarrow 2I$	3.1	10.8	1.0
	$I \leftrightarrow U$	5.2	16.5	3.5
F56S	$N_2 \leftrightarrow 2I$	2.3	10.3	1.0
	$I \leftrightarrow U$	5.1	15.9	3.1
F56S/R81A	$I \leftrightarrow U$	4.6	10.1	2.0 (2.5)[b]

[a] Data for wild-type and F56S taken from references (*16*) and (*10*), respectively. [b] Value calculated according to reference (*91*).

Amide HDX and Structural Dynamics. Pepsin digestion yields 42 well-resolved peptides that are common to the native, F56S and F56S/R81A proteins representing coverage of 97% of the sequence (Figure 25). The two regions not covered are residues 28-33 and residues 47-48. The profile of rapidly exchanging amide protons for selected peptides from native, F56S (*92*) and F56S/R81A are shown in Figure 25. The kinetic profile of the F56S/R81A mutant resembles that for the native and F56S proteins indicating that the combined F56S and R81A mutations do not induce major changes in the core structure of the monomeric protein, a result consistent with the structural data presented above.

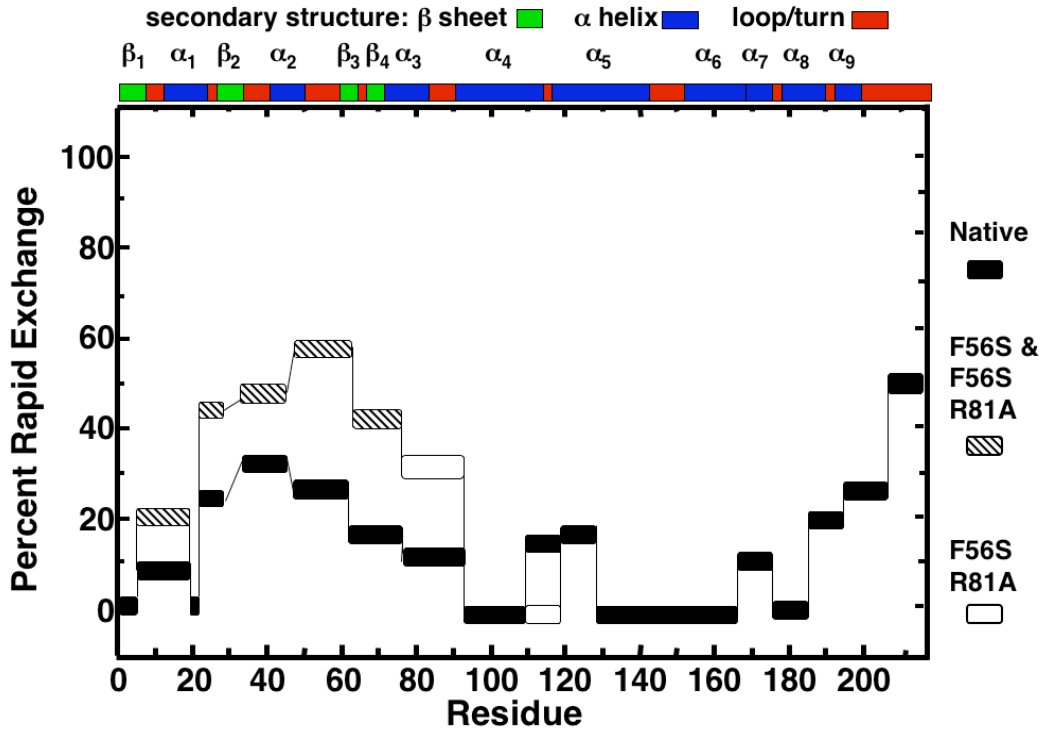

Figure 25. Amide protons exchanged by the first 15 sec for peptides from native, F56S (*92*), and F56S/R81A rGSTM1-1. Deviations of F56S and F56S/R81A from the native are shown as hashed boxes. Deviations of the F56S/R81A from both native and F56S are open boxes.

Although the HDX kinetics of the F56S and F56S/R81A mutants are similar, they do exhibit interesting differences. For example, when compared to F56S, the F56S/R81A mutant shows enhanced HDX kinetics for peptides 75-91 and 92-96 but reduced rates of exchange for peptide 110-119 as illustrated in Figures 25 and 26. Peptides 92-96 and 75-91 (which contains the R81A mutation) are located at the core of the charge cluster. These two peptides are primarily involved in intersubunit interactions and would be expected to show increases in HDX kinetics upon loss of the dimeric structure. The decrease in solvent accessibility of peptide 110-119 is most likely due to the reorganization of the junction between helices α4 and α5 (Figure 26a). Reorganization of this junction is not unexpected because these helices are involved in many of the intersubunit interactions (Figure 9c). The loss of solvent accessibility indicates that the junction and the *a*4 and *a*5 helices form a tighter interaction or are folded in toward the core of the monomer structure. The α4 and α5 helices are part of a channel that controls access to the active site in the native enzyme (*73*). The alternate conformation of this junction, as reflected in the decreased amide HDX, may contribute to the reduced catalytic activity observed in the double mutant.

The lack of an increase in amide HDX in peptides 19-21 in helix α1, 97-100 in helix α4, and 158-163 in helix α6 (Figures 25 and 27), demonstrates that the conformation and stability of these regions are preserved after dissociation of the dimer to form the F56S/R81A monomer. Peptide 97-100 is involved in intersubunit interactions and becomes exposed to solvent upon disruption of the dimer, yet shows no increase in exchange. This could result from a close interaction with peptide 158-163 (Figure 27) and may indicate an important structural motif for the stability of domain 2. Peptide 158-163

is also in close proximity to peptide 19-21. The absence of increases in exchange for either of these peptides in the monomeric F56S/R81A mutant may indicate an important interdomain interaction.

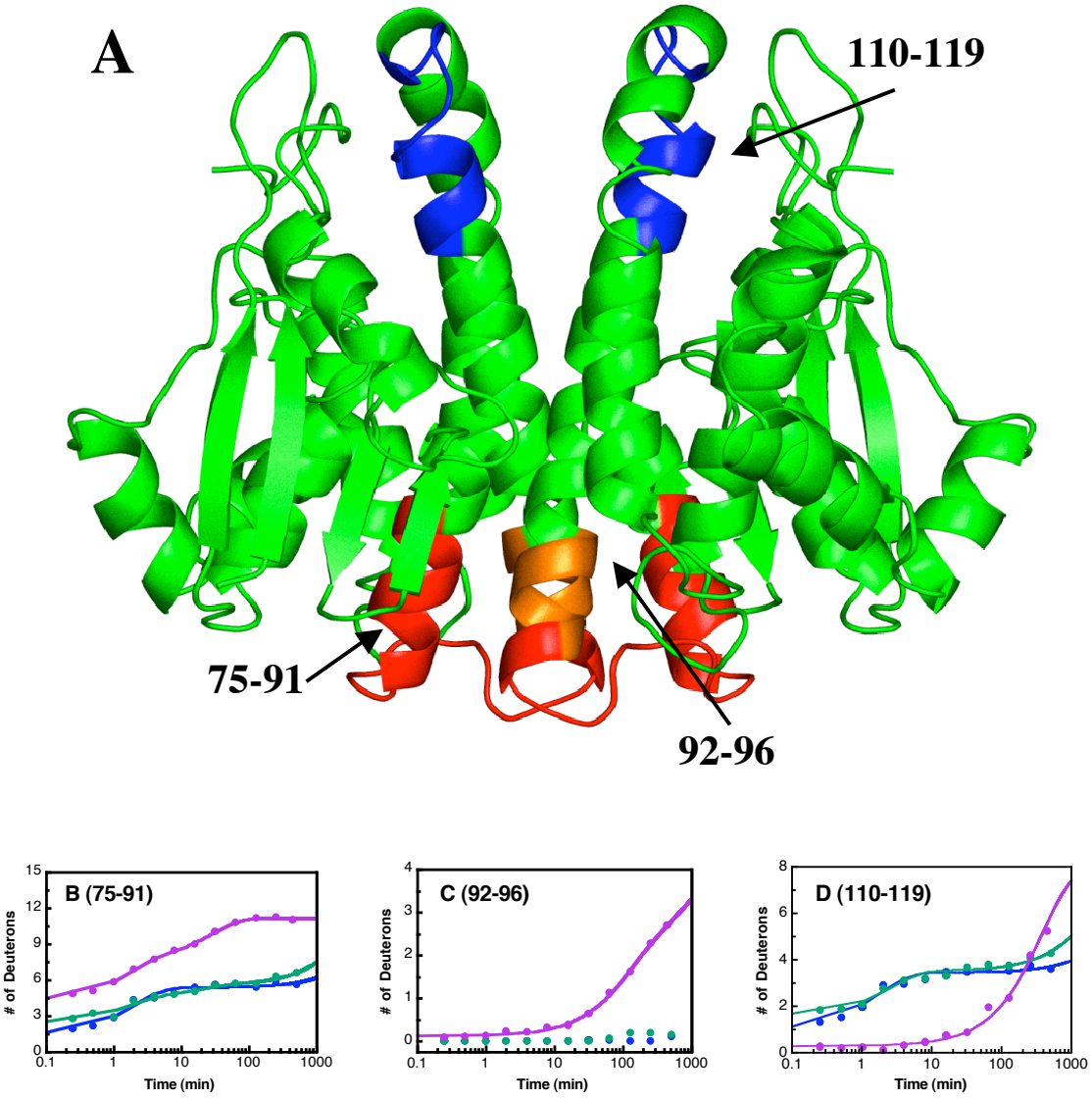

Figure 26. Peptides in F56S/R81A with exchange behavior that differs from F56S. Panel A is a ribbon diagram of the rGSTM1-1 backbone (green) showing increases in fast phase exchange (red), increases in slow phase exchange (orange), and decreases in exchange (blue). The kinetics of amide H/D exchange for the three peptides is illustrated in panels B (peptide 75-91), C (peptide 92-96) and C (peptide 110-119). The kinetic profiles for the native enzyme, the F56S mutant (*92*) and the F56S/R81A mutant are shown in blue, green and magenta, respectively.

Table 7: Rate constants and amplitudes for backbone amide HDX into F56S R81A rGSTM1-1 peptides 75-91, 92-96, and 110-119 (Figure 26).

Peptide	A_1 (D)	k_1 (min^{-1})	A_2 (D)	k_2 (min^{-1})
75-91	3.1 ± 0.3	0.6 ± 0.2	3.6 ± 0.3	0.042 ± 0.006
92-96	1.8 ± 0.5	0.009 ± 0.002	2.1 ± 0.5	0.001 ± 0.0005
110-119	7.7 ± 0.1	0.003 ± 0.0001		

Discussion

Properties of a Stable Monomer. We have previously shown that wild-type rGSTM1-1 undergoes a reversible dissociation of its subunits with an approximate K_d of 0.012 μM. Disruption of the ball-and-socket motif, with the introduction of the F56S mutation, shifts the equilibrium toward the monomeric species (K_d of 0.5 μM) (*42*). In the present study, the inter-subunit charge cluster motif was disrupted with the R81A mutation. This site was chosen because it is the only residue in the cluster that directly participates in an intersubunit interaction. While mutations at either the ball-and-socket motif or the charge cluster motif have been shown to produce equilibrium mixtures of dimeric and monomeric forms of GSH transferases (*42, 43*), this study demonstrates that the simultaneous introduction of single mutations in both motifs is sufficient to generate a monomeric enzyme with a compact folded structure, albeit with greatly reduced catalytic activity.

Dimer-Dependent Enzyme Activity. The binding of GSH or the inhibitor GSO_3^- to the F56S mutant of rGSTM1-1 restores a more native-like conformation in the active site (*8*). At sufficiently high GSH concentrations, the F56S mutant exhibits robust catalytic

activity (*8, 23*). The F56S mutant does not have a fully functional hydrophobic ball-and-socket motif required to stabilize the 56-loop between α2-β3 near the active site. In fact, residues in the 56-loop are in contact with Y6 in the active site, a residue that is crucial for efficient catalysis. Although the backbone of the 56-loop appears to have similar HDX characteristics in the F56S and F56S/R81A mutants (Figure 25), native-like activity cannot be achieved in the monomer (Table 5). These facts suggest that the dimer interface helps enforce the conformation of the loop that is vital for GSH binding and efficient catalysis.

The disruption of the 56-loop and the inability to bind GSH in a productive manner is probably the principal reason for the reduced catalytic efficiency of the F56S and F56S/R81A mutants. However, the HDX results do indicate a change in structure and dynamics at the junction between the α4 and α5 helices (peptide 110-119). This region contains Y115, a residue that is located atop a channel that is important for substrate access and product release in the dimer (*14*). The reduced HDX suggests a tighter interaction between the two helices or with the rest of the monomer. At this point it is unclear whether the change in structure and dynamics of this region contributes to the further impairment of the catalytic efficiency of the monomer.

Cooperative Unfolding. The tertiary structure of the F56S/R81A mutant enzyme is more loosely packed than that of either the native enzyme or the F56S mutant. However the double mutation does not significantly impact the intrasubunit interactions between domains 1 and 2 as suggested by the similarity in the HDX kinetics. Nevertheless, the equilibrium unfolding data for the double mutant demonstrates that intersubunit

interactions make significant contributions to stabilizing the tertiary structures of subunits in GSH transferase dimers as in the native and F56S proteins. These interactions are not obligatory for the stabilizing interaction of domain 1 and 2 in each subunit. At equilibrium, domains 1 and 2 do not unfold independently but unfold in a concerted manner.

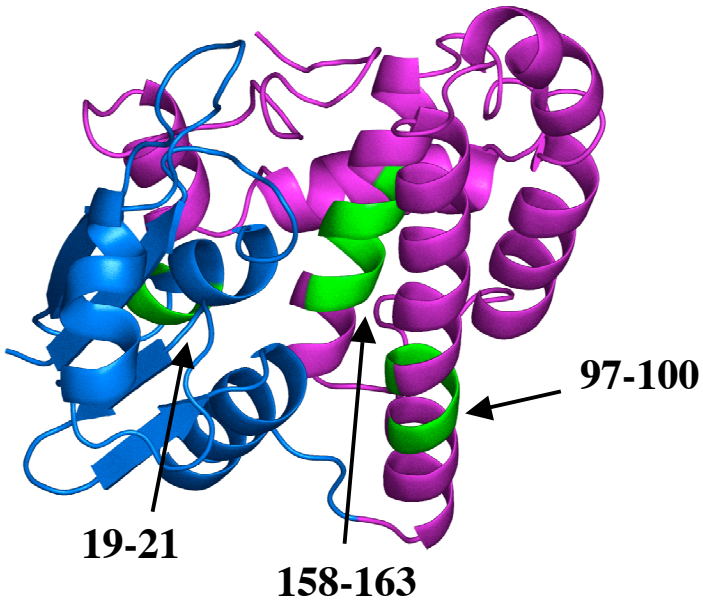

Figure 27. Ribbon diagram of one subunit of rGSTM1-1: domain 1 (blue) and domain 2 (magenta). F56S/R81A peptides that show no H/D exchange during the length of the experiment are shown in green: 19-21, 97-100, and 158-163. Native and F56S also show no HDX into these peptides during the length of the experiment.

Molecular Basis for Domain Cooperativity. A concerted unfolding model for the monomeric double mutant suggests interdomain cooperativity. The strongest evidence for an interdomain interaction comes from the HDX behavior of peptides 19-21, 97-100, and 158-163 (Figure 27). These peptides show no amide HDX during the time course of the experiment, a fact that indicates a very stable monomeric fold and not a molten globule-

like state. The fact that these protein regions are in close proximity to each other and cross the domain barrier [domain 1 (19-21) and domain 2 (158-163)] could indicate a stable core of interactions between domain 1 and 2 that constitute the cooperative link.

The stability of individual GSH transferase subunits in the absence of the dimer interface suggests that the evolution of intersubunit interactions has arisen more recently than evolution of the monomer itself. This is consistent with the hypothesis that the canonical GSH transferases arose from enzymes similar to glutaredoxin 2 (*22*). It also suggests that the selectivity of intersubunit interactions for isoenzymes of a particular class arose to fine tune the enzyme structure to broaden substrate specificity and biological function.

CHAPTER VI

A GLUTATIONE COFACTOR AND KAPPA FOLD DEMONSTRATE THAT 2-HYDROXYCHROMENE-2-CARBOXLATE ISOMERASE IS A KAPPA CLASS GLUTATHIONE TRANSFERASE

Results

Steady-state kinetics of HCCA Isomerase with GSH and CDNB, HCCA, or tHBPA. The enzyme showed a slow but significant activity toward CDNB (Table 8). Due to low affinity of the enzyme for CDNB and solubility limits of the compound, saturation of CDNB could not be reached. k_{cat}/K_m was determined directly from linear regression of the initial velocity data. Its efficiency for this reaction (Table 8) is two orders of magnitude lower than that for Kappa (*22*). Lineweaver-Burk regression of the velocity data gave an estimated turnover number of 2 s^{-1}. Slow turnover of the enzyme (in the CDNB reaction) suggested the possibility of product release as the rate-limiting step. This possibility was dismissed when transient state kinetic experiments showed no burst phase for the enzymatic progress curve (data not shown).

In the Kappa GST, S16 was shown to be key in the enzymatic catalysis as the GSH ionizing residue. Sequence alignments suggested that S11 (Figure 11) should have the same role in HCCA Isomerase. The S11A mutant was created but no soluble protein could be extracted from the bacteria to test enzymatic activity.

Once pure substrate was available (see methods), measurement of native kinetics was possible. Due to background reaction of GSH with product (tHBPA) and the enzymatic conversion of product back to substrate, HCCA, tHBPA, and GSH dependent kinetics

were carried out using stopped-flow (see methods). Upon mixing HCCA or tHBPA with 100 nM enzyme and 100 μM GSH or mixing GSH with 100nM enzyme and 1 mM HCCA, the absorbance at 340 nm increased for HCCA and GSH dependent reactions or decreased for tHBPA dependent reactions following a model of a single exponential followed by a steady state. The velocity of the steady state increased with increasing [substrate] and fit well to a Michealis-Menten model for HCCA and GSH dependent reactions or a Michealis-Menten model with incomplete substrate inhibition for tHBPA dependent reactions giving the parameters in Table 8. The amplitude of the exponential phase showed hyperbolic dependence on concentration for HCCA and GSH dependent reactions and fit well to a single-site binding hyperbola yielding both a K_m and K_d in one experiment (Table 8).

Table 8: Kinetic and affinity parameters for HCCA Isomerase

	k_{cat} (s^{-1})	K_m (μM^{-1})	k_{cat}/K_m (M^{-1} s^{-1})	K_i (μM^{-1})	K_d (μM^{-1})
$CDNB_{(GSH)}$			200 ± 7		
$HCCA_{(GSH)}$	47 ± 2	84 ± 10	5.6 ± 0.7 x 10^5		19 ± 5
$tHBPA_{(GSH)}$	19 ± 7	138 ± 72	1.3 ± 0.9 x 10^5	136 ± 100	
$GSH_{(HCCA)}$	39 ± 1	17 ± 2	2.3 ± 0.3 x 10^6		14 ± 3

Multi-wavelength stopped-flow analysis of the exponential phase for both HCCA dependent reactions yielded an extracted UV spectrum that correlated to the product tHBPA (data not shown); however, the extinction coefficient of the change in amplitude is too large to be the build-up of product in the active site and consistent with multiple

turnovers of the enzyme during the exponential phase. This result is consistent with product inhibition (*93, 94*).

GSH and HCCA Isomerase chemistry. The role of GSH in HCCA Isomerase chemistry is an unanswered question. It has been suggested to activate the enzyme, stabilize it, and/or be essential for catalysis (*52-54*). One possible source of this ambiguity is GSH contamination of the enzyme preparation. As shown in Table 2, our recombinant enzyme had significant activity without the addition of exogenous GSH (Table 9) and the presence of exogenous thiol in the enzyme preparation was detected by titration with DTNB with the Ellman assay (*75*) (see methods). The identity of the exogenous thiol was determined to be GSH by detection of a CDNB-GSH conjugate (see methods) formed upon mixing the enzyme preparation with CDNB, vortexing with chloroform, and then injecting a sample onto an HPLC (see methods). A peak eluted corresponding to a GSH-CDNB standard.

GSH was removed via dialysis against 1 M KCl (see methods) (Figure 28). The concentration of GSH (using the CDNB/HPLC assay) and the corresponding enzymatic activity was monitored during dialysis. The results showed that loss of one equivalent of GSH per dimer was accomplished after 4 rounds of dialysis and had little effect on the residual activity (Figure 28) while the last equivalent was more difficult to extract taking 12 additional dialysis steps and showed a 5 fold drop in activity (Table 9 and Figure 28). The activity of "apo" enzyme was still 7 fold higher then that enzyme in the presence of GSO_3^- (Table 9 and Figure 28). Addition of 100 μM GSH at any time before or after

GSH removal resulted in similar activity (data not shown). This "native activity" was 29 fold higher than enzyme prior to GSH removal (Table 9).

Additional "apo" protein was created for GSH binding experiments. Prior to 1M KCl dialysis both the Ellman (*75*) and CDNB/HPLC assays showed 1.8 ± 0.1 equivalents of extra thiol/GSH per dimer. Following 172 L of dialysis over 28 days (with an ~50% loss of protein), both assays showed 0.14 ± 0.01 equivalents of extra thiol/GSH per dimer. To avoid further protein loss, the dialysis was halted. Binding experiments were conducted at this level of GSH contamination.

Table 9. Activity of recombinant HCCA Isomerase

Added Cofactor	Specific Activity (μmol s^{-1} mg^{-1})
1 mM GSO_3^-	(1.5 ± 0.7) x 10^{-3}
None (after GSH removal)	(1.0 ± 0.1) x 10^{-2}
None (prior to GSH removal)	(4.5 ± 0. 5) x 10^{-2}
100 μM GSH	1.3 ± 0.1

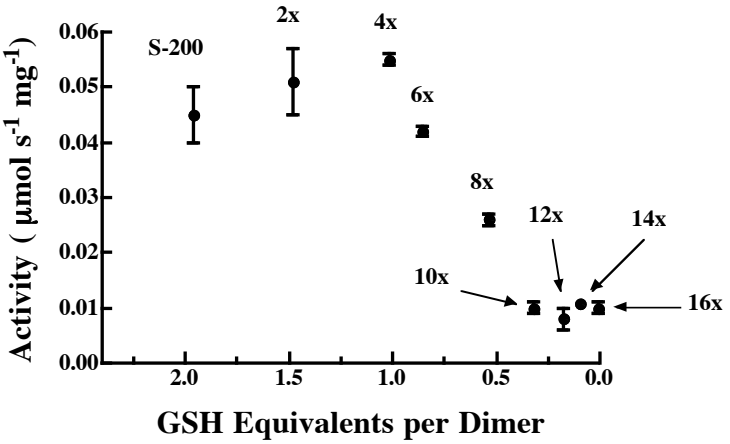

Figure 28. Activity and GSH equivalents measured during 1 M KCl dialysis. Each step is labeled from the enzyme after gel filtration (S-200) to that after 16 rounds (16x) of dialysis.

GSH binding to HCCA Isomerase. GSH in the enzyme preparation suggested that the enzyme binds the ligand very tightly. First trials at measuring the binding affinity failed due to the instability of the "apo" enzyme at 25^0C. When experiments were repeated at 10^0C, precipitation was no longer an issue and the experiments proceeded normally.

Upon mixing HCCA Isomerase with GSH there is an increase in absorbance at 239 nm (Figure 29a) (see methods) (*9*). The absorbance increase fit well to a double exponential (Figure 29a). A plot of k_{obs} versus [GSH] shows linear correlation for both exponentials consistent with two-step binding model (Scheme 2) and yielded bimolecular rate constants (k_1 and k_2) for both steps (Table 10). The intercepts for both fits were negative giving no indication of the off-rate for either step (Table 10). The amplitude of step 1 was consistently ~25% less than step 2 with the amplitude of step 2 corresponding to an extinction coefficient of 3,500 M^{-1} cm^{-1} for the thiolate chromophore.

Scheme 2

$$E + GSH \underset{k_{-1}}{\overset{k_1}{\rightleftharpoons}} E\text{-}GS^- + GSH \underset{k_{-2}}{\overset{k_2}{\rightleftharpoons}} E\text{-}2GS^-$$

The off-rate of thiolate anion was measured by trapping the enzyme with GSO_3^- (see methods). Upon mixing HCCA Isomerase (pre-loaded with GSH) and GSO_3^- the absorbance at 239 nm went down in a biphasic manner that fit well to a double exponential (Figure 29b). The k_{obs} and amplitude for the first exponential showed a linear relationship to [GSO_3^-] with a negative and positive slope respectively. This is consistent with a two-step model for loss of the first thiolate (Scheme 3) in which a slow conformational change occurs prior thiolate leaving the active site. In this case, the slope

and intercept (of k_{obs} vs $[GSO_3^-]$) gave k_3 and k_{-3} respectively (Table 10). The k_{obs} for the second exponential showed no dependence on $[GSO_3^-]$ consistent with a single step (Scheme 4) and provided a direct measure of the off-rate of the second thiolate (when one site is bound with GSO_3^-) (Table 10). With this additional information, the GSH binding model in Scheme 1 was revised to that shown in Scheme 5.

Scheme 3

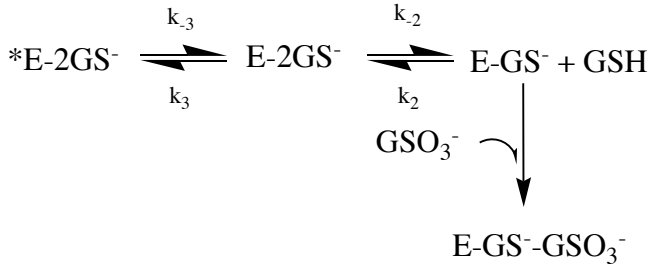

Scheme 4

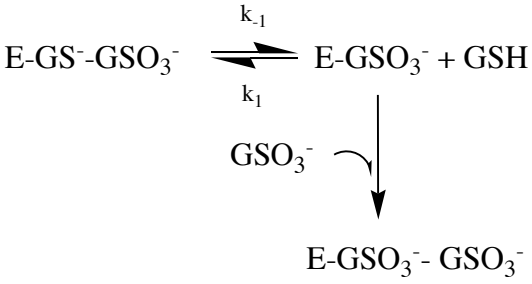

Scheme 5

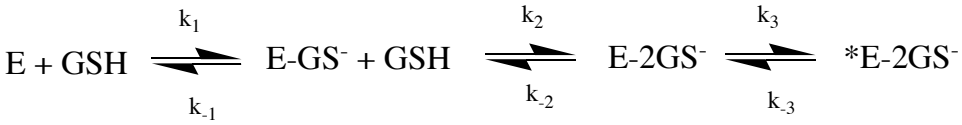

Upon mixing HCCA Isomerase with GSH the intrinsic protein fluorescence increased and then decreased (Figure 29c). The increase fit well to two exponentials while the decrease fit well to one (Figure 29c). This is consistent with the three-step binding model proposed in Scheme 5. k_{obs} for the first two exponentials showed a linear correlation

versus [GSH] and yielded bimolecular rate constants (k_1 and k_2) for both steps (Table 10). The first exponential gave a negative intercept and thereby no information about k_{-1} while the second exponential gave a positive intercept and good measure of k_{-2} (Table 10).

The final exponential (slow phase) took 100 s to reach equilibrium and showed no dependence of k_{obs} on [GSH] over the range of concentrations suitable to fit all three phases together. In order to determine if the slow phase showed concentration dependence, it was monitored independent of the other phases (ie. the first two became too fast to measure) at [GSH] up to 100 mM (see methods). It showed concentration dependence consistent with saturation as it increased from ~0.025 s^{-1} to ~0.06 s^{-1}. These minima and maxima were good measures of k_{-3} and k_3 respectively (Table 10).

The change in intrinsic protein fluorescence was globally modeled to Scheme 4 using the program Dynafit (Figure 29d). The results gave good correlation to the overall model including good residuals for both x and y coordinates (data not shown). The resulting rate constants (Table 10) showed good correlation to those extracted from absorbance and fluorescence measurements with one major exception, k_{-1}. The program tried to drive its value to zero (Table 10). This is not unexpected considering the slow off-rate for that step (Table 10). Global fitting of the data with k_{-1} fixed at zero gave similar rate constants (data not shown) as those given in Table 10.

Using the on and off rates extracted from all of the various measurements apparent dissociation constants were calculated for each bound GSH molecule (Table 11). The least confident value generated was the K_d for the high affinity site because k_{-1} is not the true off-rate with one GSH (GS^-) bound. This value is the off-rate of GSH (GS^-) with it bound in one site and GSO_3^- bound in the second site.

Table 10: Rate constants for GSH binding to HCCA Isomerase					
	Linear Regression of A_{239}	Loss of A_{239} via GSO_3^- Trapping	Linear Regression of Fluorescence	Slow Phase	Global Modeling of Fluorescence Data
k_1 ($M^{-1}s^{-1}$)	$(2.0 \pm 0.1) \times 10^5$		$(5.5 \pm 0.6) \times 10^5$		$(3.5 \pm 0.1) \times 10^5$
k_{-1}(s^{-1})	negative intercept	$(9.0 \pm 6.0) \times 10^{-4}$	negative intercept		$(1.0 \pm 1500) \times 10^{-9}$
k_2 ($M^{-1}s^{-1}$)	$(1.5 \pm 0.1) \times 10^4$		$(2.7 \pm 0.1) \times 10^4$		$(3.1 \pm 0.1) \times 10^4$
k_{-2}(s^{-1})	negative intercept		0.3 ± 0.1		0.07 ± 0.04
k_3(s^{-1})		0.054 ± 0.015		~0.06	0.016 ± 0.001
k_{-3}(s^{-1})		0.020 ± 0.002		~0.025	0.023 ± 0.002

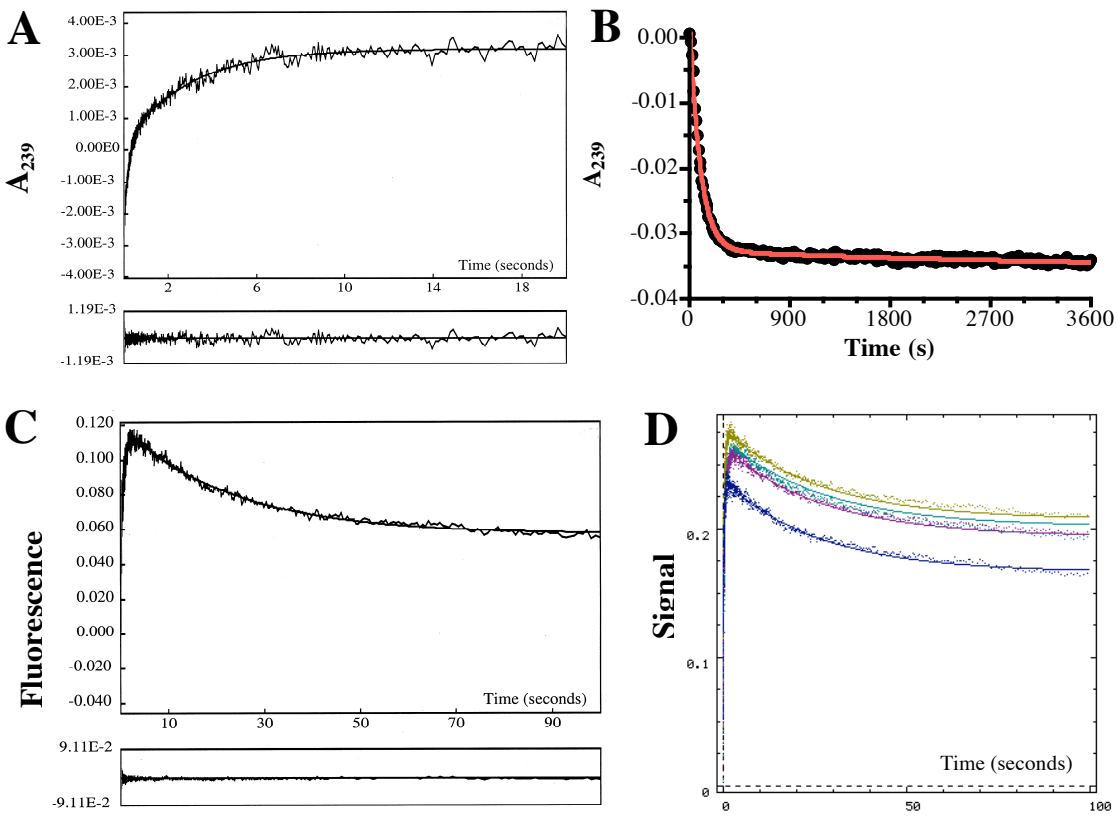

Figure 29. Approach to equilibrium measurements of GSH binding to HCCA Isomerase. Panel A shows the increase in A_{239} upon mixing 40 μM GSH and 10 μM HCCA Isomerase. Panel B shows decrease in A_{239} upon mixing 10 μM HCCA Isomerase loaded with 100 μM GSH and 200 mM GSO_3^-. Panel C shows the changes in intrinsic protein fluorescence upon mixing 40 μM GSH and 500 nM HCCA Isomerase. Panel D shows the changes in intrinsic protein fluorescence upon mixing 30 μM (cyan), 50 μM (magenta), 80 μM (yellow), or 150 μM (blue) GSH and 500 nM HCCA Isomerase. Data from panels A and B are fit to double exponentials, panel C is fit to a triple exponential, and panel D is a global fit to the model in Scheme 4 using the program Dynafit.

Table 11. Calculated dissociation constants for high and low affinity GSH binding sites		
	High Affinity (μM^{-1})	Low Affinity (μM^{-1})
A_{239} on & off rates	0.005 ± 0.003	
Fluorescence on & off rates		11 ± 4
Modeling of Fluorescence Data		2 ± 1

Overall Structure of HCCA Isomerase. The crystal structure of HCCA Isomerase was solved to 1.8 Å (see methods). The asymmetric unit contained 1 HCCA Isomerase monomer, 1 molecule of GSH and a mix of HCCA and tHBPA (Table 13). We know from gel filtration studies (data not shown) that the native enzyme is a dimer, so the dimer was reconstructed using the appropriate symmetry operations (Figure 30 and Table 13). The topology of the HCCA Isomerase (Figure 30a) is similar to the Kappa GST (Figure 30b) as was predicted (*28*). The thioredoxin fold is interrupted by the insertion of an alpha helical domain. The backbone RMSD between the enzymes is 2.2Å (for a monomer overlay Figure 30c). The computer models predicted that HCCA Isomerase would have a helix preceding the thioredoxin fold. This is not the case.

The structures have two major differences. The first difference is an additional helix in the helical domain of Kappa (F87-K94) that is a loop structure in HCCA Isomerase (A82-N85) (Figure 30c). The second is at the C-terminus. In HCCA Isomerase, the final helix of the thioredoxin fold continues almost to the C-terminus while in Kappa this helix is shorter with longer loop structure extending to the C-terminus (Figure 30c).

Table 12: X-ray data collection and processing statistics for HCCA Isomerase with native Ligands

	SeMet	Native
space group	$P2_12_12$	$P2_12_12$
cell parameters (a,b,c) (Å)	71.34,76.05,38.37	71.13,75.83,38.30
wavelength of data collection (Å)	1.541	1.541
no. of measured intensities	214,768	798,759
no. of unique reflections (I+ ≠ I-)	53,221	44,029
resolution of data (Å)		23,499
highest resolution shell (Å)	1.60	1.70
R_{sym} (overall/high resolution shell)	1.66-1.60	1.76-1.70
completeness (%)(overall/high resolution shell)	0.043/0.273	0.053/0.273
redundancy (overall/high resolution shell)	100/100	100/100
mean I/σ (overall/high resolution shell)	4.04/3.83	18.14/17.47

Table 13: Final refinement statistics table for HCCA Isomerase with native ligands

resolution limits (Å)	20.0-1.8
number of reflections used	22,223
R-factor (overall/high resolution shell)	0.186/0.265
R_{free} (overall/high resolution shell)	0.236/0.356
non-protein molecules (not water)	1 glutathione, 0.5 HCCA, 0.5 HBPA, 3 CAPS, 2 phosphates
number of water molecules	157
rms deviation bond length (Å)	0.022
rms deviation angle (°)	1.96
average B main chain/side chain/water ($Å^2$)	23.0/25.6/34.4

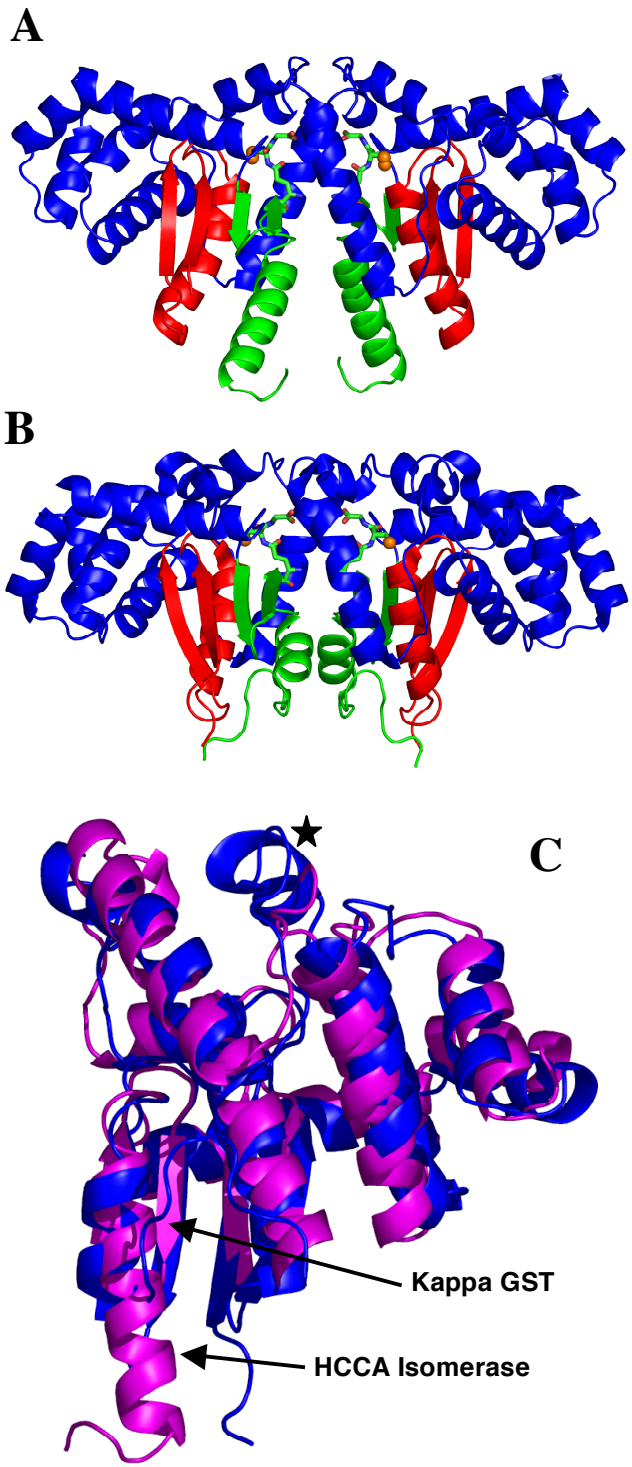

Figure 30. Backbone comparison of HCCA Isomerase (A) and Kappa GSH transferase (B). GSH is shown as a stick model with the cysteine sulfur colored orange (sulfur has two conformations in HCCA Isomerase). Panel C is an overlay of the individual monomers from HCCA Isomerase (magenta) and the Kappa GST (blue). The two major structural differences between the enzymes are an extra helix in Kappa (star) and the loop (Kappa) versus helix (HCCA Isomerase) at the C-terminus (arrows). All images were created in PYMOL (*44*), and the overlay was done in DALI (*95*).

GSH Binding Site. The crystal structure confirms that the GSH binding residues conserved in the sequence alignment (Figure 11) bind to GSH in HCCA Isomerase. These include S11, V168 (mainchain N and CO), N48, N181, and D182 from the host monomer as well as K59 and R183 that reach across the dimer interface (Figure 31). There are subtle changes in the GSH binding site that yield two more interactions with GSH not found in Kappa. The first of these arises from the ring nitrogen in W179 (F in Kappa) donating an additional hydrogen bond to the cysteine carboxyl group (Figure 31). The second comes from the orientation of a H_2O molecule. In Kappa, the side chain of S200 interacts directly with the carboxyl end of the γ-glutamate (*22*). There is a conservative change in HCCA Isomerase to asparagine at this position (Figure 11). N181 uses its main chain N to interact with the carboxyl end of γ-glutamate while its side chain (along with main chain N of D182 and the side chain of R183) orient a H_2O molecule that also hydrogen bonds to the carboxyl end of the γ-glutamate. The overall gain from W179 and the ordered H_2O is two additional hydrogen-bonding partners to GSH.

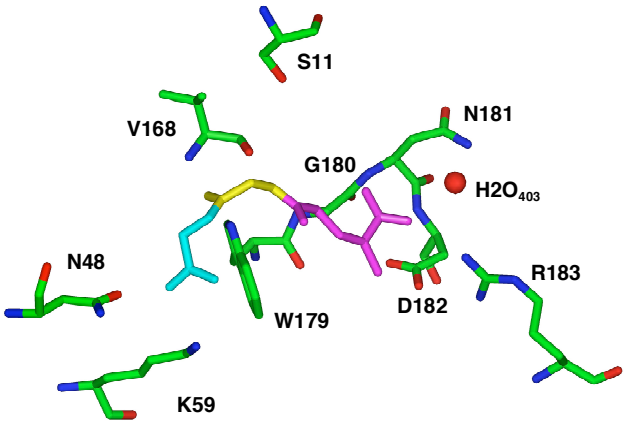

Figure 31. GSH binding residues in HCCA Isomerase. GSH is labeled as glycine (cyan), cysteine (yellow), and γ-glutamate (magenta). G180 does not interact with GSH. Cysteine side chain of GSH (two conformations) has been removed for clarity. This figure was made in the program Insight (*51*).

Active Site. The active site of the enzyme is shown in Figure 32a. The electron density in the active site could not be fit well to either HCCA or tHBPA alone; however, a model using 0.5 occupancy (Table 13) gave a good fit to the data. In addition, the sulfur side chain of GSH appears in two conformations.

The far end of the active site contains a group of hydrophobic side chains that forms a pocket that accepts the aromatic end of HCCA (Figure 32b). The opposing side of the active site is capped by a series of polar/charged side chains that hydrogen bond to charged ends of both HCCA and tHBPA (Figure 32b-c). In addition, the carboxyl group of tHBPA has an interaction with the main chain glycine N of GSH (Figure 32c). The side chain sulfur of GSH is in two conformations. One conformation is closer to S11 (2.61Å in Figure 32b) while the other is further away (3.28Å in figure 32c). The conformation may be influenced by which ligand is present in the active site but both are at a good distance for hydrogen bonding to S11. The sulfur (GSH) shows no electron density corresponding to a covalent bond between HCCA (Figure 32a); however, it does make a close approach to C7 of HCCA (Figure 32b).

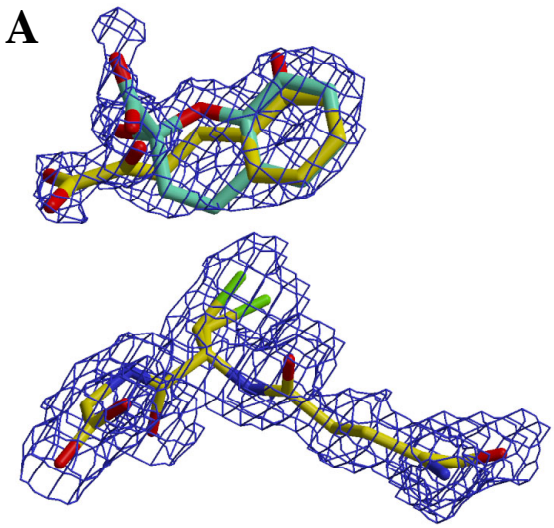

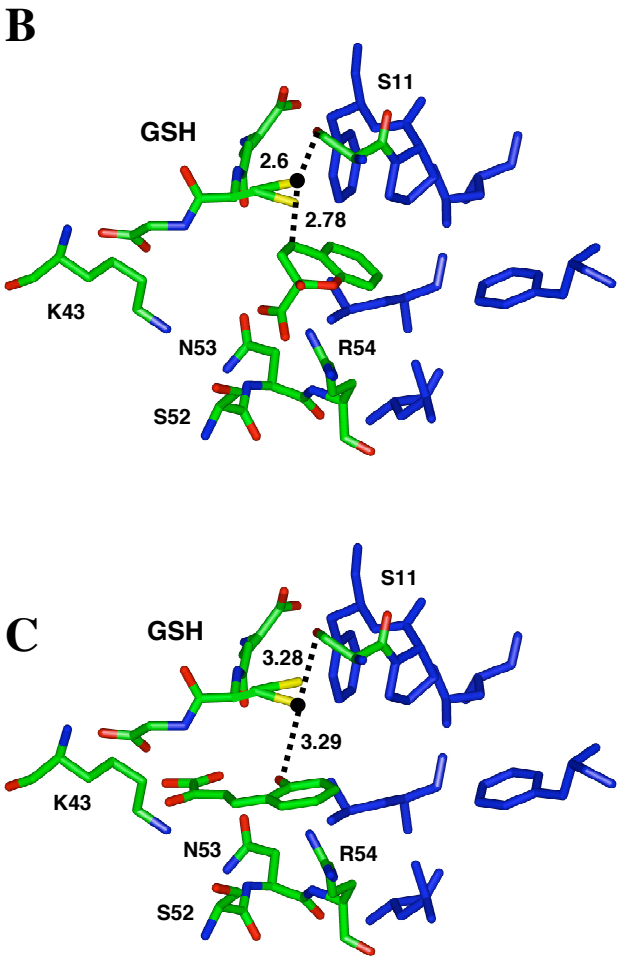

Figure 32. The active site of HCCA Isomerase containing native ligands. P12, F13, L60, L63, L67, and F80 (blue) form a hydrophobic binding pocket to accept the aromatic end of HCCA while K43, S52, N53, and R54 interact with the charged groups on HCCA and/or tHBPA (colored by atom and labeled by residue). Panel A is a sigma style 2mFo-DFc map with a contour level of 0.6 sigma showing the electron density of the active site containing GSH, HCCA (cyan), and tHBPA (yellow). Panels B and C show HCCA and tHBPA (respectively) in the active site including the distance of the sulfur to S11 and C7 (B) or the aromatic hydroxyl group (C). Panels B and C where made in Insight (*51*).

Discussion

GSH and HCCA Isomerase chemistry. The ability of HCCA Isomerase to catalyze the conjugation of GSH and CDNB, albeit at a slow rate, indicates that this enzyme activates GSH toward nucleophilic addition reactions, and suggests that native chemistry could

involve a GSH conjugate. Native chemistry does show dependence on [GSH] following Michealis-Menten kinetics (Table 8). This includes an overall activation of 145 fold over "apo" enzyme (Table 9). GSH dependent activation has been seen previously (*52-54*) but its catalytic role remained elusive. When the inhibitor, GSO_3^-, was added almost all activity was lost (Table 9) indicating direct involvement of the cysteinyl sulfur in catalysis at the active site. Since "apo" protein shows 7x higher activity than enzyme with inhibitor bound (Table 9) the active site maintains some catalytic potential beyond that donated by GSH.

Complexity of GSH binding. The detection of GSH after the final purification step (Figure 28) suggested high affinity of the protein and ligand. Inability to easily remove all of the GSH even with harsh salt treatment indicated this affinity was likely much higher than is typical (10 to 100 μM) for canonical or Kappa GSH transferases (*4, 22, 23, 27*). Approach to equilibrium binding measurements confirmed this suspicion showing 3 orders of magnitude tighter binding (for the highest affinity site, Table 11). It is noteworthy, however, that the lower affinity site falls within the typical affinity range (Table 11) and that maximum activity is not achieved until this site is saturated (Tables 8 and 9).

HCCA Isomerase's cooperative GSH binding (Figure 28, Scheme 5, Tables 10 and 11) is another characteristic atypical for canonical or Kappa GSH transferases (*4, 22, 23, 27*). The only GSH transferase known to show cooperative GSH binding is the MGST1 (*14, 16, 17*). It is a membrane bound trimer that binds GSH in its reduced form in two sites and anion form in the last (*96*). The cooperativity seen in HCCA Isomerase is not

unexpected considering the close approach of GSH molecules in the structure (Figure 30a). In hind-sight, it is surprising that Kappa shows no cooperativity (*22*) considering the location of GSH molecules is almost identical (Figure 30b).

The Kappa fold and GSH binding. Canonical GSH transferases typically have around 12 interactions with GSH (*27*) generating dissociation constants within the range given above. Kappa has only eight (*22*) and has a K_d at the low end of that range. HCCA Isomerase has two additional interactions (Figure 31), and has affinities both similar and tighter than in Kappa (Table 11). This suggests that the Kappa fold contains structural characteristics that incorporate additional binding energy upon association with GSH.

GSH and HCCA Isomerase Stability. Enzyme in which both active sites were not occupied with GSH showed diminished stability (data not shown). This is consistent with observations seen previously (*52*) and suggests that GSH also performs a structural role. The amount of catalytic enhancement could be partially a result of a more ordered active site as well as the addition of a nucleophile for catalysis. Interestingly, no reports have shown a loss of structural integrity for "apo" Kappa.

GSH as a cofactor. Because the enzymatic product is not a GSH conjugate it is difficult to demonstrate that GSH is directly involved in catalysis. The enzymatic activation seen with GSH suggests that it is involved in chemistry; however, the low activity with one GSH bound and the instability of the enzyme suggests that stabilization of the active site is also a major contributor to the activation. If GSH is involved in

catalysis the most likely scenario would be nucleophilic attack at C7 altering the hybridization, and freeing the C7-C8 dihedral for rotation to the opposing isomer (Figure 33). The crystal structure shows the GSH sulfur is in a good position to attack C7 of HCCA even though the electron density of the region shows multiple constructs occupy the active site (Figure 32b).

The lack of significant electron density between the sulfur and C7 suggests that little adduct (if formed) is present at any one time in the active site. This is consistent with the increase in absorbance during the exponential phase of the reaction. Addition of GSH to C7 would cause a drop in the UV spectrum of HCCA or tHBPA. Because the burst phase of the reaction shows an absorbance increase, any conjugate formed must be extremely transient.

If a conjugate is formed, it could leave the active site and fall apart to the opposing conformer. This is unlikely however because of the transient nature of this adduct. It is likely formed and cleaved at a rate much faster than any adduct could leave the active site. Consider that the off-rate for the low affinity GSH is slow (0.3 s^{-1} at 10^0C, Table 10) compared to the turnover number of the enzyme (47s^{-1} at 25^0C, Table 8). We know that the adduct formation must be much faster than the turnover number (because we do not see it even in the exponential phase). Therefore the adduct formation must increase the off-rate of GSH by several orders of magnitude: a factor extremely unlikely considering the instability of the GSH free enzyme.

HCCA Isomerase Mechanism. In order for the isomerization reaction to occur, two key events must happen. Their order, however, is unknown. First, the hybridization at C7

(HCCA) must change from sp^2 to sp^3 to allow free rotation around the C7-C8 bond. Second, the ketal bond between O1 and C9 must be broken. There are two possible GSH dependent mechanisms that satisfy both of these criteria and are consistent with the data. The first is a concerted mechanism in which GSH adds to C7, altering the hybridization at the carbon and breaking the ketal bond all at once (Figure 33a). The second is an ordered mechanism in which a transiently formed ring-opened intermediate (cHBPA) is attacked by the sulfur nucleophile (Figure 33b). Both of these mechanisms facilitate a change to sp^3 hybridization at C7 and free rotation to the trans isomer. The E-GS^- complex is then eliminated in a retro-Michael reaction, freeing product (tHBPA) to leave the active site (Figure 33).

The second mechanism seems more likely due to the characteristics of the intermediate formed after ring opening. This molecule (cHBPA) is a precursor in formation of the HCCA (Figure 12b) during enzymatic digestion of naphthalene and has been detected in equilibrium mixtures of HCCA and tHBPA (*52*). Its structure is similar to PBO (Figure 34), a known GSH transferase substrate (*20, 97, 98*). GSH transferase reactions with PBO are 1,4 Michael additions of GSH to the electrophile. This is the same GSH addition reaction suggested in Figure 33b.

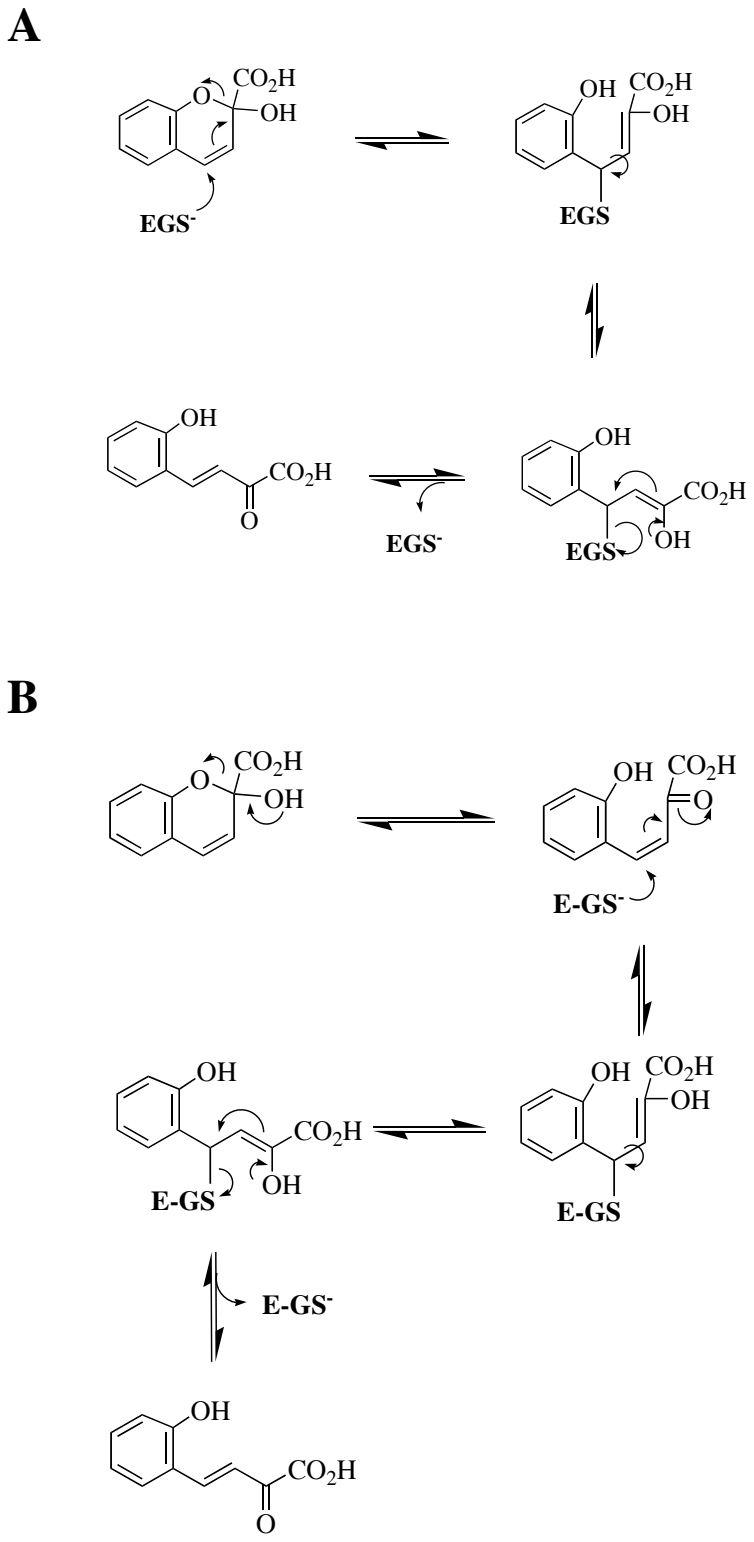

Figure 33. Proposed enzymatic mechanisms of HCCA Isomerase. Both involve the nucleophilic attack of GSH at C7. This leads to a transient covalent intermediate and free rotation around C7-C8 bond. Elimination of GSH in a retro-Michael reaction yields the tHBPA product. Panel A is a concerted mechanism in which GSH addition and ring opening occur in a single step while panel B is an ordered mechanism in which the ring opens and then GSH adds in a 1,4 Michael fashion.

HCCA Isomerase and the Kappa GST. The structural relationship between HCCA Isomerase and Kappa firmly places the enzyme into the Kappa class; however, it does not give an evolutionary relationship. Because of its bacterial origins, HCCA Isomerase most likely arose first. But there is no evidence that Kappa came from it. They could both have evolved separately from DsbA (their most likely progenitor). Their relationship is at least intriguing because Kappa is primarily a mitochondrial enzyme and might be a bacterial relic from the distant past still present in mammals today.

Acknowledgements. The P. putida plasmid DNA was a gift from Dr. Richard Eaton (Environmental Protection Agency). Dr. Simona Codreanu who subcloned HCCA Isomerase. Dr. Joel Harp (Vanderbilt Center for Structural Biology) was a great help in the use of the X-ray facility. Dr. Jane Ladner who solved the crystal structure for us.

CHAPTER VII

A cHBPA INTERMEDIATE AND A TRANSIENT MICHEAL ADDUCT HIGHLIGHT THE HCCA/tHBPA ISOMERIZATION CATALYZED BY HCCA ISOMERASE

Transient GSH conjugates could be an efficient method for the catalysis of isomerizations at α,β unsaturated carbonyls (via reversible Michael adducts) by altering hybridization at the 4 position. A transient conjugate is suspected in the isomerization of the unsaturated keto compound MAA (Figure 34a) when it is transformed into its trans isomer FAA by the Zeta class GSH transferase (Figure 34a) (*99, 100*).

When assaying GSH transferases for Michael activity the model substrate, PBO (Figure 34b), is often used (*97, 98*). Interestingly, the chemical structure of this compound is very similar to tHBPA (Figure 34c): the product of an isomerization reaction catalyzed by HCCA Isomerase (Figure 34c). We and others (*52-54*) have suggested that the enzymatic mechanism could pass through a transient Michael conjugate.

The major caveat with this mechanism is that the predominant cis isomer (at neutral pH) is not an α,β unsaturated carbonyl (due to formation of ring via an acetal bond) (Figure 34c, d). Enzymatic addition of GSH to HCCA could occur in a conjugation addition scenario altering hybridization and breaking the acetal bound all at once or the acetal bond could be broken first and then GSH added (Figure 33). Breaking of the acetal bond gives the compound cHBPA (Figure 34d) an intermediate in the enzymatic breakdown of naphthalene (Figure 12), and a compound that can accept a standard 1,4 Michael adduct.

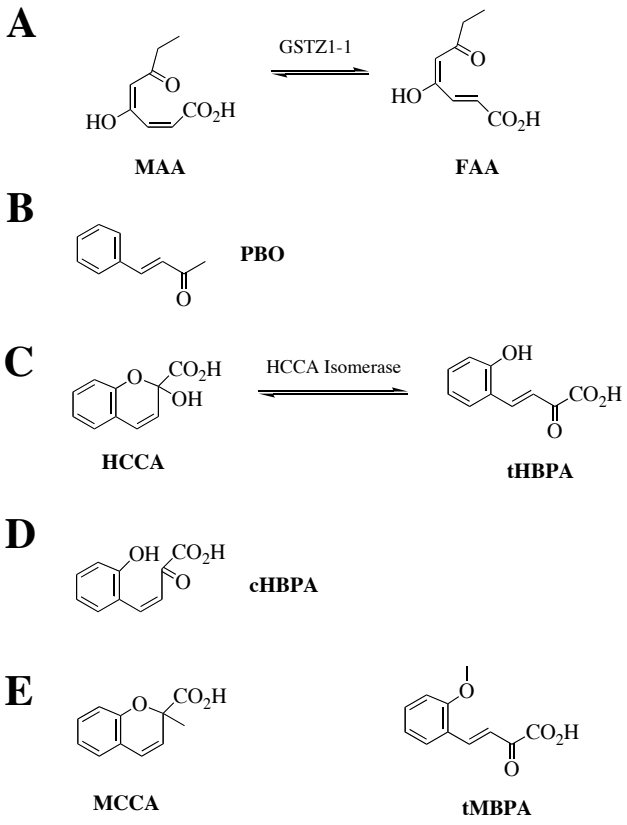

Figure 34. Compounds of interest in Chapter VII. Panel A shows the isomerization of maleylacetonacetate (MAA) to fumarylacetonacetate (FAA) catalyzed by the Zeta class GSH transferase (*100*). Panel B shows the structure of trans-4-phenyl-3-buten-2-one (PBO). Panel C shows the isomerization of 2-hydroxychromene-2-carboyxlic acid (HCCA) to trans-*o*-hydroxybenzylidene pyruvic acid (tHBPA) catalyzed by HCCA Isomerase. Panel D shows the structure of cis-*o*-hydroxybenzylidene pyruvic acid (cHBPA). Panel E shows the analogs synthesized for this study: 2-methylchromene-2-carboyxlic acid (MCCA) and trans-*o*-methoxybenzylidenepyruvic acid (tHBPA).

Results

Thermodynamic equilibrium between HCCA and tHBPA. It has been shown previously (*52*) that the equilibrium between HCCA and tHBPA favored HCCA 55% to 45% at neutral pH. We repeated these measurements by integrating both the areas of their alkene trans/cis H-NMR peaks and RP-HPLC peak (at A_{296} correcting for ε), and found similar results: 61% HCCA and 39% tHBPA corresponding to a K_{eq} of 1.53.

The nonenzymatic approach to equilibrium between HCCA and tHBPA. The observed rate of the approach to equilibrium between HCCA and tHBPA was measured at variable pH from 1 to 14 (Figure 35, see methods). From pH 1 to 3 and pH 10 to 13, the log of the observed rate constant showed a linear relationship (Figure 35). Neither slope was indicative of general acid or base catalysis; however, the observed rate constant increased almost 2 orders of magnitude from pH 10 to pH 13.

The pH dependence of HCCA and tHBPA UV-Vis spectra. UV-Vis scans of tHBPA in relation to pH (see methods) showed a change in the spectral characteristics from pH 7 up to pH 11 (Figure 36a) consistent with those seen previously (*52*); however above pH 11, no more changes were observed (Figure 36a). Spectra of HCCA were also then taken while varying pH (Figure 36b). Between pH 7 and 11 there were small changes at 340 to 420 nm consistent with those for tHBPA (Figure 36b). This indicated (as was known) that a small amount of tHBPA was present in the HCCA preparation. Above pH 11, significant changes began to occur in the HCCA spectrum at 256, 296, and 420 nm (Figure 36b). The appearance of a band at 420 nm was consistent with the formation of phenolate anion (*52*). Transient state measurements showed that the jump in absorbance at 420 nm was complete within the first ms (data not shown) indicating an observed rate constant for this step was at minimum a 1,000 s^{-1}. Because the isomerization rate is 0.005 s^{-1} at pH 14.0 (Figure 35) the absorbance was not coming from the phenolate of tHBPA. This spectral change was most likely a result of cHBPA (Figure 34d) formation via the loss of the hydroxyl proton, formation of the carbonyl, and cleavage of the acetal bond.

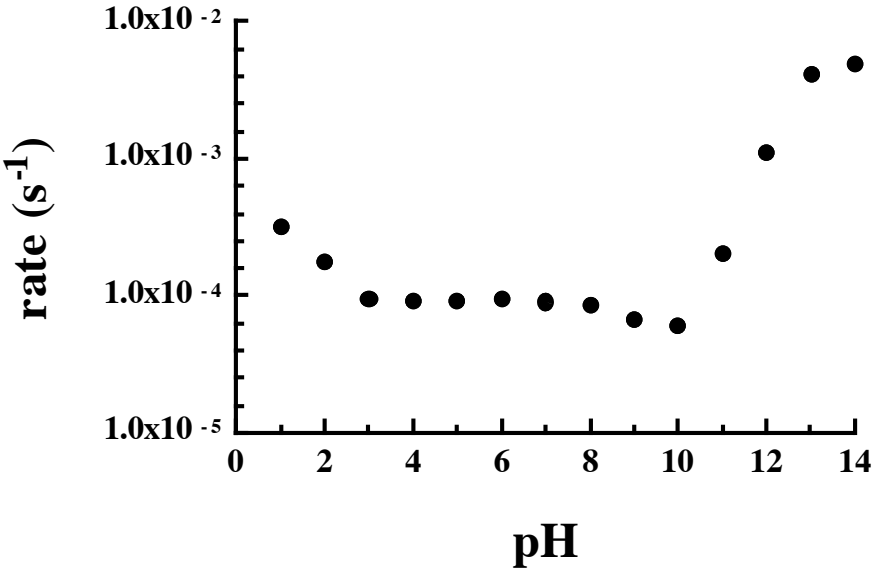

Figure 35. pH profile of the observed rate of approach to equilibrium between HCCA and tHBPA.

The pH dependence of absorbance at 420 nm. In a separate experiment, the pH dependence of the absorbance of HCCA (with slight tHBPA contaminate) at 420 nm was measured from pH 8 to 14 (Figure 36c, see methods). The absorbance change versus pH fit well to a double pKa model with an R^2 of 0.9981 (Figure 36c). This observation was also consistent with the appearance of cHBPA. The first pKa was loss of tHBPA's phenolic proton (*52*) while the second was the loss of the hydroxyl proton of HCCA (Figure 36c). Together these data indicated that cHBPA was formed at high pH and its absorbance characteristics are similar to HCCA and tHBPA having strong absorbance bands at 256, 296, and 420 nm at pH 14. Note that at pH 7.0 the phenolic oxygen would be protonated and the 420 nm band would shift to 340 nm just as seen in tHBPA (Figure 36a).

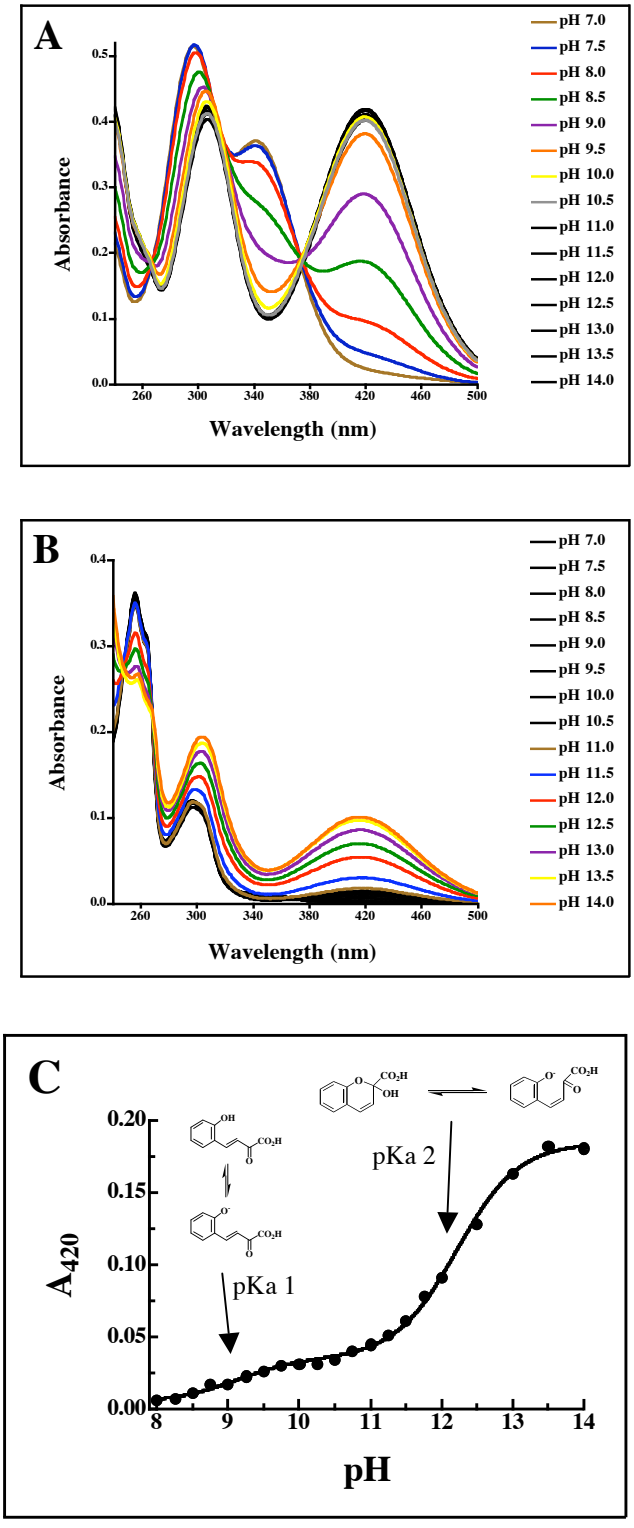

Figure 36. pH dependence of the UV-Vis spectrum of HCCA (A) and tHBPA (B). Panel C shows the change in absorbance at 420 nm of HCCA at varied pH values. The data were fit to a double pKa model: pKa 1 = 9.1 ± 0.1 and pKa 2 = 12.21 ± 0.03.

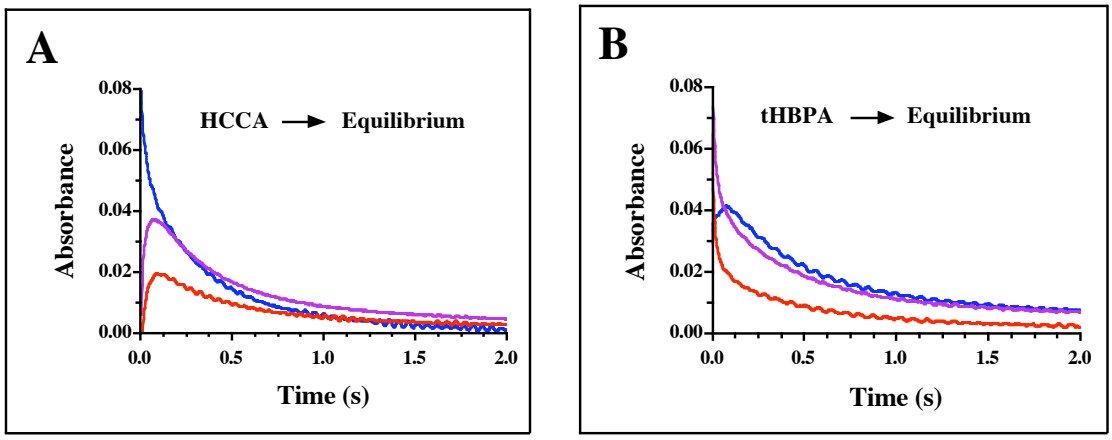

Figure 37. Absorbance change during a single turnover of HCCA Isomerase with HCCA (A) or tHBPA (B) recorded at 256 (blue), 296 (magenta), or 340 (red) nm. Data were fit to a double exponential (fit not shown). Observed rate constants are given in Table 1.

Table 14. Observed rate constants for a single turnover of HCCA Isomerase with HCCA and tHBPA

		256 nm	296 nm	340 nm	250-360 nm global fit
HCCA	$k_{1\ obs}$ (s^{-1})	28.9 ± 0.6	52.5 ± 0.5	48.5 ± 0.5	46.8 ± 0.2
	$k_{2\ obs}$ (s^{-1})	2.60 ± 0.01	2.38 ± 0.01	2.17 ± 0.02	2.52 ± 0.01
tHBPA	$k_{1\ obs}$ (s^{-1})	30.2 ± 0.8	56.8 ± 0.7	67 ± 1	77.6 ± 0.3
	$k_{2\ obs}$ (s^{-1})	2.06 ± 0.01	2.25 ± 0.01	2.26 ± 0.02	2.24 ± 0.01

Single turnover of HCCA Isomerase with HCCA and tHBPA. In order to determine if any intermediates were present along the enzyme catalyzed reaction coordinate, single turnover experiments were employed (Figure 37). With equilibrium as background (an absorbance of zero means the reaction is complete), excess HCCA Isomerase loaded with GSH was rapidly mixed with HCCA or tHBPA (see methods). The resulting absorbance change at 256, 296, and 340 nm is given in Figure 37. The data showed a biphasic response consistent with a two-step process. Fitting of the data to double exponentials

gave good fits yielding the observed rate constants (k_{obs}) given in Table 14. The values of $k_{1\ obs}$ and $k_{2\ obs}$ were consistent at all wavelengths and with both ligands indicating an intermediate along the reaction path.

In order to identify the UV-Vis spectrum of the intermediate single turnover multiwavelength global analysis experiments were undertaken (see methods). Single turnover data were obtained at every other wavelength between 250 and 360 nm. These data were then fit to a two-step model using the global analysis software provided (see methods) to extract both the observed rate constants ($k_{1\ obs}$ and $k_{2\ obs}$, Table 14) as well as the UV-Vis spectrum (Figure 38b,c) associated with the intermediate. Figure 38a shows the UV-Vis spectrum of both HCCA and tHBPA in relation to equilibrium. They have characteristic positive and negative absorbances consistent with their extinction coefficients at these wavelengths (*52*). Global fitting of the single turnover multiwavelength experiment gave good correlation of the UV-Vis spectrum of HCCA (Figure 38b) and tHBPA (Figure 38c) indicating that no chemistry is occurring in the dead time (1-2 ms) of the experiment. Because of the faster $k_{1\ obs}$ for tHBPA (Table 14) some of the absorbance at 256 nm is lost so that it does not go entirely negative (Figure 38c) (also seen in Figure 37b for 256 nm). The model also finds the UV-Vis spectrum at equilibrium (Figure 38b,c) to be about zero as would be expected. These data indicate that the global fit is correctly identifying the starting material as well as the product. The extracted spectrum of the intermediate shows positive absorbance bands at 256, 296, and 340 nm (Figure 38b, c). These strong absorbance bands are not indicative of a GSH conjugate (loss of pi conjugation means loss of absorbance) but are more consistent with the absorbance characteristics of cHBPA (Figure 36b).

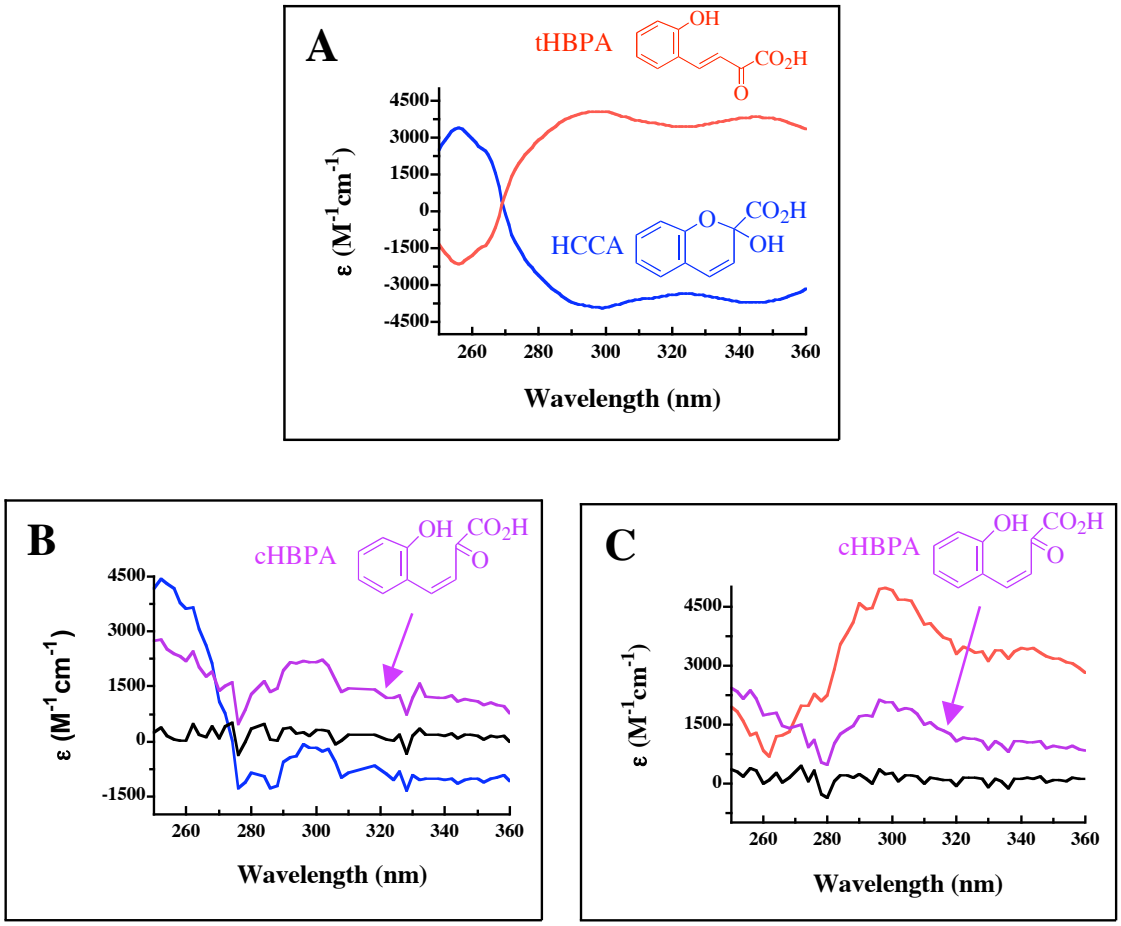

Figure 38. Global modeling of the UV-Vis changes during a single turnover of HCCA Isomerase with HCCA or tHBPA. Panel A shows the UV-Vis spectra of HCCA (blue) and tHBPA (red) scanned using equilibrium as a background. Panels B and C show the UV-Vis spectra extracted from a global fit of the single turnover multiwavelength stopped-flow data. The starting material (HCCA in B and tHBPA in C) is shown as well as the extracted intermediate (magenta) and equilibrium (black) spectra. Observed rate constants are given in Table 14.

Enzymatic activity toward the substrate analog MCCA. In order to explore the role of the acetal bond/hydroxyl group of HCCA in catalysis, the substrate analog MCCA was synthesized using a variation on the Kabbe condensation (*81, 82*) (see methods). This compound has a methyl group in place of the hydroxyl of interest (Figure 34c,e). Activity assays with 2 μM HCCA Isomerase, 500 μM GSH, and 250 μM MCCA (see

methods) showed no measurable activity after 8 hrs of incubation (Table 15). When reactions were run for 48 hrs with 10 μM enzyme, some measurable GS-MCCA conjugate was formed; however, similar levels were detected in the background reaction (data not shown).

Enzymatic activity toward the product analog tMBPA. In order to test if a transient conjugate could be formed during turnover, we synthesized the product analog tMBPA (see methods). It has a methoxy group in place of the aromatic hydroxyl of tHBPA (Figure 34c,e). Incubation of 2 μM HCCA Isomerase, 800 μM GSH, and 80 μM tMBPA (see methods) showed modest activity (Table 15). Overall absorbance dropped significantly across the spectrum (Figure 39a) indicating GSH conjugation. RP-HPLC showed the appearance of two peaks each with a mass corresponding to a GS-MPBA conjugate (data not shown). This is consistent with the formation of two diastereomers (see methods). The conjugate's absorbance spectrum (Figure 39a) was obtained by capture of its peaks from the RP-HPLC. Due to instability, its extinction coefficient is unknown, but the concentration was estimated at 200 μM. Together, these data suggest that the enzyme forms a GSH-tMBPA conjugate at C7 (Figure 39a).

Measurement of the steady state kinetics of the HCCA Isomerase catalyzed GSH/tMBPA conjugation were done at 343 nm (see methods) due to the absence of absorbance of the conjugate at that wavelength (Figure 39a). The kinetics showed strong substrate inhibition (Table 15). At high substrate concentrations the activity was zero. Turnover is slow while affinity for the Michealis complex is high (Table 15). k_{cat}/K_m shows an overall low enzymatic efficiency (Table 15).

Table 15. Activity of HCCA Isomerase with analogs					
Analog	Activity	k_{cat} (s^{-1})	K_m (μM^{-1})	k_{cat}/K_m ($M^{-1}s^{-1}$)	K_i (μM^{-1})
$tMBPA_{(GSH)}$	yes	0.07 ± 0.1	30 ± 7	(2.3 ± 0.7) x 10^3	40 ± 10
$MCCA_{(GSH)}$	no				

Single turnover of HCCA Isomerase with tMBPA. Single turnover experiments were employed to determine the rate of the chemical step in the HCCA Isomerase catalyzed conjugation of GSH and tMBPA. Excess HCCA Isomerase loaded with GSH was rapidly mixed with tMBPA while monitoring changes in absorbance at 343 nm (see methods). Initially, we believed the reaction was complete within the dead time of the experiment; however, close inspection of short time scales (10 ms) showed a drop in absorbance (Figure 39b). The last 8 ms of the data fit well to a single exponential (Figure 39b) with an amplitude (0.0257 ± 0.0006) consistent with the absorbance of 20 μM tMPBA in a 0.2 cm cell (absorbance = 0.0292). The observed rate constant is given in Table 16.

Further evidence that this step was in fact chemistry came from a single turnover multiwavelength global fit of the data. As before, single turnover experiments were performed every 2 nm from 250 to 360 nm (see methods). These data were compiled and then the last 8 ms of the data was fit to a one-step model using the associated software (see methods). The model yielded UV spectra for the starting material and product consistent with that of tMBPA and GS-MBPA, respectively (Figure 39a, c). The observed rate constant (k_{obs}) matched well that of the single wavelength experiment (Table 16). A reversible model gave similar spectra (data not shown) and individual rate constants corresponding to a chemical step of 1100 s^{-1} (Table 16).

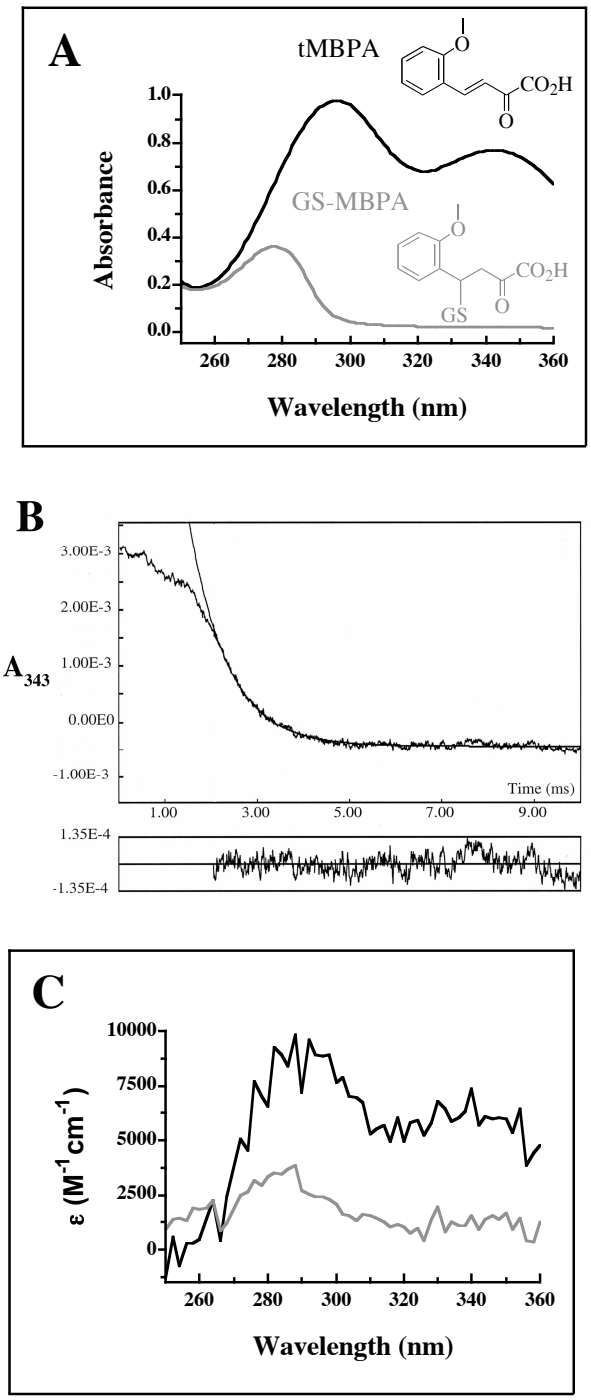

Figure 39. Global modeling of the UV-Vis changes during a single turnover of HCCA Isomerase with tMBPA. Panel A shows the UV-Vis spectrum of 100 μM tMBPA (black) and ~200 μM GS-MBPA conjugate (gray). Panel B shows a single turnover of enzyme at 343 nm fit to a single exponential (fit starts at 2 ms). Panel C shows the UV-Vis spectrum extracted from a global fit of the single turnover multiwavelength stopped-flow data. The spectra of the starting material (tMBPA in black) and the product (gray) are shown. Observed rate constants are given in Table 16.

Table 16. Observed rate constants for a single turnover of HCCA Isomerase with tMPBA

	k_{obs} (s^{-1})	k_1 (s^{-1})	k_{-1} (s^{-1})
343 nm	1220 ± 9		
250-360 nm global fit	1093 ± 5	1096 ± 5	0.051 ± 0.004

Table 17: X-ray data collection and processing statistics for HCCA Isomerase with tMPBA

space group	$P2_12_12$
cell parameters (a,b,c) (Å)	71.34,76.05,38.37
wavelength of data collection (Å)	1.541
no. of measured intensities	214,768
no. of unique reflections (I+ ≠ I-)	53,221
resolution of data (Å)	1.75
highest resolution shell (Å)	1.60
R_{sym} (overall/high resolution shell)	1.66-1.60
completeness (%)(overall/high resolution shell)	0.043/0.273
redundancy (overall/high resolution shell)	100/100
mean I/σ (overall/high resolution shell)	4.04/3.83

Table 18: Final refinement statistics table for HCCA Isomerase with tMPBA

resolution limits (Å)	30.0-1.8
number of reflections used	16,582
R-factor (overall/high resolution shell)	0.195/0.251
R_{free} (overall/high resolution shell)	0.253/0.328
non-protein molecules (not water)	1 glutathione, 1 tMBPA, 3 CAPS, 2 phosphates
number of water molecules	193
rms deviation bond length (Å)	0.021
rms deviation angle (°)	1.92
average B main chain/side chain/water ($Å^2$)	24.0,26.1,33.4

Crystallization of HCCA Isomerase with tMBPA. Similar crystallization conditions were used for tMBPA as for native ligands (see methods). The data collection and statistics are given in Tables 17 and 18. The space group, resolution, etc. were all very similar to the structure with the native ligand.

Active site of HCCA Isomerase with tMBPA. Overlay of the active site with native ligands and the product analog show high correlation (Figure 40). The hydrophobic pocket, GSH, and the polar/charged side chains overlay nicely with the exception of R54 and the cysteinyl sulfur of GSH (Figure 40). The side chain of R54 has moved inward toward tMPBA. The absence of the second ring structure seen in HCCA frees up space for this movement. The side chain sulfur is now locked into position (Figure 40). The phenyl rings of tMPBA and HCCA overlay well. This positional correlation extends out to C7 of both ligands (Figure 40).

Atomic positions of tMBPA in the active site. The electron density around GSH and tMBPA shows density between C7 and the sulfur of GSH (Figure 41a). The distance between these atoms is 2.1 Å (Figure 41b). The temperature (B) factors for atoms in the active site (Figure 41b) show that GSH and the phenyl ring of tMBPA are ordered. In contrast, atoms beyond C7 of tMPBA are highly dynamic. The dihedral angles associated with this carbon chain (Figure 41c) show an offset down C6-C9 (Figure 41c, left) and planarity down C7-C10 (Figure 41c, right). These data indicated a loss of the double bond character between C7-C8 and an increase in double bond character between C8-C9 as if the double bond has moved down one carbon atom.

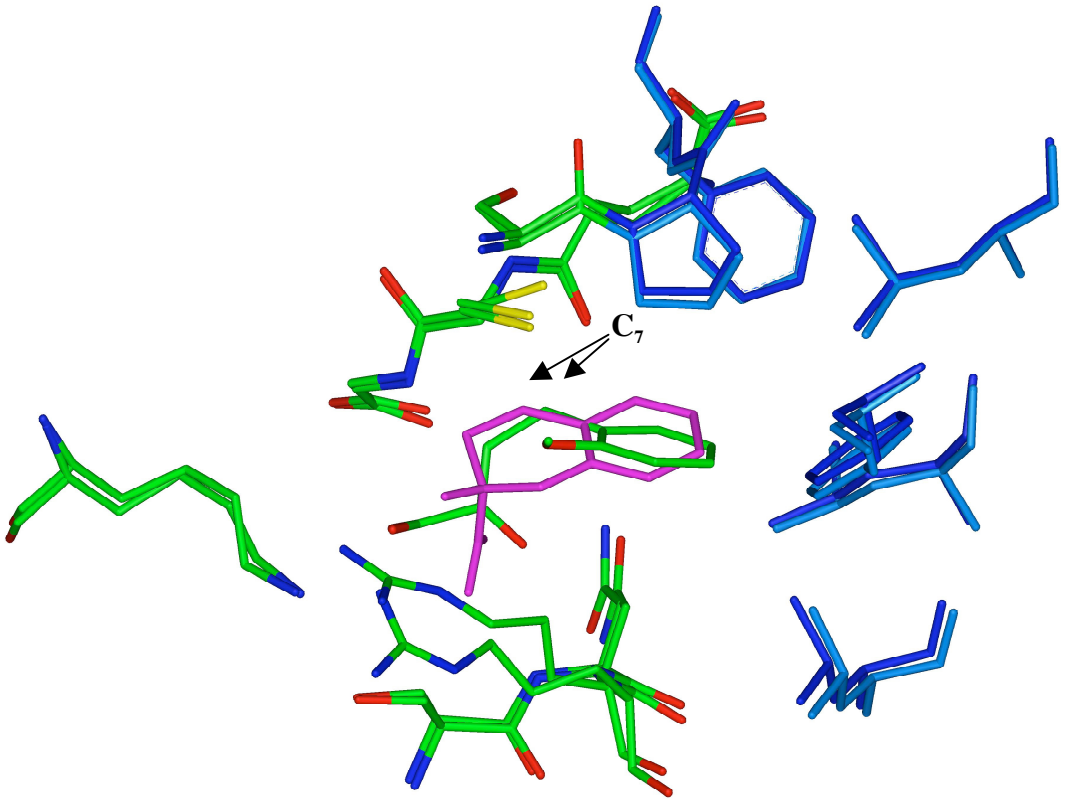

Figure 40. Overlay the HCCA Isomerase structures containing HCCA (magenta) and tMBPA (colored by atom) in the active site. The HCCA structure is cyan and has two sulfur conformations. The tMPBA structure is blue and has one sulfur conformation. This figure was made with the program Insight II (*51*).

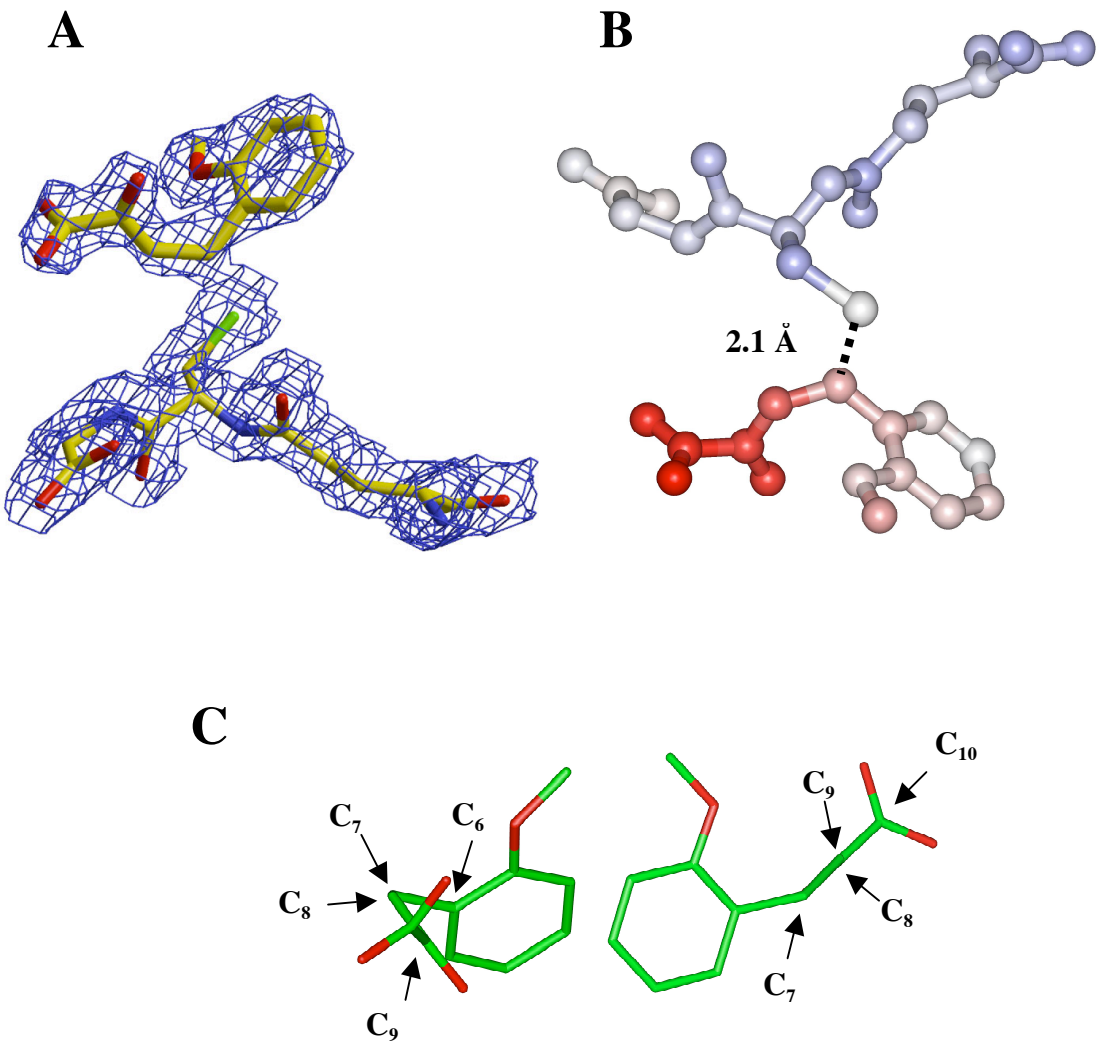

Figure 41. tMBPA in the active site of HCCA Isomerase. Panel A shows the electron density around tMBPA (top) and GSH (bottom). The map is a sigma style 2mFo-DFc with a contour level of 1.0 sigma. Panel B shows the temperature factors associated with the atoms of GSH (top) and tMBPA (bottom). The gradient runs from blue (small) to red (large). Panel C shows the dihedral angles of C6-C9 (left) and C7-C10 (right). Panels B and C were made with the program Insight II (*51*).

Global mechanism of HCCA Isomerase. These results suggest that both ring opening and a transient GSH adduct could be involved in native catalysis. Figure 42a shows our hypothesis about the mechanistic path of HCCA Isomerase. In the first step, cHBPA is formed by proton extraction or transfer. Then a 1,4 Michael adduct is formed changing

hybridization and freeing the molecule for rotation around C7-C8. Next, the Michael adduct is removed, and then tHBPA is released from the active site.

Initially, global models of this mechanism (Figure 42a) showed poor results when fit to single turnover data. The global model was then altered by the addition of known inhibitory complexes. It has been shown previously (Chapter 6) that the enzyme turns over several times (27 in the HCCA to tHBPA direction and 7 in the tHBPA to HCCA direction) during the burst phase: a result consistent with product inhibition (*93, 94*), and that the trans isomer, tHBPA, shows substrate inhibition (Table 8).

Product and substrate inhibitory complexes (Figure 42b) were then used in the model of Figure 42a to globally fit a single turnover reaction of HCCA to tHBPA (including in values for HCCA and tHBPA binding affinity, the tHBPA substrate inhibition constant, and the response given by formation of cHBPA and then a return to equilibrium), the model converges and shows fair correlation for both x and y residuals. It yields inhibitory binding constants for EPS and ESP that are both nanomolar (Table 19): consistent with the number of turnovers of the enzyme during the burst phase. As a whole the resulting rate constants are consistent with known values: the rate constants for Michael chemistry (Table 19, k_2 and k_{-3}) are similar to those measured for the tMPBA reaction (Table 16); the rate of deprotonation of HCCA to cHBPA (Table 19, k_1) is much faster than the known lower limit for that step (1,000 s^{-1}); and the slowest steps (Table 19, k_2 and k_{-3}) are consistent with turnover of the enzyme (47 s^{-1}, Table 8). The best test of the model is its ability to recapitulate the known equilibrium constant between HCCA and tHBPA. A combination of the forward and reverse rate constant gives a K_{eq} of 2.7 ± 1.5. This is within error of the known value of 1.53.

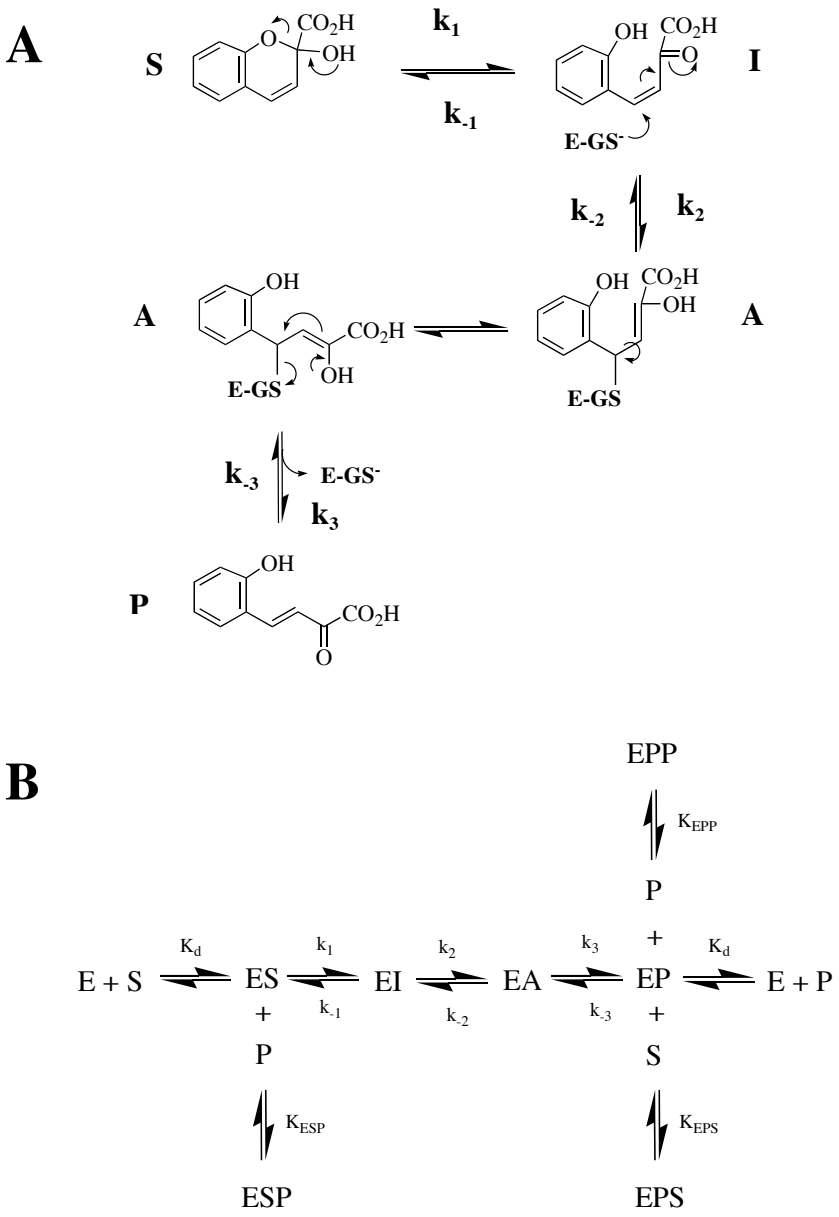

Figure 42. Global model of HCCA Isomerase catalysis where S = HCCA, I = cHBPA, A = GSH adduct, and P = tHBPA. Panel A shows the hypothetical pathway of catalysis beginning with the formation of cHBPA, followed by a GSH adduct at C7, rotation to the trans conformer, and then release of tHBPA. Panel B shows the global model used to fit single turnover data. Inhibitory complexes are formed with either HCCA and tHBPA or two tHBPA molecules in the active site.

Table 19. Rate and Binding Constants from the Global Fit of Single Turnover Data							
k_1 (s^{-1})	k_{-1} (s^{-1})	k_2 (s^{-1})	k_{-2} (s^{-1})	k_3 (s^{-1})	k_3 (s^{-1})	K_{ESP} (nM)	K_{EPS} (nM)
(3.2 ± 1.8) x 10^3	(8.8 ± 5.4) x 10^3	540 ± 20	122 ± 5	200 ± 100	(1.6 ± 0.7) x 10^3	440 ± 70	210 ± 150

Discussion

The HCCA/cHBPA equilibrium. At neutral pH, the ring closed (HCCA) form of the cis conformer predominates (*52*). This is the most likely reason that the cis/trans equilibrium favors the cis conformation at neutral pH. During pH titration (from pH 11 to pH 14), HCCA goes through significant changes in its UV-Vis spectrum consistent with the formation of a phenolate anion (Figure 36b, c). The phenol is only present in the cHBPA and tHBPA conformers. Because the increase happens so fast (at more than 1,000 s^{-1}), the phenolate absorbance must be due to the formation of cHBPA. The dual pKa fit of the phenolate absorbance is also consistent with the formation of cHBPA. The phenolic proton of tHBPA is ionized first (pKa 1), and then hydroxyl of HCCA is removed (pKa 2) breaking the acetal bond and forming the cHBPA and its phenolate.

The shifting of the HCCA/cHBPA equilibrium should have two consequences. First, breakage of the acetal bond leads to a sterically hindered cis conformation instead of a stable ring structure. The result should be an equilibrium shift toward the trans conformer. It is known that above pH 10, the trans conformer, tHBPA, predominates (*52*). The equilibrium is trans dominant where it should be; however, up to pH 12 (Figure 36b) a large amount of HCCA still exists. Therefore factors beyond just cHBPA formation must contribute to this equilibrium shift. Second, increasing concentrations of cHBPA would be expected to increase the rate of approach to equilibrium between the cis and trans conformers. Figure 35 demonstrates that increasing pH increases the rate of approach to equilibrium.

In concert, these data indicate the absorbance changes seen during the pH titration of HCCA (Figure 36b) are a result of cHBPA formation. This means that cHBPA has

absorbance characteristics similar to HCCA and tHBPA. At neutral pH, it has major bands at 256, 296, and 340 nm (ie. 420 nm shifts to 340 nm at neutral pH).

The acetal bond and native HCCA Isomerase catalysis. Two chemical transformations must occur to isomerize HCCA to tHBPA: the acetal bond must be broken and the hybridization at C7 must be changed from sp^2 to sp^3 (Figure 42). It has been suggested that the hybridization at C7 could be changed via addition of GSH (*52-54*). Such adducts break pi conjugation and cause a loss of the molecular absorbance characteristics (Figure 39a). Single turnover reactions of HCCA Isomerase with HCCA and tHBPA do indicate the build up of an intermediate along the enzyme catalyzed reaction coordinate; however, the intermediate shows robust absorbance (Figure 38b, c) whose bands are consistent with those of cHBPA (Figure 36b).

Though the model does not give the individual rate constants for each step, the resulting observed rate constants for steps 1 and 2 (Table 14) are consistent among all experiments. Single turnover reactions beginning with either isomer yield the same extracted UV-Vis spectrum for the intermediate (Figure 38b, c). The intermediate decays at the same rate in both cases (Table 14). Finally, the observed rate constants for the first step in either direction are consistent with the thermodynamic equilibrium between isomers. The measured equilibrium constant between HCCA and tHBPA is 1.53 (pH 7.0). Division of $k_{1\ obs}$ for HCCA by $k_{1\ obs}$ tHBPA gives a K_{eq} of 1.52 (in a HCCA/tHBPA equilibrium $k_{1\ obs}$ for HCCA = k_1 and $k_{1\ obs}$ for tHBPA = k_{-1}).

The appearance of cHBPA along the reaction coordinate suggests that the enzymatic mechanism likely involves two distinct steps. First, is ring cleavage and the second is

isomerization (Figure 42). To determine if the enzyme could perform both of these steps in a concerted manner, MCCA [a compound without the chromene ring hydroxyl group (Figure 34c)] was synthesized and assayed. The enzyme showed no activity toward MCCA (Table 15). This suggests that acetal ring cleavage must occur for catalysis to proceed. These results are consistent with an ordered mechanism (Figure 42) and makes the concerted mechanism proposed previously (Figure 33a) unlikely.

HCCA Isomerase and the product analog tMBPA. Cleavage of the acetal ring is only one of the factors important for catalysis. The other is alteration of orbital hybridization at C7 (Figure 34c). It is known that GSH is vital for efficient catalysis (Table 9), but single turnover reactions with the native substrate/product showed no indication of a GSH adduct (Figure 38b, c). This does not mean that one is not occurring: it could be transient. The product analog tMBPA was synthesized to determine if C7 was a viable site for GSH addition and to possibly capture an adducted intermediate in the active site. Due to its bulk at the ortho position (Figure 34e), all cis isomers (HCCA and cHBPA) are highly unlikely; therefore, the GSH adduct and not free ligand might be the most stable structure in the active site.

HCCA Isomerase showed activity in the catalytic conjugation of GSH with tMBPA. The conjugation occurs at C7 as expected (Figure 41a). Overlay of the active site with HCCA or tMBPA bound (Figure 40) shows the correlation of C7 for each. This suggests C7 is viable site for nucleophilic attack during native turnover. Steady state turnover with tMBPA is slow (Table 15); however, single turnover reactions show that the enzyme

catalyzes chemistry at a rate of ~1100 s^{-1} (Table 16). This indicates that Michael chemistry is fast and makes a transient conjugate during native turnover possible.

The crystal structure of the active site of HCCA Isomerase containing tMBPA contains many of the characteristics expected of a GSH adduct (ie. a native-like intermediate). The electron density suggests most of the crystal contains GSH-tMBPA adduct (Figure 41a). The temperature factors show high dynamic motion beyond C7, as would be expected for isomerization back and forth (Figure 41b). The dihedral angles suggest the hybridization at C7 has single bond characteristics (Figure 41c).

Global mechanism of HCCA Isomerase. Figure 42 shows our hypothesis about the mechanistic path of this enzyme. This mechanism is based on evidence from crystallographic and transient state kinetic studies with HCCA/tHBPA and the analog tMPBA including the absence of activity toward the substrate analog MCCA. The apparent flaw in this model is the inconsistency between two kinetic observations. First, the observed rate constant for the burst seen during multiple turnover analysis of HCCA and tHBPA tops out at ~5 s^{-1} (at high ligand concentrations): a result inconsistent with the turnover number of the enzyme. Second, single turnover analysis of HCCA and tHBPA (Figure 37 and 38) showed a two-step process whose second step gave an observed rate constant of ~2.5 s^{-1} (Table 14), again inconsistent with turnover. The clue to reconciling these observations comes from the multiple turnover reactions. During the burst phase, the enzyme travels through several turnovers before reaching the steady state. This suggested that product inhibition maybe key (*93, 94*). In conjunction with the substrate inhibition seen by tHBPA, these inhibitory complexes resulted in a good global fit to our

model. The fit converges and shows moderate correlation for both x and y residuals. It yields inhibitory binding constants for EPS and ESP that are similar and nanomolar: a result consistent with severe product inhibition. It also results in rate constants consistent Michael chemistry, the known lower limit for the rate of deprotonation of HCCA, and the turnover number of the enzyme.

Acknowledgements. Dr. Joel Harp (Vanderbilt Center for Structural Biology) was a great help in the use of the X-ray facility. Dr. Jane Ladner who solved the crystal structure for us.

APPENDIX

THE HDX-MS DATA OBTAINED ON THE LIGAND BOUND AND APO FORMS OF NATIVE rGSTM1-1 (N) AND THE F56S MUTANT AS WELL AS THE CURVES AND KINETIC CONSTANTS DERIVED FROM FITTING OF THE DATA

Enzyme		A_1 (D)	k_1 (m^{-1})	A_2 (D)	k_2 (m^{-1})	A_3 (D)	k_3 (m^{-1})
N N+GSH F56S F56S+GSO_3^-	1-4	0.3±0.1	0.03±0.01	2.6±0.1	0.001±0.00006		
N N+GSH F56S F56S+GSO_3^-	5-18	4.6±0.7 1.4±0.1 4.9±0.3 1.7±0.2	0.9±0.3 0.4±0.1 0.8±0.1 0.4±0.1	2.6±0.7 4.2±0.4 1.3±0.4 3.6±0.3	0.09±0.04 0.01±0.002 0.04±0.03 0.02±0.004	4.2±0.2 5.3±0.4 3.3±0.4 6.1±0.4	0.001±0.0003 0.004±0.002 0.002±0.0004 0.0006±0.0002
N N+GSH F56S F56S+GSO_3^-	7-18	4.4±0.5 1.2±0.1 4.3±0.3 1.4±0.1	0.8±0.2 0.2±0.03 0.8±0.2 0.3±0.05	1.9±0.5 3.8±0.2 0.8±0.3 3.1±0.2	0.06±0.001 0.01±0.002 0.03±0.025 0.02±0.003	3.7±0.3 4.3±0.3 3.2±0.4 5.5±0.2	0.001±0.0003 0.0002±0.0001 0.002±0.0004 5±0.9x10^{-4}
N N+GSH F56S F56S+GSO_3^-	7-20	4.2±0.4 0.9±0.1 4.1±0.2 1.3±0.2	0.7±0.2 0.3±0.04 0.8±0.1 0.3±0.07	1.9±0.4 3.6±0.1 1.2±0.3 2.9±0.2	0.05±0.02 0.01±0.001 0.02±0.01 0.02±0.003	5.8±0.3 7.0±0.1 5.3±0.3 7.9±0.2	0.0006±0.0001 2±0.4x10^{-4} 0.0006±0.0002 4±0.6 x10^{-4}
N N+GSH F56S F56S+GSO_3^-	8-20	3.2±0.3 0.8±0.1 3.4±0.2 1.0±0.2	0.9±0.2 0.2±0.04 0.7±0.1 0.3±0.09	1.8±0.3 3.1±0.1 1.4±0.3 2.3±0.1	0.04±0.004 0.01±0.001 0.01±0.008 0.02±0.004	6.0±0.2 6.6±0.9 5.0±0.5 7.7±0.1	0.0006±0.0001 8±4x10^{-4} 0.0005±0.0002 2±0.4 x10^{-4}
N N+GSH F56S F56S+GSO_3^-	19-21						
N N+GSH F56S F56S+GSO_3^-	20-29	5.8±0.4 5.6±0.3 5.0±0.3 5.8±0.2	0.7±0.1 0.3±0.05 0.5±0.1 0.5±0.1	1.5±0.2 1.2±0.2 1.0±0.1 1.7±0.1	0.0002±0.0005 0.0008±0.0008 0.0006±0.0006 0.0004±0.0003		
N N+GSH F56S F56S+GSO_3^-	22-27	2.1±0.4 2.5±0.2 0.9±0.2 2.7±0.5	1.1±0.4 0.7±0.1 0.8±0.4 2.3±0.6	1.7±0.1 0.9±0.1 1.3±0.1 1.9±0.1	0.0003±0.0003 0.0004±0.0004 0.0003±0.0003 0.0002±0.0002		
N N+GSH F56S F56S+GSO_3^-	23-33	6.1±0.5 4.5±0.4	1.2±0.2 1.1±0.2	2.4±0.1 2.4±0.3	3.0±2.0 x10^{-7} 0.06±0.02	2.5±0.2	0.0003±0.0002
N N+GSH F56S F56S+GSO_3^-	34-46	4.3±0.5 4.7±0.4 2.9±0.4 3.5±0.4	0.8±0.2 0.3±0.1 0.5±0.2 1.7±0.4	3.9±0.2 3.8±0.3 2.5±0.2 2.5±0.3	0.001±0.0003 0.0005±0.03 0.0004±0.0004 0.09±0.01	3.3±0.3	0.0005±0.0002

N N+GSH F56S F56S+GSO_3^-	49- 56	6.2±0.5 6.4±0.3	1.6±0.2 0.9±0.1				
N N+GSH F56S F56S+GSO_3^-	49- 59	7.8±0.5 6.9±0.3 1.9±0.5 4.7±0.3	1.4±0.1 0.8±0.1 0.9±0.5 2.3±0.9	1.6±0.1 1.6±0.2 0.9±0.1	0.01±0.003 0.001±0.0001 0.04±0.01	2.9±0.1	0.0008±0.0001
N N+GSH F56S F56S+GSO_3^-	49- 62	6.6±0.4 5.1±0.4 2.5±0.6 5.4±0.3	1.1±0.1 0.8±0.1 0.9±0.5 2.4±0.1	2.5±0.1 1.9±0.4 2.5±0.2 1.4±0.1	0.0003±0.0002 0.04±0.01 0.01±0.001 0.04±0.01	3.8±0.1	0.0006±0.0001
N N+GSH F56S F56S+GSO_3^-	51- 62	5.7±0.4 4.5±0.4	1.3±0.2 0.3±0.1	2.7±0.1 3.9±0.2	0.0005±0.0002 0.0007±0.0003		
N N+GSH F56S F56S+GSO_3^-	57- 74	3.7±0.4 3.8±0.3	1.0±0.3 0.4±0.1	2.0±0.3 10.4±0.2	0.03±0.01 0.0007±0.0003	8.5±0.3	0.0002±0.0001
N N+GSH F56S F56S+GSO_3^-	60- 74	2.7±0.5 3.3±0.2 3.5±0.4 3.4±0.1	1.1±0.4 0.7±0.1 0.3±0.08 2.0±0.2	2.0±0.4 9.2±0.1 7.5±0.2 1.5±0.1	0.05±0.02 0.0001±0.00004 0.0006±0.0001 0.07±0.008	7.7±0.3 9.2±0.1	0.0004±0.0003 2.0±0. 2x10^{-4}
N N+GSH F56S F56S+GSO_3^-	63- 74	2.9±0.5 3.1±0.3 3.7±0.3 3.2±0.3	0.9±0.4 1.1±0.2 0.5±0.1 1.6±0.4	2.2±0.4 0.8±0.2 3.7±0.2 1.4±0.2	0.04±0.02 0.07±0.05 0.001±0.0003 0.1±0.04	4.3±0.3 6.0±0.1 6.2±0.1	0.0004±0.0003 8.0±7.0x10^{-5} 5.0±0.6x10^{-4}
N N+GSH F56S F56S+GSO_3^-	75- 91	3.9±0.3 4.1±0.3 2.1±0.6 3.0±0.3	0.5±0.1 0.3±0.1 0.6±0.4 1.7±0.4	9.6±0.2 8.9±0.1 1.1±0.6 1.5±0.2	9.0±7.0 x10^{-5} 8.0±7.0 x10^{-5} 0.05±0.06 0.1±0.03	9.4±0.3 9.7±0.1	0.0002±0.0001 4.0±3.0x10^{-5}
N N+GSH F56S F56S+GSO_3^-	89- 96	1.2±0.3 1.4±0.1 2.7±0.2 1.5±0.2	0.9±0.6 1.1±0.3 0.5±0.1 1.2±0.3	1.8±0.3 0.6±0.1 2.6±0.1 0.9±0.3	0.04±0.02 0.09±0.04 0.001±0.0002 0.06±0.03	3.1±0.2 4.4±0.1 4.3±0.1	0.0005±0.0002 1.0±0.4x10^{-5} 6.0±0.8x10^{-5}
N N+GSH F56S F56S+GSO_3^-	92- 96						
N N+GSH F56S F56S+GSO_3^-	92- 100						
N N+GSH F56S F56S+GSO_3^-	93- 100						

N N+GSH F56S F56S+GSO_3^-	97- 100						
N N+GSH F56S F56S+GSO_3^-	101- 110	1.9±0.2 1.4±0.1 5.2±0.4 1.8±0.1	0.8±0.2 0.09±0.01 0.15±0.02 0.06±0.06	3.4±0.3 7.7±0.1 3.8±0.4 7.2±0.1	0.02±0.004 0.0002±0.00002 0.007±0.001 0.0004±0.00003	4.0±0.3	0.001±0.0002
N N+GSH F56S F56S+GSO_3^-	103- 110	2.9±0.3 0.5±0.3 4.4±0.3 0.8±0.1	0.03±0.01 0.09±0.02 4.6±0.9 0.03±0.006	3.8±0.3 6.5±0.3 2.4±0.3 6.2±0.1	0.001±0.0003 8.0±8.0x10^{-5} 0.005±0.001 0.0004±0.00005		
N N+GSH F56S F56S+GSO_3^-	110- 119	2.5±0.2 2.6±0.2 1.9±0.2 1.9±0.2	0.6±0.1 0.3±0.1 0.4±0.1 1.9±0.3	4.5±0.1 4.1±0.1 4.5±0.1 0.9±0.1	1.1±0.9x10^{-5} 0.0001±0.0001 0.0004±0.00009 0.12±0.03	 4.8±0.1	 6.0±3.0x10^{-5}
N N+GSH F56S F56S+GSO_3^-	111- 113	1.2±0.1 0.2±0.03 1.3±0.06 0.1±0.02	0.05±0.01 0.3±0.1 0.01±0.001 0.05±0.02	0.7±0.1 1.8±0.0 0.7±0.1 1.8±0.0	0.001±0.0005 0.0005±0.00004 0.0009±0.0002 0.0003±0.00003		
N N+GSH F56S F56S+GSO_3^-	114- 126	6.7±0.4 4.0±0.5 6.6±0.4 3.4±0.5	0.5±0.1 0.7±0.2 0.3±0.05 0.9±0.3	0.9±0.2 4.8±0.5 0.6±0.3 5.5±0.5	0.0002±0.001 0.03±0.006 0.002±0.0002 0.05±0.008		
N N+GSH F56S F56S+GSO_3^-	116- 126	4.7±0.5 4.5±0.4 5.6±0.4 5.6±0.3	0.05±0.01 0.03±0.005 0.08±0.01 0.04±0.005	2.5±0.5 2.8±0.4 1.9±0.4 1.9±0.3	0.003±0.001 0.002±0.0005 0.005±0.002 0.0009±0.0005		
N N+GSH F56S F56S+GSO_3^-	120- 126	3.8±0.3 1.7±0.2 3.4±0.2 1.8±0.2	0.6±0.1 1.0±0.3 0.2±0.03 1.9±0.3	0.5±0.1 3.0±0.1 0.3±0.1 3.3±0.1	0.0006±0.001 0.03±0.003 0.002±0.9 0.003±0.003		
N N+GSH F56S F56S+GSO_3^-	127- 136	2.5±0.3 2.2±0.1 2.7±0.1 2.6±0.1	1.1±0.3 0.9±0.1 0.7±0.2 1.7±0.1	2.5±0.3 2.2±0.1 2.6±0.1 2.2±0.1	0.04±0.01 0.03±0.003 0.03±0.004 0.02±0.001	3.0±0.3 3.6±0.1 2.5±0.1 3.6±0.1	0.001±0.0003 3.0±0.7x10^{-5} 0.001±0.0002 5.0±0.6x10^{-5}
N N+GSH F56S F56S+GSO_3^-	137- 140	3.0±0.04 3.0±0.01 2.5±0.1 2.0±0.1	0.002±0.002 8.0±0.4x10^{-5} 0.09±0.09 0.03±0.003	 0.6±0.1 1.0±0.1	 0.0003±0.0003 0.001±0.0004		
N N+GSH F56S F56S+GSO_3^-	141- 154	4.2±0.2 4.5±0.1 4.6±0.2 4.3±0.2	0.07±0.008 0.06±0.005 0.1±0.01 0.08±0.008	7.5±0.2 7.2±0.1 7.1±0.2 7.4±0.1	0.0003±0.00001 0.0002±0.00007 0.0002±0.00008 0.0002±0.00006		
N N+GSH F56S F56S+GSO_3^-	141- 157	4.2±0.1 4.5±0.1 4.5±0.2 4.1±0.2	0.06±0.005 0.06±0.005 0.1±0.02 0.07±0.01	11±0.1 10±0.1 10±0.2 10±0.2	0.0003±0.00004 0.0002±0.00004 0.0002±0.00006 0.0002±0.00007		
N N+GSH F56S F56S+GSO_3^-	158- 163						
N N+GSH	164- 174	2.6±0.3 2.4±0.1	1.0±0.2 0.6±0.1	5.5±0.1 5.3±0.1	0.005±0.00008 0.0001±0.00005		

F56S F56S+GSO_3^-		2.2±0.2 2.9±0.2	0.6±0.1 1.2±0.2	5.1±0.1 4.9±0.1	0.0004±0.00007 0.0001±0.00006		
N N+GSH F56S F56S+GSO_3^-	167-174	1.6±0.1 1.6±0.05 2.2±0.2 1.6±0.08	0.4±0.07 0.3±0.03 0.6±0.1 0.5±0.06	3.8±0.1 3.7±0.1 5.1±0.1 3.6±0.1	0.002±0.00006 0.0001±0.00004 0.0004±0.00007 $9.0\pm5.0\times10^{-5}$		
N N+GSH F56S F56S+GSO_3^-	175-184	3.5±0.2 3.4±0.2 4.3±0.2 3.7±0.2	0.03±0.004 0.03±0.005 0.07±0.008 0.05±0.006	4.2±0.2 4.3±0.2 3.5±0.2 3.7±0.2	0.0005±0.0001 0.0007±0.0002 0.0005±0.0002 0.0004±0.0002		
N N+GSH F56S F56S+GSO_3^-	177-184	2.1±0.1 2.2±0.2 2.6±0.1 1.0±0.2	0.05±0.008 0.04±0.0007 0.08±0.01 0.4±0.16	3.6±0.1 3.5±0.2 3.1±0.1 2.0±0.2	0.0007±0.0001 0.0007±0.0002 0.0005±0.0001 0.02±0.005	 2.6±0.2	 0.0002±0.0002
N N+GSH F56S F56S+GSO_3^-	177-187	2.4±0.3 2.9±0.4 2.3±0.4 2.0±0.2	1.1±0.3 0.2±0.1 0.6±0.2 1.3±0.3	1.9±0.2 4.6±0.3 1.7±0.4 1.7±0.2	0.03±0.01 0.0005±0.0002 0.04±0.02 0.06±0.01	3.9±0.2 3.4±0.2 4.3±0.1	0.0005±0.0002 0.0006±0.0002 $2.0\pm0.8\times10^{-5}$
N N+GSH F56S F56S+GSO_3^-	185-195	3.7±0.3 3.6±0.2 3.7±0.2 3.6±0.1	0.4±0.1 0.3±0.04 0.5±0.08 0.4±0.04	5.1±0.1 4.9±0.1 4.7±0.1 4.7±0.1	0.0003±0.0001 0.0002±0.00008 0.0002±0.0001 0.0002±0.00007		
N N+GSH F56S F56S+GSO_3^-	188-195	3.5±0.2 3.6±0.1 3.6±0.2 3.4±0.1	0.4±0.1 0.3±0.03 0.5±0.08 0.4±0.04	2.1±0.1 1.8±0.1 1.7±0.1 1.9±0.1	0.0003±0.0003 0.0002±0.0002 0.0003±0.0003 0.0001±0.0001		
N N+GSH F56S F56S+GSO_3^-	196-202	3.2±0.2 4.0±0.2 3.6±0.2 3.5±0.1	0.4±0.1 0.2±0.03 0.4±0.06 0.3±0.02	1.8±0.1 0.7±0.1 0.9±0.1 1.6±0.1	0.00005±0.0002 0.0008±0.0008 0.0004±0.0004 0.0003±0.0002		
N N+GSH F56S F56S+GSO_3^-	196-208	7.1±0.5 7.3±0.4 7.1±0.8 6.1±0.3	0.7±0.1 0.3±0.05 0.8±0.2 1.1±0.1	1.5±0.2 1.4±0.3 0.9±0.3 2.7±0.4	0.0001±0.0006 0.001±0.001 0.002±0.002 0.1±0.02	 1.7±0.1	 0.0006±0.0002
N N+GSH F56S F56S+GSO_3^-	209-217	3.7±0.4 5.2±0.3 2.5±0.3 5.8±0.2	1.0±0.2 0.8±0.1 0.9±0.2 0.9±0.07	0.9±0.1 0.7±0.1 0.5±0.1 0.8±0.1	0.0005±0.0005 0.0009±0.0009 0.0008±0.0008 0.0004±0.0004		
N N+GSH F56S F56S+GSO_3^-	212-217	2.5±0.3 3.1±0.2 1.7±0.2 3.1±0.1	1.2±0.3 0.8±0.1 1.0±0.2 1.1±0.07	0.8±0.3 0.6±0.1 0.6±0.1 1.0±0.1	0.0004±0.0004 0.0008±0.0007 0.0004±0.0004 0.0001±0.0001		

Peptide 1-4 (3)

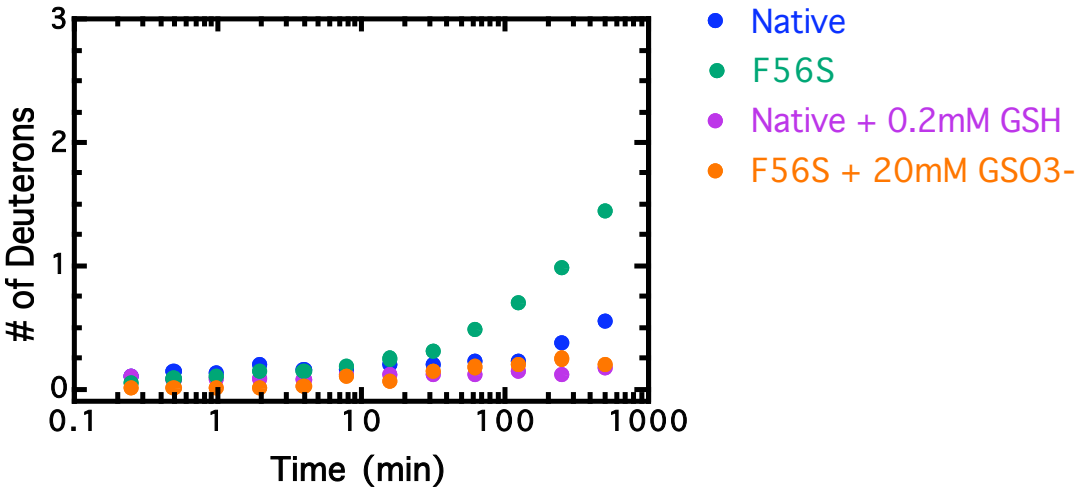

Peptide 5-18 (12)

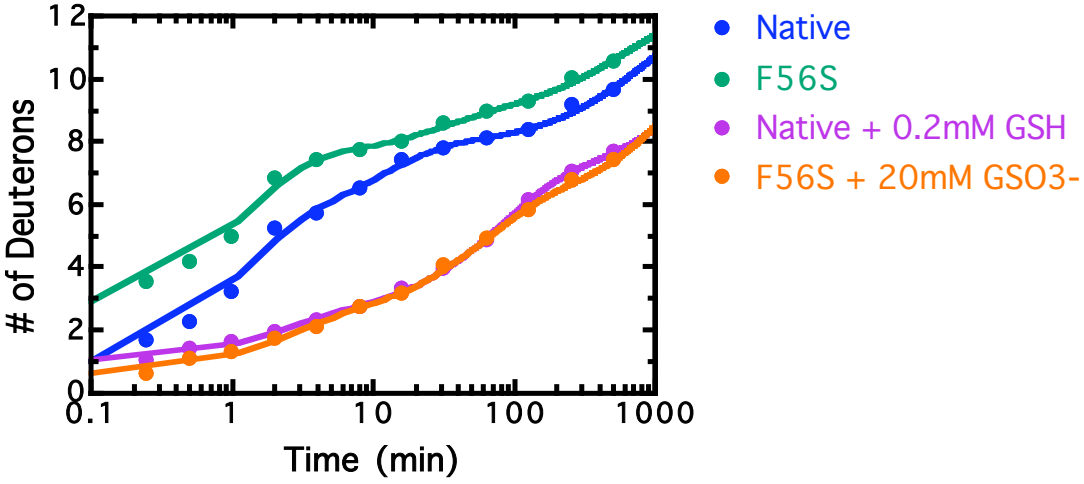

Peptide 7-18 (10)

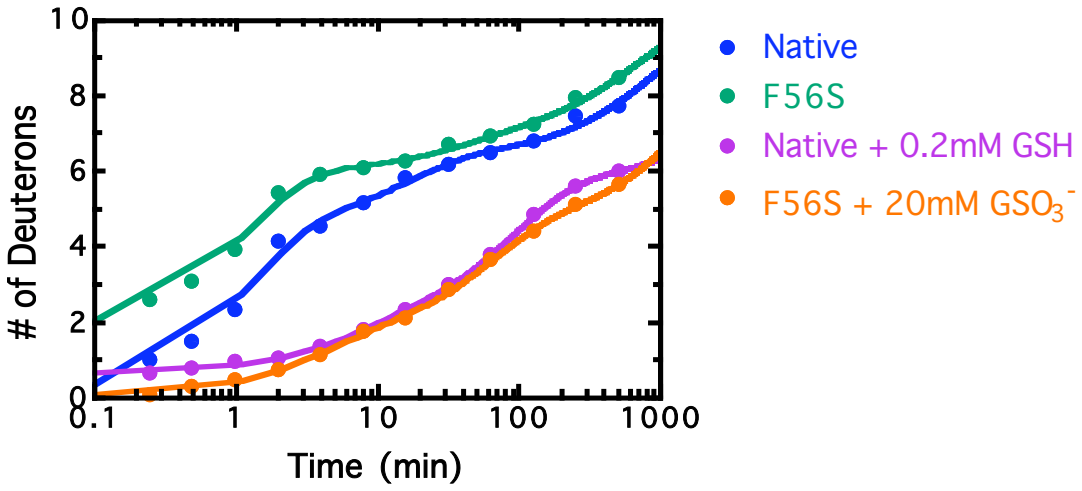

Peptide 7-20 (12)

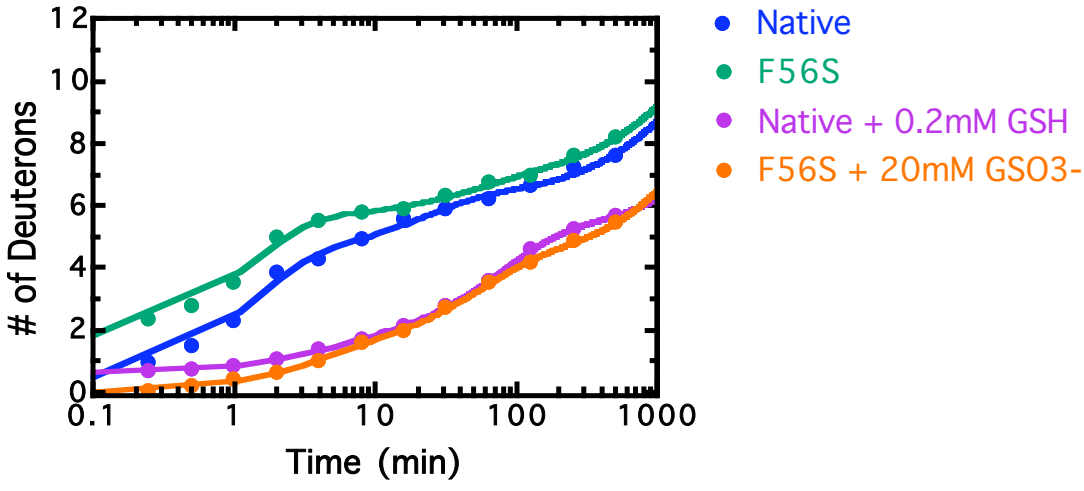

Peptide 8-20 (11)

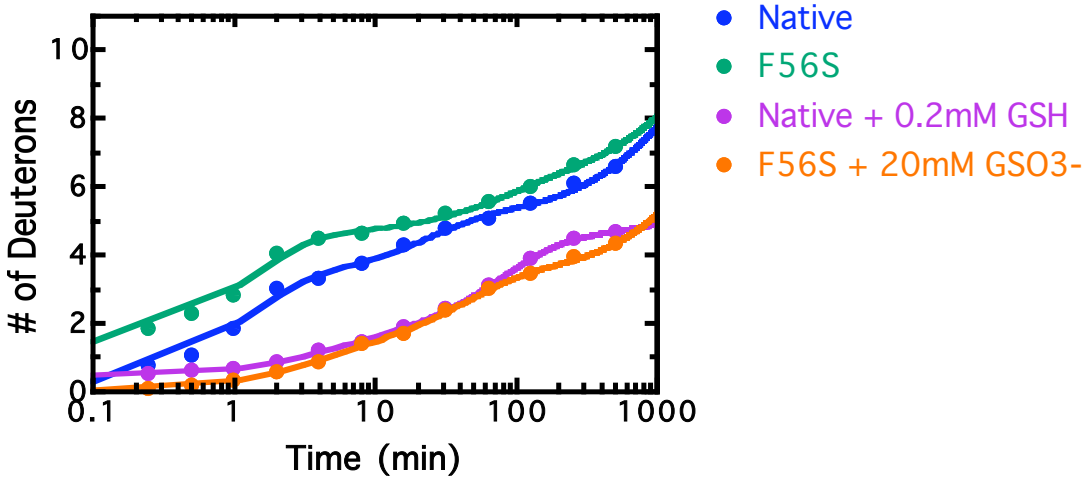

Peptide 19-21 (2)

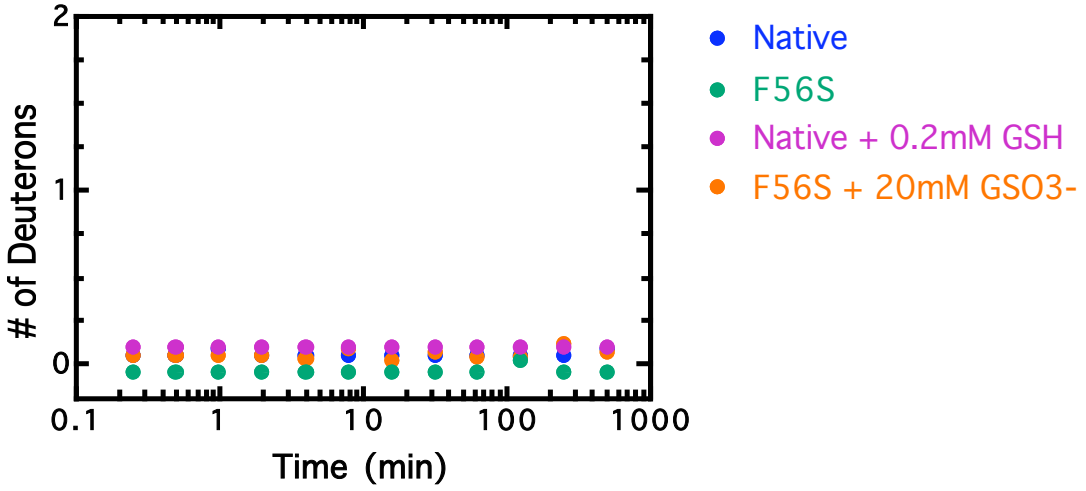

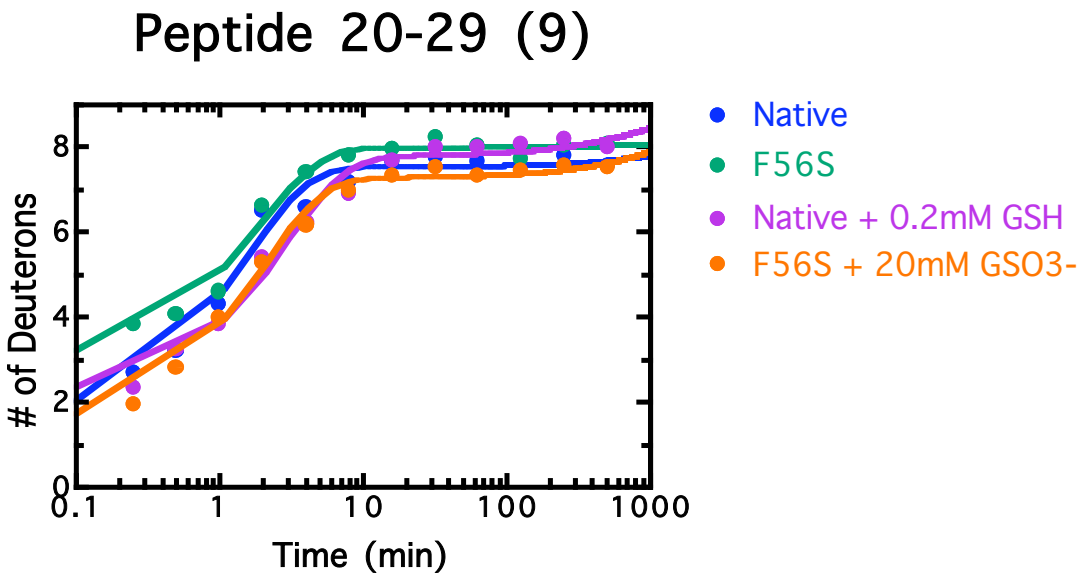
Peptide 20-29 (9)
# of Deuterons
Time (min)
0.1
1
10
100
1000
0
2
4
6
8
Native
F56S
Native + 0.2mM GSH
F56S + 20mM GSO3-

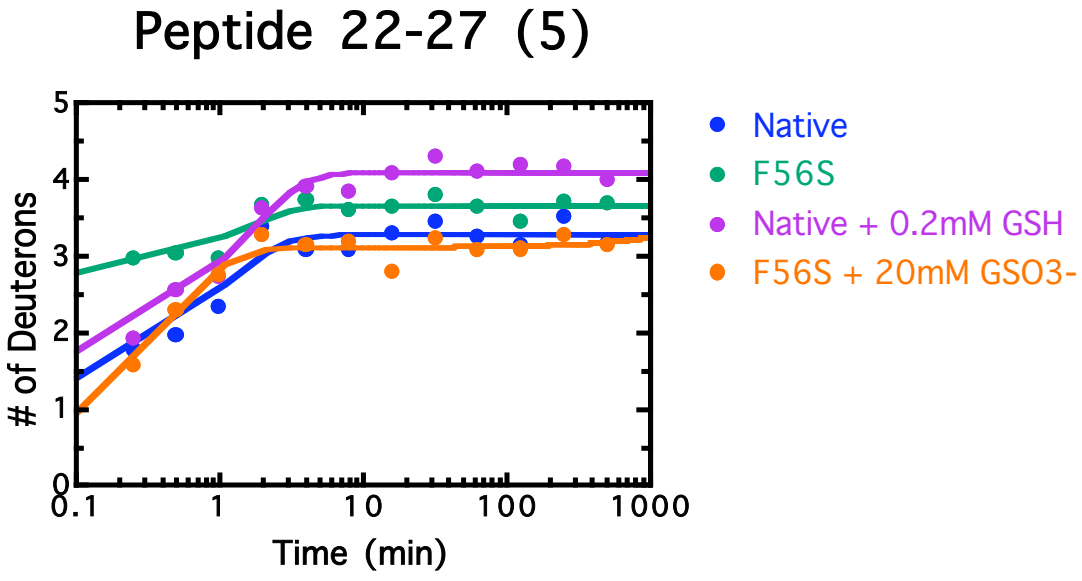
Peptide 22-27 (5)
# of Deuterons
Time (min)
0.1
1
10
100
1000
0
1
2
3
4
5
Native
F56S
Native + 0.2mM GSH
F56S + 20mM GSO3-

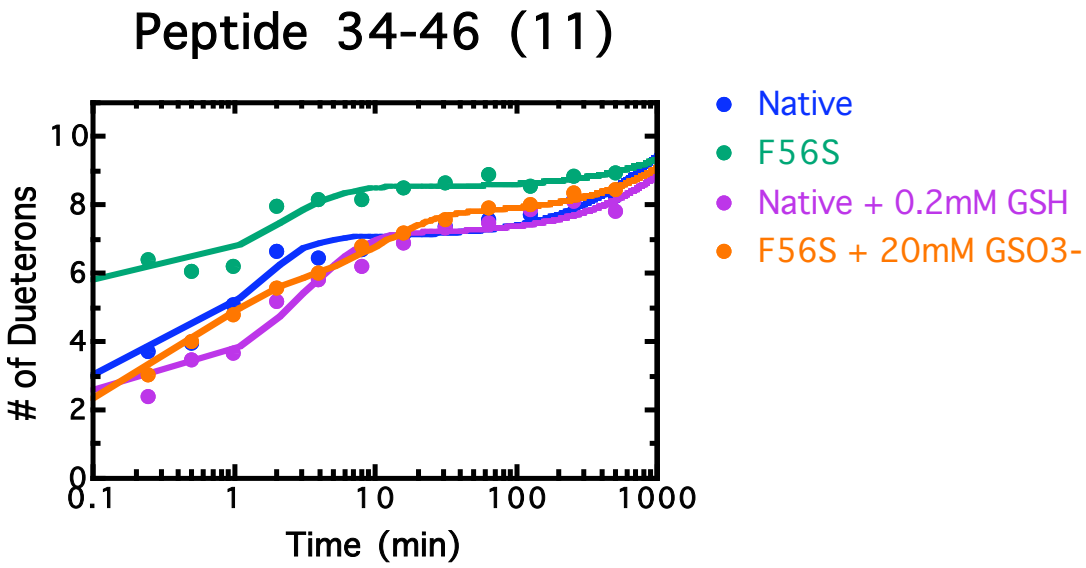
Peptide 34-46 (11)
# of Dueterons
Time (min)
0.1
1
10
100
1000
0
2
4
6
8
10
Native
F56S
Native + 0.2mM GSH
F56S + 20mM GSO3-

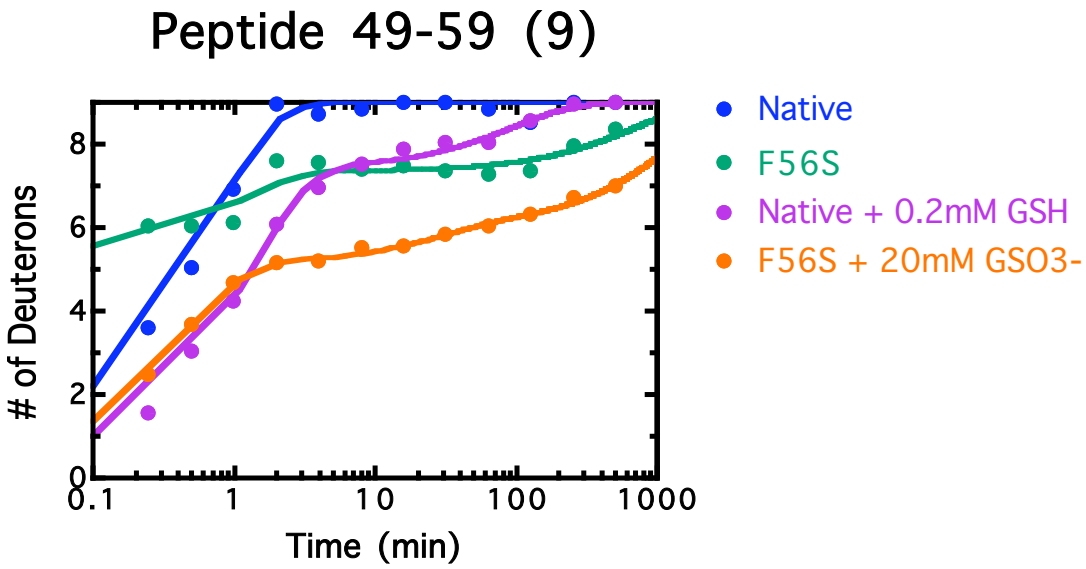
Peptide 49-59 (9)
# of Deuterons
Time (min)
0.1
1
10
100
1000
0
2
4
6
8
Native
F56S
Native + 0.2mM GSH
F56S + 20mM GSO3-

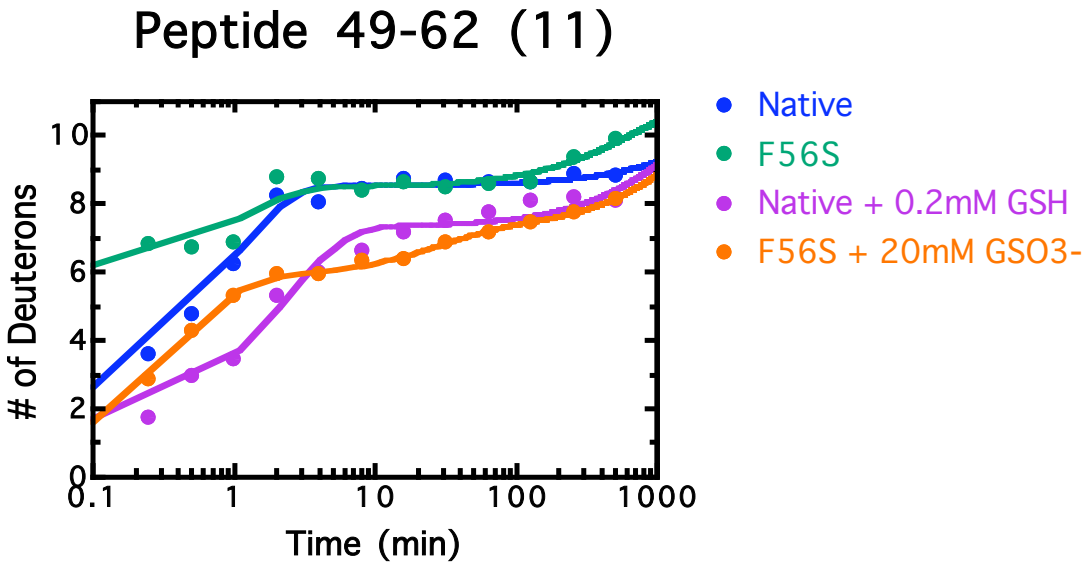
Peptide 49-62 (11)
# of Deuterons
0
2
4
6
8
10
0.1
1
10
100
1000
Time (min)
Native
F56S
Native + 0.2mM GSH
F56S + 20mM GSO3-

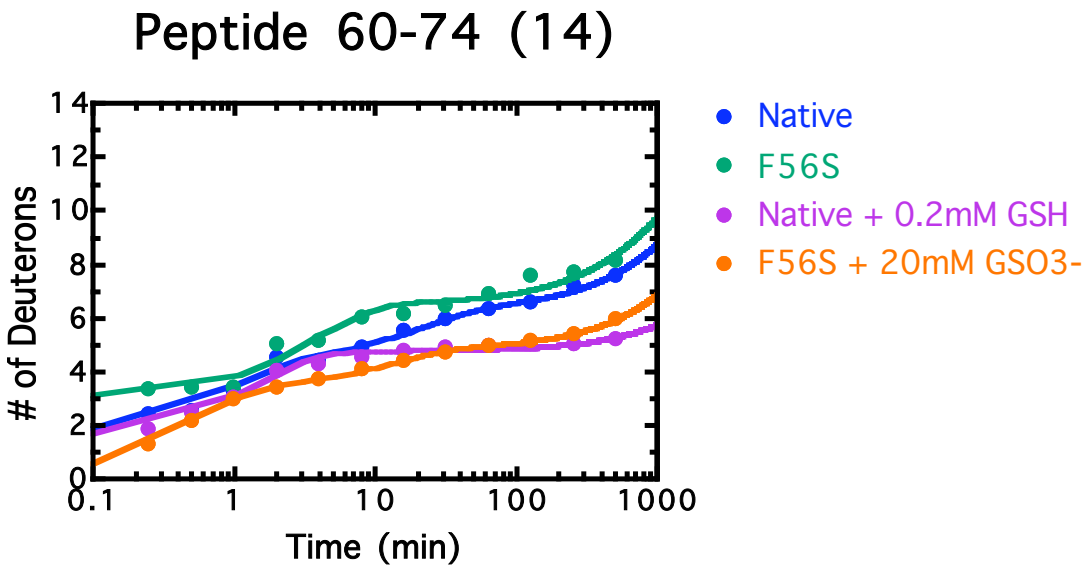
Peptide 60-74 (14)
# of Deuterons
0
2
4
6
8
10
12
14
0.1
1
10
100
1000
Time (min)
Native
F56S
Native + 0.2mM GSH
F56S + 20mM GSO3-

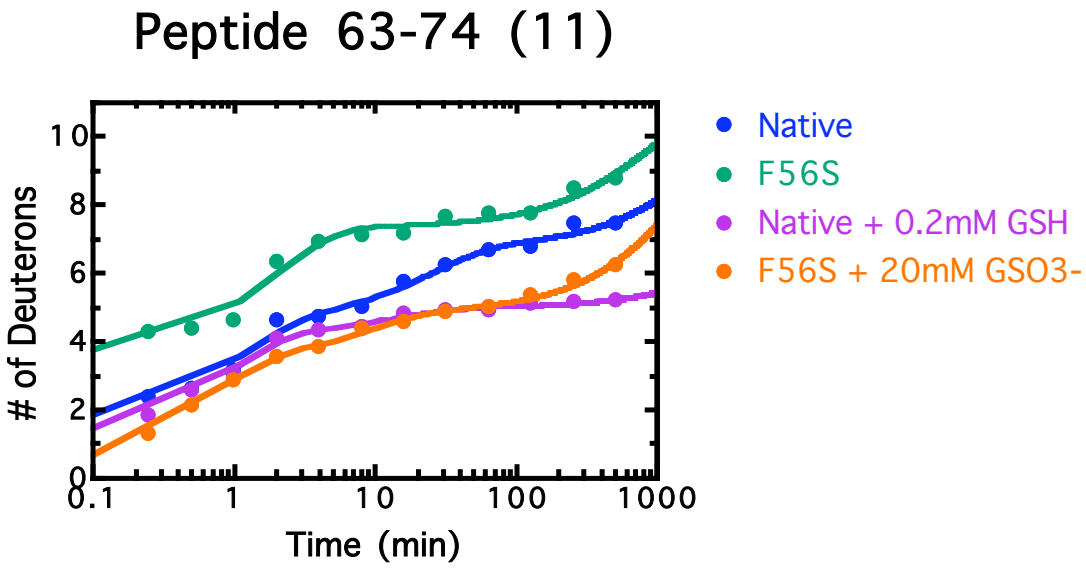
Peptide 63-74 (11)
# of Deuterons
Time (min)
0.1
1
10
100
1000
0
2
4
6
8
10
Native
F56S
Native + 0.2mM GSH
F56S + 20mM GSO3-

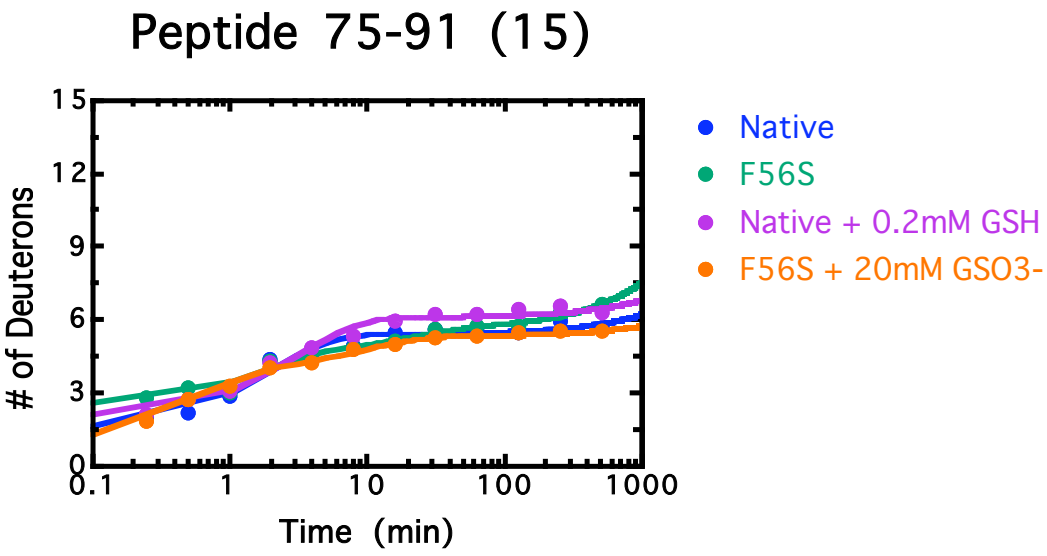
Peptide 75-91 (15)
# of Deuterons
Time (min)
0.1
1
10
100
1000
0
3
6
9
12
15
Native
F56S
Native + 0.2mM GSH
F56S + 20mM GSO3-

Peptide 89-96 (7)

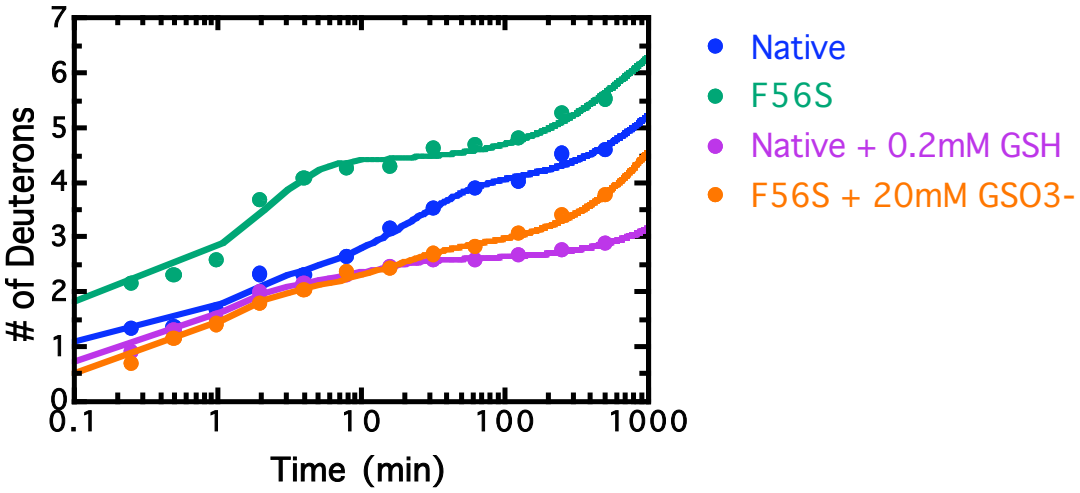

Peptide 92-96 (4)

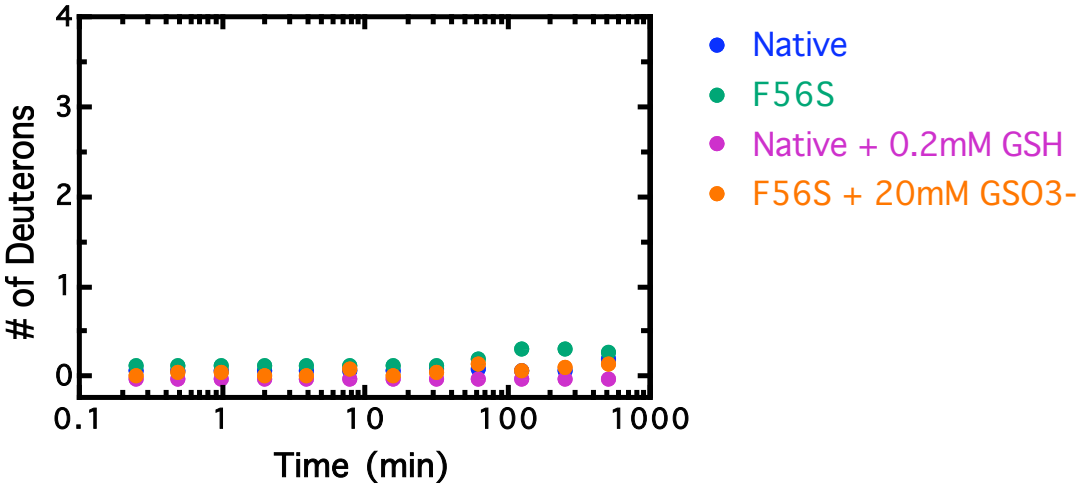

Peptide 92-100 (8)

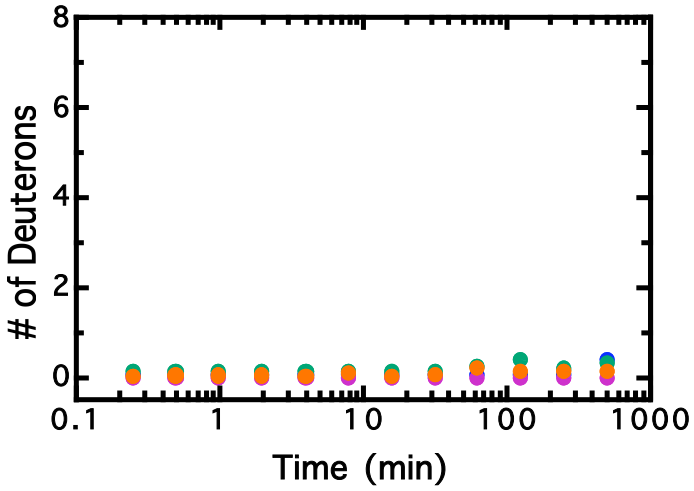

Peptide 93-100 (7)

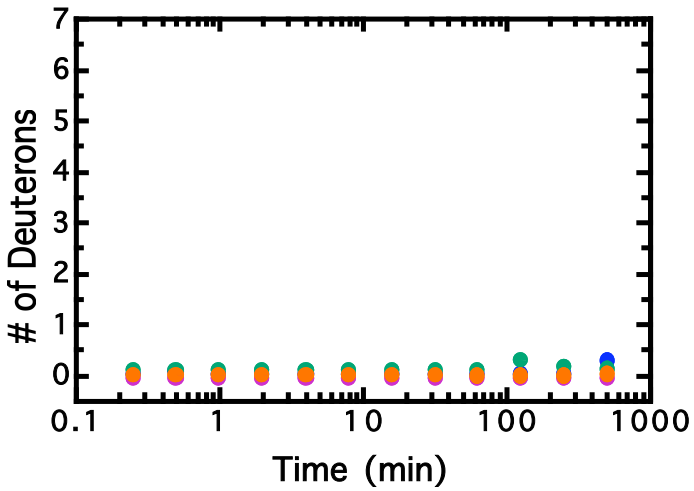

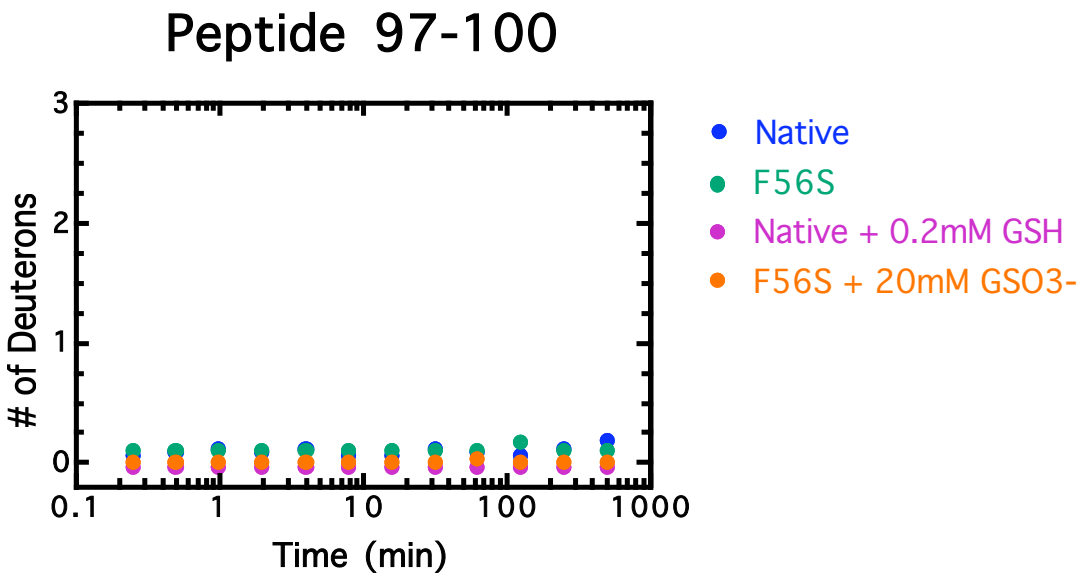
Peptide 97-100
# of Deuterons
Time (min)
0.1
1
10
100
1000
0
1
2
3
Native
F56S
Native + 0.2mM GSH
F56S + 20mM GSO3-

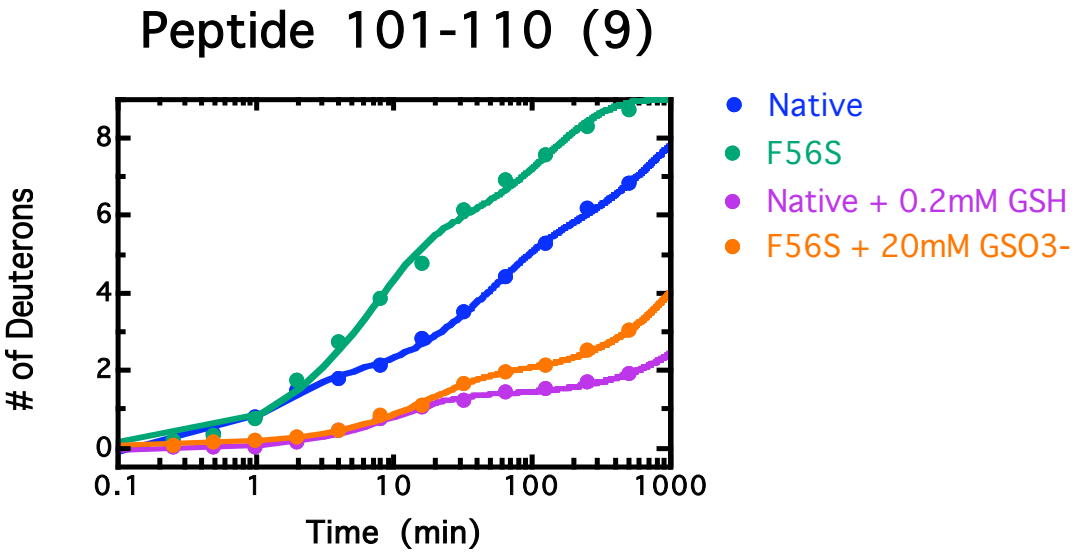
Peptide 101-110 (9)
# of Deuterons
Time (min)
0.1
1
10
100
1000
0
2
4
6
8
Native
F56S
Native + 0.2mM GSH
F56S + 20mM GSO3-

Peptide 103-110 (7)

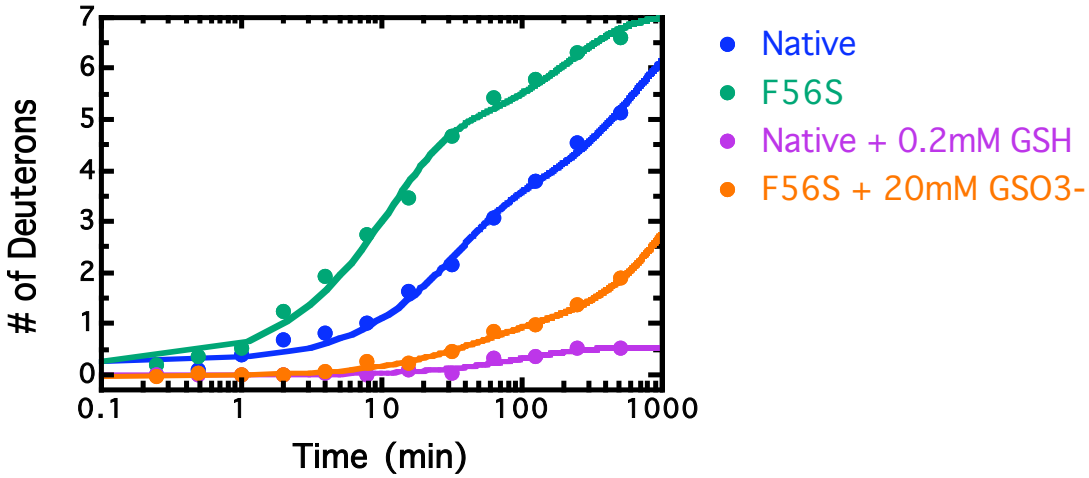

Peptide 110-119 (8)

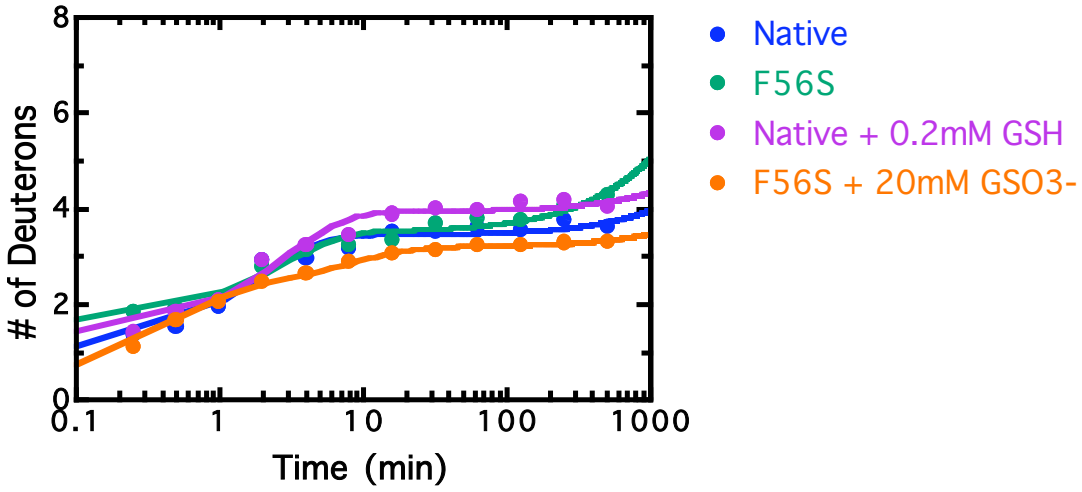

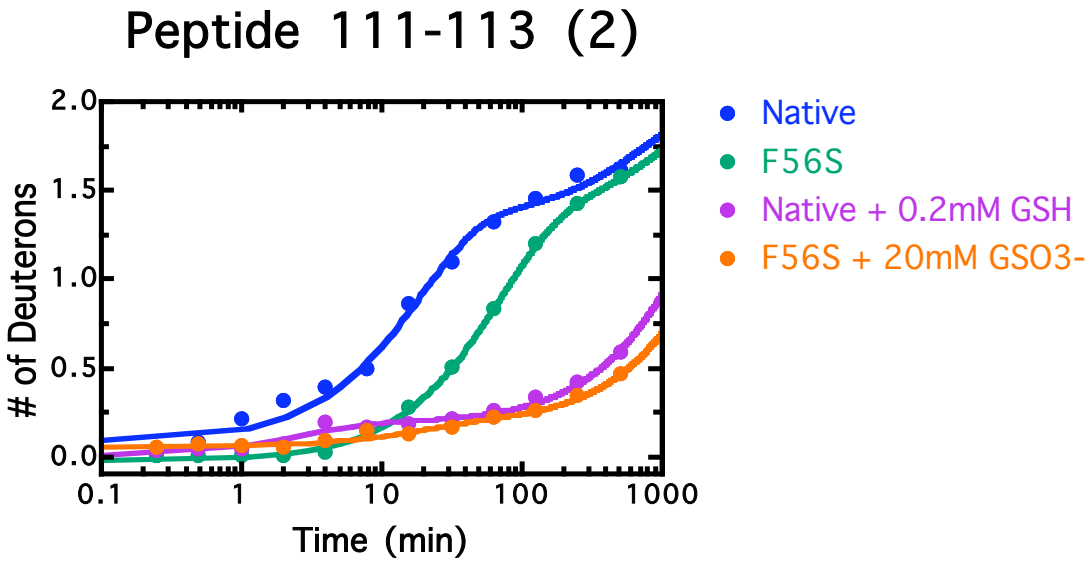
Peptide 111-113 (2)
# of Deuterons
2.0
1.5
1.0
0.5
0.0
0.1
1
10
100
1000
Time (min)
Native
F56S
Native + 0.2mM GSH
F56S + 20mM GSO3-

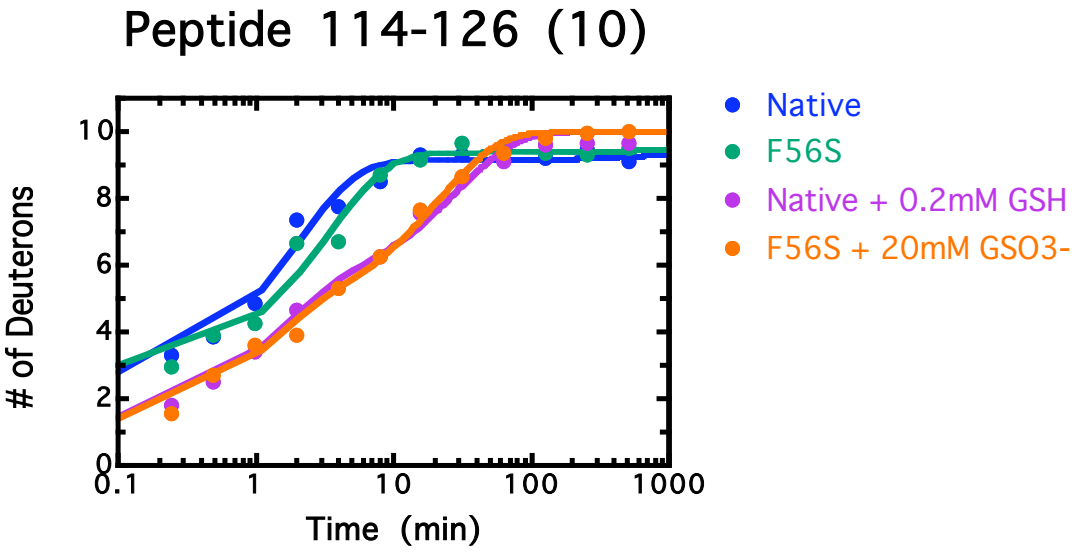
Peptide 114-126 (10)
# of Deuterons
10
8
6
4
2
0
0.1
1
10
100
1000
Time (min)
Native
F56S
Native + 0.2mM GSH
F56S + 20mM GSO3-

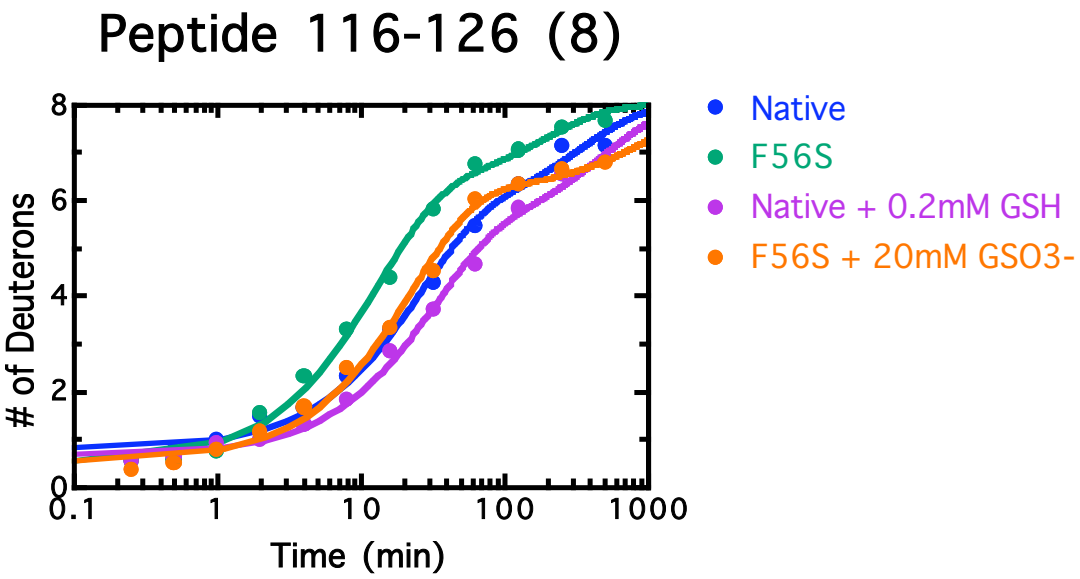
Peptide 116-126 (8)
# of Deuterons
Time (min)
0.1
1
10
100
1000
0
2
4
6
8
Native
F56S
Native + 0.2mM GSH
F56S + 20mM GSO3-

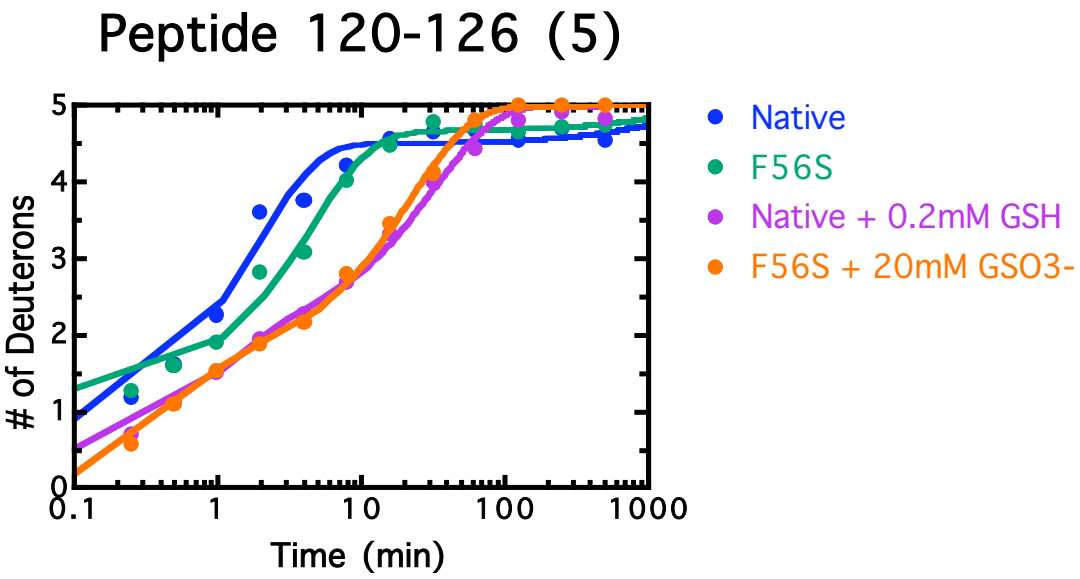
Peptide 120-126 (5)
# of Deuterons
Time (min)
0.1
1
10
100
1000
0
1
2
3
4
5
Native
F56S
Native + 0.2mM GSH
F56S + 20mM GSO3-

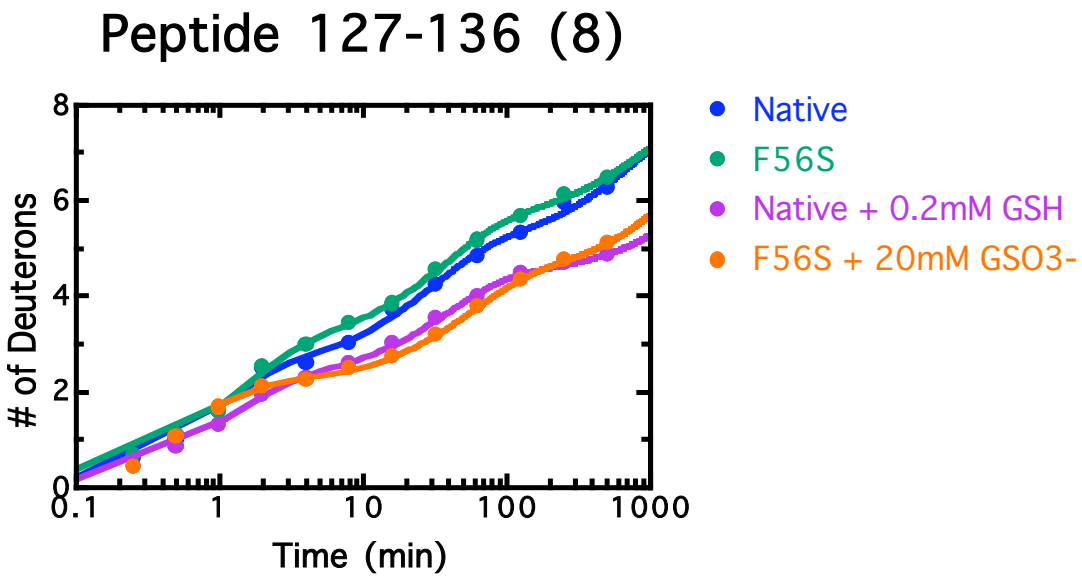
Peptide 127-136 (8)
# of Deuterons
Time (min)
0.1
1
10
100
1000
0
2
4
6
8
Native
F56S
Native + 0.2mM GSH
F56S + 20mM GSO3-

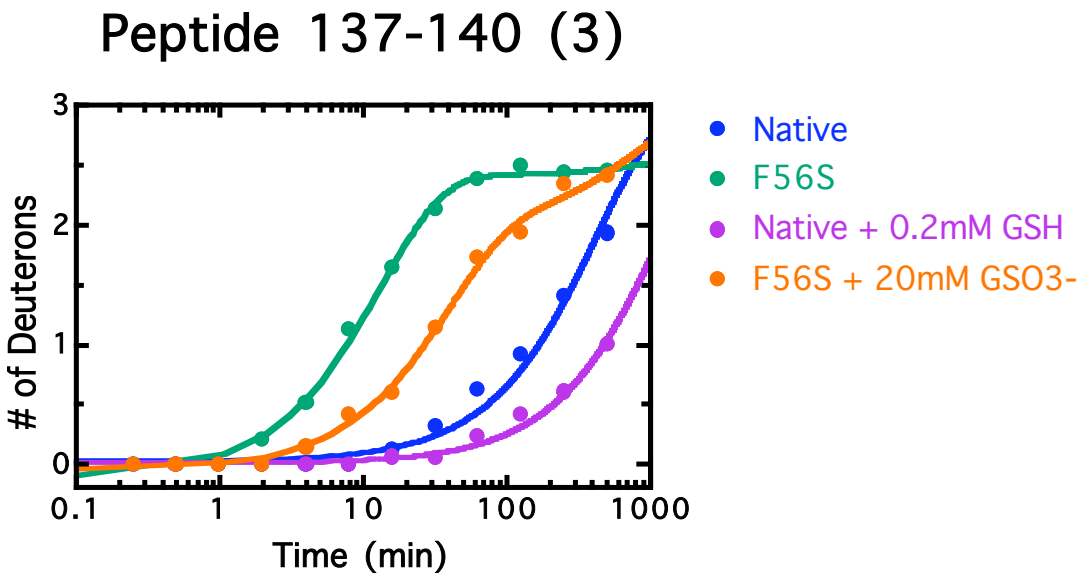
Peptide 137-140 (3)
# of Deuterons
Time (min)
0.1
1
10
100
1000
0
1
2
3
Native
F56S
Native + 0.2mM GSH
F56S + 20mM GSO3-

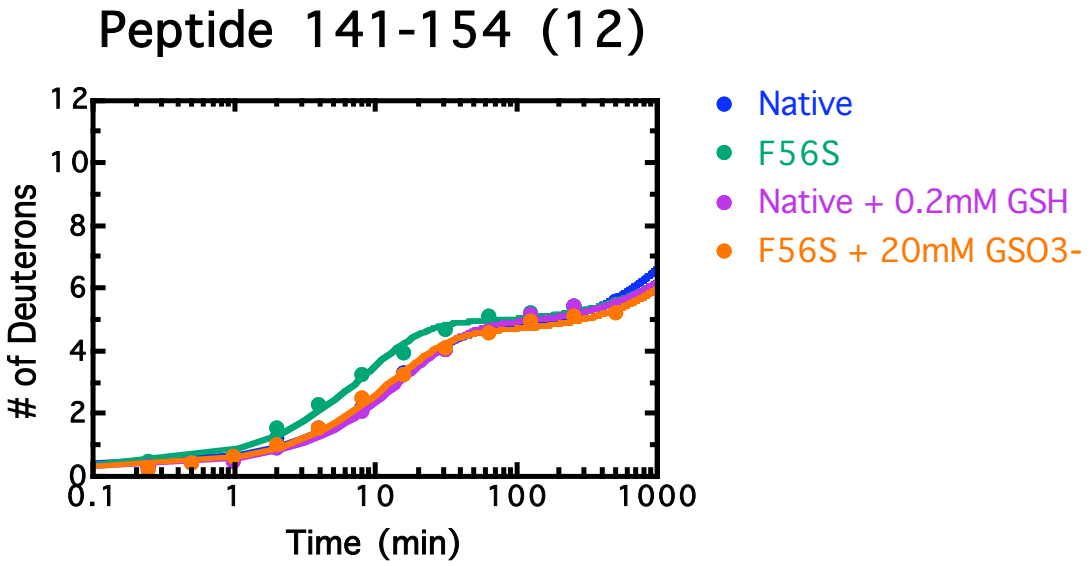
Peptide 141-154 (12)
# of Deuterons
Time (min)
0.1
1
10
100
1000
0
2
4
6
8
10
12
Native
F56S
Native + 0.2mM GSH
F56S + 20mM GSO3-

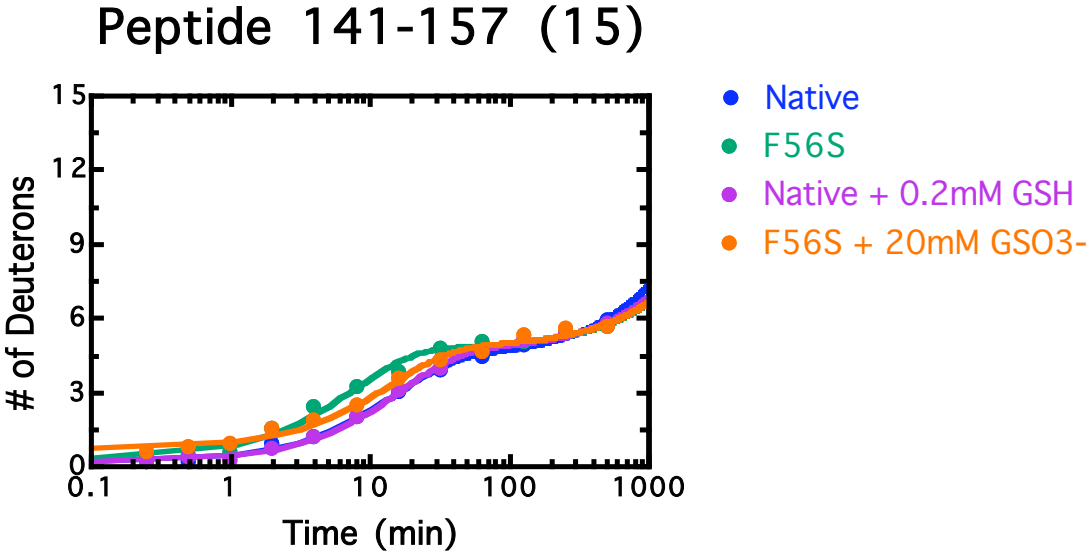
Peptide 141-157 (15)
# of Deuterons
Time (min)
0.1
1
10
100
1000
0
3
6
9
12
15
Native
F56S
Native + 0.2mM GSH
F56S + 20mM GSO3-

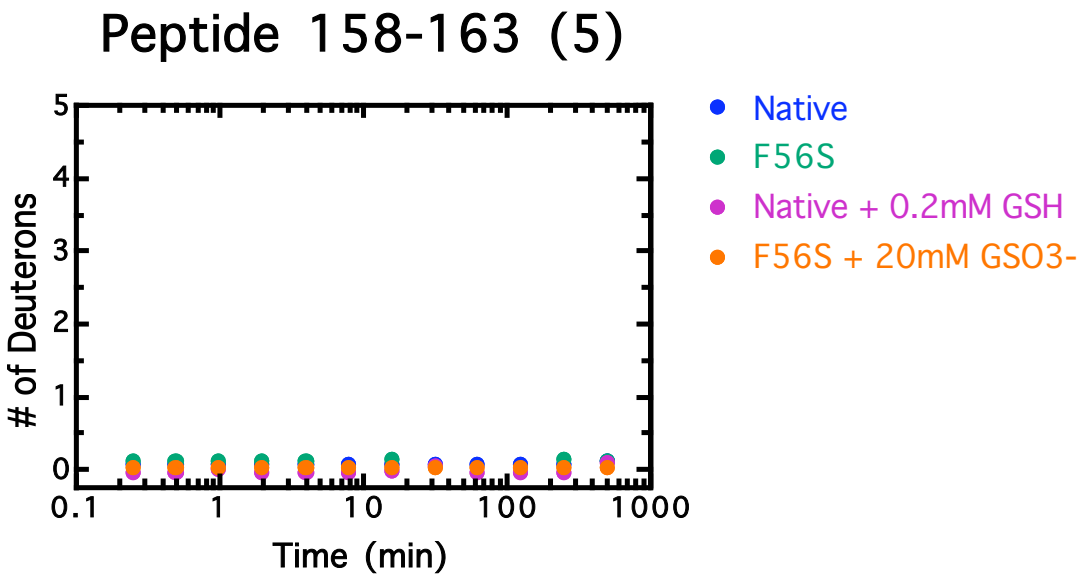
Peptide 158-163 (5)
# of Deuterons
Time (min)
0.1
1
10
100
1000
0
1
2
3
4
5
Native
F56S
Native + 0.2mM GSH
F56S + 20mM GSO3-

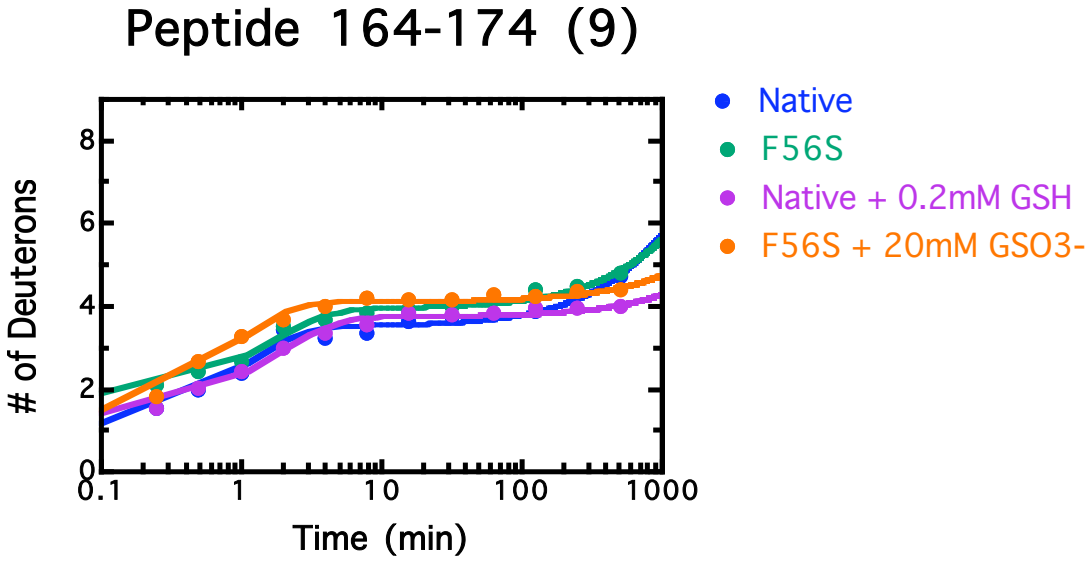
Peptide 164-174 (9)
# of Deuterons
Time (min)
0.1
1
10
100
1000
0
2
4
6
8
Native
F56S
Native + 0.2mM GSH
F56S + 20mM GSO3-

Peptide 167-174 (6)

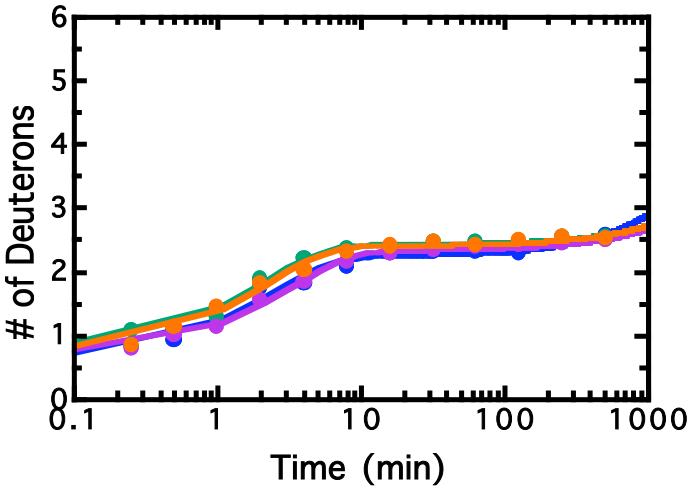

Peptide 175-184 (8)

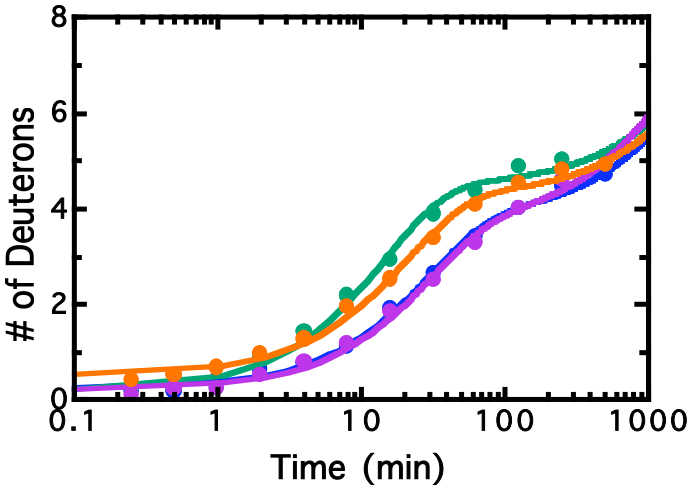

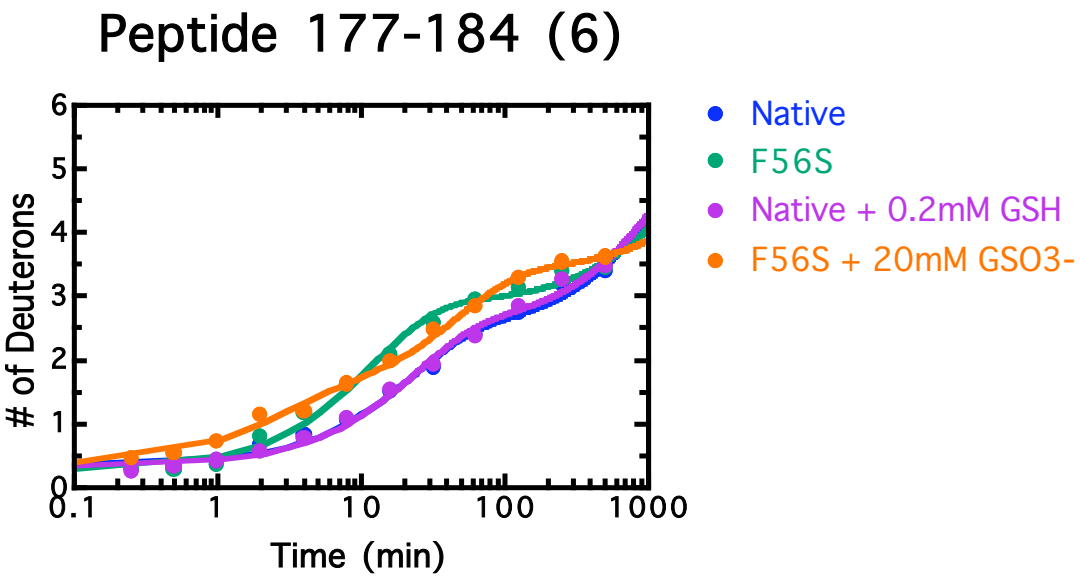
Peptide 177-184 (6)
# of Deuterons
Time (min)
0.1
1
10
100
1000
0
1
2
3
4
5
6
Native
F56S
Native + 0.2mM GSH
F56S + 20mM GSO3-

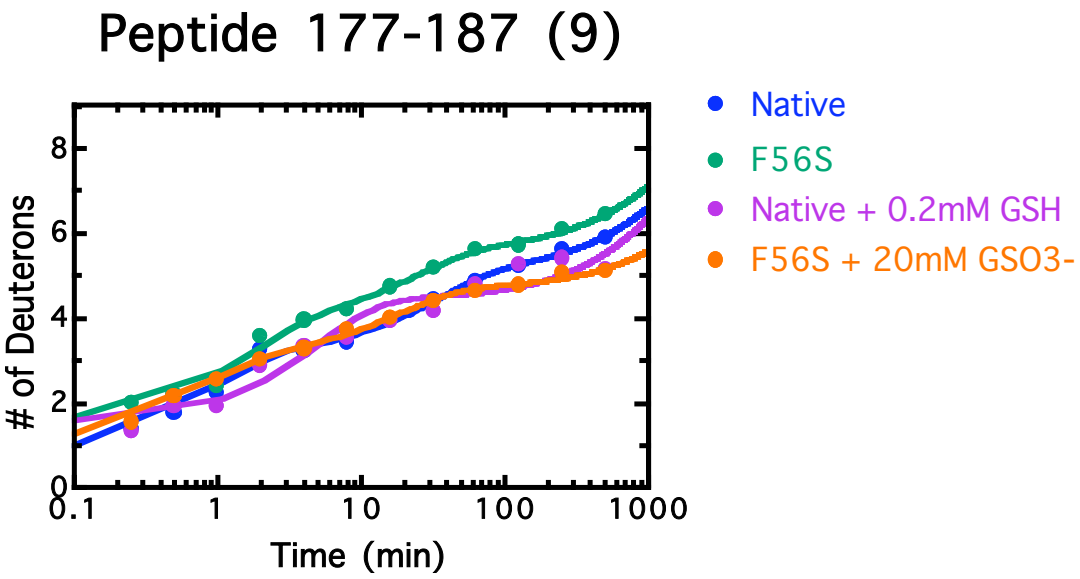
Peptide 177-187 (9)
# of Deuterons
Time (min)
0.1
1
10
100
1000
0
2
4
6
8
Native
F56S
Native + 0.2mM GSH
F56S + 20mM GSO3-

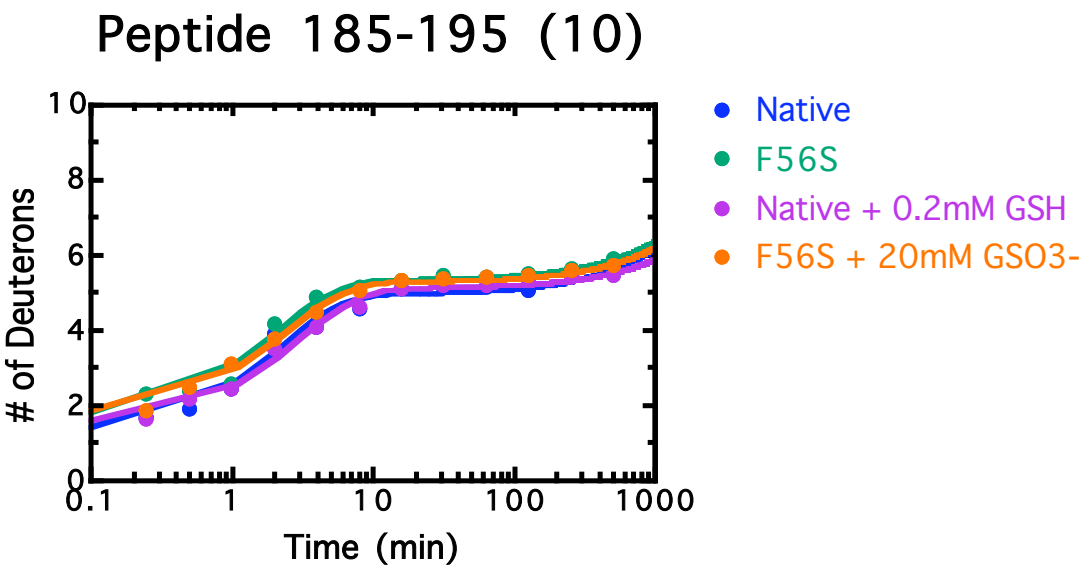
Peptide 185-195 (10)
# of Deuterons
Time (min)
0.1
1
10
100
1000
0
2
4
6
8
10
Native
F56S
Native + 0.2mM GSH
F56S + 20mM GSO3-

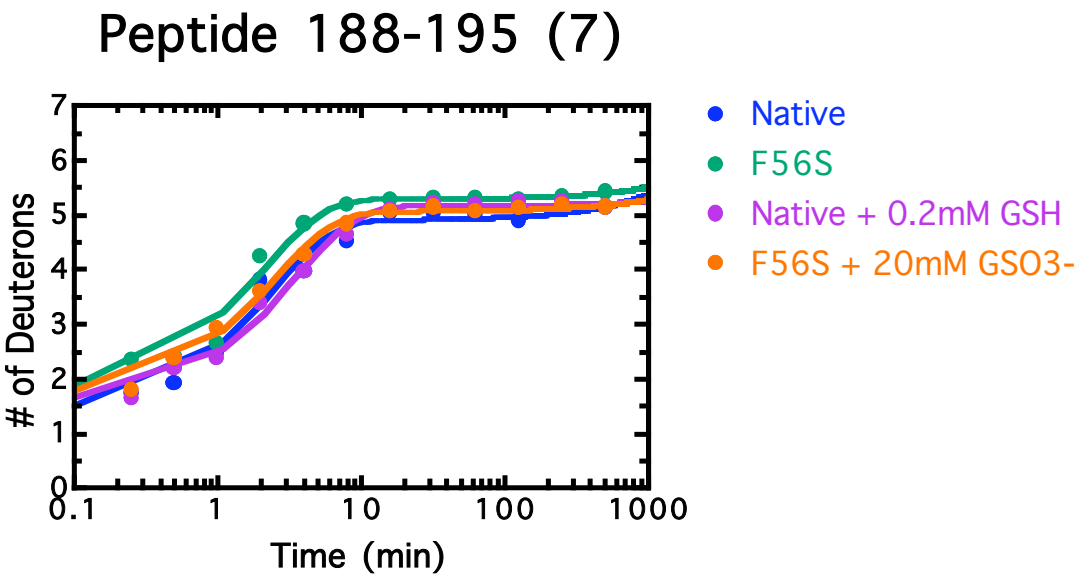
Peptide 188-195 (7)
# of Deuterons
Time (min)
0.1
1
10
100
1000
0
1
2
3
4
5
6
7
Native
F56S
Native + 0.2mM GSH
F56S + 20mM GSO3-

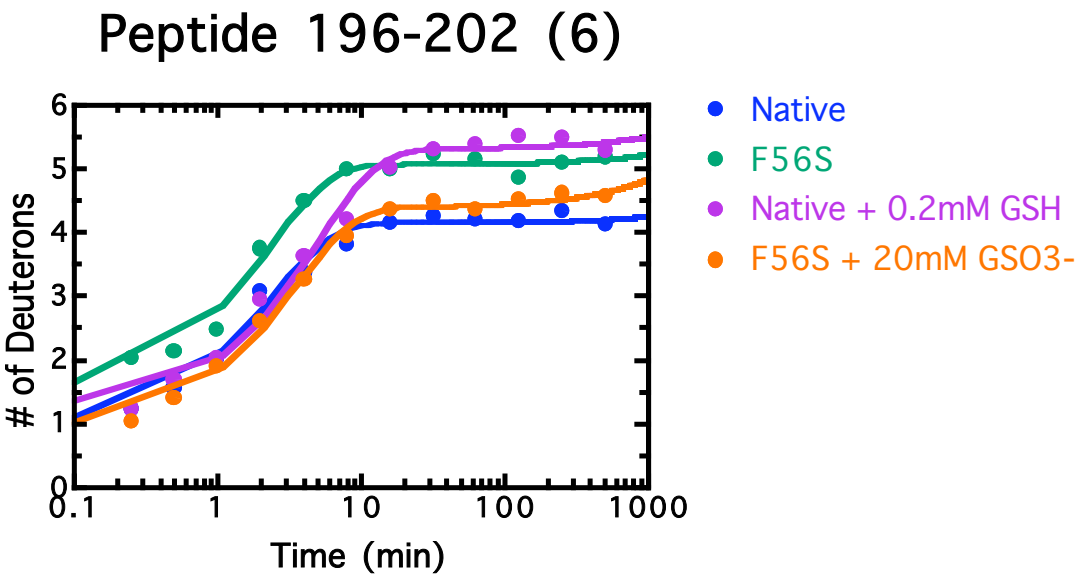
Peptide 196-202 (6)
# of Deuterons
Time (min)
0.1
1
10
100
1000
0
1
2
3
4
5
6
Native
F56S
Native + 0.2mM GSH
F56S + 20mM GSO3-

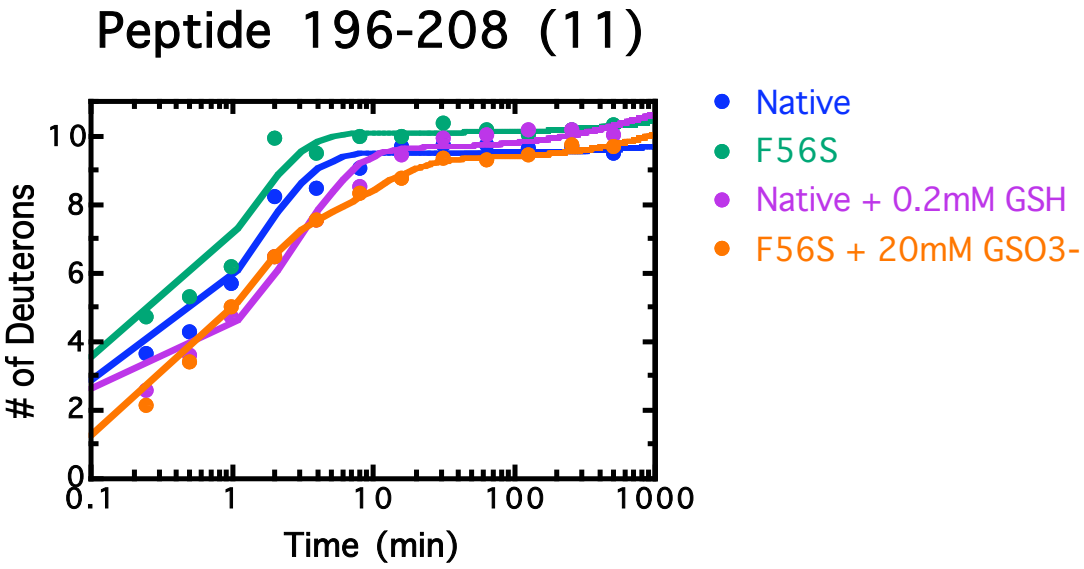
Peptide 196-208 (11)
# of Deuterons
Time (min)
0.1
1
10
100
1000
0
2
4
6
8
10
Native
F56S
Native + 0.2mM GSH
F56S + 20mM GSO3-

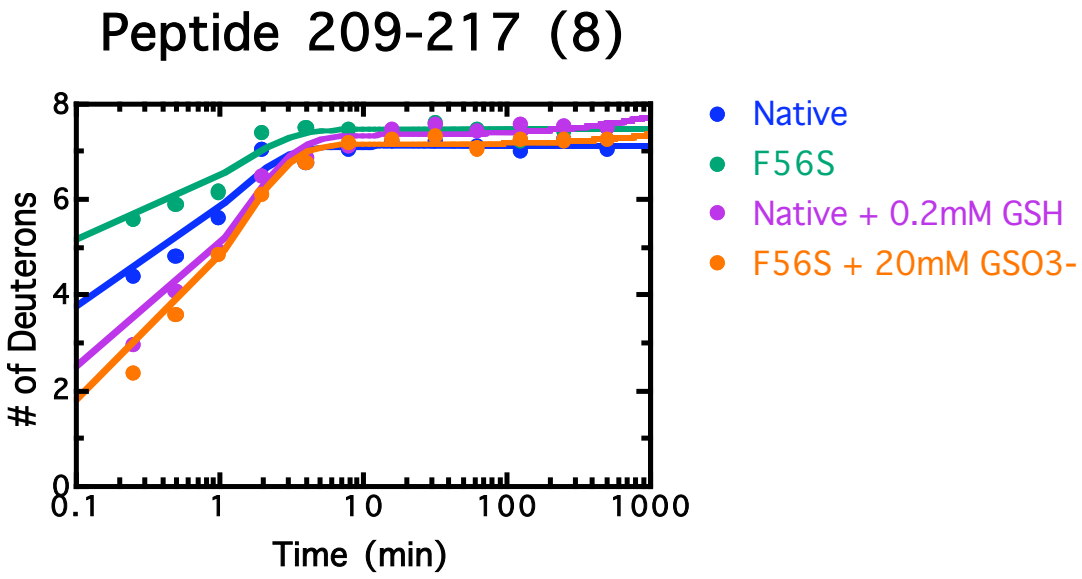
Peptide 209-217 (8)
# of Deuterons
Time (min)
0.1
1
10
100
1000
0
2
4
6
8
Native
F56S
Native + 0.2mM GSH
F56S + 20mM GSO3-

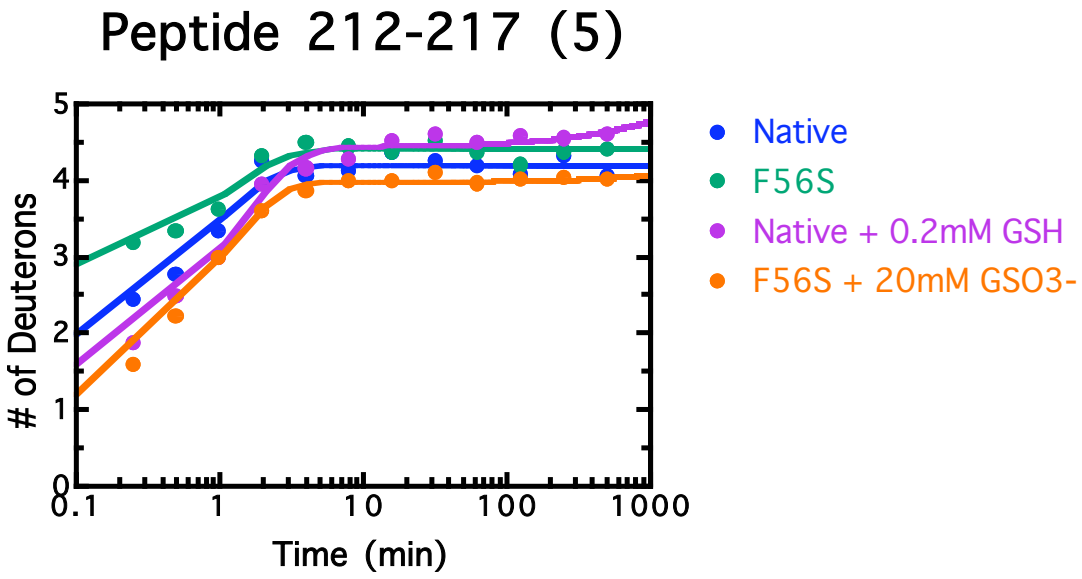
Peptide 212-217 (5)
# of Deuterons
Time (min)
0.1
1
10
100
1000
0
1
2
3
4
5
Native
F56S
Native + 0.2mM GSH
F56S + 20mM GSO3-

THE HDX-MS DATA OBTAINED ON THE F56S R81A MUTANT OF rGSTM1-1AS WELL AS THE CURVES AND KINETIC CONSTANTS DERIVED FROM FITTING OF THE DATA

Peptide	A_1 (D)	k_1 (m^{-1})	A_2 (D)	k_2 (m^{-1})	A_3 (D)	k_3 (m^{-1})
1-4	0.5±0.1	0.03±0.01	2.2±0.1	0.0014±0.0002		
5-18	4.4±0.3	0.9±0.2	2.5±0.3	0.04±0.01	3.3±0.3	0.0007±0.0003
7-18	3.6±0.2	0.6±0.1	1.6±0.2	0.03±0.01	2.8±0.2	0.0006±0.0002
7-20	3.6±0.2	0.6±0.1	1.8±0.3	0.019±0.006	4.6±0.3	0.0003±0.0002
8-20	2.8±0.2	0.7±0.1	1.6±0.2	0.028±0.009	5.1±0.2	0.0005±0.0001
19-21						
20-29	3.6±0.5	0.4±0.1	1.0±0.1	0.05±0.03		
22-27	0.9±0.2	0.6±0.3				
34-46	1.8±0.1	1.0±0.2	1.9±0.1	0.073±0.008		
49-59	1.5±0.2	0.5±0.1	2.0±0.1	0.0019±0.003		
49-62	2.2±0.2	0.6±0.1	1.1±0.1	0.008±0.002		
60-74	2.1±0.2	0.6±0.1	2.7±0.2	0.027±0.006	4.4±0.2	0.0005±0.0002
63-74	2.3±0.2	0.9±0.1	1.6±0.2	0.031±0.007	2.7±0.2	0.0003±0.0002
75-91	3.1 ± 0.3	0.6 ± 0.2	3.6 ± 0.3	0.042 ± 0.006		
89-96	1.3±0.1	1.0±0.2	1.4±0.1	0.03±0.006	1.5±0.1	0.0004±0.0002
92-96	1.8 ± 0.5	0.009 ± 0.002	2.1 ± 0.5	0.001 ± 0.0005		
92-100	4.82 ± 0.02	0.0048 ± 0.0001				
93-100	3.86 ± 0.03	0.0052 ± 0.0002				
97-100						

101-110	3.8±0.2	0.29±0.03	3.6±0.2	0.02±0.002		
103-110	2.1±0.2	0.4±0.1	3.5±0.2	0.04±0.004		
110-119	7.7 ± 0.1	0.003 ± 0.0001				
111-113	0.3±0.1	0.03±0.02	1.5±0.1	0.003±0.0003		
114-126	2.7±0.5	0.8±0.3	3.3±0.6	0.08±0.02		
116-126	1.2±0.4	0.3±0.1	4.6±0.4	0.03±0.003		
120-126	1.1±0.2	1.6±0.7	2.6±0.2	0.09±0.009		
127-136	2.0±0.1	0.8±0.1	2.9 ±0.1	0.019±0.001	2.7±0.1	0.0003±0.0001
137-140	2.17±0.03	0.048±0.002				
141-154	4.4±0.2	0.070±0.006	0.7±0.1	0.001±0.001		
141-157	1.7±0.3	0.3±0.1	3.7±0.3	0.035±0.004		
158-163						
164-174	1.6±0.1	0.50±0.07	0.55±0.06	0.010±0.003		
167-174	1.33±0.06	0.36±0.04	0.51±0.03	0.0007±0.0004		
175-184	1.0±0.2	0.25±0.09	3.5±0.3	0.028±0.003		
177-184	1.0±0.2	0.23±0.08	2.0±0.2	0.026±0.004		
177-187	2.1±0.2	0.36±0.07	1.8±0.2	0.021±0.04		
185-195	2.9±0.1	0.34±0.03	0.69±0.05	0.0019±0.0005		
188-195	2.8±0.1	0.31±0.02				
196-202	3.0±0.1	0.22±0.02				
196-208	4.6±0.8	0.6±0.1	1.8±0.8	0.1±0.04		
209-217	3.0±0.2	0.68±0.08				
212-217	1.9±0.1	0.8±0.1	0.30±0.04	0.002±0.001		

Peptide 1-4 (3)

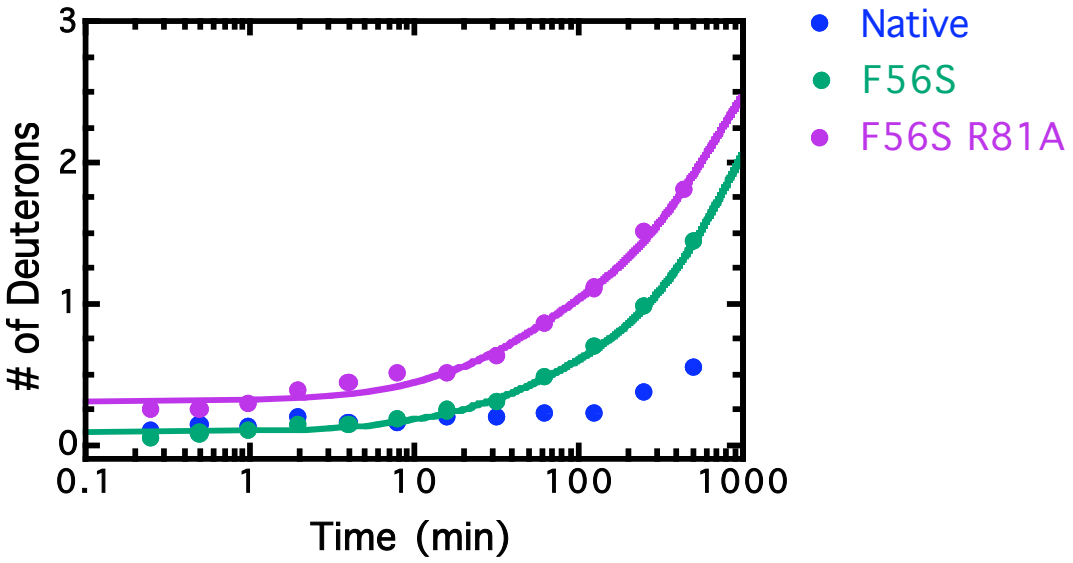

Peptide 5-18 (12)

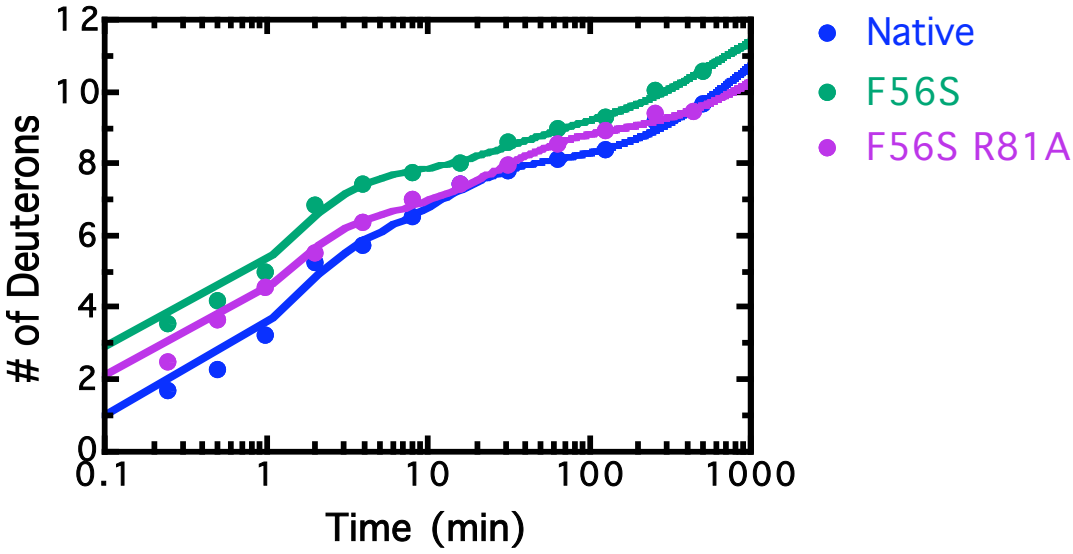

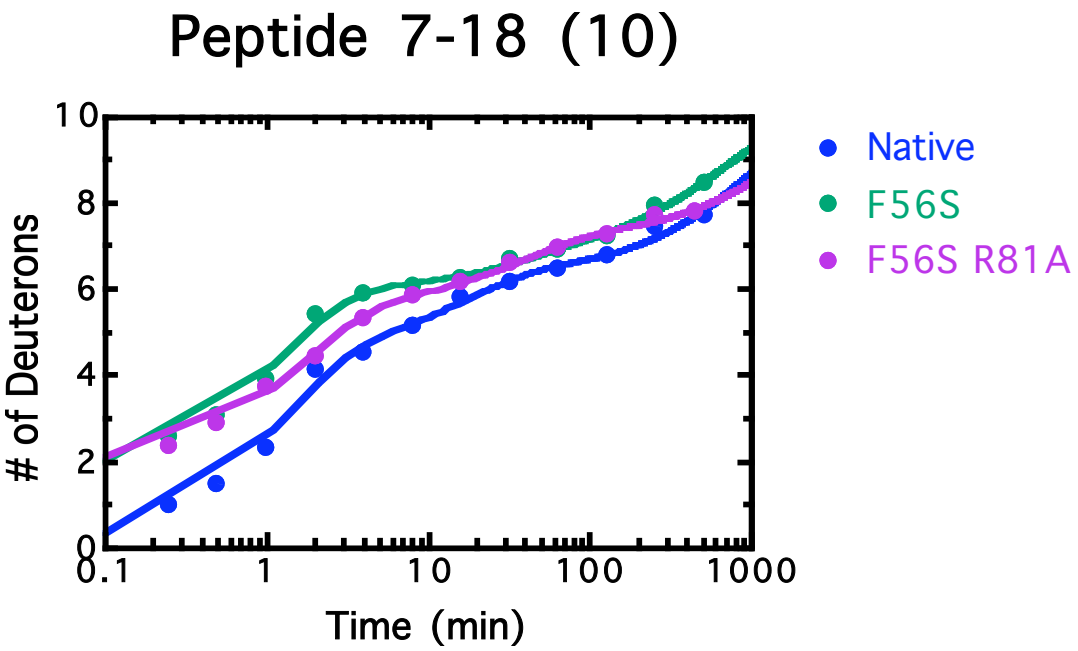
Peptide 7-18 (10)
# of Deuterons
Time (min)
0.1
1
10
100
1000
0
2
4
6
8
10
Native
F56S
F56S R81A

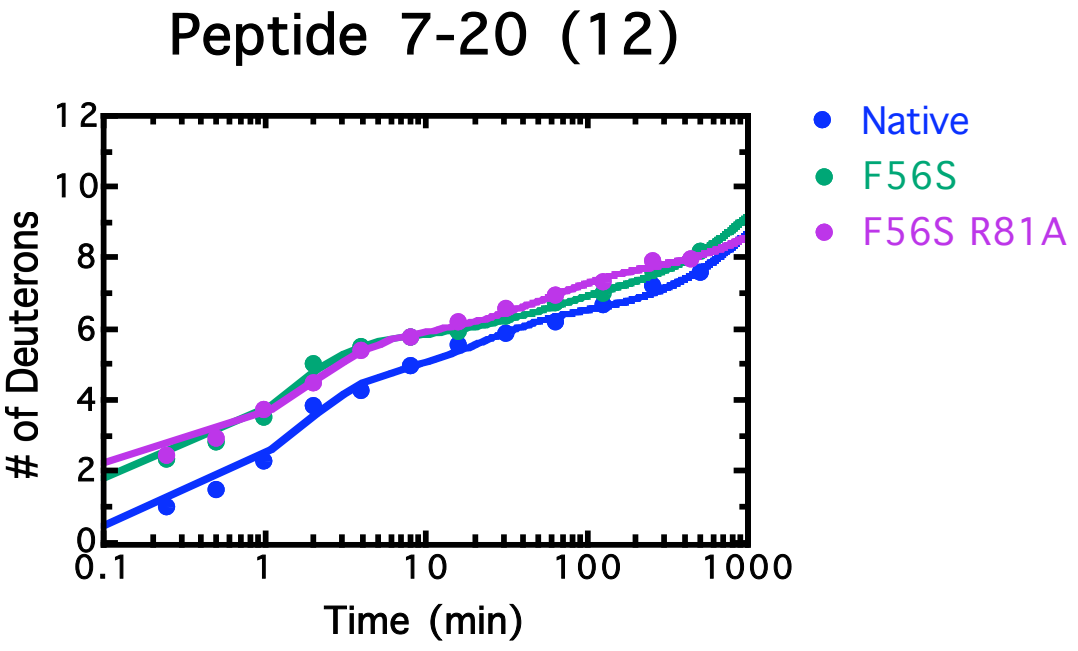
Peptide 7-20 (12)
# of Deuterons
Time (min)
0.1
1
10
100
1000
0
2
4
6
8
10
12
Native
F56S
F56S R81A

Peptide 8-20 (11)

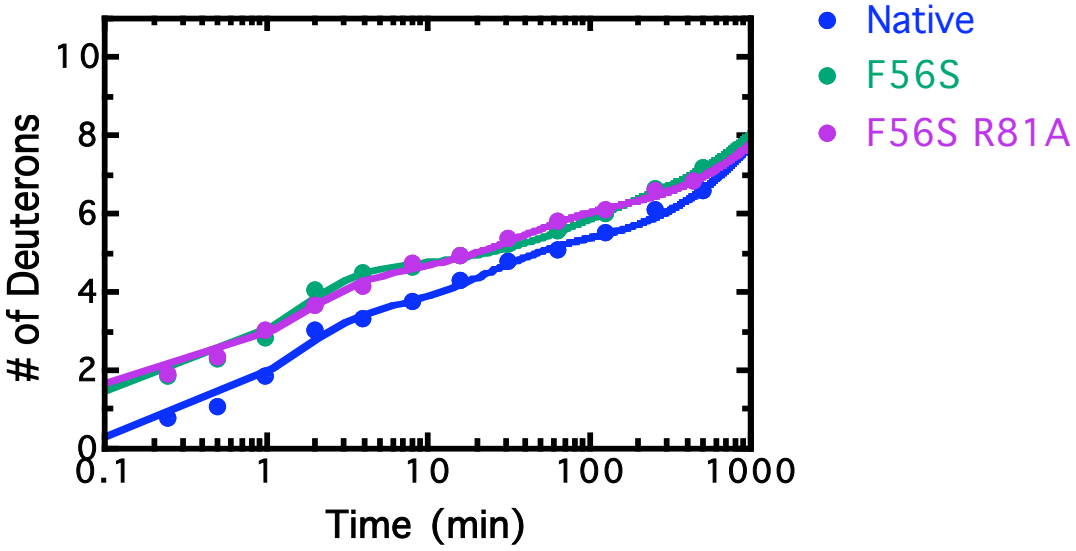

Peptide 19-21 (2)

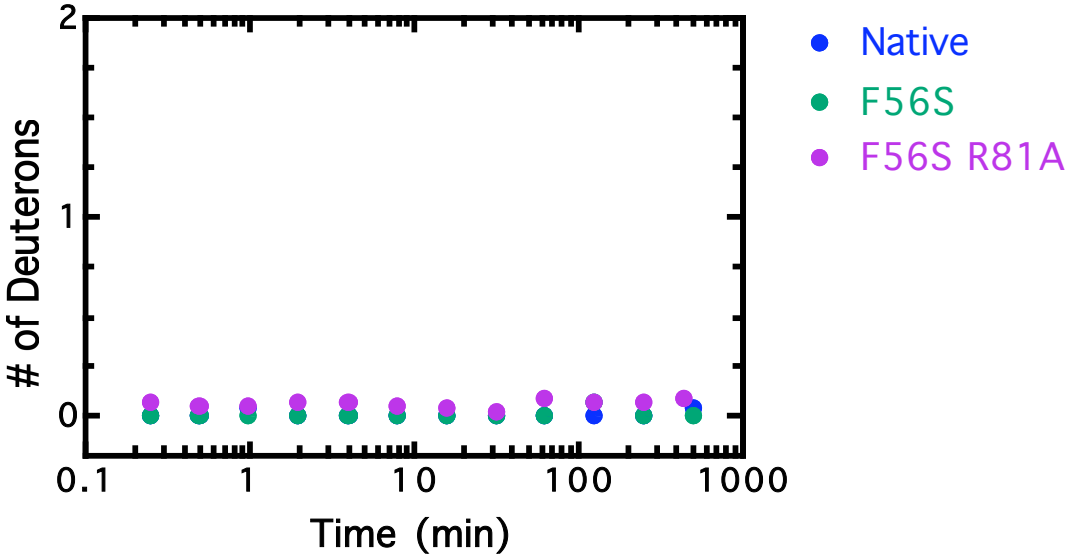

Peptide 20-29 (9)

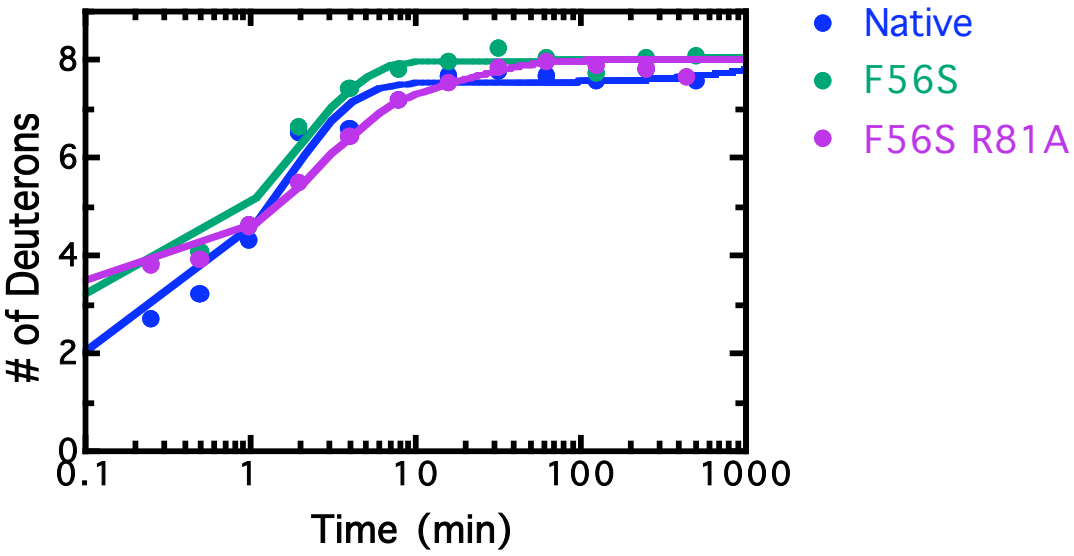

Peptide 22-27 (5)

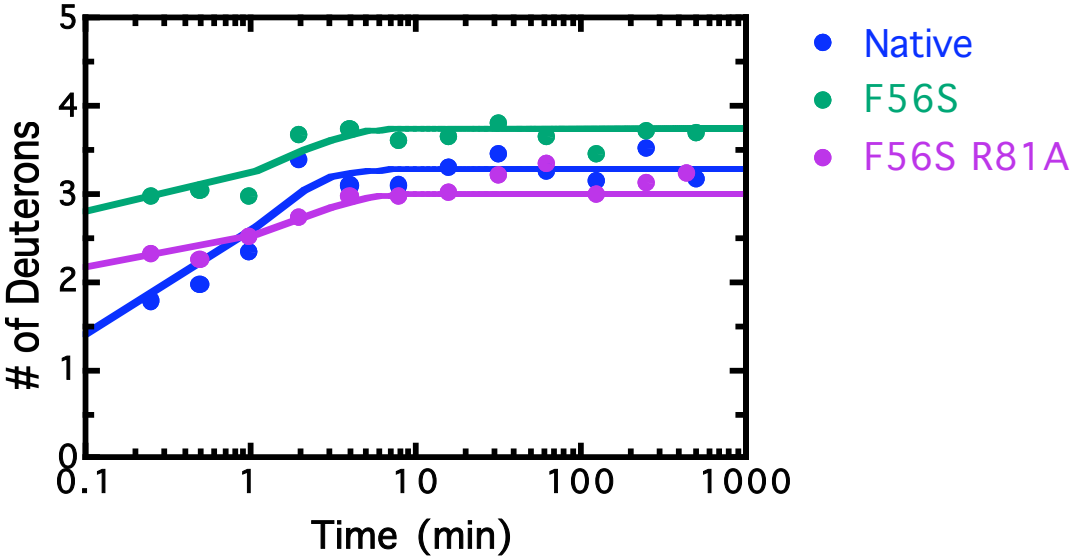

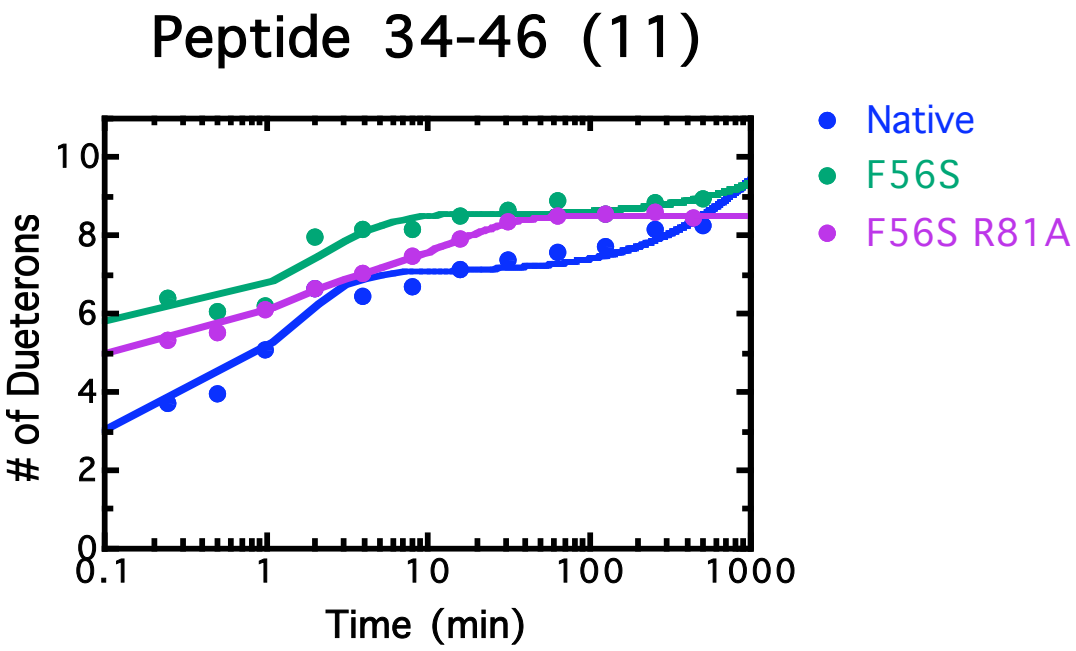
Peptide 34-46 (11)
# of Dueterons
Time (min)
0.1
1
10
100
1000
0
2
4
6
8
10
Native
F56S
F56S R81A

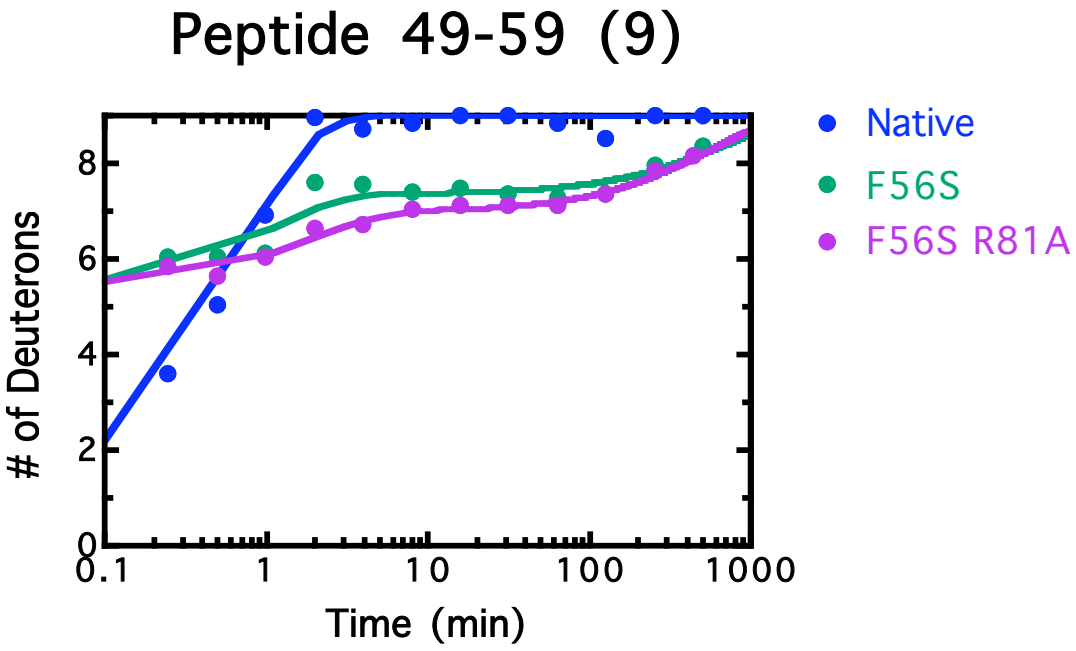
Peptide 49-59 (9)
# of Deuterons
Time (min)
0.1
1
10
100
1000
0
2
4
6
8
Native
F56S
F56S R81A

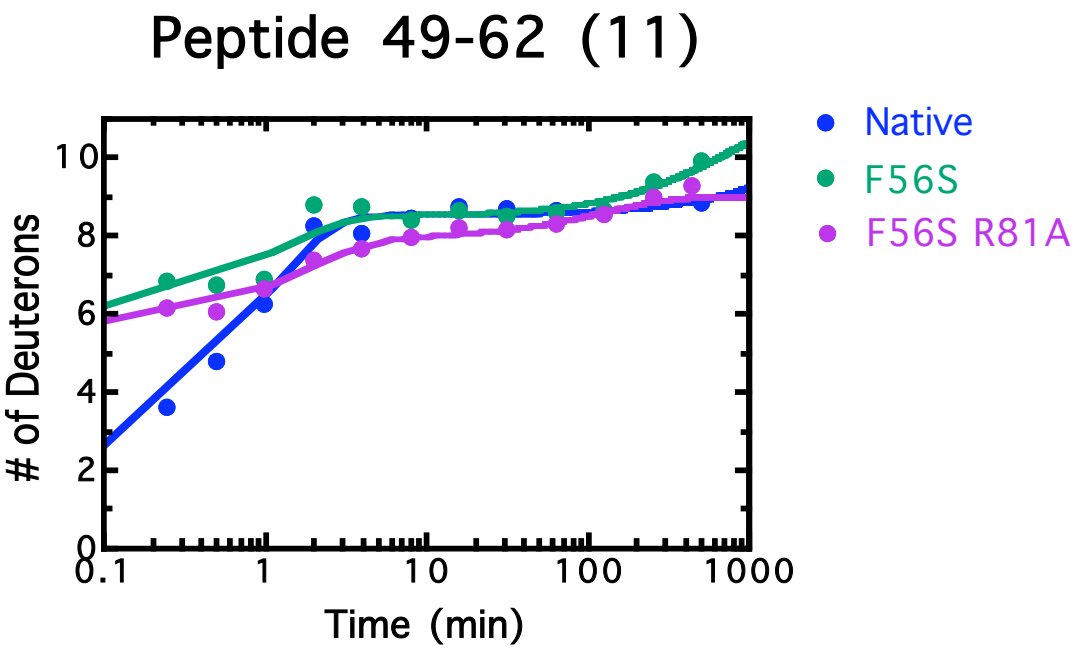
Peptide 49-62 (11)
# of Deuterons
0
2
4
6
8
10
0.1
1
10
100
1000
Time (min)
Native
F56S
F56S R81A

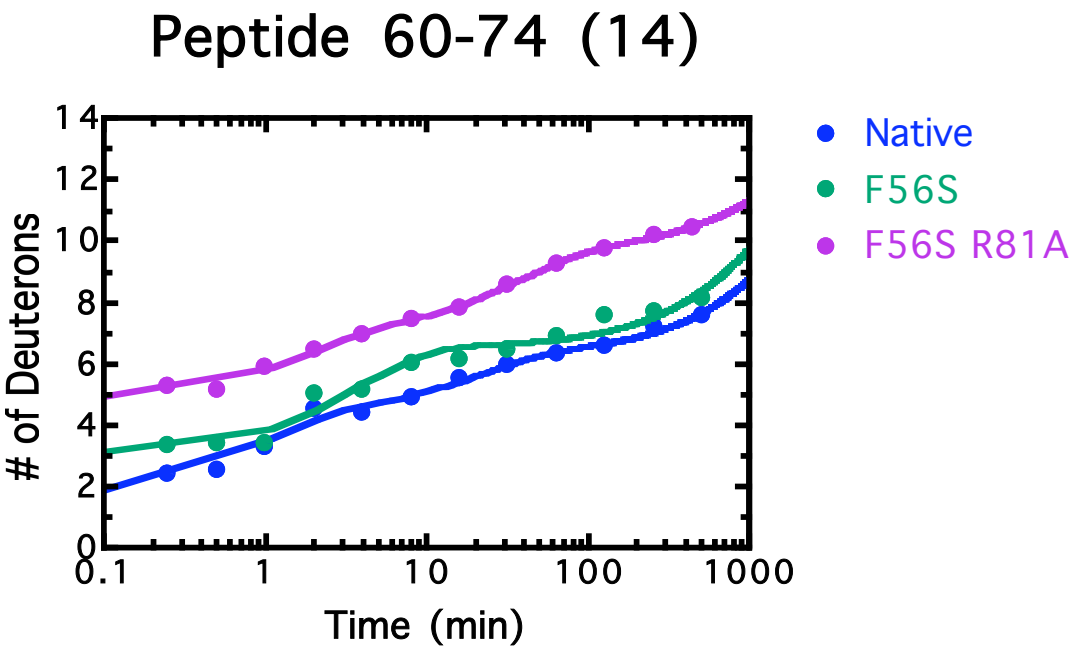
Peptide 60-74 (14)
# of Deuterons
0
2
4
6
8
10
12
14
0.1
1
10
100
1000
Time (min)
Native
F56S
F56S R81A

Peptide 63-74 (11)

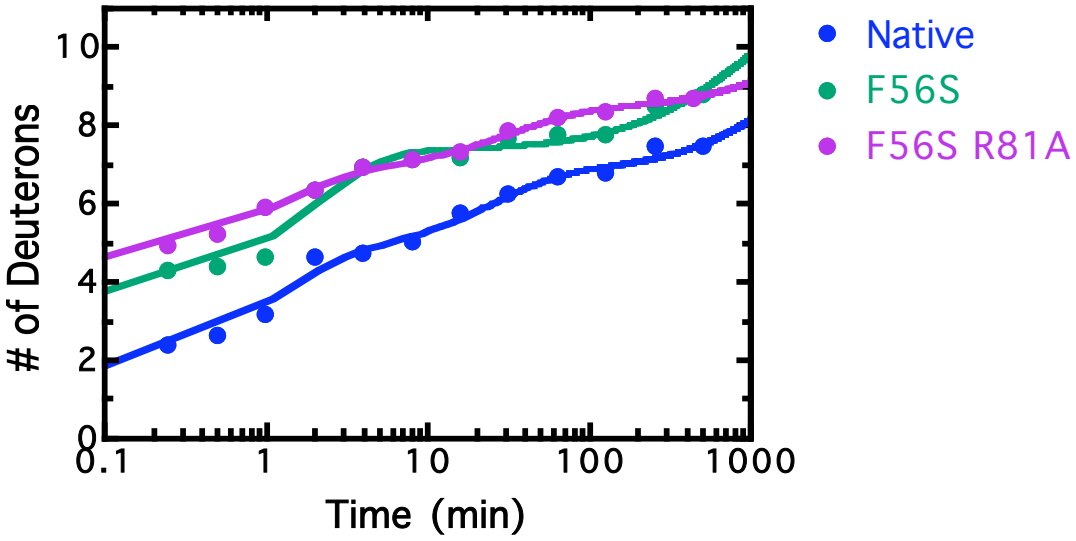

Peptide 75-91 (15)

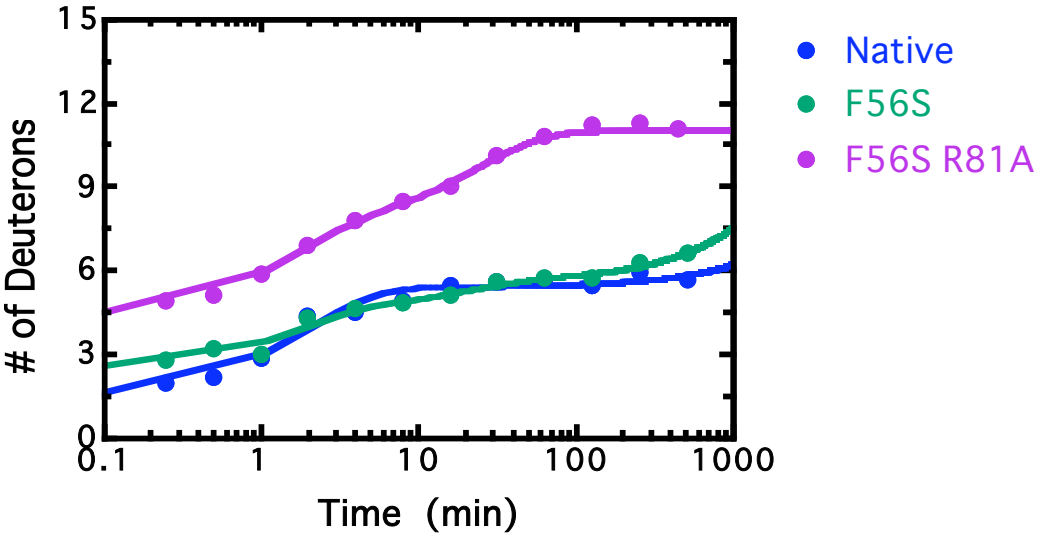

Peptide 89-96 (7)

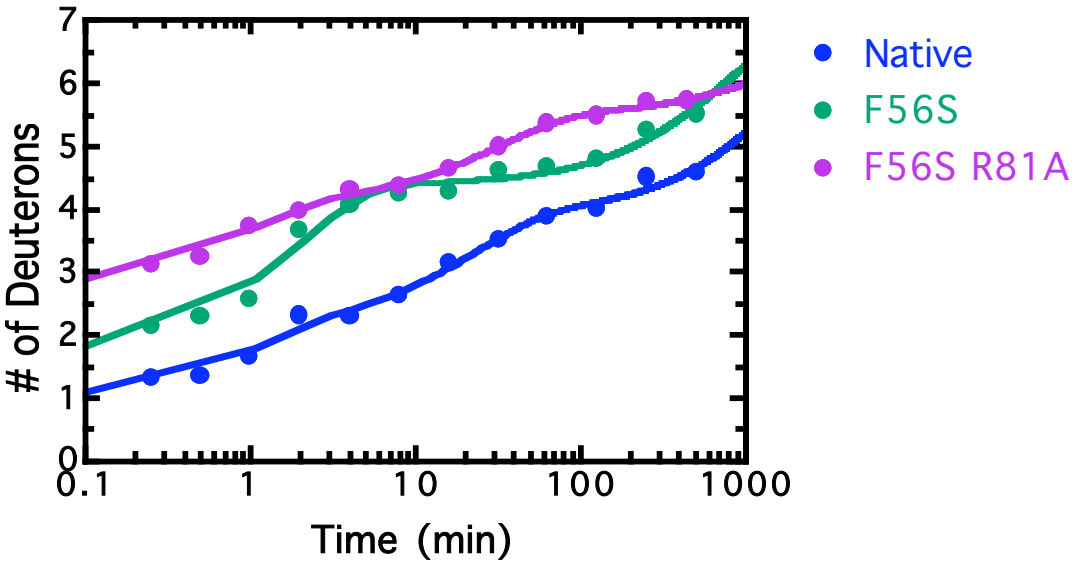

Peptide 92-96 (4)

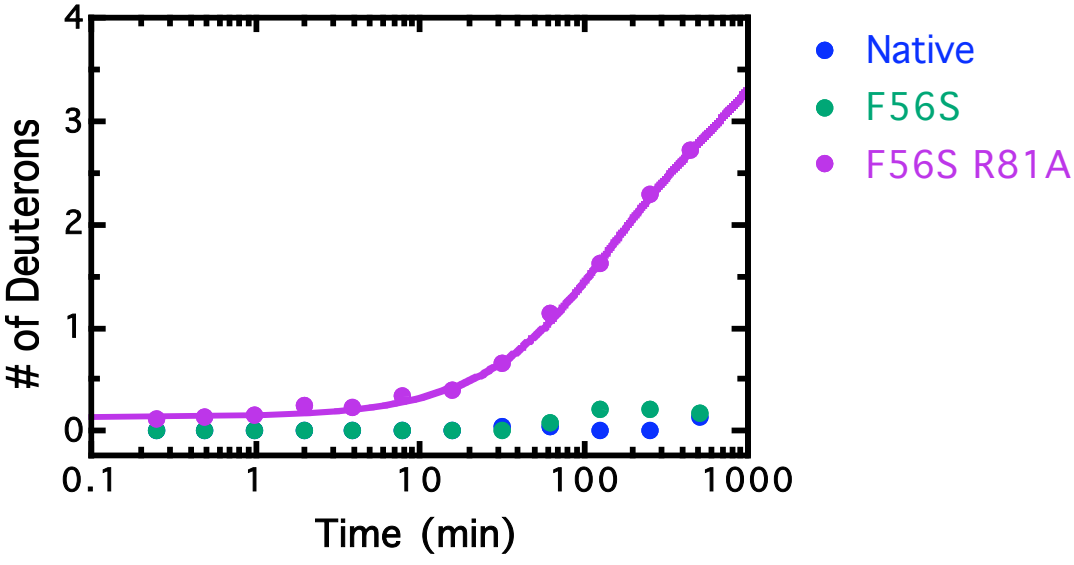

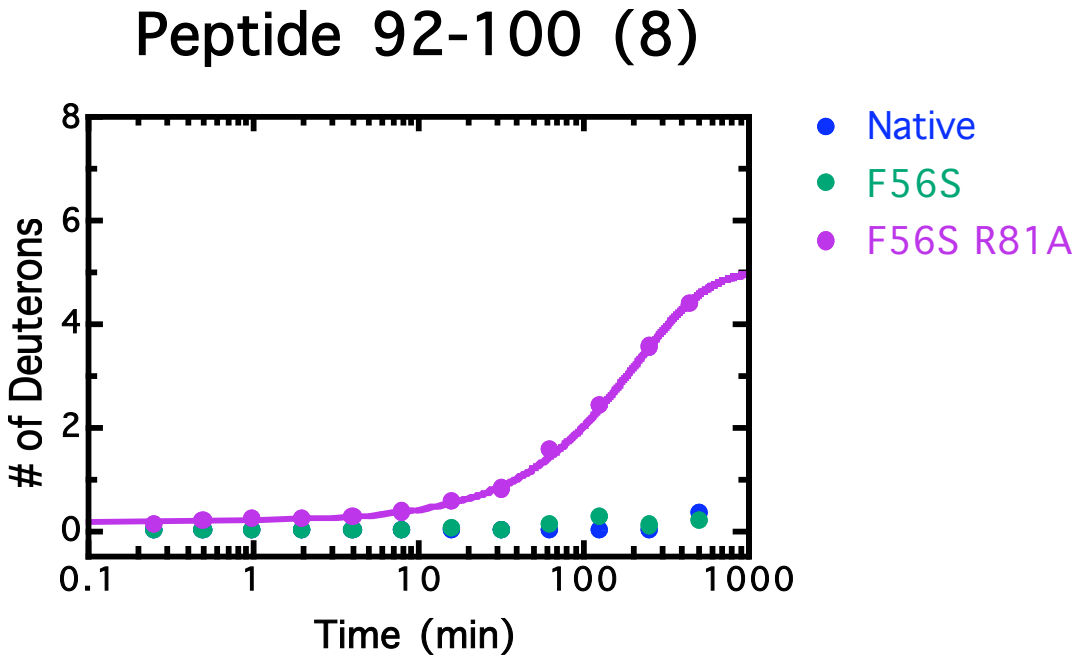
Peptide 92-100 (8)
# of Deuterons
Time (min)
0.1
1
10
100
1000
0
2
4
6
8
Native
F56S
F56S R81A

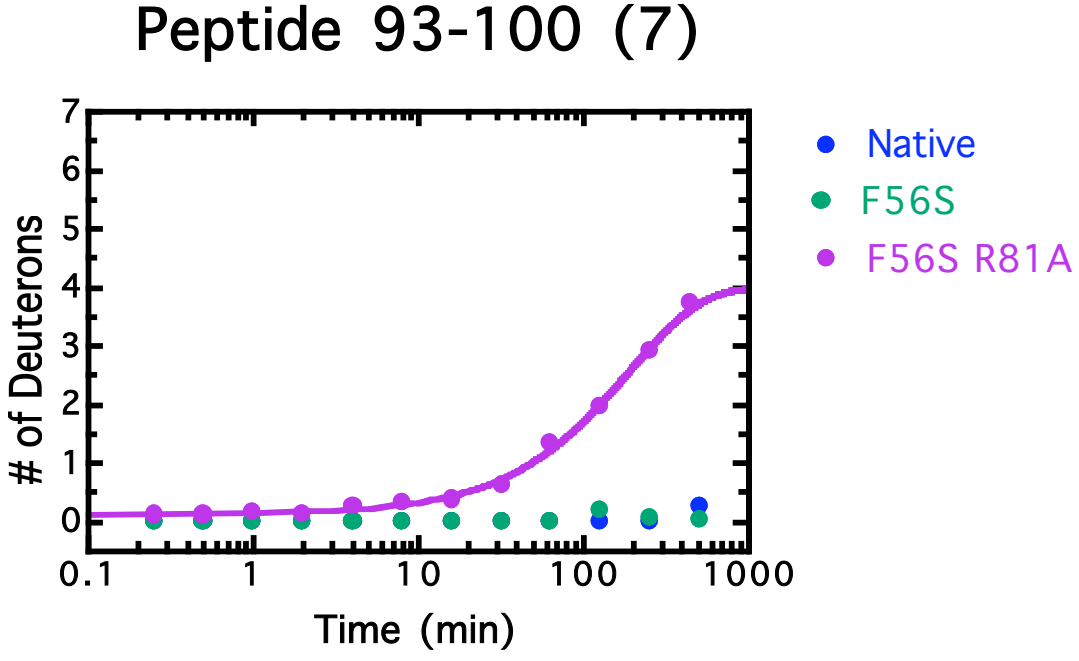
Peptide 93-100 (7)
# of Deuterons
Time (min)
0.1
1
10
100
1000
0
1
2
3
4
5
6
7
Native
F56S
F56S R81A

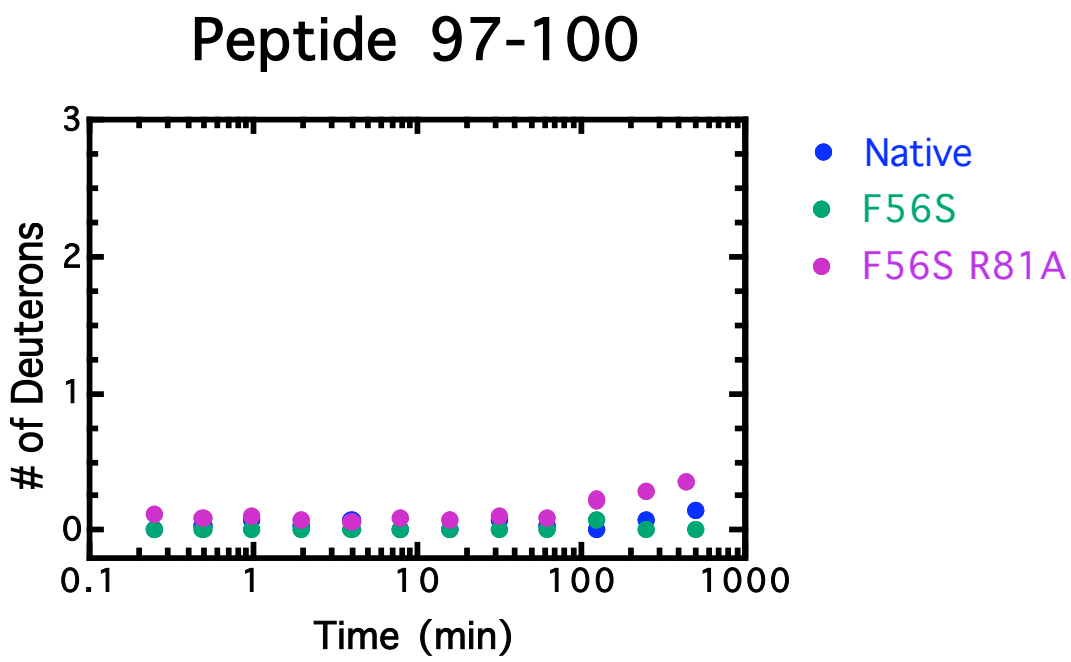
Peptide 97-100
# of Deuterons
Time (min)
Native
F56S
F56S R81A

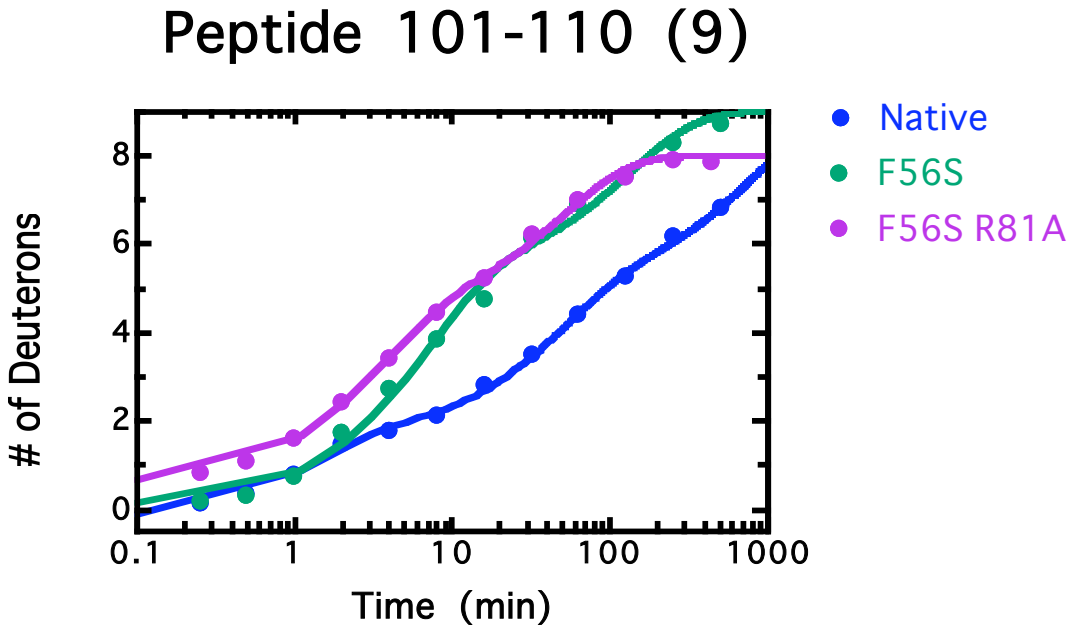
Peptide 101-110 (9)
# of Deuterons
Time (min)
Native
F56S
F56S R81A

Peptide 103-110 (7)

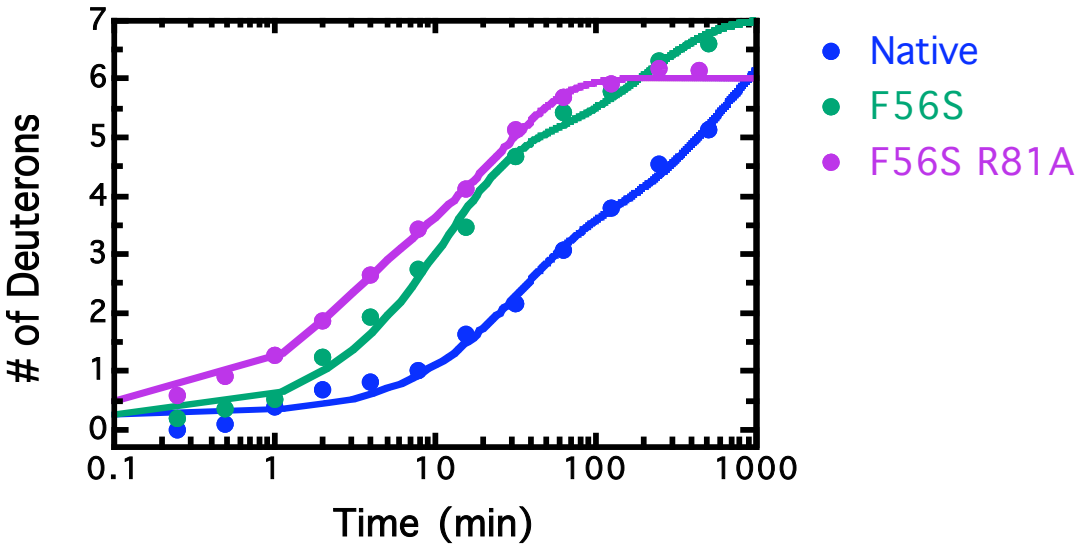

Peptide 110-119 (8)

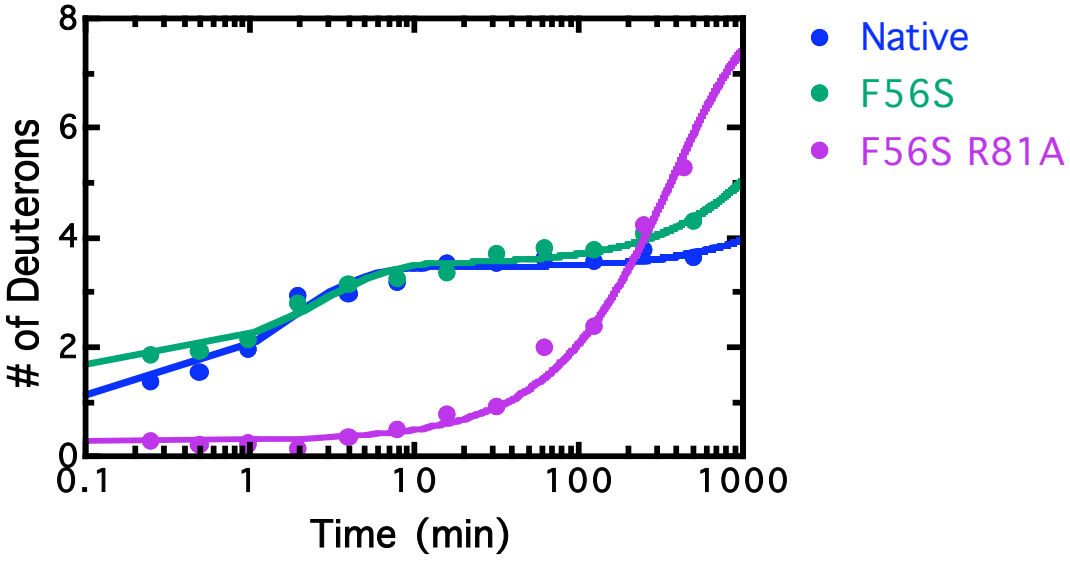

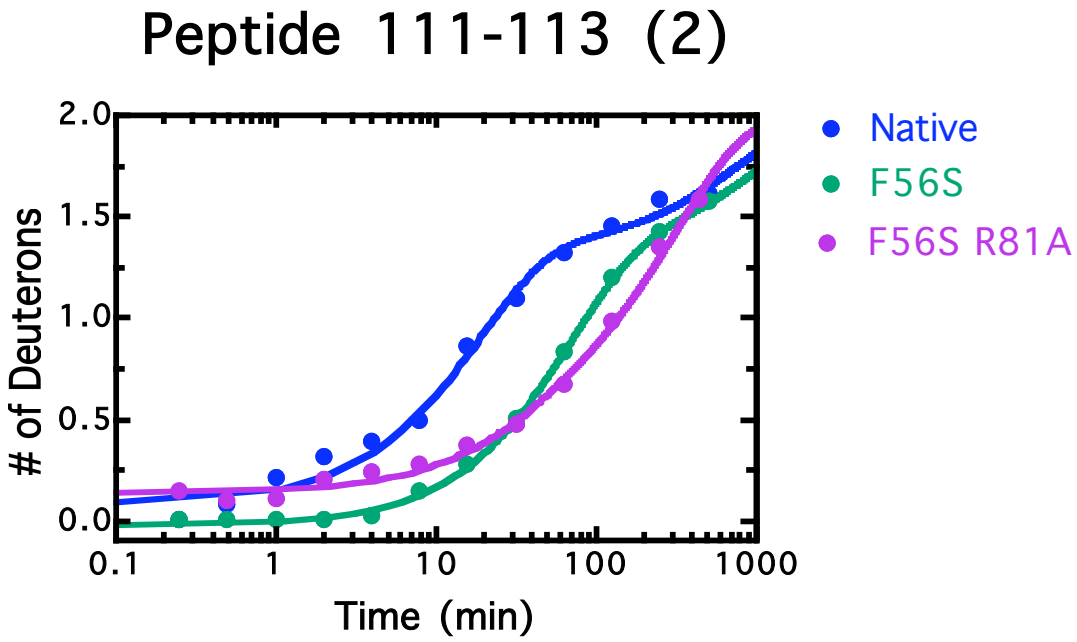
Peptide 111-113 (2)
# of Deuterons
2.0
1.5
1.0
0.5
0.0
0.1
1
10
100
1000
Time (min)
Native
F56S
F56S R81A

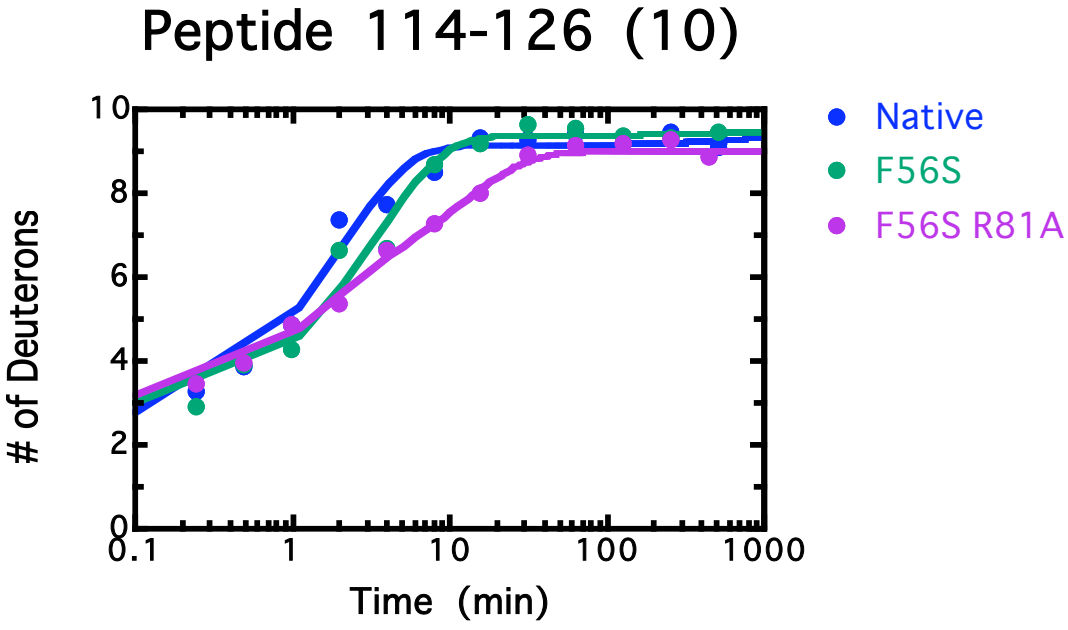
Peptide 114-126 (10)
# of Deuterons
10
8
6
4
2
0
0.1
1
10
100
1000
Time (min)
Native
F56S
F56S R81A

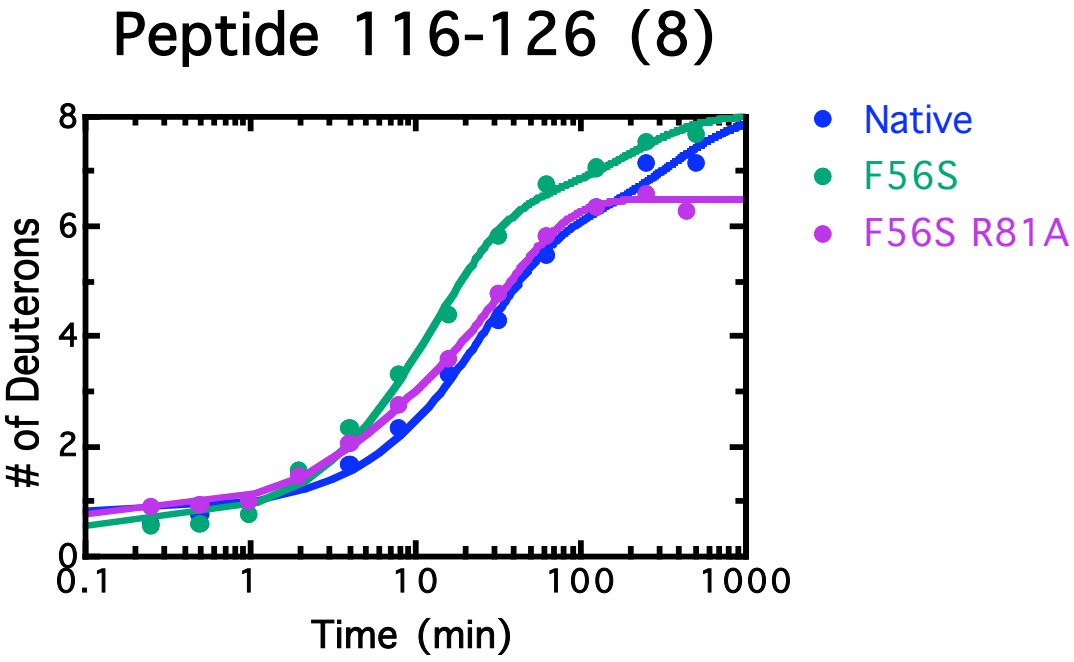
Peptide 116-126 (8)
# of Deuterons
Time (min)
0.1
1
10
100
1000
0
2
4
6
8
Native
F56S
F56S R81A

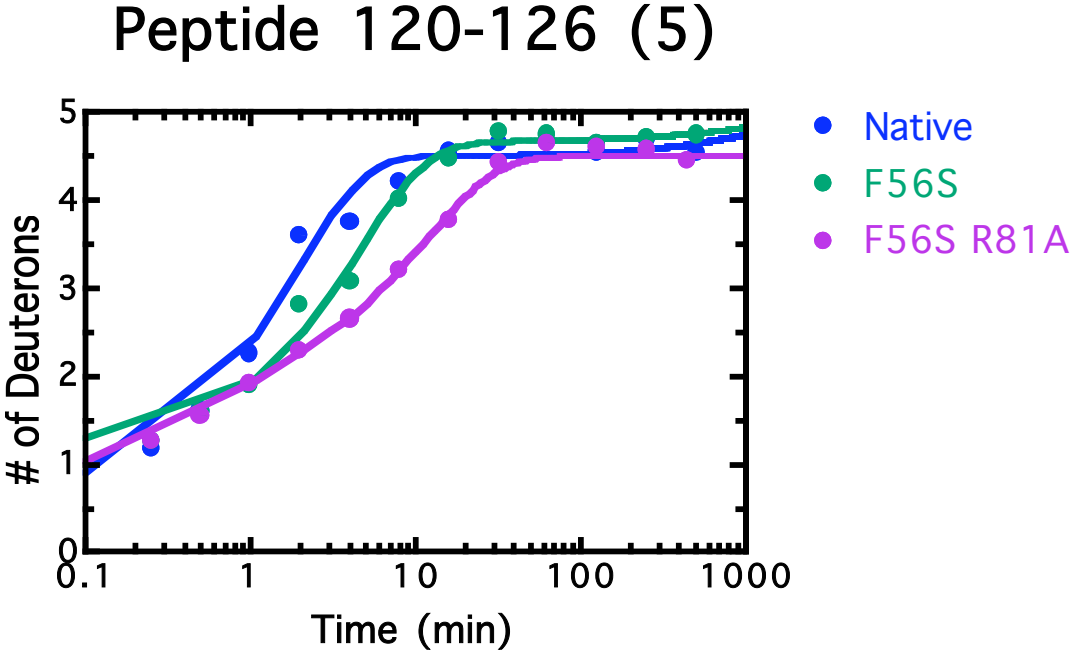
Peptide 120-126 (5)
# of Deuterons
Time (min)
0.1
1
10
100
1000
0
1
2
3
4
5
Native
F56S
F56S R81A

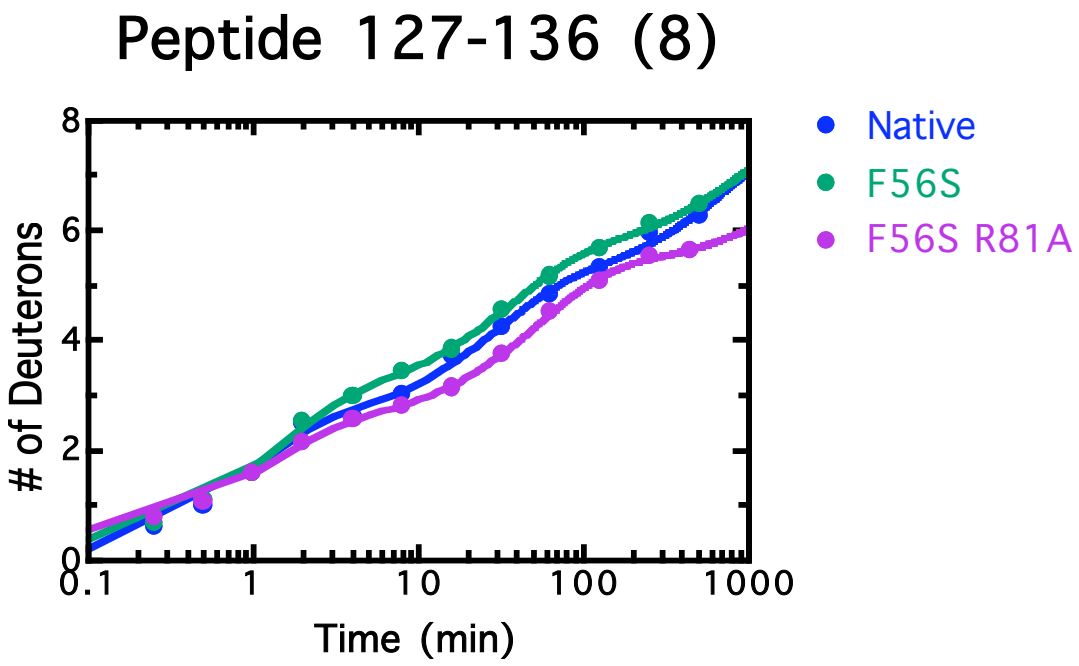
Peptide 127-136 (8)
# of Deuterons
Time (min)
0.1
1
10
100
1000
0
2
4
6
8
Native
F56S
F56S R81A

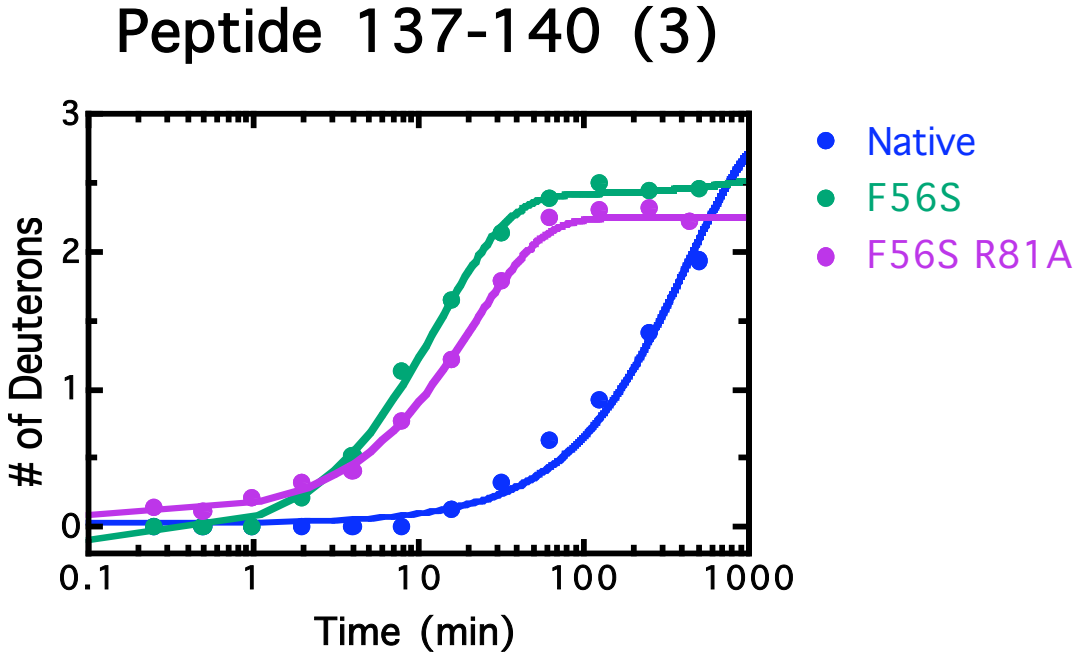
Peptide 137-140 (3)
# of Deuterons
Time (min)
0.1
1
10
100
1000
0
1
2
3
Native
F56S
F56S R81A

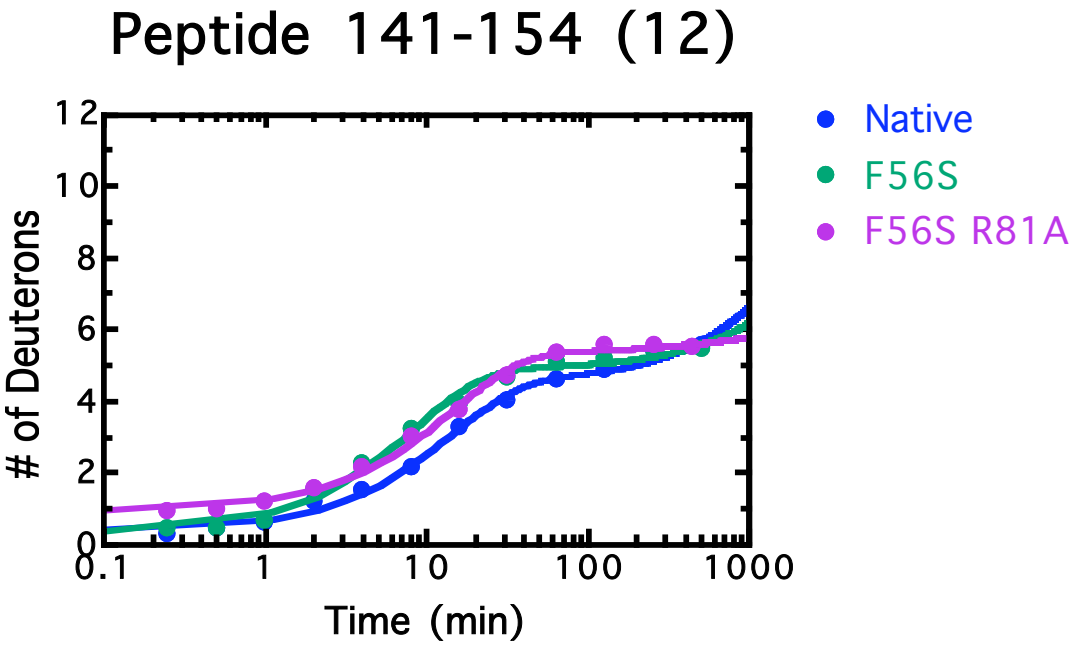
Peptide 141-154 (12)
# of Deuterons
Time (min)
0.1
1
10
100
1000
0
2
4
6
8
10
12
Native
F56S
F56S R81A

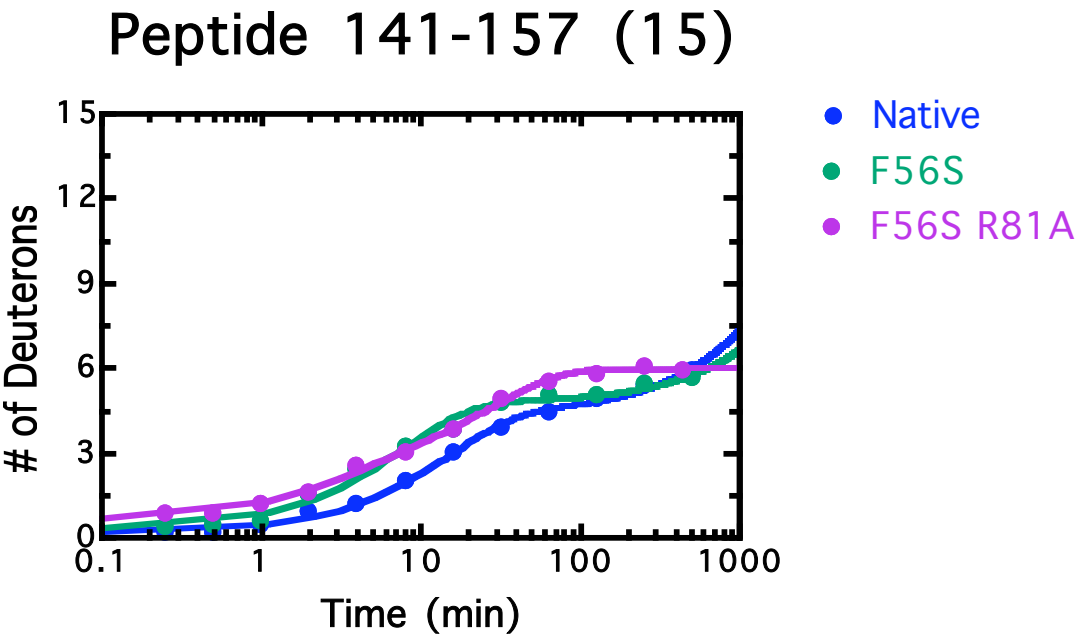
Peptide 141-157 (15)
# of Deuterons
Time (min)
0.1
1
10
100
1000
0
3
6
9
12
15
Native
F56S
F56S R81A

Peptide 158-163 (5)

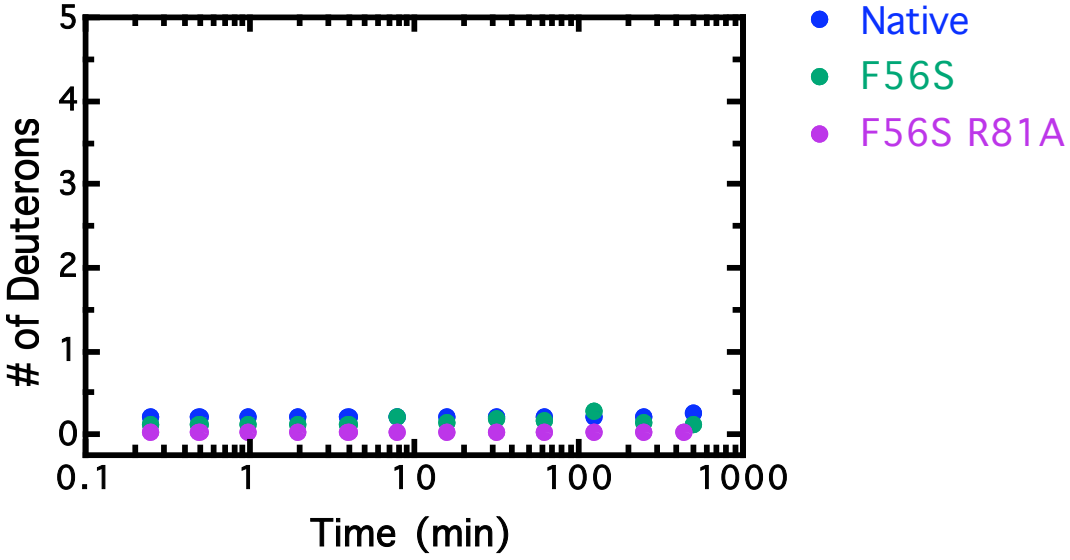

Peptide 164-174 (9)

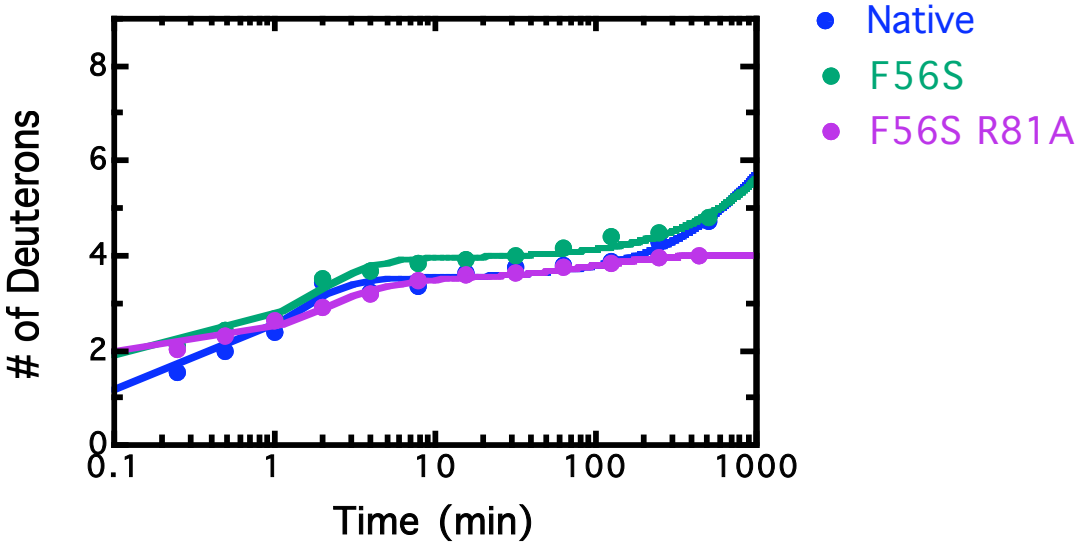

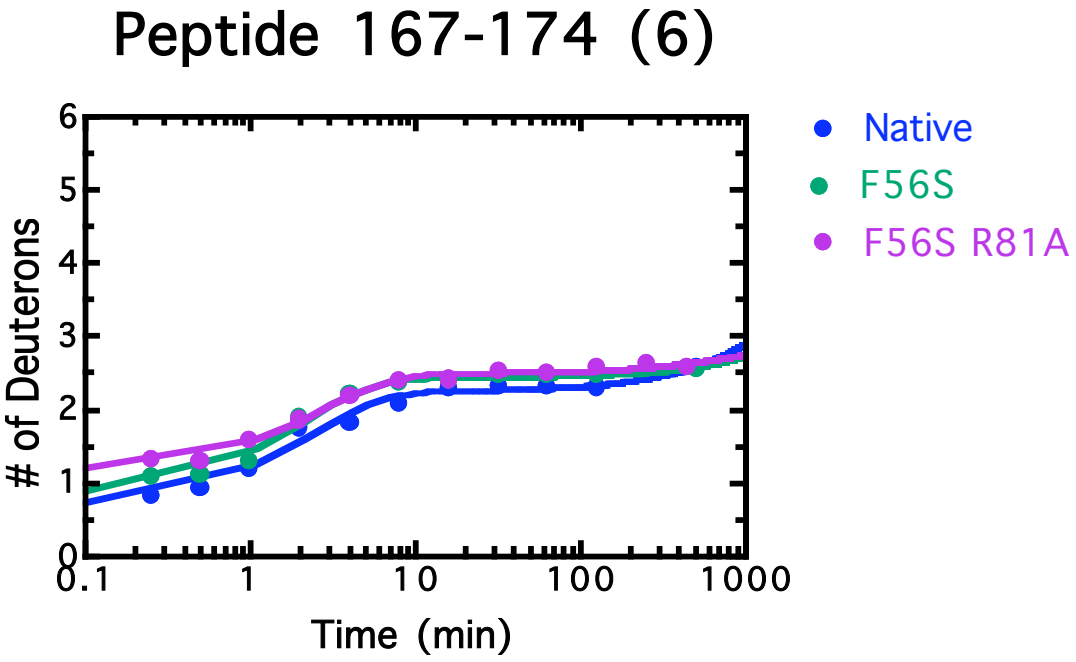
Peptide 167-174 (6)
# of Deuterons
Time (min)
0.1
1
10
100
1000
0
1
2
3
4
5
6
Native
F56S
F56S R81A

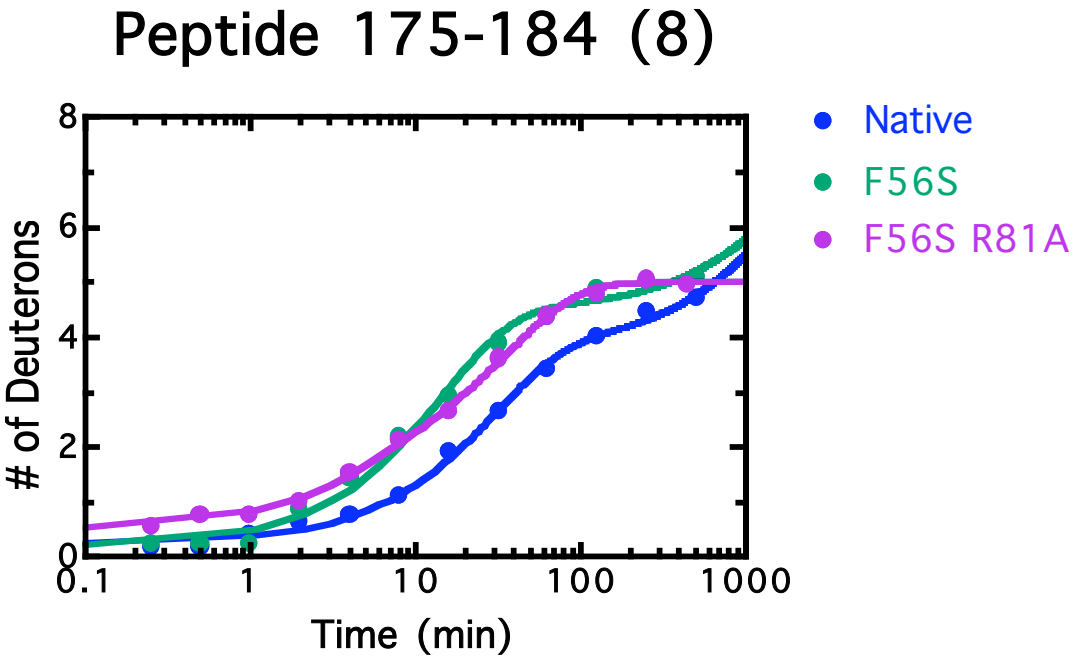
Peptide 175-184 (8)
# of Deuterons
Time (min)
0.1
1
10
100
1000
0
2
4
6
8
Native
F56S
F56S R81A

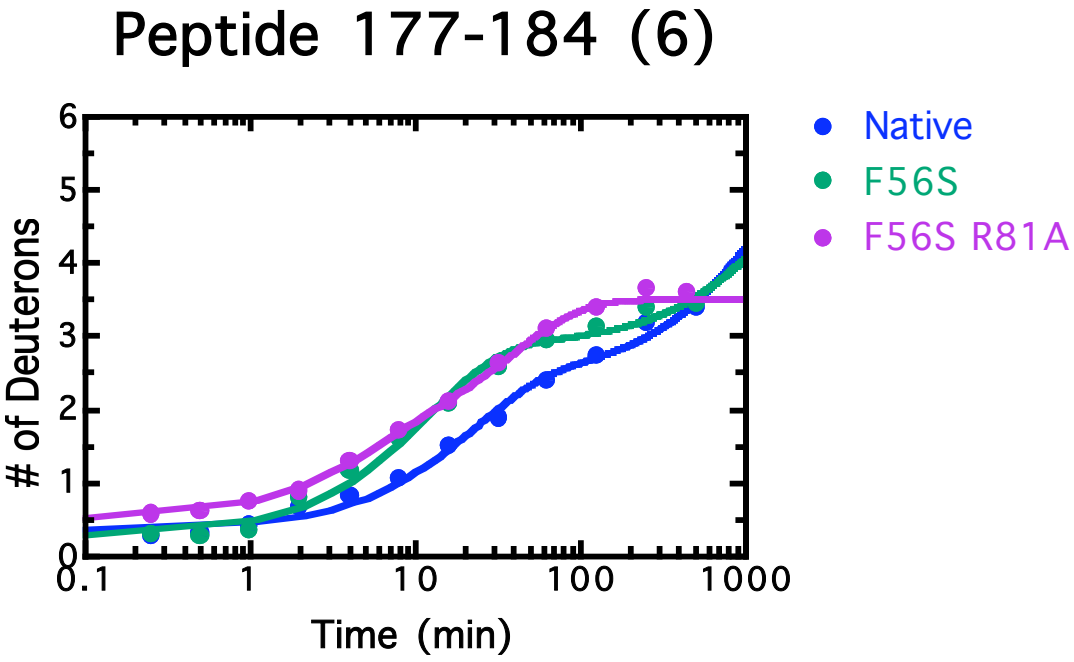
Peptide 177-184 (6)
# of Deuterons
Time (min)
0.1
1
10
100
1000
0
1
2
3
4
5
6
Native
F56S
F56S R81A

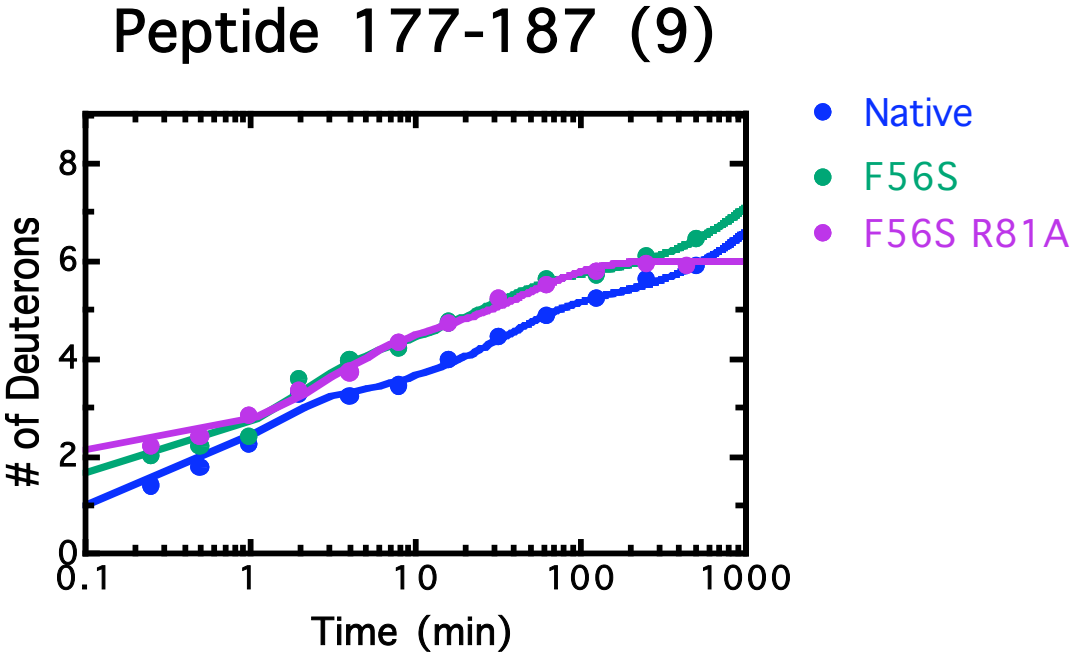
Peptide 177-187 (9)
# of Deuterons
Time (min)
0.1
1
10
100
1000
0
2
4
6
8
Native
F56S
F56S R81A

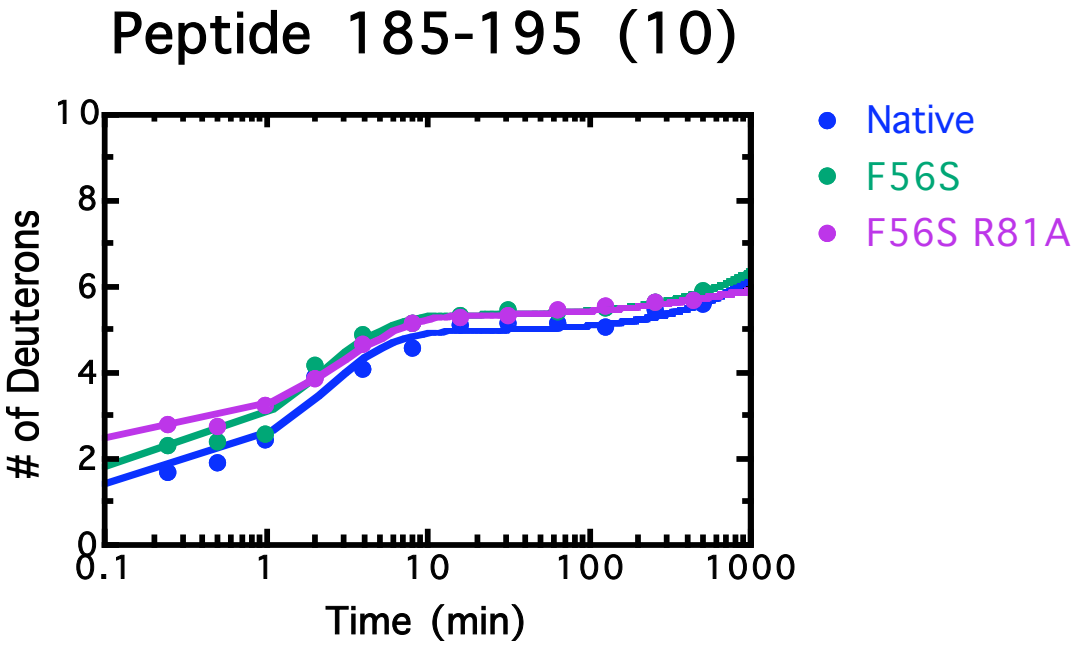
Peptide 185-195 (10)
# of Deuterons
Time (min)
0.1
1
10
100
1000
0
2
4
6
8
10
Native
F56S
F56S R81A

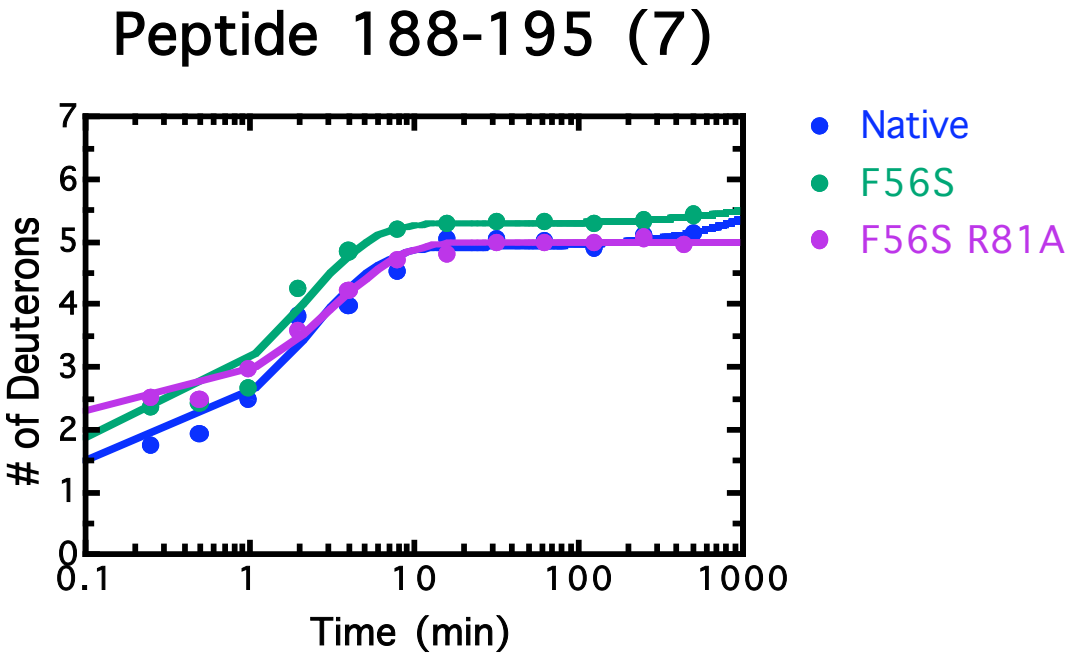
Peptide 188-195 (7)
# of Deuterons
Time (min)
0.1
1
10
100
1000
0
1
2
3
4
5
6
7
Native
F56S
F56S R81A

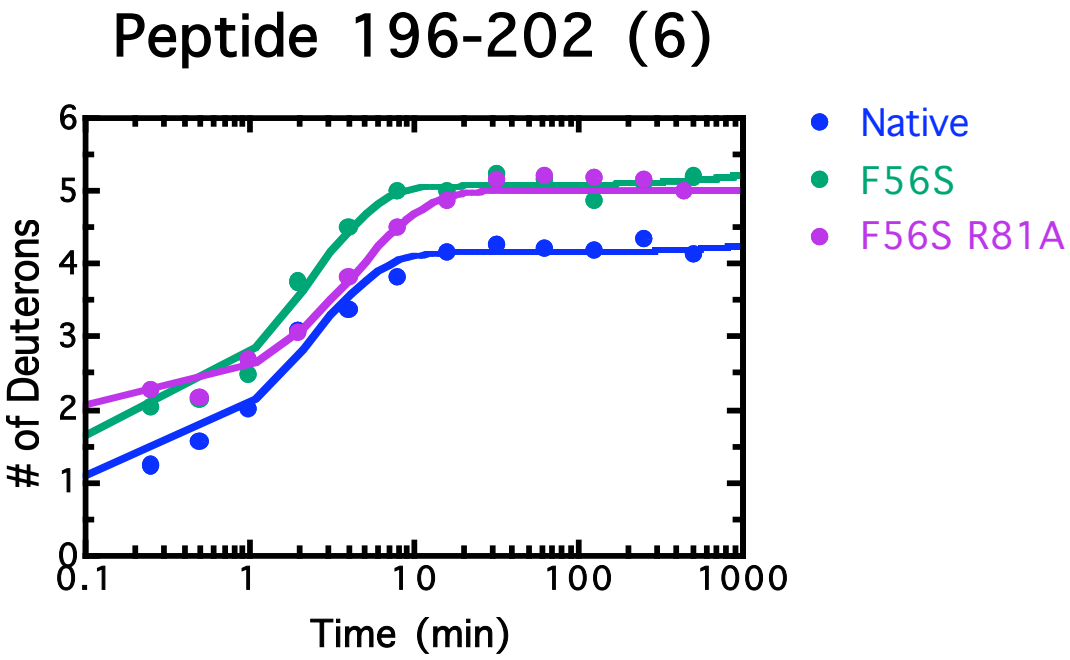
Peptide 196-202 (6)
# of Deuterons
Time (min)
0.1
1
10
100
1000
0
1
2
3
4
5
6
Native
F56S
F56S R81A

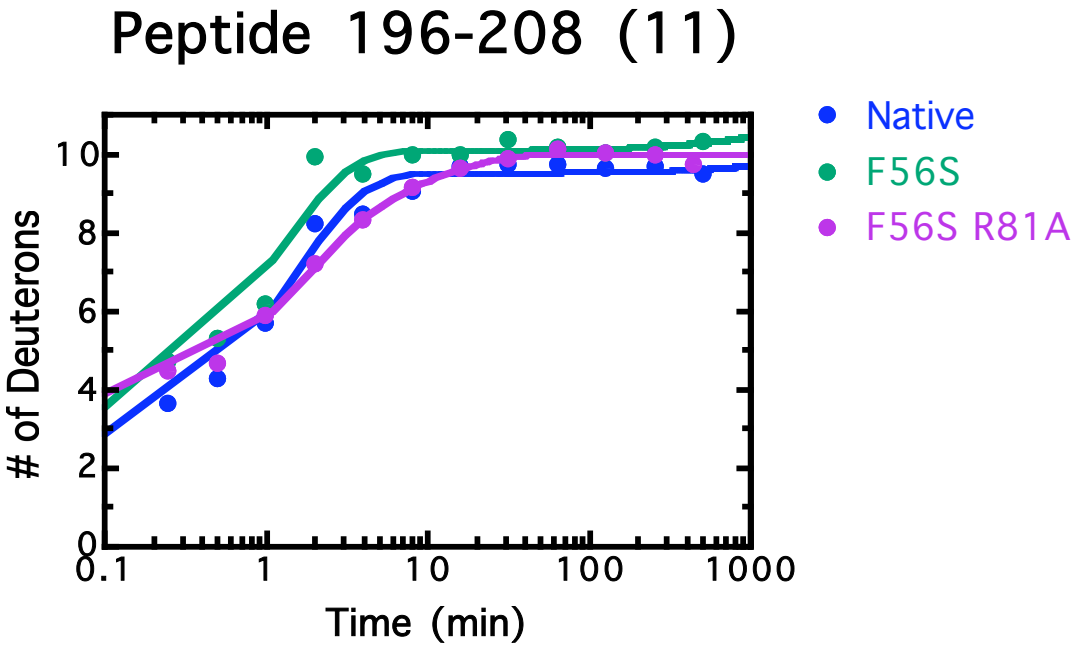
Peptide 196-208 (11)
# of Deuterons
Time (min)
0.1
1
10
100
1000
0
2
4
6
8
10
Native
F56S
F56S R81A

REFERENCES

(1) Klaussen, C. D. (2001) pp 1177, McGraw-Hill.

(2) Meister, A., and Anderson, M. E. (1983) Glutathione. *Annu Rev Biochem 52*, 711-60.

(3) Anderson, M. E. (1998) Glutathione: an overview of biosynthesis and modulation. *Chem Biol Interact 111-112*, 1-14.

(4) Armstrong, R. N. (1997) Structure, catalytic mechanism, and evolution of the glutathione transferases. *Chem Res Toxicol 10*, 2-18.

(5) Fahey, R. C., and Sundquist, A. R. (1991) Evolution of glutathione metabolism. *Adv Enzymol Relat Areas Mol Biol 64*, 1-53.

(6) Arias, I. a. J., WB. (1976) in *Kroc Foundation Series*, Raven Press, New York.

(7) Meister, A. (1973) On the enzymology of amino acid transport. *Science 180*, 33-9.

(8) Dickinson, D. A., and Forman, H. J. (2002) Glutathione in defense and signaling: lessons from a small thiol. *Ann N Y Acad Sci 973*, 488-504.

(9) Graminski, G. F., Kubo, Y., and Armstrong, R. N. (1989) Spectroscopic and kinetic evidence for the thiolate anion of glutathione at the active site of glutathione S-transferase. *Biochemistry 28*, 3562-8.

(10) Liu, S., Zhang, P., Ji, X., Johnson, W. W., Gilliland, G. L., and Armstrong, R. N. (1992) Contribution of tyrosine 6 to the catalytic mechanism of isoenzyme 3-3 of glutathione S-transferase. *J Biol Chem 267*, 4296-9.

(11) Vuilleumier, S. (1997) Bacterial glutathione S-transferases: what are they good for? *J Bacteriol 179*, 1431-41.

(12) Vuilleumier, S., and Pagni, M. (2002) The elusive roles of bacterial glutathione S-transferases: new lessons from genomes. *Appl Microbiol Biotechnol 58*, 138-46.

(13) Oakley, A. J. (2005) Glutathione transferases: new functions. *Curr Opin Struct Biol 15*, 716-23.

(14) Bresell, A., Weinander, R., Lundqvist, G., Raza, H., Shimoji, M., Sun, T. H., Balk, L., Wiklund, R., Eriksson, J., Jansson, C., Persson, B., Jakobsson, P. J., and

Morgenstern, R. (2005) Bioinformatic and enzymatic characterization of the MAPEG superfamily. *Febs J 272*, 1688-703.

(15) Sheehan, D., Meade, G., Foley, V. M., and Dowd, C. A. (2001) Structure, function and evolution of glutathione transferases: implications for classification of non-mammalian members of an ancient enzyme superfamily. *Biochem J 360*, 1-16.

(16) Jakobsson, P. J., Morgenstern, R., Mancini, J., Ford-Hutchinson, A., and Persson, B. (2000) Membrane-associated proteins in eicosanoid and glutathione metabolism (MAPEG). A widespread protein superfamily. *Am J Respir Crit Care Med 161*, S20-4.

(17) Jakobsson, P. J., Morgenstern, R., Mancini, J., Ford-Hutchinson, A., and Persson, B. (1999) Common structural features of MAPEG -- a widespread superfamily of membrane associated proteins with highly divergent functions in eicosanoid and glutathione metabolism. *Protein Sci 8*, 689-92.

(18) Edwards, R., Dixon, D. P., and Walbot, V. (2000) Plant glutathione S-transferases: enzymes with multiple functions in sickness and in health. *Trends Plant Sci 5*, 193-8.

(19) Bakke, J. E. (1990) Biochemical and physiological dispositions of glutathione conjugates. *Drug Metab Rev 22*, 637-47.

(20) Habig, W. H., Pabst, M. J., and Jakoby, W. B. (1974) Glutathione S-transferases. The first enzymatic step in mercapturic acid formation. *J Biol Chem 249*, 7130-9.

(21) Laughlin, L. T., Bernat, B. A., and Armstrong, R. N. (1998) Mechanistic imperative for the evolution of a metalloglutathione transferase of the vicinal oxygen chelate superfamily. *Chem Biol Interact 111-112*, 41-50.

(22) Ladner, J. E., Parsons, J. F., Rife, C. L., Gilliland, G. L., and Armstrong, R. N. (2004) Parallel evolutionary pathways for glutathione transferases: structure and mechanism of the mitochondrial class kappa enzyme rGSTK1-1. *Biochemistry 43*, 352-61.

(23) Pearson, W. R. (2005) Phylogenies of glutathione transferase families. *Methods Enzymol 401*, 186-204.

(24) Dyson, H. J., Gippert, G. P., Case, D. A., Holmgren, A., and Wright, P. E. (1990) Three-dimensional solution structure of the reduced form of Escherichia coli thioredoxin determined by nuclear magnetic resonance spectroscopy. *Biochemistry 29*, 4129-36.

(25) Katti, S. K., LeMaster, D. M., and Eklund, H. (1990) Crystal structure of thioredoxin from Escherichia coli at 1.68 A resolution. *J Mol Biol 212*, 167-84.

(26) Bushweller, J. H., Billeter, M., Holmgren, A., and Wuthrich, K. (1994) The nuclear magnetic resonance solution structure of the mixed disulfide between Escherichia coli glutaredoxin(C14S) and glutathione. *J Mol Biol 235*, 1585-97.

(27) Dirr, H., Reinemer, P., and Huber, R. (1994) X-ray crystal structures of cytosolic glutathione S-transferases. Implications for protein architecture, substrate recognition and catalytic function. *Eur J Biochem 220*, 645-61.

(28) Robinson, A., Huttley, G. A., Booth, H. S., and Board, P. G. (2004) Modelling and bioinformatics studies of the human Kappa-class glutathione transferase predict a novel third glutathione transferase family with similarity to prokaryotic 2-hydroxychromene-2-carboxylate isomerases. *Biochem J 379*, 541-52.

(29) Xia, B., Vlamis-Gardikas, A., Holmgren, A., Wright, P. E., and Dyson, H. J. (2001) Solution structure of Escherichia coli glutaredoxin-2 shows similarity to mammalian glutathione-S-transferases. *J Mol Biol 310*, 907-18.

(30) Bardwell, J. C., McGovern, K., and Beckwith, J. (1991) Identification of a protein required for disulfide bond formation in vivo. *Cell 67*, 581-9.

(31) Martin, J. L., Bardwell, J. C. A., and Kurylan, J. (1993) Crystal structure of the DsbA protein required for disulphide formation in vivo. *Letters to Nature 365*, 464-468.

(32) Fabianek, R. A., Hennecke, H., and Thony-Meyer, L. (2000) Periplasmic protein thiol:disulfide oxidoreductases of Escherichia coli. *FEMS Microbiol Rev 24*, 303-16.

(33) Chivers, P. T., Prehoda, K. E., and Raines, R. T. (1997) The CXXC motif: a rheostat in the active site. *Biochemistry 36*, 4061-6.

(34) Lundstrom, J., Krause, G., and Holmgren, A. (1992) A Pro to His mutation in active site of thioredoxin increases its disulfide-isomerase activity 10-fold. New refolding systems for reduced or randomly oxidized ribonuclease. *J Biol Chem 267*, 9047-52.

(35) Wilkinson, B., and Gilbert, H. F. (2004) Protein disulfide isomerase. *Biochim Biophys Acta 1699*, 35-44.

(36) Li, J., Xia, Z., and Ding, J. (2005) Thioredoxin-like domain of human kappa class glutathione transferase reveals sequence homology and structure similarity to the theta class enzyme. *Protein Sci 14*, 2361-9.

(37) Ji, X., Zhang, P., Armstrong, R. N., and Gilliland, G. L. (1992) The three-dimensional structure of a glutathione S-transferase from the mu gene class. Structural analysis of the binary complex of isoenzyme 3-3 and glutathione at 2.2-A resolution. *Biochemistry 31*, 10169-84.

(38) Thom, R., Cummins, I., Dixon, D. P., Edwards, R., Cole, D. J., and Lapthorn, A. J. (2002) Structure of a tau class glutathione S-transferase from wheat active in herbicide detoxification. *Biochemistry 41*, 7008-20.

(39) Jones, S., and Thornton, J. M. (1995) Protein-protein interactions: a review of protein dimer structures. *Prog Biophys Mol Biol 63*, 31-65.

(40) Sayed, Y., Wallace, L. A., and Dirr, H. W. (2000) The hydrophobic lock-and-key intersubunit motif of glutathione transferase A1-1: implications for catalysis, ligandin function and stability. *FEBS Lett 465*, 169-72.

(41) Stenberg, G., Abdalla, A. M., and Mannervik, B. (2000) Tyrosine 50 at the subunit interface of dimeric human glutathione transferase P1-1 is a structural key residue for modulating protein stability and catalytic function. *Biochem Biophys Res Commun 271*, 59-63.

(42) Hornby, J. A., Codreanu, S. G., Armstrong, R. N., and Dirr, H. W. (2002) Molecular recognition at the dimer interface of a class mu glutathione transferase: role of a hydrophobic interaction motif in dimer stability and protein function. *Biochemistry 41*, 14238-47.

(43) Vargo, M. A., Nguyen, L., and Colman, R. F. (2004) Subunit interface residues of glutathione S-transferase A1-1 that are important in the monomer-dimer equilibrium. *Biochemistry 43*, 3327-35.

(44) Delano, W. L. PYMOL (The PyMOL Molecular Graphics System [http://www.pymol.org]).

(45) Harris, J. M., Meyer, D. J., Coles, B., and Ketterer, B. (1991) A novel glutathione transferase (13-13) isolated from the matrix of rat liver mitochondria having structural similarity to class theta enzymes. *Biochem J 278 (Pt 1)*, 137-41.

(46) Pemble, S. E., Wardle, A. F., and Taylor, J. B. (1996) Glutathione S-transferase class Kappa: characterization by the cloning of rat mitochondrial GST and identification of a human homologue. *Biochem J 319 (Pt 3)*, 749-54.

(47) Jowsey, I. R., Thomson, R. E., Orton, T. C., Elcombe, C. R., and Hayes, J. D. (2003) Biochemical and genetic characterization of a murine class Kappa glutathione S-transferase. *Biochem J 373*, 559-69.

(48) Thomson, R. E., Bigley, A. L., Foster, J. R., Jowsey, I. R., Elcombe, C. R., Orton, T. C., and Hayes, J. D. (2004) Tissue-specific expression and subcellular distribution of murine glutathione S-transferase class kappa. *J Histochem Cytochem 52*, 653-62.

(49) Morel, F., Rauch, C., Petit, E., Piton, A., Theret, N., Coles, B., and Guillouzo, A. (2004) Gene and protein characterization of the human glutathione S-transferase kappa and evidence for a peroxisomal localization. *J Biol Chem 279*, 16246-53.

(50) Hayes, J. D., Flanagan, J. U., and Jowsey, I. R. (2005) Glutathione transferases. *Annu Rev Pharmacol Toxicol 45*, 51-88.

(51) Accelrys.

(52) Eaton, R. W., and Chapman, P. J. (1992) Bacterial metabolism of naphthalene: construction and use of recombinant bacteria to study ring cleavage of 1,2-dihydroxynaphthalene and subsequent reactions. *J Bacteriol 174*, 7542-54.

(53) Ohmoto, T., Kinoshita, T., Moriyoshi, K., Sakai, K., Hamada, N., and Ohe, T. (1998) Purification and some properties of 2-hydroxychromene-2-carboxylate isomerase from naphthalenesulfonate-assimilating Pseudomonas sp. TA-2. *J Biochem (Tokyo) 124*, 591-7.

(54) Kuhm, A. E., Knackmuss, H. J., and Stolz, A. (1993) 2-Hydroxychromene-2-carboxylate Isomerase from Bacteria that Degrade Naphthalenesulfonates. *Biodegradation 4*, 155-162.

(55) Fernley, H. N., and Evans, W. C. (1958) Oxidative metabolism of polycyclic hydrocarbons by soil Pseudomonads. *Nature 182*, 373-5.

(56) Davies, J. I., and Evans, W. C. (1964) Oxidative metabolism of naphthalene by soil pseudomonads. The ring-fission mechanism. *Biochem J 91*, 251-61.

(57) Barnsley, E. A. (1976) Naphthalene metabolism by pseudomonads: the oxidation of 1,2-dihydroxynaphthalene to 2-hydroxychromene-2-carboxylic acid and the formation of 2'-hydroxybenzalpyruvate. *Biochem Biophys Res Commun 72*, 1116-21.

(58) Shamsuzzaman, K. M., and Barnsley, E. A. (1974) The regulation of naphthalene metabolism in pseudomonads. *Biochem Biophys Res Commun 60*, 582-9.

(59) Patel, T. R., and Barnsley, E. A. (1980) Naphthalene metabolism by pseudomonads: purification and properties of 1,2-dihydroxynaphthalene oxygenase. *J Bacteriol 143*, 668-73.

(60) Yen, K. M., and Gunsalus, I. C. (1982) Plasmid gene organization: naphthalene/salicylate oxidation. *Proc Natl Acad Sci U S A 79*, 874-8.

(61) Connors, M. A., and Barnsley, E. A. (1982) Naphthalene plasmids in pseudomonads. *J Bacteriol 149*, 1096-101.

(62) Yen, K. M., and Serdar, C. M. (1988) Genetics of naphthalene catabolism in pseudomonads. *Crit Rev Microbiol 15*, 247-68.

(63) Eaton, R. W. (1994) Organization and evolution of naphthalene catabolic pathways: sequence of the DNA encoding 2-hydroxychromene-2-carboxylate isomerase and trans-o-hydroxybenzylidenepyruvate hydratase-aldolase from the NAH7 plasmid. *J Bacteriol 176*, 7757-62.

(64) Smith, D. L., Deng, Y., and Zhang, Z. (1997) Probing the non-covalent structure of proteins by amide hydrogen exchange and mass spectrometry. *J Mass Spectrom 32*, 135-46.

(65) Busenlehner, L. S., and Armstrong, R. N. (2005) Insights into enzyme structure and dynamics elucidated by amide H/D exchange mass spectrometry. *Arch Biochem Biophys 433*, 34-46.

(66) Zhang, Z., and Smith, D. L. (1993) Determination of amide hydrogen exchange by mass spectrometry: a new tool for protein structure elucidation. *Protein Sci 2*, 522-31.

(67) Bai, Y., Milne, J. S., Mayne, L., and Englander, S. W. (1993) Primary structure effects on peptide group hydrogen exchange. *Proteins 17*, 75-86.

(68) Eriksson, M. A., Hard, T., and Nilsson, L. (1995) On the pH dependence of amide proton exchange rates in proteins. *Biophys J 69*, 329-39.

(69) Ehring, H. (1999) Hydrogen exchange/electrospray ionization mass spectrometry studies of structural features of proteins and protein/protein interactions. *Anal Biochem 267*, 252-9.

(70) Hoofnagle, A. N., Resing, K. A., and Ahn, N. G. (2003) Protein Analysis by Hydrogen Exchange Mass Spectrometry. *Annu Rev Biophys Biomol Struct*.

(71) Hvidt, A., and Linderstrom-Lang, K. (1954) Exchange of hydrogen atoms in insulin with deuterium atoms in aqueous solutions. *Biochim Biophys Acta 14*, 574-5.

(72) Busenlehner, L. S., Codreanu, S. G., Holm, P. J., Bhakat, P., Hebert, H., Morgenstern, R., and Armstrong, R. N. (2004) Stress sensor triggers

conformational response of the integral membrane protein microsomal glutathione transferase 1. *Biochemistry 43*, 11145-52.

(73) Codreanu, S. G., Ladner, J. E., Xiao, G., Stourman, N. V., Hachey, D. L., Gilliland, G. L., and Armstrong, R. N. (2002) Local protein dynamics and catalysis: detection of segmental motion associated with rate-limiting product release by a glutathione transferase. *Biochemistry 41*, 15161-72.

(74) Zhang, Z., Post, C. B., and Smith, D. L. (1996) Amide hydrogen exchange determined by mass spectrometry: application to rabbit muscle aldolase. *Biochemistry 35*, 779-91.

(75) Ellman, G. L. (1959) Tissue sulfhydryl groups. *Arch Biochem Biophys 82*, 70-7.

(76) Edelhoch, H. (1967) Spectroscopic determination of tryptophan and tyrosine in proteins. *Biochemistry 6*, 1948-54.

(77) Zhang, Z., and Marshall, A. G. (1998) A universal algorithm for fast and automated charge state deconvolution of electrospray mass-to-charge ratio spectra. *J Am Soc Mass Spectrom 9*, 225-33.

(78) Wyatt, J. P. (1993) Light scattering and the absolute characterization of macromolecules. *Analytica Chimica Acta 272*, 1-40.

(79) Habig, W. H., and Jakoby, W. B. (1981) Assays for Differentiation of Glutathione-S-transferases. *Method Enzymol 77*, 398-405.

(80) Reimer, M., and Howard, M. (1928) Addition Reactions of Unsaturated Alpha-Ketonic Acids. *JACS 50*, 2506-2512.

(81) Kabbe, H. J. (1978) Eine einfache Synthese von 4-Chromanonen. *Synthesis*, 886-887.

(82) Kabbe, H. J., and Widdig, A. (1982) Synthesis and Reactions of 4-Chromanones. *Angewante Chemie (International ed. in English) 21*, 247-256.

(83) Wang, J., Araki, T., Ogawa, T., Matsuoka, M., and Fukuda, H. (1999) A method of graphically analyzing substrate-inhibition kinetics. *Biotechnol Bioeng 62*, 402-411.

(84) Otwinowski, Z., and Minor, W. (1997) Processing of X-ray Diffraction Data Collected in Oscillation Mode. *Method Enzymol 276*, 307-326.

(85) Resing, K. A., Hoofnagle, A. N., and Ahn, N. G. (1999) Modeling deuterium exchange behavior of ERK2 using pepsin mapping to probe secondary structure. *J Am Soc Mass Spectrom 10*, 685-702.

(86) Hornby, J. A., Luo, J. K., Stevens, J. M., Wallace, L. A., Kaplan, W., Armstrong, R. N., and Dirr, H. W. (2000) Equilibrium folding of dimeric class mu glutathione transferases involves a stable monomeric intermediate. *Biochemistry 39*, 12336-44.

(87) Parsons, J. F., Xiao, G., Gilliland, G. L., and Armstrong, R. N. (1998) Enzymes harboring unnatural amino acids: mechanistic and structural analysis of the enhanced catalytic activity of a glutathione transferase containing 5-fluorotryptophan. *Biochemistry 37*, 6286-94.

(88) Dirr, H. W., Little, T., Kuhnert, D. C., and Sayed, Y. (2005) A conserved N-capping motif contributes significantly to the stabilization and dynamics of the C-terminal region of class alpha glutathione S-transferases. *J Biol Chem 280*, 19480-7.

(89) Stevens, J. M., Hornby, J. A., Armstrong, R. N., and Dirr, H. W. (1998) Class sigma glutathione transferase unfolds via a dimeric and a monomeric intermediate: impact of subunit interface on conformational stability in the superfamily. *Biochemistry 37*, 15534-41.

(90) Sluis-Cremer, N., Naidoo, N. N., Kaplan, W. H., Manoharan, T. H., Fahl, W. E., and Dirr, H. W. (1996) Determination of a binding site for a non-substrate ligand in mammalian cytosolic glutathione S-transferases by means of fluorescence-resonance energy transfer. *Eur J Biochem 241*, 484-8.

(91) Myers, J. K., Pace, C. N., and Scholtz, J. M. (1995) Denaturant m values and heat capacity changes: relation to changes in accessible surface areas of protein unfolding. *Protein Sci 4*, 2138-48.

(92) Codreanu, S. G., Thompson, L. C., Hachey, D. L., Dirr, H. W., and Armstrong, R. N. (2005) Influence of the Dimer Interface on Glutathione Transferase Structure and Dynamics Revealed by Amide H/D Exchange Mass Spectrometry. *Biochemistry 44*, 10605-10612.

(93) Copeland, R. A. (2000) *Enzymes: A Practical Introduction to Structure, Mechanism, and Data Analysis*, 2nd ed., Wiley,VCH, Inc., United States of America.

(94) Johnson, K. A. (2003) *Kinetic Analysis of Macromolecules*, Vol. 267, Oxford University Press, New York.

(95) Holm, L., and Sander, C. (1993) Protein structure comparison by alignment of distance matrices. *J Mol Biol 233*, 123-38.

(96) Morgenstern, R., Svensson, R., Bernat, B. A., and Armstrong, R. N. (2001) Kinetic analysis of the slow ionization of glutathione by microsomal glutathione transferase MGST1. *Biochemistry 40*, 3378-84.

(97) Chen, J., and Armstrong, R. N. (1995) Stereoselective catalysis of a retro-Michael reaction by class mu glutathione transferases. Consequences for the internal distribution of products in the active site. *Chem Res Toxicol 8*, 580-5.

(98) Kubo, Y., and Armstrong, R. N. (1989) Observation of a substituent effect on the stereoselectivity of glutathione S-transferase toward para-substituted 4-phenyl-3-buten-2-ones. *Chem Res Toxicol 2*, 144-5.

(99) Seltzer, S. a. M., L. (1979) Maleylacetone *cis-trans*-Isomerase. Mechanism of the Interaction of Coenzyme Glutathione and Substrate Maleylacetone in the Presence and Absence of Enzyme. *Journal of the American Chemical Society 101*, 3091-3097.

(100) Polekhina, G., Board, P. G., Blackburn, A. C., and Parker, M. W. (2001) Crystal structure of maleylacetoacetate isomerase/glutathione transferase zeta reveals the molecular basis for its remarkable catalytic promiscuity. *Biochemistry 40*, 1567-76.